Absorption studies of thin-film and silicon materials for cryogenic gravitational wave detectors

Ross Johnston

SUBMITTED IN FULFILMENT OF THE REQUIREMENTS FOR THE DEGREE OF
DOCTOR OF PHILOSOPHY

SCHOOL OF PHYSICS AND ASTRONOMY

COLLEGE OF SCIENCE AND ENGINEERING

2025

To my parents,
Louise and David Johnston

Contents

Abbreviations

aLIGO	Advanced Laser Interferometer Gravitational-Wave Observatory
A-MCZ	Advanced magnetic-field-induced Czochralski
AdV	Advanced Virgo
ASD	Amplitude spectral density
ADP	As deposited
BS	Beam splitter
BHs	Black holes
CVD	Chemical vapor deposition
CTN	Coating thermal noise
CBC	Compact binary coalescence
CE	Cosmic Explorer
CEC	Cutting Edge Coatings
CZ	Czochralski
DS	Directional solidification
ET	Einstein Telescope
EM	Electromagnetic
ETMs	End test masses
EPOC	Extreme Performance in Optical Coatings
FOM	Figure of merit

FZ	Float zone
FDT	Fluctuation-dissipation theorem
FAs	Foreign Atoms
FTIR	Fourier transform infrared spectroscopy
FCA	Free carrier absorption
GIXRD	Grazing incidence X-ray diffraction
GR	General Relativity
GWs	Gravitational waves
GWDs	Gravitational wave detectors
HG	Hermite-Gaussian
HF	High frequency
HR	High reflectivity
IBS	Ion beam sputtering
ITMs	Input test masses
KAGRA	Kamioka Gravitational Wave Detector
LMA	Laboratoire Des Matériaux Avancés
LIDT	Laser induced damage threshold
LIGO	Laser Interferometer Gravitational-Wave Observatory
IKZ	Leibniz-Institut für Kristallzüchtung
LVK	LIGO-Virgo-KAGRA
LF	Low frequency
MCZ	Magnetic-field-induced Czochralski
MIT	Massachusetts Institute Of Technology
NIR	Near-infrared
NSEMO	Neutron Star Extreme Matter Observatory

NS	Neutron stars
PTD	Photothermal deflection
PCI	Photothermal common-Path interferometry
PBS	Polarising beam splitters
PRM	Power recycling mirror
PSD	Power spectral density
QPD	Quadrant photodiode
QWL	Quarter wavelength
QM	Quasi-monolithic
RMS	Reactive magnetron sputtering
RT	Room temperature
RBS	Rutherford backscattering spectrometry
SRM	Signal recycling mirror
SL	Single layer
SQL	Standard quantum limit
TCS	Thermal compensation system
TIS	Total integrated scatter
TD	Thermal donor
TMM	Transfer matrix method
TPA	Two-photon absorption

List of Figures

List of Tables

Acknowledgements

I remember the first gravitational wave discovery, back when I was a first year undergraduate student at the University. The rapturous applause, the hungover lecturers and the general buzz throughout the department. Despite three engaging undergraduate projects that followed across this very field, I honestly never expected to do a PhD and at times to finish it. I never expected to love the solitude of the laser lab. Nor did I expect to give a PhD showcase at a conference in Japan, or to fully embrace public outreach, for example, in conducting an improvised gravitational wave orchestra in Cottiers, Glasgow. There are so many highlights and opportunities, like this, that I simply would never have otherwise experienced.

Through deep and focussed research, I have gained good and somewhat predictable habits. Though, most of the understating and support has to be attributed to a few friends and family members. Throughout this research journey, they have emotionally propped me up whilst also helping to shape me into a better person.

To my parents David and Louise, thanks for never telling me what to do, but instead simply asking what I would like to do. Your constant curiosity has really rooted itself at the core of my personality, and for that I now benefit from some deep-friendships. If given the chance, I know that you would have both excelled at university.

To my best friends Alexander and Gregor, thanks for motivating me to be that crazy scientist friend, to catch-up with other things in life and for starting up the whisky and brewing society. To my flatmate Federico, thanks for always keeping the stove on even as I burned the oil at both ends. Thanks for teaching me, through example, to love and respect my family even when they are only down the road. To my partner Jess thanks for always providing me with the best company and chat.

As part of my research Journey, I went on a long-term attachment to LIGO Hanford in America. I was supported there by many great people. Thanks to Tony for keeping me safe behind the deer shields on the highways, and to Camilla for opening me up to new social spheres. Whilst in America, I was grateful to also be hosted by Ashot at Stanford and for the many insightful discussions on state of the world and how the subject of physics can serve as a form of escapism for many.

In Glasgow, thanks to Billy I learned a lot about maintaining a tidy workspace. As for the office, thanks Leigh, Thejas, Naren, Victoria, Storm and Harry for all the chats and for sharing in this journey with me. To Colin and the rest of the workshop staff, thanks for helping me to realise quick mechanical prototypes with short turn around. In the lab, thanks Simon for always being there to blast the tunes and answer my questions. Graeme thanks for teaching me to be more precise and for your extended support across wider studies. Peter, thanks for all the support with the cryostat, the levelled head and of course for all the sarcasm. To Angus, thanks for helping me to prioritise my research and for instilling me with the confidence to pivot where necessary. As for my primary supervisor, Iain, thanks for your due-diligence and ever detailed feedback on my work. Over these past years, given your consistent support, I have gained a significant amount of confidence in both my research and writing abilities. As for all the other colleagues and friends that have passed, thanks for all the memories.

I have been honoured to contribute to the collective knowledge of humanity. I look forward to seeing the materials studied and experiments implemented be further developed as a result of my work. The coming decades will hopefully see what started as some small curiosities in the lab contribute to the construction and sensitivity of billion dollar detectors. For that alone, I am a contented researcher.

Preface

This thesis is an account of research carried out within the Institute for Gravitational Research (IGR) at the University of Glasgow. The focus of the research was on the optical loss characterization of thin-film coatings and bulk silicon optics to support the development of future gravitational wave detectors. Absorbed heat, if not mitigated, would critically limit detector operation due to thermal deformation of the detector mirrors and, in the case of cryogenic detectors, due to heating of the mirror above the required operating temperature. In the lab, the experimental work contained in this thesis leveraged these thermal effects to characterise the absorption of materials. In the process, low absorbing thin-film materials, production methods of silicon and various measurement techniques were investigated.

Chapter 1 serves as an introduction to the field of gravitational wave detection. This chapter moves the discussion from detectors of the past through, the present and onto those proposed for the future. This chapter then highlights the need to reduce the absorption inside the mirrors: to motivate the experimental studies presented in this thesis.

Chapter 2 introduces the theory and historical development in reducing absorption in thin-film coating stacks applicable for gravitational wave detectors. The technique used to measure the absorption called the photothermal commonpath interferometer is then discussed in detail. The sections which follow in this chapter are distinguished by the coating material of interest. Studies made on both titania doped silica and titania doped germania were shared with the author, Dr. S Tait and G. McGhee.

For the titania doped silica, comparison data was provided from N. Demos of Massachusetts Institute of Technology on a distinct optical setup. The absorption work reported on in this thesis led to co-authorship in the publication in Physical Review Letters titled "Titania Mixed with Silica: A Low Thermal-Noise Coating Material for Gravitational-Wave Detectors".

For the titania doped germania, comparison data was provided from D. Diksha of Maastricht University from a different photothermal common path interferometer. The work on titania doped germania coatings reported in this thesis was published in Classical and Quantum Gravity in a paper titled "Optical properties of germania and titania at 1064 nm and at 1550 nm", of which the author of this thesis was a co-author.

Chapter 3 presents the lowest extinction values for aluminium oxide coatings. These measurements when considered alongside previous work by Raymond Robie allowed for theoretical estimates of the coating's performance if integrated into a multilayer coating. This is explored through a detailed design study aimed towards the low-frequency Einstein Telescope detector. Significant theoretical improvements are shown through the use of the alumina materials alongside and in comparison to current baseline materials. The potential for these novel designs to offer preferentially low absorption in the input test masses and increase the overall sensitivity of the detector is made clear.

Chapter 4 introduces the distinct methods of producing high-purity crystalline silicon and how these couple through to affect the optical absorption. This coupling follows through a detailed account of the underlying near infrared absorption mechanisms. The absorption measurements made in this chapter are direct measurements with a transmission setup. The techniques are widely applicable for measurements of cm-thick bulk optics down to absorbance level of a few percent. This work provides a method for establishing the absorption of calibration samples used throughout this thesis.

Chapter 5 details photothermal commonpath interferometric measurements made on silicon samples made with a novel growth technique. For this work, the author received short-author recognition in the publication titled "Quasi-monocrystalline silicon for low-noise end mirrors in cryogenic gravitational-wave detectors". To fully show the promise of this novel silicon growth method for future gravitational wave detectors, these measurements are considered alongside the work of colleagues Peter Murray and Maya Kinley-Hanlon into the mechanical properties and collaborators Frank M. Kiessling and Iryna Buchovska from Leibniz-Institut für Kristallzüchtung (IKZ) Berlin into parallel measurements and the growth of the silicon. The factors limiting the absorption were investigated, and clear recommendations for producing silicon at a scale required for gravitational wave detectors are made.

Chapter 6 showcases a photothermal deflection based technique that is capable of spatially resolving absorption features in bulk silicon optics. This technique was implemented with the support of Dr. A Bell. The alignment, detection and noise improvement methodologies are discussed. The silicon samples measured throughout this chapter were previously sourced by the author, Z. Tornasi, Dr. A Bell and Dr. I Martin. The need to mitigate select spatial variances are presented for the first time, and a clear case for mapping silicon samples is shown. The spatial-absorption was investigated for high absorbing samples and no significant trends were found. A novel type of silicon was investigated with the support of Ashot Markosyan using a similar setup at Stanford University. Although a low average absorption was found, significant longitudinal absorption trends were observed in the samples measured. Methods of improving the absorption with post-deposition treatments are discussed, and as a result the promise of this technique for producing optics suitable for future detectors is made clear.

Chapter 6 introduces a novel optical calorimetric technique. The methodology behind the design, analysis and improvements as such are discussed. The setup was used to measured high-resistivity silicon optics down to cryogenic temperatures. In line with previous studies of lower-resistivity silicon, no significant trend with absorption was found. The potential for this novel technique to be improved and to provide a quick and accurate method for investigating absorption as a function with temperature of bulk materials is discussed in detail.

Summary

One hundred years passed from the postulation of general relativity by Einstein to the measurement of one of its profound realisations. Gravitational waves arising from accelerating mass distributions were for a long time considered to be too faint to detect, even accounting for the most massive events in the Universe. This doubt passed over the years through the development of distinct detectors from resonant bars through to the Fabry-Pérot interferometer used today. These were only made possible in part due to the significant advancements in laser technologies, optical and mechanical metrology and digital sensing. Not only have these advancements benefitted humanity the world over, but the accumulation of many detections have provided a profound insight into the nature of the Universe itself.

In current detectors, coating thermal noise sets the limit at their most sensitive frequency. In order for new coatings to be validated, they need to also have an extremely low optical absorption. Extensive studies were made into the optical absorption of a range of coating materials. Germania and perovskite materials were studied, and showed improvements in their optical absorption on towards the targets required for gravitational wave detectors. Both titania-germania and titania-silica coatings were extensively studied to support their down selection for detector upgrades. For each material, the studies ranged between multiple coating deposition vendors; over different post-deposition treatments and between coatings deposited in both single layers and stacks. The work by the author showed that these materials can reach the same level as that found in the current coatings of gravitational wave detectors. In consideration alongside parallel studies, that demonstrated noise improvements, the coating materials are both actively being developed for future upgrades.

As of 2021 at the end of the 3rd observing run, 90 events had been published. In the current observing run, which started in 2023, excellent candidate events with a high probability of being genuine GW signals have been observed at a rate of approximately a few per week, with the current generation of gravitational wave detectors. To bring a stepped improvement and a sensitive detector distance that pushes towards the edge of the observable Universe, a new generation of detectors will be developed. In Europe,

Einstein Telescope is scheduled to come online in the 2030s as an array of six detectors. Three of these will be termed the low-frequency (ET-LF) detectors for their increased sensitivity to gravitational waves towards the low end of the audible frequency band. To reach this sensitivity, they must operate their core optics at cryogenic temperatures. One of the main challenges expected in operating at this temperature regime is the heat loading. Due to a complex multitude of material requirements, the optic materials from substrate to coating will all have to be distinctly different from those used in current detectors. However, these materials have yet to meet the optical absorption requirements and so the problem with heat loading persists. This problem was met recently within a Japanese detector called KAGRA in part due to the bulk absorption of sapphire. Within the frame of ET-LF, this thesis is broadly motivated by the need to reduce the optical absorption for a range of candidates materials.

For improvements to the coatings, aluminium oxide was investigated, and after a heat treatment study was shown to have an extremely low absorption. As previous research also found that coatings deposited in the same batch had low-thermal noise, it was interesting to design coatings which included this material. From these designs, the theoretical performance if integrated in specifically the low-frequency Einstein Telescope detector was evaluated. Compared to the baseline design, significant improvements are shown through the use of alumina oxide materials. These designs are shown to be capable of not only increasing the overall sensitivity of the detector to a viable level, but as a result of these absorption measurements to reduce the expected heat load in critical core optics.

Alongside sapphire, silicon is one of two materials being considered for use as the bulk substrate of these core optics. As silicon optics are considered as the baseline for the Einstein Telescope but have not been demonstrated to have a low enough absorption, it is imperative that they are researched in detail. Motivated by this, the research focussed on measuring a range of different silicon samples. The optical absorption of two novel types of silicon were mapped for the first time. One type, grown through directional solidification, showed both a high baseline and variability in its absorption. The origins were investigated through empirical modelling of the formation rates of absorbing sites. The discrepancy indicated that undesired defects dominated this localised increase in absorption. In supporting the characterisation of this silicon, this work could enable the material, to be the first substrate capable of meeting the physical scale required for the core optics of future detectors such as ET-LF.

The absorption levels of materials are typically considered to be independent of operational temperature. However, recent measurements and theories had suggested that the low-absorption of silicon measured at room temperature might be significantly different at cryogenic temperatures. A calorimetric technique was set up to be able to measure small scale samples. For low-purity silicon, good agreement was found with other measurements at room temperature. However at cryogenic temperatrues there was a significant percentage increase. This increase was also found for a high-purity silicon sample. Although, this sample alongside a mid-resistivity sample showed an excess absorption at room temperature. Optical scatter was identified as a potential source of this excess absorption through scatter measurements. Through improvements to the scatter shielding the level of scatter was significantly reduced. Following this experimental design, there is promise for a minimal setup and high-throughput measurement system. Further development of the setup will be essential to ensure that there are no additional head loads that might otherwise exceed the operational budget for future detectors.

For the benefit of other cryogenic detectors such as Cosmic Explorer and Voyager, the limiting effect not just of a high absorption but for spatial variation as such is discussed for the first time. To mitigate this effect from limiting the operation of future detectors, it is important that the absorption profile of all bulk substrates is mapped prior to integration. Through the setup of a photothermal deflection technique at Glasgow, the potential for this technique was demonstrated. High absorbing samples were measured, but no variation was found. As the source of variation is expected to largely come from impurities, the second type of novel silicon measured was one that was expected to have a distinctly low concentration. The sample was processed and measurements made indicated a significant variation, which could in itself lower the acceptable head load.

There is hope that these results and techniques developed and shown throughout this thesis can further be accelerated through upcoming industrial partnership. It is promising that German research groups such as IKZ Berlin and DZA are pledging to bring production and measurement of silicon materials in house. Given the University of Glasgow historical breadth in research of materials, further expanded by the work contained in this thesis, there is a clear path for progression ahead.

Declaration

I declare that, except where explicit reference is made to the contribution of others, that this dissertation is the result of my own work and has not been submitted for any other degree at the University of Glasgow or any other institution.

Ross Johnston

Chapter 1

Gravitational wave detection

1.1 Introduction

From the first direct detection of gravitational waves (GWs) from a binary black-hole merger (known as GW150914) on the 14$^{\text{th}}$ of September 2015 [1] through to April 2021, there have been 90 published detection events made with the Laser Interferometer Gravitational-Wave Observatory (LIGO) and Virgo interferometers [2, 3, 4]. In subsequent runs, many more candidate events have been detected. The detector network [5], ability to triangulate the source [6] and network sensitivity are all set to grow, with existing detectors being upgraded to extend their operation to 2030. In the decades that follow, a 3$^{\text{rd}}$ generation of detectors, notably consisting of Einstein Telescope (ET) [7] and Cosmic Explorer (CE) [8], is also expected to come online.

There are a few distinct research pathways which will enable 3$^{\text{rd}}$ generation detectors to be sensitive to a wider range of events and further back towards the edge of the Universe. One distinct research pathway, for next-generation detectors, involves operating the main detector mirrors at cryogenic temperatures [9]. This leads to a separate set of challenges which must be overcome to ensure stable operation. Keeping the mirrors, used to reflect the light within the interferometer, at cryogenic temperatures is one of the significant challenges. This will require reduction to the absorbed heat loads: notably that from the optical power absorbed as it is transmitted through the mirror [7, 10]. This chapter will serve as an introductory summary to the field of GW detection from historical progress; to current limiting noise sources and expected challenges on the way to operational cryogenic temperature detectors. In particular, this chapter will highlight the need to reduce the absorption inside the mirrors: to motivate the experimental studies presented in this thesis.

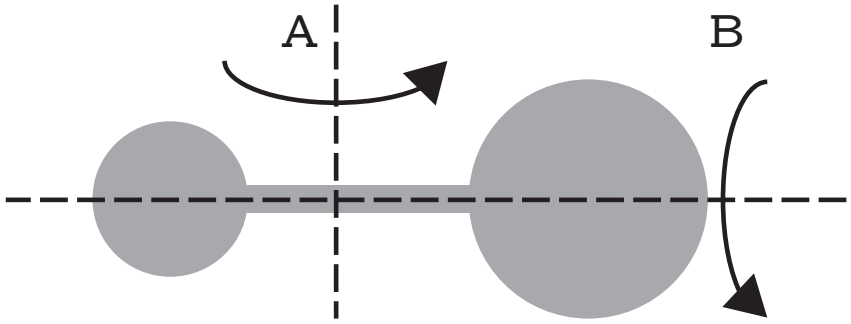

Figure 1.1: Accelerations around axis A will produce GWs. However, accelerations around symmetric axis B will not produce GWs.

1.2 Gravitational waves

Gravitational waves were first postulated by Einstein in 1916 [11], a year after he published his general theory of relativity (GR) [12]. It took decades more research to arrive at a mathematically accurate description [13] and for a detection method to be initially proposed [14].

The general theory of relativity defines gravity as the curvature imparted into spacetime by an object's mass. As the mass evolves with time, curvature changes are propagated outwards at the constant speed of light (c). When a mass distribution, as shown in figure 1.1 [15], accelerates, energy will be radiated away from the system in the form of GWs.

Most of our understanding of the Universe has come from the detection of electromagnetic (EM) waves, which mainly have dipolar nature. In contrast, GWs are quadrupolar in nature, as there is only one sign to mass. Also, due to the weakness of the gravitational force, the strength of GWs is considerably weaker [15] such that only the most massive and compact of sources are detectable with current gravitational wave detectors (GWDs).

The quadrupolar GW permitted by GR have two polarization states of $\times$ and $+$ [16] with the latter distinguished by a 45-degree rotation and shown in figure 1.2 [17]. The strain amplitude of this wave is a unitless distance ratio between the change in the separation ($\mathrm{d}L$) and the intrinsic separation (L) of two reference masses [18]. In the plane perpendicular to the propagating direction, a gravitational wave simultaneously expands in one

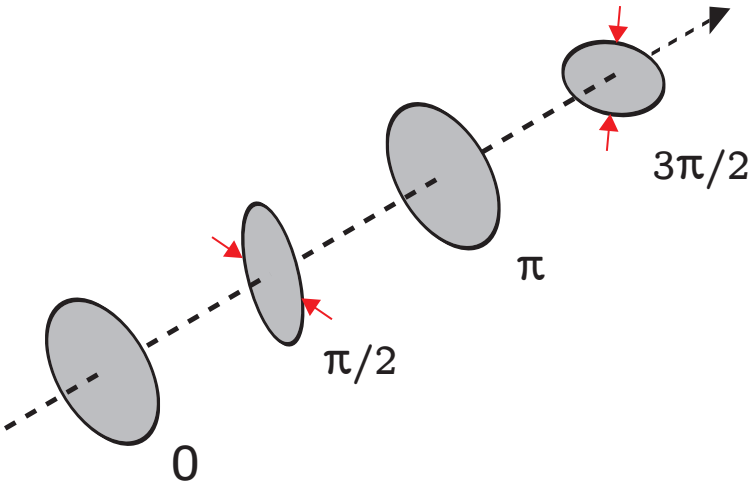

Figure 1.2: The isometric figure shows how a circular ring, representative of space, is stretched in the plane perpendicular to the propagation direction of a plus (+) polarised GW. The cross (×) polarised wave is rotated by 45 degrees around the axis of propagation.

axis whilst contracting in an orthogonal axis. An ideal wave would then be incident on a ground-based GW detector, discussed in section 1.3.2, with its oscillatory plane parallel to the measurement plane of the detector. This relative measurement between two axes gives an additional factor of two to the measured strain amplitude (h) as

$$h = \frac{2\mathrm{d}L}{L}\,. \tag{1.1}$$

From current ground-based GW detectors, discussed in section 1.3.3 through to the next-generation detectors, the range of astrophysical sources from which we expect to detect GWs are divided into several categories, as detailed below.

Compact binary coalescence sources (CBCs): Black holes (BH) and neutron stars (NS) paired as (BH/BH), (NS/NS) or (BH/NS) in binary systems have all been detected as compact binary coalescing (CBC) [19] events. This is characterised by a decay in the pair's orbital separation prior to them merging together. At the time of publication, all detected events are CBCs with most of these being BH/BH [2, 3, 4]. The GW strain signal recovered from these events over a short ($< 1\,$s for BH-BH and $< 100\,$s for NS-NS) timescale shows a simultaneous rise in frequency and strain as the pair move towards merger. It is inside the final few orbits that the GW strain peaks into the observational

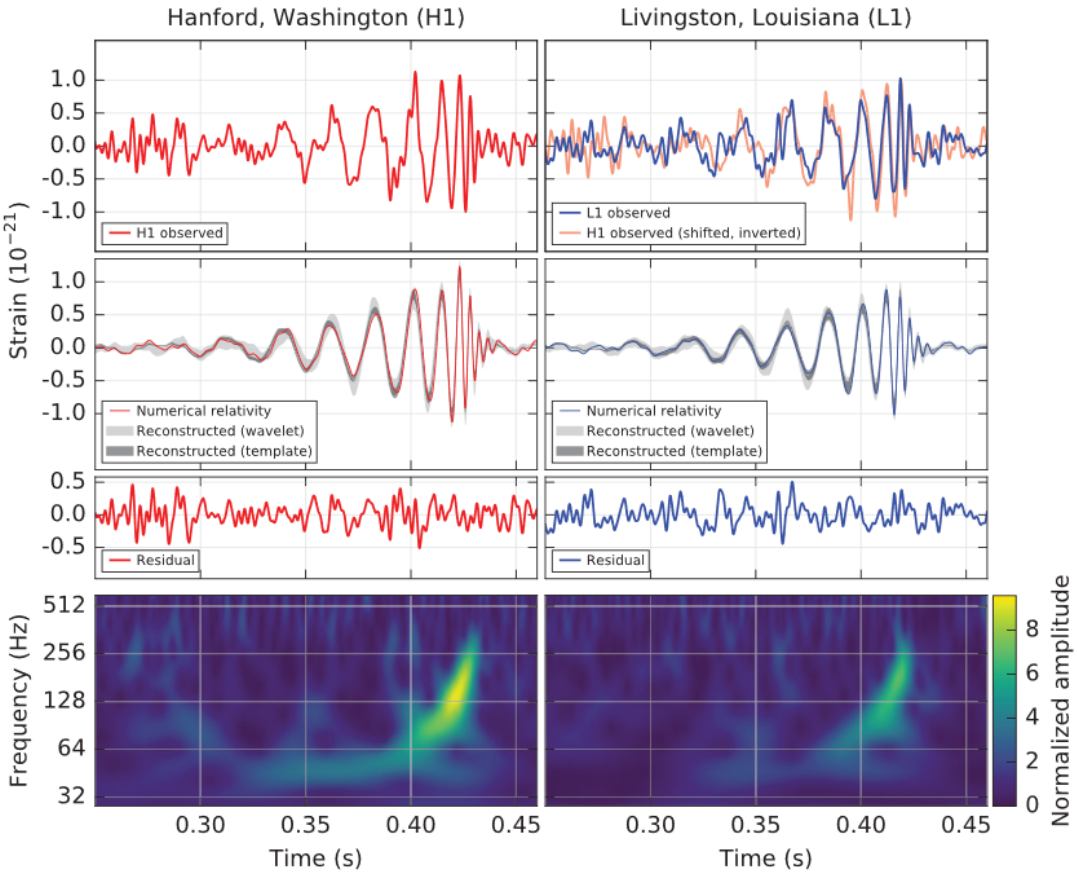

Figure 1.3: The first observed GW, titled GW150914. The two columns show the signal as measured and processed in the two separate LIGO detectors at Hanford (left) and Livingston (right). The Hanford trace is shifted back in time by 6.9 ms, across all plots, as it took longer for the GW to reach this detector. Applied data processing changes between rows, with the first showing the strain data for each detector, and the second shows the reconstruction of the strain from numerical relativity waveforms and filtered within $35 - 350$ Hz band of interest (solid lines). The third row shows the residual calculated from the difference of the first and second rows. The fourth shows the time-frequency representation of the strain data, illustrating the characteristic frequency shift as the pair inspiral [1].

window. Once the pair has merged, the single vibrating mass continues to release GWs as it enters the ringdown phase, where the GW signal begins to decay [20]. This CBC process can be easily followed from the signal evolution on the frequency domain, as shown for the first event on figure 1.3.

Burst sources: Bursts are typically short lived events for which the origins are not well understood [21]. As a result, there are large uncertainties in the potential signal's frequency-time evolution. This makes it difficult to search for events, as they might resemble noise spikes in the detector. An event which, for example, is expected to produce detectable bursts GWs is the non-symmetric core collapse of a star [22] as happens during a supernova event.

Continuous waves: A continuous wave is a signal whose frequency is either constant or changing very slowly with time. The most notable example is expected to come from a rotating neutron star with an asymmetric mass distribution [23]. This asymmetry is expected to arise either due to the accretion from a companion object or by vibrational modes in the NS itself. If the NS is a pulsar beaming EM waves towards earth, then the pulse frequency can be matched to the spin frequency of the NS and then further matched onto the GW frequency [24].

Stochastic background: A stochastic GW background level is expected to arise from two sources. Significant contributions are expected from the superposition of many individual and unresolvable CBCs, including those from white dwarf stars. The other distinct source are signals from the early Universe [15], which could provide a window into the inflation period coming from $< 1\,\mathrm{s}$ after the Big Bang. This is considerably further back than the electro-magnetic equivalent, as the cosmic microwave background occurred $100,000\,\mathrm{years}$ after. Distinguishing these GW sources will require significant data from future space-based detectors [25].

Detecting more sources of GWs from each of these four categories will allow us to better understand many aspects of the Universe. For specific astronomical objects such as black holes, the improved demographics from further detections might reveal a prominent population of masses in previously unseen ranges [26] and help distinguish any that are from primordial origins as opposed to stellar. With a significant increase in neutron star detections their internal structure, physics, and role as progenitor masses for short gamma ray bursts will be better understood. When combined with EM measurements, the continued study of neutron star mergers will clarify their contribution in producing heavy elements in the Universe [27, 28]. The broad sensitivity range, enabled by future ground and space based detectors, will allow a considerable amount of fundamental physics to be tested. Different magnitudes of source merger masses will allow the testing of GR in different gravity regimes, alternative theories of gravity and of some of the biggest challenges in cosmology [29, 30].

1.3 Past and present gravitational wave detectors

The first indirect detection of GWs came from observations by Hulse and Taylor, starting in 1975, of the orbital period decay in a binary pulsar system [31]. By observing the system for 30 years, the agreement of this decay with that proposed by GR due to the emission of GWs was found to be accurate within 0.1 % [32]. Prior to this, efforts to directly detect GWs started in the 1960s with Joseph Weber's resonant bar detectors [33].

1.3.1 Resonant bar detectors

Bar detectors were initially motivated by a thought experiment that questioned if the GW strain could be recovered by the potential energy imparted from the stretch and compression of a large solid bar. Treating this bar as point masses between a spring, defined by the material's mechanical properties, theoretically showed that it should be possible to see the GW signal exciting the bars resonant modes [21]. However, the bars were also excited by room temperature thermal fluctuations in the medium [34], which alongside electronic readout error [35] set the sensitivity to a level of $h \approx 10^{-16}$: two orders of magnitude less sensitive than strain detected, for example, from the first event [1]. Weber on several occasions with solid aluminium bar detectors up to 3000 kg claimed to detect GWs [36, 37, 38]. This inspired other research groups across the globe to replicate such a measurement [39, 40, 41] and to further improve the sensitivity through cryogenic cooling [42, 43] and alternative spherical shapes [44, 45]. Despite these continued efforts and a network of detectors that each operated at around 900 Hz with a sensitivity on the order of $h \approx 10^{-21}$ [46], where detections have since been made, no other GW detections by a resonant bar have been reported. Fundamentally, the operational sensitivity and very narrow bandwidth were limited by the dimensions and mass of the resonant bar [46]. Important lessons learned from this research carried into the design and operation of modern detectors. Notably, the need to routinely evaluate the limiting noise sources in order to improve the sensitivity of GW detectors [47] alongside independent measurements from geographically separated locations [48].

1.3.2 Interferometric gravitational wave detectors

Despite proposals to combine all the resonant bar advancements into an upscaled detector with a proposed sensitivity of $h \approx 10^{-22}$ and across a 200 Hz bandwidth [49] this technique eventually gave way to interferometric detection methods. Interferometry was, first, proposed as a method of monitoring the resonant bar's displacement [50], but when realised in a new configuration offered an even wider bandwidth. For ground-based observations in the audio frequency band, from $10 - 10^4$ Hz, the method which has directly detected GWs and is being considered for future detectors is a derivative of the Michelson interferometer [51].

The Michelson interferometer compares the length of orthogonal arms to measure any changes due to the passing of a GW. The optical path for the Michelson is shown in figure 1.4. The input laser beam is directed to a beam splitter (BS) which sends light equally along both arms, where it travels the length of the arms before being reflected from the end mirrors and returning to the beam splitter. Here it will interfere, and if the path length is offset by an integer multiple of a half-wavelength ($n\frac{\lambda}{2}$), then theoretically no light will exit towards the photodiode. When a GW passes, the cross polarisation of the wave will periodically expand and contract both arms relative to each other. This will change the relative phase between the arms, the interference pattern, and as a result will be measurable as a variation in the intensity output. This is a simplified case for ease of understanding. In reality, interferometers operate by trying to maintain a constant, close to zero, intensity output. The GW signal is recovered then from the calibrated signal on the photodiode output. To achieve this in real-time there are complex control loops to ensure the target crossover gains in optical power are met both across the instrument and the frequency space. These control systems act to effectively keep the arm-lengths constant.

The best strain sensitivity measured with a white light Michelson interferometer in the late 1960s was $h \approx 6 \times 10^{-15}$ [52]. A simple way to increase the signal size with the Michelson interferometer design is to increase the length of the arms. This will increase the length (L) of the effective object acted on such that the same GW strain amplitude (h) given in equation 1.1 will produce a larger change in length ($\mathrm{d}L$). However, the curvature of the Earth makes it difficult without significant infrastructure and expense to reach the optimal detector length [15]. This optimal length scales inversely with frequency and therefore linearly with the GW wavelength, before the strain flips direction. In account of the

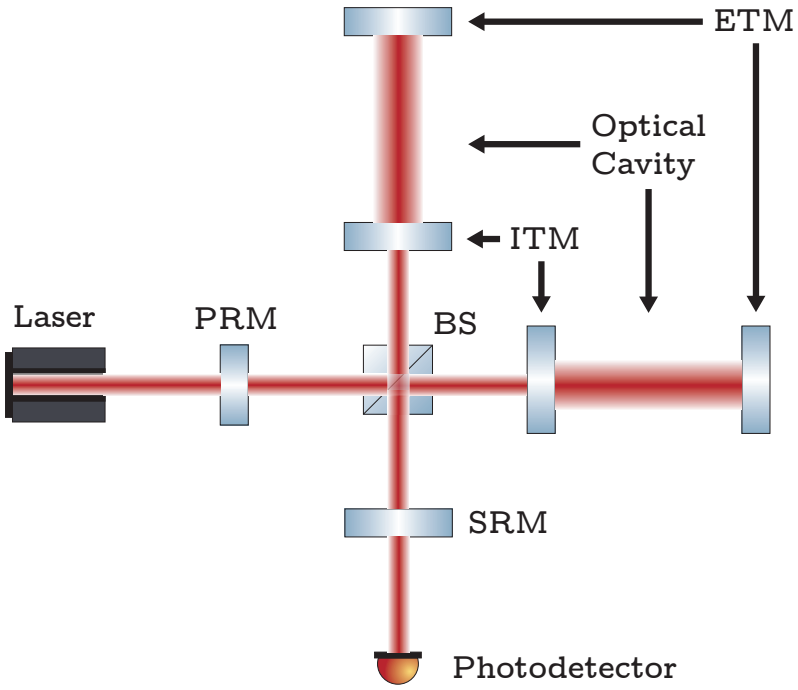

Figure 1.4: Simplified schematic layout of 2nd generation GW detectors. The standard Michelson interferometer is formed from the beam splitter (BS) and the end test masses (ETM). GW detectors notably make use of Fabry-Pérot optical cavities with the addition of the input test masses (ITM). Before the BS there is a power recycling cavity represented for simplicity here with a single, power recycling mirror (PRM). After the BS, there is likewise a signal recycling mirror (SRM).

phase evolution of the wave (see figure 1.2) and the light's round-trip, the optimal length is a quarter of a GWs wavelength. For a 100 Hz GW roughly in the middle of the sensitive logarithmic frequency space, the optimal arm length of this Michelson interferometer would be 750 km [53]. This is too long for a ground-based GW detector.

In order to improve the sensitivity of the Michelson interferometer so that it is suitable for GW detection, novel technologies were developed [54]. Only a subset of these technologies which overlap with the fundamental operation of the interferometer and the research in this thesis are shown in figure 1.4 and detailed below.

Laser: The input laser for the interferometer of current GW detectors is a complex multiple stage system. The 1064 nm Nd:YAG continuous-wave laser source is passed through a series of control systems to ensure the desired output laser quality [55]. There is notably a high degree of stabilization in the frequency, beam direction and intensity required to prevent unwanted intensity changes on the photodiode: which could otherwise mask or

create a false GW signal. In current GW detectors, high laser output power of up to 180 W [55] is also necessary to provide a high GW signal relative to shot noise. Overall, the laser was a key enabling technology that arose alongside the first clear proposal for interferometric GW detectors [18].

Fabry-Pérot interferometer: The effective arm length is increased through the addition of semi-reflective mirrors between the beam splitter and the end mirrors of each arm. Between these two mirrors, an optical Fabry-Pérot cavity is formed, which allows light to constructively interfere inside. The Fabry-Pérot cavity technique was first devised in 1899 [56] and later applied to GW detector design from 1980 [57] onwards. Constructive interference is equivalent to light being stored inside the cavity for many round-trips. This effectively acts to increases the detector arm length beyond the sensitivity if it was a simple Michelson interferometer. The increase in signal is a quantified by the finesse of the cavity which is inversely proportional to the number of photons lost per round trip. In reality, the power and therefore sensitivity gain of the cavity varies with frequency and the cavity in itself acts as an optical equivalent to a low-pass filter. The bandwidth of this filter allows frequnecy sidebands which may carry the gravitational wave signal, in the audible range and within the cavities linewidth, to be resonant in the cavity and therefore be transmitted out for measurement [58]. Furthermore, the increase in circulating arm power will impact the noise levels as discussed in section 1.4.3.

Highly reflective test mass mirrors: There are thousands of optical components that go into GW detectors, but the most expensive due to extensive state-of-the-art R&D into metrology and measurement of intrinsic physical properties are the input test mass (ITM) and end test mass (ETM) cavity mirrors. To obtain a high circulating power requires high reflectivity (HR) coatings. The underlying physics behind this reflectivity level is explained in section 2.4. Maintaining the optical power here sets strict thresholds on the acceptable scattering and absorption from test mass substrates and coatings. Chapter 2 will contain detailed absorption studies of coatings for future GW detectors.

Mirror suspension: In order to isolate the test masses, they are each suspended at the end of a multi-stage pendulum [15]. A single pendulum acts as a low-pass filter by strongly attenuating the through coupling of frequencies above its resonance. In the detectors, the individual pendulum stages have close and precisely picked resonances. The equivalent cascaded low-pass filter acts then to minimize the seismic noise transferred from the ground to the end test mass. This reduction allows displacement, of these almost free-masses [15, 48], along the intended optical path the GW signals [18] to be measured.

Power and signal recycling: To both increase the signal and reduce the noise, light is recycled inside the detector with the placement of additional mirrors [59]. One of these mirrors is called the power recycling mirror (PRM), as it is aligned to reflect back into the interferometer the significant light power that would otherwise be lost from the BS towards the laser input. The effect of this is to increase the power passed forward into the interferometer cavity relative to the required input laser power. An additional mirror called the signal recycling mirror (SRM) positioned before the photodiode in a similar sense resonantly enhances light. However, in this case, it amplifies the otherwise small GW-induced light amplitude coming from the interferometer output [59, 60]. This essentially forms another optical cavity with its own resonant frequency, linewidth and bandwidth. The bandwidth and peak gain of the GWD as a whole can be tuned by adjusting the position of the SRM and therefore length of the equivalent cavity [58]. This allows the GWD to be optimised for a target gravitational wave spectrum and therefore for a particular astrophysical source.

Vacuum system: The vacuum system of each detector reaches 10^{-9} Torr and spans the arm length between the ITM and ETM mirrors. They are therefore some of the largest ultra-high vacuum systems in the world. If the air was otherwise in the chamber, it would notably impart limiting noises through thermal Brownian vibrations on the test masses and the scattering of the cavity light [61].

1.3.3 Current gravitational-wave detectors and their detections

The current GW detector network is entirely ground-based and in its 2^{nd} generation. This generation includes the Advanced Laser Interferometric Gravitational-Wave Observatory (aLIGO) as a detector pair in the USA with LIGO Hanford Observatory, Washington, and the other, 3000 km away in Louisiana called the LIGO Livingston Observatory [55]. As part of the wider international network, there is also Advanced Virgo (AdV) in Italy [62, 63] and the Kamioka GW Detector (KAGRA) in Japan [64]. KAGRA, through its novel design choices of operating underground and with its mirrors preferentially at cryogenic temperatures, is closer to some cryogenic 3^{rd} detectors designs discussed in section 1.5. At the time of writing, the sensitivities of AdV and KAGRA are being optimized to bring them closer to that of aLIGO. This collective detector network is called the LIGO-Virgo-KAGRA (LVK) collaboration. Since these detectors came online in the early 2000s [65, 66], except for KAGRA in 2020, they have always been distinguished as Fabry-Pérot arms in an L-shape interferometer configuration. In LIGO the arms are 4 km long compared to

the 3 km arms of both Virgo and KAGRA. Operating at this scale alongside additional smaller tested interferometers [67, 68] and reaching high sensitivities, as $h = 6 \times 10^{-22}$ in the case of LIGO [69], were some notable achievements from the 1st generation of detectors.

The advanced prefix for the aLIGO and AdV is in reference to the upgrades made, from 2008-2015, in between initial science runs to bring what was formerly initial LIGO and Virgo up to their 2nd generation status. These upgrades are discussed in section 1.4 in the context of the noises sources that they helped to mitigate. After being upgraded, aLIGO came online in 2015 for a scientific observing run called O1. Just before the run officially started, the first GW event was detected exclusively by aLIGO in 2015 with a peak strain of $h \approx 10^{-21}$ [1]. This detection opened the world to a new-era of astronomy and earned Rainer Weiss, Barry Barish and Kip Thorne the 2017 Nobel Prize in Physics [70]. Since then, the LVK network has detected 90 confirmed events across the first three observing runs [2, 3, 4]. Another landmark discovery from the 2nd generation detectors was made in 2017 by the detection of GWs and EM, notably gamma-ray, radiation [71] from the same event, a neutron star merger. This unified the formerly distinct branches of astronomy and further transitioned us into an era of multi-messenger astronomy.

At the time of writing, aLIGO detectors are in observing run O4 and detecting events every few days with a strain sensitivity of $h \approx 10^{-23}$ in the audio frequency band. During observation downtime, further upgrades will bring the detector up to its new status as A+LIGO, with a sensitivity hopefully approaching $h \approx 2 \times 10^{-24}$ [72]. In the case of LIGO detectors, there are plans to extend the lifetime towards the end of the 2020s, with proposed upgrades named LIGO A# [73]. In a similar timeframe, LIGO India should be constructed and come online with similar sensitivities to other 2nd generation detectors [5, 74, 75].

1.4 Limiting noise sources in gravitational wave detectors

Current detector research is focused, for a large part, on reducing the individual noise sources to bring the combined total down. At the lower and higher end of the operational bandwidth, limiting noises come from generally distinct sources. At the lower frequencies of below 10 Hz, seismic noise significantly contributes to the limiting noise floor. Once

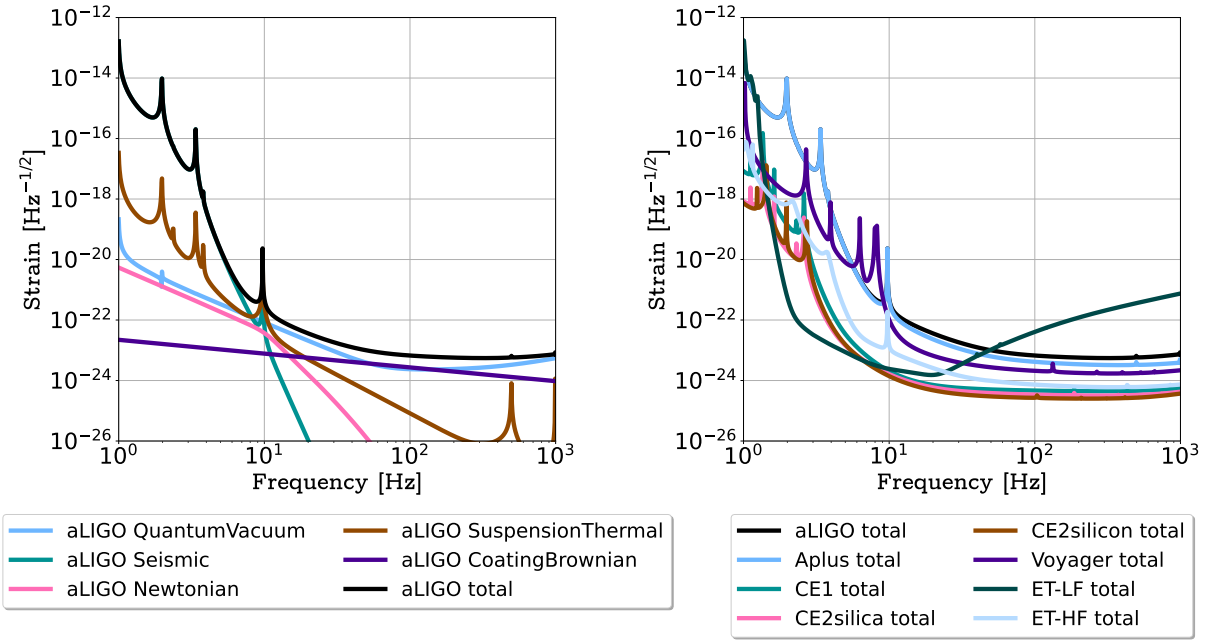

Figure 1.5: ASD strain noise curves for different GW detectors. The (left) plot shows each of the noise sources discussed throughout section 1.4. There are additional noise sources, but as they are not expected to limit the noise of aLIGO or future detectors, they are not shown here. The (right) plot shows, by comparison, the proposed total noise curves of future detectors discussed in section 1.5. The future detectors which would operate at cryogenic temperatures are CE2 silicon, Voyager and ET-LF.

this has been adequately filtered, and we move to the mid-frequency band around $10 - 100$ Hz, thermal noise becomes problematic. Across the full frequency bandwidth, quantum effects from the action and detection of the laser beam have a sizeable contribution to the noise floor. Each of these prominent noise sources are shown for aLIGO in figure 1.5 and discussed throughout this section.

The noises sources will take the form of power spectral density (PSD) equations, which would evaluate to have units of strain^2/Hz. Although, these will not be evaluated in detail here, if considered against the overall target PSD for the detector they should be added together. To further compare these to the total amplitude spectral density (ASD) strain targets discussed throughout this chapter, the square root of the total PSD must be taken to get units of strain/Hz$^{\frac{1}{2}}$. These ASD targets in total and individual contributions are shown for aLIGO in the figure 1.5.

1.4.1 Seismic noise

The seismic noise fundamentally arises from the vibrations in the Earth as sensed on the surfaces of the detector test masses. To best mitigate this noise, each test mass is suspended to form an ideal passively isolating pendulum. For the noise not to limit the sensitivity a reduction in the noise from the ground by at least a factor of a billion is required [76]. This is achieved by combining multiple low-resonance pendulum stages above the test mass [77]. However, this comes at the expense of large resonance spikes, which without active mitigation would be seismically excited and limit operation. Other active and passive control techniques are also found, further up the pendulum chain, to further reduce the ground vibrations [78, 79]. The seismic noise curve in figure 1.5 shows the benefit of low frequency suspension resonances as the ASD seismic noise floor drops by $\approx 1/f^2$ for with increasing frequency, for each suspended pendulum stage in the chain.

1.4.2 Thermal noise

In current detectors, the thermal noise sets a limit around the most sensitive operational frequency of 100 Hz. Brownian thermal noise [80] arises from the thermally induced molecular vibrations of both the test masses and suspensions. These vibrations lead to an excitement of the resonant modes whilst the intrinsic damping, commonly referred to as the mechanical loss, quantifies the rate at which energy is dissipated away from these modes. Materials with a low mechanical loss have sharper resonances: in which more thermal motion occurs close to the resonant frequency. The PSD of the underlying thermal force was originally derived by Callen [81, 82, 83]. To understand the noise, it is more convenient to express this with PSD of the thermal motion as described by the Fluctuation-Dissipation theorem (FDT):

$$S_{\mathrm{x}}(f) = \frac{4k_B T}{(2\pi f)^2} \Re\{\frac{1}{Z(f)}\}\,. \tag{1.2}$$

The frequency-dependent impedance $Z(f)$ is the resistance to the internally derived movement, k_{B} is the Boltzmann constant and T is the temperature dependence. For a simple harmonic oscillator system, the impedance

$$Z = f + i\omega m + \frac{k}{i\omega} \tag{1.3}$$

with mass (m) and spring-constant (k) can be substituted into equation 1.2. As shown in Martin [84], following the treatment of Saulson [85], this can be simplified further down to give the thermal noise

$$S_{\mathrm{x}}(f) = \frac{k_{\mathrm{B}} T \phi(f)}{2\pi^3 m f_0^2 f}, \quad \text{for } f \ll f_0. \tag{1.4}$$

for the low frequency, relative to resonance frequency (f_0) limit. In this regime, the noise is then linearly dependent on the mechanical loss ($\phi(f)$).

The low-frequency solution presented is relevant for GW detector test masses as their resonances are designed, unlike resonant bar detectors, to be far above the upper limit of the detector's operational bandwidth: with a frequency ($> 10\,\mathrm{kHz}$). In the case where the mechanical loss is spatially homogeneous, the multiple resonant modes combine to form the thermal noise with the summation weighted on the overlap between the mirror's motion and the beam intensity incident on the surface [86].

In reality, the loss is not spatially homogenous. For example, the test mass mirrors are made by depositing a micrometer-scale thin coating onto a large substrate bulk. Unfortunately, the reflective coating materials have a mechanical loss many orders of magnitude higher than that of the substrate [87, 88]. As a consequence, Levin, starting from the FDT, showed that the mode summation breaks down and that the interferometer will be most sensitive to thermal noise originating close to the place of interaction between the laser beam and the mirror [89]. Therefore, coating thermal noise (CTN) dominates over the thermal noise of the substrate. A general form of this was derived by Yam [90] and later corrected in Tait [91]

$$S_{\mathrm{CTN}}(f) = \frac{2k_{\mathrm{B}}T}{\pi^2 f} \frac{1}{w^2} \frac{1 - \sigma_{\mathrm{sub}} - 2\sigma_{\mathrm{sub}}^2}{Y_{\mathrm{sub}}} \sum_{\mathrm{j}} b_{\mathrm{j}} d_{\mathrm{j}} \phi_{\mathrm{k}} \tag{1.5}$$

$$b_{\mathrm{j}} = \left[\frac{(1-2\sigma_{\mathrm{j}})(1+\sigma_{\mathrm{j}})}{(1-2\sigma_{\mathrm{sub}})(1+\sigma_{\mathrm{sub}})} \right] \frac{1}{1-\sigma_{\mathrm{j}}} \times \left[\left(1 - n_{\mathrm{j}} \frac{\partial \theta_{\mathrm{c}}}{\partial \theta_{\mathrm{j}}} \right)^2 \frac{Y_{\mathrm{sub}}}{Y_{\mathrm{j}}} + \frac{(1 - \sigma_{\mathrm{sub}} - 2\sigma_{\mathrm{sub}}^2)^2}{(1+\sigma_{\mathrm{j}})^2 (1-2\sigma_{\mathrm{j}})} \frac{Y_{\mathrm{j}}}{Y_{\mathrm{sub}}} \right]. \tag{1.6}$$

The main factors setting the magnitude of the CTN are temperature (T), beam radius (w) and for each layer which makes up the full coating its contributions sum together with index j starting from the outermost layer. For each layer, the thickness (d_j) is combined with the mechanical loss (ϕ_j) and a correction term (b_j). The correction term carries the Young's modulus of the coating layer (Y_c) relative to the substrate (Y_s), the Poisson ratios for the coating layer (σ_j) and substrate (σ_sub) and the coating, refractive index (n_j). Lastly, ($\frac{\partial\theta_\mathrm{c}}{\partial\theta_\mathrm{j}}$) is the sensitivity of the phase of the light reflected from the coating (θ_c) to fluctuations in the round-trip phase (θ_j) in each layer. The total detector CTN is evaluated from the sum of the uncorrelated individual ETM and ITM mirrors CTN contributions [92]

$$S_{\mathrm{CTN}_{\mathrm{Detector}}}(f) = 2 \times \left(S_{\mathrm{CTN}_{\mathrm{ETM}}} + S_{\mathrm{CTN}_{\mathrm{ITM}}}\right). \tag{1.7}$$

Beyond the linear scaling from the frequency and temperature, measurements of coatings show a significant variation in the mechanical loss with both temperature [93, 94, 95, 96] and frequency [97, 98]. For the next observing run O5, A+LIGO is looking to further improve the beyond the current aLIGO coatings by notably reducing the thermal noise by a factor of two [99], and so continued efforts are under way to measure this on smaller optics either directly [100] or indirectly through the mechanical loss of the coating material [101, 102]. The optimization of materials and their geometries here is further constrained by the need for low optical losses. This loss can either come from scattering or extinction of light due to absorption. Chapter 2 will further introduce absorption and its impact on coating design, prior to discussing experimental work carried out to minimize it.

At lower frequencies, a significant noise contribution arises from the thermal Brownian noise in the suspension fibres. The noise level for aLIGO is shown in figure 1.5 and derived likewise starting from the FDT as shown in Cumming [76]. The minimization of this otherwise broadband limiting noise is achieved through the geometric design of the long and thin-fibres [17]. There are additional thermal noise contributions, as the random localized temperature fluctuations within the mirror effectively displace the mirror surface. This is called thermo-optic noise, and it is a combination of thermal expansion [103] and thermally-induced changes in the refractive index [104] arising in both the mirror substrate and coating [105]. This noise is currently well below the limiting noise floor of current detectors [106] and not expected to be a problem for future detectors.

1.4.3 Quantum noise

The quantum noise inside the detectors is a combination of radiation pressure noise and shot noise. Radiation pressure is the momentum transferred from an optical beam as it reflects from a surface. In the Fabry-Pérot cavity where the power (P) is maximized on free-falling mirror masses (m), noise in the light will couple through to noise in the mirror displacement [107, 108]. This is the radiation pressure noise (S_{RP}) and the PSD is given by [109]

$$S_{\mathrm{R\,P}} = \left(\frac{1}{mf^2L}\right)^2 \frac{\hbar P}{2\pi^3 c\lambda}\,. \tag{1.8}$$

The additional terms here are the cavity, length (L), frequency (f) and the fundamental constants of the speed of light (c) and the reduced Planck's constant ($\hbar$). This noise is characterized by favouring low operational power and high mass. Conversely, shot noise $S_{\mathrm{S\,N}}$ arises simply from the variations in the arrival rate of photons at the photodetector and is therefore introduced, for simplicity, here as a counting error. The PSD form of shot noise is shown in equation 1.9 [110]:

$$S_{\mathrm{S\,N}}(f) = \frac{1}{L^2}\frac{\hbar c\lambda}{2\pi P}. \tag{1.9}$$

The shot noise in PSD is inversely proportional to the number of photons arriving in a time internal and therefore with the power circulating in the detector arms. With both of these noise sources being independent, the total quantum noise is given by adding them together. The crossing point of this noise is called the Standard Quantum Limit (SQL) and it is reached, at a specific frequency, by choosing the optimal power [111]. However, it is possible to surpass the SQL, in a narrow frequency band, at the expense of increased quantum noise elsewhere. Following the success of the GEO600 test-bed interferometer [112] the first in-situ utilization of this inside a large-scale GW detector appeared in A+LIGO during O4 [113] through the squeezing [114] of light. To appreciate the fundamentals of squeezing requires a quantum mechanical description of the interferometer and these noise sources [107, 115, 116].

1.5 Next-generation cryogenic detectors

The next-generation of ground based detectors is referred to here as the 3rd generation of detectors. This generation of detectors will see a broadband sensitivity improvement of at least a factor of ten compared to aLIGO. As a measure of distance, this carries into the sensitive volume and detection rate with a cubic factor [4]. Consequently, the detection rates could be three orders of magnitude higher and equate to a significant percentage of all the expected events from the observable Universe [117, 118].

Some next-generation GW detectors plan to hold the mirrors at cryogenic temperatures as low as 10 K. Measurements made of the mechanical loss of fused silica, near to this temperature, shows that it increases by six orders of magnitude [119, 120] and so the material choice of the mirror substrates and suspensions must be changed. Crystalline silicon alongside sapphire [121] are two candidate mirror substrates that have sufficiently low intrinsic mechanical loss [122] and therefore thermal Brownian noise contributions from the mirror substrates, at least, that are below the target noise floor. The distinct challenges of using silicon will be introduced in sections 1.6-1.7. As for the coating, the scale reduction in temperature, from room temperature, will reduce coating Brownian noise, as shown in equation 1.5. However, for the coatings used in current detectors, this is opposed by an increase in mechanical loss at low temperatures. As discussed in chapter 3 the choice of different coating materials could considerably reduce the CTN.

Instead, this section will cover the specific details of 3rd generation detectors and compare the detectors which will operate at cryogenic temperature to those, at room temperature.

1.5.1 LIGO Voyager & NEMO

LIGO Voyager is a potential upgrade to the existing LIGO interferometers that has been proposed for after A+LIGO to achieve a factor of five sensitivity improvement compared to aLIGO [77] (see figure 1.5). This upgrade would use silicon substrates, of around 200 kg, that are 45 cm in diameter, operated at a temperature of 123 K and suspended from a monolithic silicon suspension chain. This temperature is chosen as the thermal expansion effects are minimal (see figure 6 in the appendix). To reduce optical scatter, angular instability caused by radiation pressure and coating absorption as discussed in section

2.4, the detector would likely operate instead at a wavelength of approximately 2000 nm [77]. Other factors such as substrate absorption, discussed in section 4, might instead lower this to 1550 nm. The reason that this has changed from the 1064 nm of current detectors is that silicon is not transparent at this wavelength as discussed in chapter 4.

Neutron Star Extreme Matter Observatory (NEMO) is another proposed GW detector which would particularly focus on measuring GWs at frequencies >1 kHz [123]. As its physical scale is comparable to the current 2nd GW detectors, it would be a suitable test-bed, prior to the 3rd generation, for large-scale silicon optics with its mirrors also proposed to be 45 cm in diameter. Its design is closely aligned with Voyager, with the ITMs and ETMs similarly expected to operate close to 123 K.

1.5.2 Cosmic Explorer

Cosmic Explorer (CE) is one of two significant next-generation detector designs that is expected to be operational in the 2030s. The 2021 CE Horizon study [8] created a strong connection between the design of CE and its scientific objectives. It is expected that CE, similar to LIGO, will be split across two sites, with each detector arm being either 20 km or 40 km in length [72]. In order for CE to achieve its noise targets in the low frequency, it would need to mitigate Newtonian noise arising from the density displacements in the surrounding environment. A proposed strategy for achieving this, would see this noise level effectively subtracted through the placement and active operation of a seismometer array [124].

The first iteration of Cosmic Explorer (CE1) is aiming to operate with 2 MW of circulating cavity power, heavier fused-silica test masses up to 320 kg and upgraded mirror fibres. Upgrades beyond this to (CE2) will look to continue to reduce both seismic and Newtonian noises, along with increasing the level of squeezing [124]. A change to silicon materials has been proposed as an option for CE2. This would notably come with an increase in cavity power up to 3 MW and the use of large silicon mirror substrates: up to 80 cm in diameter [124]. The potential noise improvements of CE1 and the two different CE2 options of CE2 Silica and CE2 Silicon, introduced here, are both shown in figure 1.5.

1.5.3 Einstein Telescope

The Einstein Telescope (ET) is another 3rd generation detector which is envisioned to be operational by 2035. It was formally conceptualized in a design study in 2011 [125] and later updated in 2020 [7]. The studies proposed, in total, six interferometers: a high-frequency (HF) room temperature detector called ET-HF (with three interferometers) and a low-frequency (LF), cryogenic detector called ET-LF (also with three interferometers). All these interferometers were proposed to have 10 km long arms and to be located on one European site: that is still to be selected between either Sardinia, Italy or Euregio of Meuse-Rhine. The three interferometers, which make up each detector, will each have their arms meet at separate corners of an equilateral triangle. Compared to current L-shaped interferometers, this shape would allow more distinct interferometers to be built in a compact space. For the ET detector as whole, the number and range of interferometers from ET-LF to ET-HF would help to maintain a high sensitivity and duty cycle whilst affording more room for redundancy.

To mitigate the seismic and Newtonian noise, ET will unlike CE place its detectors up to 200 m underground. The expected noise curves in figure 1.5 show that ET-HF is expected to have improved sensitivity compared to ET-LF at 200 Hz and above. The design of ET-HF will be close to that of the 2nd generation of GW detectors in its operation at room-temperature; with established 1064 nm laser and optic technologies and use of silica substrates: albeit scaled up to 200 kg and 62 cm in diameter. In contrast, ET-LF is expected to use large silicon test mass mirrors (200 kg but smaller in diameter at 45 cm) alongside new 1550 nm or 2000 nm laser and optic technologies: where silicon is considerably more transparent relative to 1064 nm. The target temperature for the ET-LF mirrors is in the range of $10 - 20$ K. This coincides with a minimum in silicon's thermal expansion and mitigates some of the thermally derived distortion problems (see figure 1.6). Maintaining this low operational temperature, in part, due to heat load effects (see section 1.7) sets a limit on the tolerable cavity power. Relative to other detectors (see table 1.1), the cavity power of ET-LF is considerably reduced 18 kW. An increase in sensitivity of ET-LF below 200 Hz and relative to other next-generation detectors is expected to come from improved seismic noise, thermal noise and lower radiation pressure noise. The latter of which follows, through equation 1.8, from the lower cavity powers.

1.6 Thermal distortion of gravitational wave detector test masses

Candidate cryogenic detectors, that would operate at high powers, would have to mitigate significant effects of thermal distortions that notably arise inside the input test mass optics. The scale and dependence of this on the optical absorption is considered here for the proposed silicon substrates and in contrast to the silica of current detectors.

In 2nd generation detectors, the beam wavefront passing through the test masses is distorted by effects of thermal expansion and small fluctuations in refractive index with temperature. These temperature dependent effects arise in both the test mass substrate and coating due to the power absorbed from the beam. The radial variation in the interferometers main beam's power therefore creates a radial distribution in the distortion. Without correction these distortions, effectively self-acting, would limit operation as GW detectors approach high operational power: explained in detail by Lawrence [126]. To actively mitigate these effects, several non-contact actuation systems are combined in current GW detectors. This includes an electrical ring heater to correct for surface distortion in each test mass and a CO_2 laser for bulk effects in the ITMs [127]. Across the whole GW detector, these two modes of actuation form the basis of the thermal compensation system (TCS). Limitations to the TCS such as the in-situ imaging's limited spatial resolution make it difficult to fully actuate and mitigate the self-action. In aLIGO, spatially inhomogeneous point-absorbers appeared. The inability to mitigate them with the TCS system set limits on the operational cavity power and therefore the sensitivity of the GW detector as a whole that were below the design targets [128, 129].

Aside from the point-absorbers, the absorption profile and therefore heating profile is treated as uniform. Different terms contribute to the overall distortion. The geometric contribution scales linearly with the ratio of the substrate's thermal expansion (α) to thermal conductivity (κ). The refractive contribution scales linearly with the ratio of refractive index gradient (β) to conductivity. The refractive index is also distorted by the mechanical strain incurred by the expansion. The coupling of these two is called the photoelastic effect, and its coefficient acts to effectively offset the distortion given by the geometric term: with the equivalent forms shown by Lawrence [126]. However, this coefficient for sapphire, silica and notably silicon from room temperature [130] to cryogenic temperatures [131] is small. As the refractive index distortion is effectively only offset by approximately 30%, it is not further considered here.

In order to estimate the significance of thermal distortion in the test masses of future detectors, the geometric and refractive distortion ratios will be scaled to those of aLIGO. This will form a figure of merit (FOM), as shown on figure 1.6. Approximating the TCS system as being the same and the distortion as being independent of absorption source, an increase in the FOM will represent the scale factor by which the tolerable absorbed power could increase relative to aLIGO. This factor could also represent the safety factor by which detector operation would be covered against unforeseen changes in the test masses' absorbed power, perhaps due to point-absorbers.

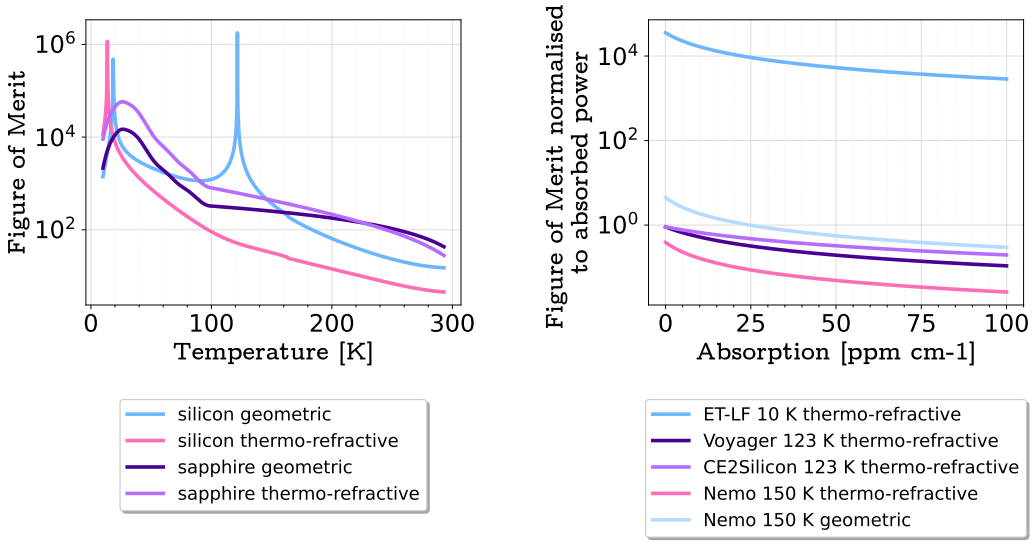

Figure 1.6: (Left) This plot inspired by J. Eicholz [132] shows a relative figure of merit (FOM) that quantifies the factor of reduction to geometric and thermo-refractive distortions in silicon or sapphire, as a function of temperature, relative to room temperature silica.
(Right) This plot shows the same FOM but for mirrors at the temperature and currently expected absorbed powers at operation, relative to aLIGO's silica mirrors at room temperature. The FOM is parameterised here on the substrate absorption to show the need for corrective TCS in all but ET-LF.
For both silicon and sapphire, the temperature dependent values for conductivity, thermal expansion and refractive index gradient are shown in appendix A.

Future cryogenic detectors are expected to operate either at 123 K which is the zero-point in the thermal expansion curve of silicon [133] or below 20 K: where experimental data (appendix A) has shown that the thermal expansion value becomes vanishingly small. Close to Voyager's proposed operational temperature of 123 K the geometric expansion

FOM is drastically increased by several orders of magnitude as shown with the theoretical singularity on figure 1.6. This factor would carry into linearly reducing the distortion caused by potential point absorbers [77]. However, the refractive distortion of the ITMs would be on the same order of magnitude as aLIGO, as shown on figure 1.6, when accounting for the higher power absorbed. It could further be mitigated by improvements to the TCS: either in current technology or development of new techniques such as lensing compensation plates [77].

NEMO and CE2 silicon would likewise have a similar level of refractive distortion if operated at 123 K. If NEMO instead operated at 150 K, as discussed in section 1.7, the geometric distortion would be comparable to current detectors and the refractive distortion could be an order of magnitude worse than aLIGO. This temperature range might not, however, be suitable for CE2 Silicon or Voyager in account of the geometry of their silicon suspensions and need to cancel out their thermoelastic contributions [134].

In contrast, ET-LF operating in the temperature range of $10 - 20$ K, would have minimal thermal distortion in its ITMs due to the thermal conductivity increase and significant reduction in operational power. Outside ET-LF, the ability for TCS systems in future cryogenic silicon detectors to correct for refractive index distortion will constrain the power that can be absorbed and notably, as one of the main contributors, the bulk absorption of silicon.

1.7 Heat load on gravitational wave detectors test masses

To maintain cryogenic operation at the required temperature, future cryogenic detectors will have to meet strict limits on the test masses total heat load [10]. One of the main contributors will be the power absorbed from the laser beam. This may set a constraint on the allowed operational power that is lower than the target set for maximum detector sensitivity. In aLIGO's test masses, around the local vicinity of the beam radius, the ratio of absorbed heat lost to radiation relative to conduction is low. However, in account of the large test mass surface, radiation acts to keep a uniform and level temperature. Radiative cooling would be the dominant cooling mechanism in CE2 Silicon, Voyager and NEMO

if they operate 123 K. Aside from heat loading factors discussed below, their steady-state operational temperature is conditioned on improvements to the radiative cooling: through emissivity (σ) the test mass, with black coatings for the barrels [77] and careful choice of optical coating for the mirror surface [132].

At the $10-20$ K operational test mass temperatures ($T_{\text{test mass}}$) for ET-LF, the radiative cooling with the surrounding environment ($T_{\text{environment}}$), held at 4 K, would effectively disappear. This is because the radiative cooling ($Q_{\text{radiative\_cooling}}$) between the cryogenic shroud shielding would drop, according to the Stefan-Boltzmann law

$$Q_{\text{radiative\_cooling}} = \sigma \times (T_{\text{test mass}} - T_{\text{environment}})^4. \tag{1.10}$$

The cooling is therefore limited only to conduction through the thin-fibres of the mirror suspension. A similar problem was faced for sapphire in KAGRA's case and so significant R&D went into reducing the heat load applied to the test mass, notably due to excess substrate absorption [121, 135, 136]. In a simplified sense, the rate of conduction limited cooling is given analytically by the heat flow ($Q_{\text{conductive\_cooling}}$) from the test to the penultimate mass ($T_{\text{penultimate mass}}$). The overall heat flow can then be found by integrating the 1D conduction equation along the length of the four suspension fibres

$$Q_{\text{conductive\_cooling}} = \int_{T_{\text{test mass}}}^{T_{\text{penultimate mass}}} \frac{\pi d^2}{4l} \kappa(d, T) \mathrm{d}T. \tag{1.11}$$

Along each fibre's length (l) there will be a gradient in temperature and therefore conductivity (κ). However, the fibre radius (d) will be approximately independent of length [137, 138]. This operational state of conductive cooling is initially reached from room temperature, in part, through radiative cooling to a surrounding cold shroud. In addition, thermal links further up the suspension chain [135] help: through maintaining the relatively colder temperature of the penultimate mass and the necessary rate of cooling. The connection pathway of these thermal links is shown on figure 1.7 and passes along a surrounding cage to mitigate unwanted seismic coupling to the test mass. There is a distinct idea for improving the heat dissipation that involves embedding a helium cooling system inside some suspension fibres [139, 140]. For a large part, the designs and continued R&D for ET-LF is focussed on improving the cooling capabilities in order to mitigate a potentially high heat load on the test mass.

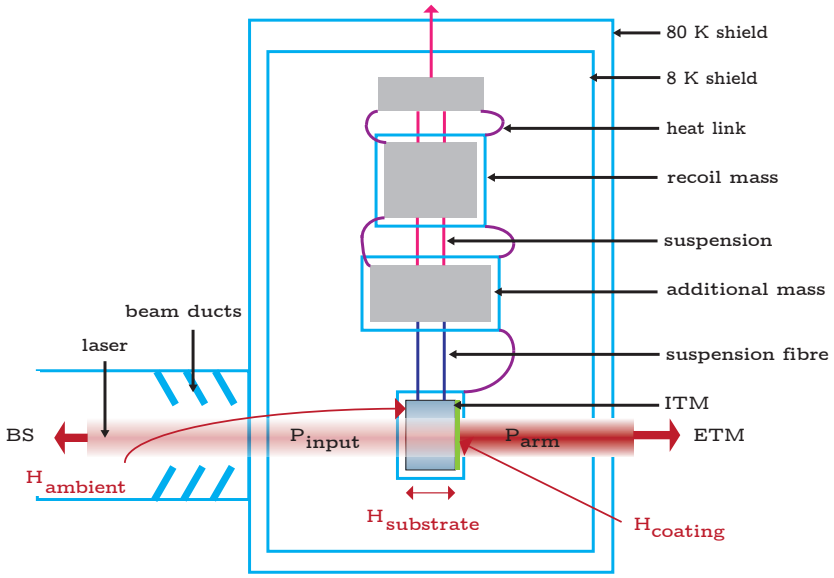

Figure 1.7: A simplified representation of the KAGRA suspension and cooling chain. The cooling chain involves radiative coupling from the test mass to the beam ducts and the surrounding shield. There is also conductive coupling from the test mass which happens through the suspensions (pink & dark blue) and heat links (purple). The latter of which is connected through recoil (light-blue) and additional masses (grey) to minimize through coupling of vibrations to the test mass. Further details can be found in Akutsu et al: the source which inspired this diagram. [135]. By comparison, the suspension fibres differ notably, with the test masses in the materials being fused silica as opposed to KAGRA's sapphire. The distinct aLIGO [141] and Virgo [62] suspension systems also do not share space with any heat links. The diagram also specifically shows the ITM and the location of the beam powers (yellow) defined in equations 1.12 and heating sources (red), equations 1.14.

For the test masses of cryogenic temperature detectors there are three distinct heat sources which the cooling power needs to balance. To estimate the heating components, the power will be considered entering into and out of the cavity shown on figure 1.7.

The input power (P_{input}) that is passed to each arm cavity

$$P_{\text{input}} = \frac{P_{\text{laser}} \cdot PRC_{\text{gain}}}{2} \tag{1.12}$$

$$P_{\text{cavity}} = \frac{P_{\text{input}} \cdot 2 \cdot \mathcal{F}}{\pi} \tag{1.13}$$

is the product of the laser power P_{laser} and the power recycling cavity's gain PRC_{gain}. The factor of two reduction follows from the 50:50 beam splitter. The input power is first absorbed inside the ITM substrate ($H_{\text{substrate\_ITM}}$) $[cm^{-1}]$ of absorption (a_{sub}) $[cm^{-1}]$ and length ($t_{\text{c\_sub}}$) $[cm]$.

$$H_{\text{substrate\_ITM}} = P_{\text{input}} \cdot a_{\text{sub}} \cdot (2 \times t_{\text{c\_sub}}) \tag{1.14}$$

$$H_{\text{substrate\_ETM}} = P_{\text{cavity}} \cdot T_{\text{coating}_{\text{ETM}}} \cdot a_{\text{sub}} \cdot (t_{\text{c\_sub}}). \tag{1.15}$$

$$H_{\text{coating}} = P_{\text{cavity}} \cdot a_{\text{coat}}. \tag{1.16}$$

The highly reflective cavity with finesse ($\mathcal{F}$) will amplify the input beam power to give a high cavity power P_{cavity}. A small amount of this light will exit out the end of the cavity and likewise be absorbed into the ETM substrate ($H_{\text{substrate\_ETM}}$) albeit at a considerably lower level due to the low ETM coating transmission ($T_{\text{coating}_{\text{ETM}}}$). The second distinct heating source is the cavity power absorbed into the coating (H_{coating}) and this will be approximately equal in both test masses (assuming the same materials are used in both). These terms are evaluated in table 1.1 for the current KAGRA detector and the four proposed next-generation cryogenic detectors mentioned previously. The absorption of the coatings is expressed in parts per million (ppm): of which individual photons will be absorbed. In contrast, the thick substrate will have an absorption which scales with thickness, and so it is expressed in units of ppm cm^{-1}. This is useful to distinguish how different substrate thicknesses will scale through and impact the heat load of future detectors. Given the high transmissivity of the ITMs in GWDs relative to that of the ETM approximately all the light will pass back through the ITM.

The third and last type of heating is the ambient heat loading. Despite the suspended test masses being surrounded by cold shrouds, there are still unavoidable pathways for thermal radiation to radiatively couple in from warm room temperature regions. For example, the shroud holes through which the interferometer beam passes would nominally provide a solid angle through which the test mass is thermally connected to this ambient load. In KAGRA, as shown on figure 1.7, this angle and the connected ambient heat load were effectively reduced with beam ducts [142]. From table 1.1 it is clear that all heating pathways considered, aside from ($H_{\text{substrate\_ETM}}$), could contribute in similar levels to the total heating. However, as these are mostly taken as design targets, the realistic total heating will only become apparent as research progresses towards manufacturing and testing the required optics at scale.

Detector	P_{input} [W]	P_{cavity} [MW]	$a_{\text{substrate}}$ [ppm/cm]	$t_{\text{substrate}}$ [cm]	a_{coating} [ppm]
Kagra (sapphire)	3.4×10^{2}	0.33	50	15	0.5
Voyager	2×10^{3}	3.0	20	55	1.0
NEMO	1.6×10^{4}	4.5	10	20	1.0
CE2 silicon	2×10^{3} *	3.0	5	27	1.0
ET-LF	3.2×10^{1}	0.018	20	57	1.0

Detector	H_{ITM} [W]	H_{ETM} [W]	H_{coating} [W]	H_{ambient} [W]
Kagra (sapphire)	0.5	2.5×10^{-3}	0.17	0.1
Voyager	4.4	1.0×10^{-2}	3.0	0.006
NEMO	6.3	4.5×10^{-3}	4.5	unknown
CE2 silicon	0.54	1.6×10^{-3}	3.0	unknown
ET-LF	0.04	9.0×10^{-5}	0.02	unknown

Table 1.1: The design targets for each future detector are taken from recent publications: Voyager [77], NEMO [132], CE2 Silicon [8, 124] and ET-LF [7, 125]. The KAGRA data is taken from recent measurements inside the current detector. Aside from the measurements from KAGRA the H_{Ambient} for the future detectors is unknown and carries a large uncertainty. As a result, the value shown for Voyager is subject to change.
* Denotes that this value was back-calculated from the cavity power, assuming the same Finesse targeted by Voyager.

For ET-LF, the minimum tolerable fibre radius for different substrate heat loads on figure 1.8 shows that the required conductive cooling rate might set the lower limit for the fibre diameter. This diameter is in comparison to the safety factor required for the suspension fibre to hold the weight of the test mass. This increase might then couple through to increasing the suspension thermal noise floor.

Theoretical noise curves, shown on figure 1.5, do not project that future cryogenic detectors will operate in a range unreachable to their room temperature counterparts. However, in the case of ET-LF, there is a notable shift in the scope of challenges presented. In particular, by largely shifting from the challenge of thermal distortions to heat loading, ET-LF ultimately increases the chances of obtaining a next-generation of GWDs with increased sensitivity in the audio frequency band. The potential change of quasi-monolithic suspended materials to silicon, in most cases, poses many mechanical and optical challenges. These include producing silicon fibres that are strong enough, bonding them to a test mass, and ensuring that the combined thermal noise is low enough [134]. Instead, the work of this thesis will focus on reducing the absorption in the test masses, of future detectors: from both the bulk silicon substrates and thin-film coatings. Beyond validating their stable operation at current designs, further reductions to the absorption might free

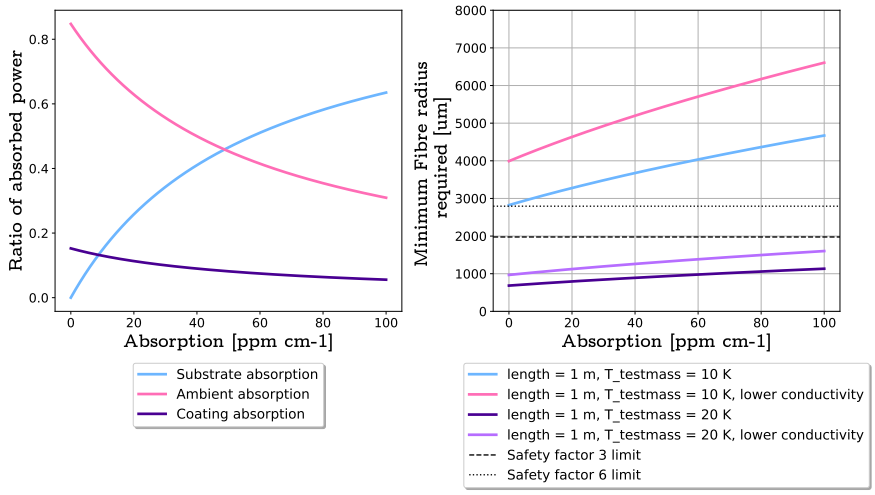

Figure 1.8: Plots for ET-LF showing the weighting of the different terms in the heat budget (beyond table 1.1) and the requirements set on the fibres in order to counteract this heat. (Left) The ratio of heat absorbed in the substrate to the total heat absorbed is shown in comparison to the other two heat loads: coming from coating absorption of 0.02 W and ambient heat loading with an optimistic 0.1 W.
(Right) Evaluating equation 1.11 for a test mass operating at 10 K relative to the additional test masses 4 K. The suspension fibre diameter minimum limit shown for different fibre lengths and conductivities is then parameterized against an increase in heating from the substrate absorption. For high levels of substrate absorption, there are clear cases where this minimum limit might exceed the required safety minimum for supporting the weight of the test mass. The safety minimum is shown for safety factors of 3 and 6 [143]

ET-LF to operate at higher powers and cover sensitivity gaps opened up by downtime in ET-HF detectors. A similar benefit might likewise be found in higher power detectors, albeit through a reduction in substrate thermal lensing. It is through these pathways that improvements to the absorption of silicon test masses could couple through to benefit the overall noise performance of cryogenic 3rd generation GW detectors.

1.8 Conclusion

This chapter introduced gravitational wave detectors as a new state-of-the-art measurement tool that is capable of detecting signals from the farthest corners of the Universe. Since the first detection, the detectors have had a considerable impact on the field of astronomy. A notable achievement of which is the heralding of a new era of multimessenger astronomy. The key design features and historical development steps to get there

are discussed. In order to extend the rate of discovery and potential new astrophysical sources, the current detectors must be upgraded. Beyond this, future detectors promise an order of magnitude improvements to the sensitivity and spectral bandwidth. This will require considerable R&D efforts in reducing each of the limiting noises as described.

Some future detectors have elected to run their test-mass mirrors at cryogenic temperatures. The benefit and challenges associated with this are considered, and in particular the need to use new materials such as mono-crystalline silicon for the mirror substrates is shown. However, silicon currently has too high an absorption. Limited efforts have also been made to scale this material up to the size required for mirrors. The absorption, as with many parameters in gravitational wave detectors, is interconnected to other design choices and research pathways in the detectors. As the experimental work in this thesis will look to minimise the absorption from the mirror substrate alongside coatings, the rest of this chapter considered the impact that it would have more broadly in future detectors.

The Voyager detector, for example, as discussed, would be subject to thermal distortions. As shown relative to current detectors, this would require active mitigation of total absorption and the resulting spatially extended distortion. As for ET-LF, the discussion focussed here on the need to reduce the substrate absorption's contribution to the overall mirror specific heat-budget. This budget carries a lot of uncertainty, and impact on the operation of the detector. To the benefit of future gravitational wave detectors, all the studies presented throughout this thesis focused on characterising and reducing, where possible, the optical absorption of silicon substrates and coatings.

Chapter 2

Measurement of the absorption of thin-film coatings

2.1 Introduction

As discussed in Chapter 1, thermal noise associated with the test-mass mirror coatings is a major sensitivity limit for gravitational wave detectors. The GW community has carried out extensive research to develop and test alternative coating materials and optimise coating deposition parameters. In addition to low mechanical loss (to provide low thermal noise), it is essential that any potential coating also has suitably low optical absorption. This chapter will present absorption measurements made at 1064 nm and 1550 nm of test mass mirror coating candidates on small-scale representative optics for current and next-generation detectors. Current mirrors for aLIGO and adV were shown to have absorption levels between $0.22 - 0.27$ ppm [144] and the maximum tolerable absorption for an aLIGO ETM is 0.5 ppm [144]. This design limit allows the detectors to stably operate at high powers by minimising the thermally induced changes to the surface curvature of the mirrors [145]. Also, at higher absorption levels the corresponding increase in optical loss inside the interferometer's cavity would act to limit the finesse. The general form of this relationship is shown in Siegman [146].

The author devoted significant effort to supporting the global initiative aimed at identifying suitable coating materials for future gravitational wave detectors. Specifically, this chapter presents absorption measurements of two promising coating material candidates for the next room-temperature upgrades of aLIGO and AdV, scheduled for implementation between mid-2025 and 2027. These two candidates consist of titania (TiO_2) mixed with silica (SiO_2) and titania mixed with germania (GeO_2), both deposited via ion beam

sputtering with varied mixing percentages. The absorption measurements on TiO_2:SiO_2 were featured in a (2023 PRL) publication [102] and described here in section 2.7. This chapter also investigated other coatings as part of a wider survey of absorption in thin-film materials. This included distinctly low absorption measurements of perovskite materials (see appendix B) and of pure germania which notably contributed towards a recent publication [147].

Although this chapter will focus its discussion on absorption and the measurements made, it will introduce each coating of interest within this wider research space. To provide context for the measurements, section 2.2 will introduce the wider theory of thin-film optics and section 2.4 will discuss historical research which has taken place. The particular measurement technique, based on the photothermal effect, utilised for accurate absorption measurements will be covered in section 2.3. Following this, the low-absorption studies and their significance for mirror coatings inside future detectors will be discussed in detail through sections (2.7,2.8,2.9,appendix B).

2.2 Theory of thin-film absorption

The propagation of light through a medium can be simply described by the complex refractive index coefficient ($\tilde{n}$). The real (n) and imaginary (k) components as a function of wavelength (λ) couple through

$$\tilde{n}(\lambda) = n(\lambda) + \mathrm{i}\kappa(\lambda) \equiv \sqrt{\tilde{\varepsilon}} \tag{2.1}$$

to change both the speed and intensity of light as it propagates through a material layer. This is often represented instead with the complex dielectric constant ($\tilde{\varepsilon}$). This interaction across the broadband spectrum of light is mediated by the coupling of energy to microscopic systems composed of damped oscillators and quantised transition states. In the NIR wavelength range of interest for gravitational wave detectors ($1064 - 2000\,\mathrm{nm}$), these systems are typically composed of electron states [148] that are either intrinsic to the specific material or extrinsic, arising from impurities. The absorption of thin-film coatings of interest here are expected to be dominated by these extrinsic impurities. However, contributions might be from a complex combination of localised coordination changes and dangling bonds which are are the unmatched valence of atoms that are themselves fixed

in a local atomic structure [149]. In the case of -OH inclusions, in the sub-ppm concentration, absorption contributions are expected across the NIR spectrum [150]. These sources of absorption are expected to vary from coating deposition parameters, environmental factors and post deposition heat treatment as discussed in section 2.4.

We know that we can not use metal coatings, as often applied to high reflectivity optics, as the high number of free electrons lead to a NIR absorption of around a few percent [17, 151] for thicknesses above the order of 100 nm [152]. Instead, the typical coating materials considered for gravitational wave detector mirrors are mostly amorphous oxides. In the NIR range, these offer a low-absorption, with typically many orders of magnitude lower κ than metal coatings. Along with this, they provide the opportunity for extremely high reflectivity through stacking multiple layers, as will be discussed in 2.4.

Optical studies of coatings in the NIR would typically involve processing the optical measurements with a suitable transmission-reflection model to yield $\tilde{n}(\lambda)$ over a wide range of wavelengths. After this, the data could be compared to a semi-analytical dispersion model [153, 154] to better understand the underlying mechanisms and to inform further optical designs. Instead of assessing the suitability of a particular dispersion model, this work will take a range of discrete optical measurements for different coatings in order to assess the coating's suitability for application on the mirrors of future GW detectors. The discrete measurements a coated material's total absorption (A) will be scaled to give an imaginary coefficient also called the absorbed extinction coefficient ($\kappa_{\text{absorption}}$). For a single layer coating, the total measured absorption must first be scaled by the coating thickness and index to give an absorption per unit length (α). In a simplified sense, this can then be scaled by the wavelength to give ($\kappa_{\text{absorption}}$) as derived by Born [155]

$$\kappa_{\text{absorption}} = \frac{\alpha\lambda}{4\pi}. \tag{2.2}$$

The full extinction coefficient (κ) includes additional optical losses due to scattering in the bulk of the material. At low levels, these are tied to distinct limits in gravitational wave detectors, and so they are often considered separately.

Scattering for typical optics is generally dominated by the surface roughness contributions. This roughness is often propagated from the substrate's surface [156] or it can result from inhomogeneities in the coating production. Fortunately, ion-based deposition techniques, such as those currently used for GWD optic production (see section 2.6), tend to produce

very homogeneous coatings that lead to almost no excess topographical inhomogeneities [157]. However, optics used in gravitational wave detectors have a low surface roughness, on the order of the spacing between atoms, thus contributions from the bulk of the coating material become significant. The scatter of the current aLIGO and adV optics was measured to be 9.5 ppm [158].

The measurement technique introduced in section 2.3 only measures the absorption and does not quantify the scattered light. The measured extinction coefficient due to absorption presented here is not representative of the full extinction value ($\kappa_{\text{absorption}} \approx \kappa$). However, for the benefit of work outwith the gravitational wave community, the value might be correlated. Following each of the coating absorption studies here, measurements of the extinction coefficient due to scatter could clarify any underlying correlations and common origin for future mitigation.

Spectroscopic techniques broadly speaking are defined as the measurement of materials with an optical probe. For a given wavelength, it is common to measure with such techniques the reflection (R) and transmission (T) of light through an optic are the standard method for simultaneously measuring both the real and imaginary coefficients across a broad wavelength range. The absorption is determined through the fitting due to the residual ($1-R-T$). However, due to the magnitude of errors in R or T they are not capable of resolving low absorptions (sub-ppm). They are also not capable of distinguishing absorption from scattering. Instead, the absorption must be measured separately from the refractive index, and in this case with a photothermal based technique. This technique (covered in section 2.3) makes use of high intensity, highly stable, coherent monochromatic light sources to achieve the desired sensitivity to absorption. Measurements are made with narrow spectral laser widths, at distinct wavelengths of 1064 nm and 1550 nm.

Outside the GW community, a widely researched parameter which can correlate with the thin-film absorption is the Laser Induced Damage Threshold (LIDT) [159]. In particular, the correlation can occur for LIDT in the continuous-wave regime where heating timescales are long (> 1 s). However, in the short-pulsed regime up to 20 ns, a previous study found no clear correlation with absorption [160]. Other work found that as the absorption increased the LIDT decreased in the case where contaminants were present [161]. Efforts to mitigate the LIDT through the design of multilayer coatings [162] has some parallels to the minimization of absorption in the coatings of GW detector optics. The experimental results shown here may also be of benefit to the general study of optical coatings for high-power continuous-wave laser applications [154]. To support the wider application

of the coating absorption measurements presented here, they are typically reported as $\kappa_{\text{absorption}}$ values throughout this chapter. The extinction coefficient was calculated by fitting the measured total absorption values to a transmission-reflection model as described in appendix C.

2.3 Photo Common-path Interferometry (PCI) setup

Photothermal Common-path Interferometry (PCI) is an established technique that is suitable for measuring the low-ppm absorption of GW detector coatings [163]. It is distinguished by its use of a high-power monochromatic modulated laser pump beam. This beam generates a measurable and localised temperature shift that is subsequently detected with a phase-sensitive detector readout. This technique relies on the linearity of the refractive index over several orders of magnitude with temperature increase due to optical absorption. The PCI technique is a photo-thermal method where a high-intensity, optically chopped, "pump" laser beam creates a periodic thermal lensing profile in a thick optical substrate. The inner region of a larger and lower intensity "probe" beam crosses through this lens and acquires an internal phase shift, whilst the outer region remains undisturbed. As both regions of the beam diverge and overlap, in a common-path, the phase difference will manifest as an interference pattern. Relative to the outer probe region the inner, acquires a new Gouy phase set instead by the size of the pump waist (w_0) at this crossing point [53]. At one Rayleigh length away (Z_{R}), from the crossing point

$$Z_{\text{R}} = \frac{\pi w_0^2}{\lambda}, \tag{2.3}$$

along the probe's path, the maximum interferences occurs. At this point the Gouy phase is offset between both regions by 90 degrees. This overlap is shown on figure 2.1 (B). As the PCI samples the probe beam in this near-field region [53, 164] (close to the sample where phase and intensity distortions are prominent) it is distinctly different from other far-field thermal lensing techniques [165]. Although different thermal lensing setups would be suitable for measuring the absorption of coatings here, some would require substrates with a much higher level of surface polishing and/or additional data processing [166]. The potential increased time and financial investment could be in conflict with a desired high measurement throughput and annealing studies.

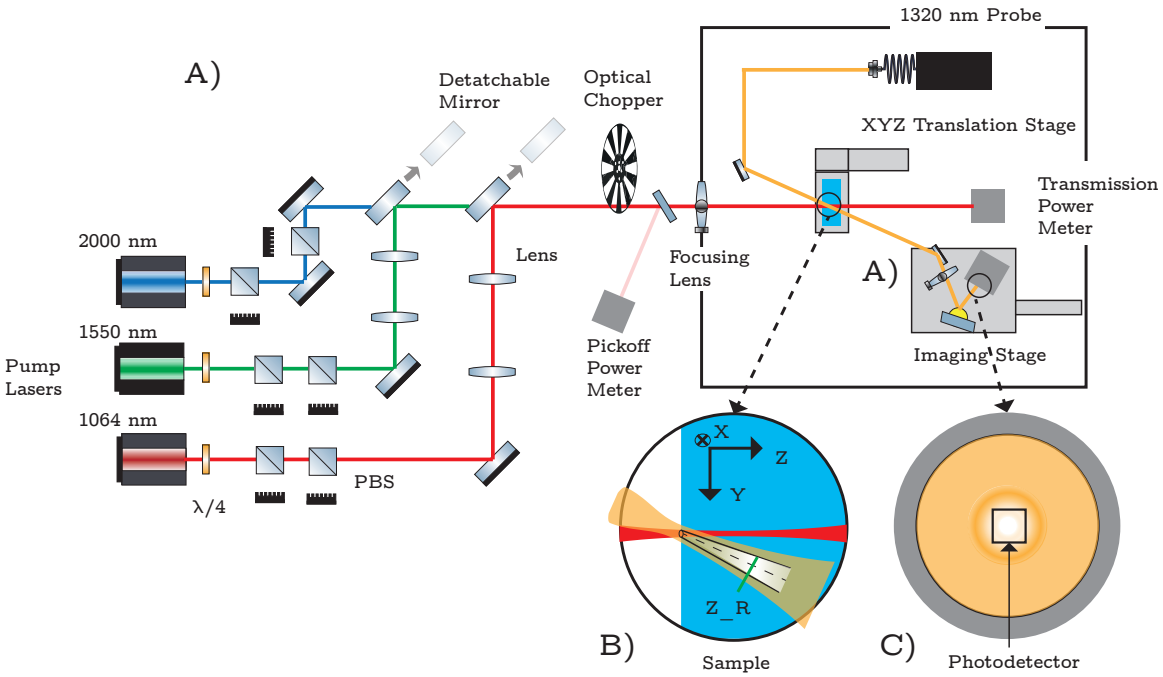

Figure 2.1: Layout of a photothermal common-path interferometer which is operational at three pump wavelengths. Figure (A) shows the overall layout of the setup. Figure (B) shows the mode-matched crossing point between the two beams positioned on the coating surface. An approximation of the interference is shown with the white gradient such that the first Rayleigh length (Z_R) occurs inside the sample. Figure (C), recreated from both Marchiò [53] and Terkowski [167], shows the beam recovered at the Rayleigh length in the 2D plane perpendicular to the probe beam's optical axis. The sensitive photodetector area over which the signal is recovered is shown by the square. To aid visualisation, the size of the interference area in (B) and intensity, from orange to white, on (C) are exaggerated.

To understand the PCI detection scheme, it is crucial to first consider the time-domain. An optical chopper provides a periodic modulation of the pump and therefore introduces a reference frequency. This is passed onto the probe with a temporal phase-offset that is characteristic of the lensing material's thermo-optic properties. The region of the probe with the maximum interference is imaged onto a photodetector, and the resulting electrical signal is processed by a lock-in amplifier. With respect to the modulation frequency and phase, this converts the out of phase signal proportional to the probe power alone into a DC voltage signal (V_{DC}). The in phase signal arising from the interference at the reference frequency is converted to an AC signal (V_{AC}). This AC signal is proportional to both power and the absorption and the measured SNR is increased through electronic filtering.

To recover a sample of interest's absorption these AC and DC signals must be compared to the same signals acquired when a calibration sample of known absorption is placed in the setup, whilst also accounting for any differences in pump power incident on the sample surface (P) during the two measurements. The comparison is mediated through the measurement of a calibration factor (R).

$$R = \frac{V_{\mathrm{AC}_{\mathrm{calibration}}}}{P_{\mathrm{calibration}} \times V_{\mathrm{DC}_{\mathrm{calibration}}}} \frac{1}{A_{\mathrm{calibration}}}. \tag{2.4}$$

This can be regarded as the responsivity of the system. It accounts for the signal and total absorption from a calibration sample's coated surface ($A_{\mathrm{calibration}}$) and allows after relative measurement of the target sample for its absorption (A_{sample}) to be determined from scaling.

$$A_{\mathrm{sample}} = \left(\frac{V_{\mathrm{AC}}}{P \times V_{\mathrm{DC}}} \right) \frac{C}{R}. \tag{2.5}$$

If the sample of interest has different thermo-optic properties to those of the calibration sample and in particular a different thermo-refractive index: a scalar correction (C) must be used. For the coating measurements discussed here, the substrate is always fused silica and so no correction is required (i.e. $C = 1$).

As the resolution of the PCI scales with the beam intensity, unlike spectroscopic measurements there is no real fundamental limit to the sensitivity. Provided that the noise is out of phase and does not drift [53], long measurement times can yield a high absorption resolution. For the high pump powers used here (up to 2.5 W incident on the sample surface) a resolution down to ≈ 0.01 ppm absorption was achieved. However, in consideration of the range of noise sources in a multi-purpose lab [168] along with the need for a high measurement throughput, measurements of sub-ppm absorption signals can be challenging. To make sure the PCI was sensitive enough to measure state-of-the-art coatings, a series of alignment and calibration procedures were developed.

2.3.1 Alignment and calibration of the PCI

The physical setup is shown in figure 2.1. The three separate p-polarised pump beams of 1064 nm, 1500 nm and 2000 nm are brought into a shared path with a combination of fixed and kinematic steering mirrors in order to allow measurements to be made at the respective wavelengths. Along each separate pump beam path, there is a $\lambda/2$ waveplate and two polarising beam splitters (PBS) to give a stable p-polarised light input for the measurement apparatus. To set the input power, the waveplate can then be rotated to change the amount of p-polarised light passed (through the PBS) to the sample input. A series of lenses is placed in each beam path to produce pump beam waists of the desired sizes and spatially overlapped with the probe beam's waist.

The probe beam can not be measured directly at the intrinsic Rayleigh range [53] as it often occurs inside the sample. This is represented in figure 2.1 (B) and calculated to within a few millimetres using equation 2.3. To recover the highest signal and therefore sensitivity, a readout photodiode is placed at the end of a telescopic imaging stage, where the beam position an integer number of Rayleigh ranges after the crossing point is imaged onto the detector. To further maximize the sensitivity, represented by R, the magnification optics were previously designed such that the size of the inner interfering region of the probe has a good overlap with the sensitive photodiode area [167] as shown in figure 2.1.

This alignment can be confirmed through three steps. Firstly, the focal points of both beams should be crossed and confirmed, ideally with a beam profiler mounted in place of the sample. Then, to confirm that the spacing of the optics on the telescopic stage is correct, a fiducial reference mark can be placed at the original Rayleigh distance. Fine adjustments, particularly to the lens spacing, should sharpen the re-imaged marker close to the photodiode surface when viewed with a beam card. Placing the marker at the correct position requires the marker's surface position to be well-defined. This is simplified by using reference mounts. For example, a similar 1" optical mount with a razor blade bonded on with rapid set epoxy had a fixed and measurable offset: which allowed it to be positioned in place of the measurement sample's surface.

Then the R value (equation 2.5) equivalent to the absorption sensitivity should be measured with a suitable calibration in place: across a range of imaging stage positions. This data can then be compared to numerical models to validate the maximum position and overall alignment through the characteristic position dependent dispersion curve as shown in 2.2. The numerical dispersion (D)[163] used here was derived as a Fourier transform of the time-domain signal, and takes many of its inputs as scaled ratios.

$$D(\omega, \varepsilon, \zeta) = P_{\mathrm{R}} \times \int_0^{\infty} \mathrm{Im}\Big(\frac{1}{1 + t - \frac{i\zeta}{1 - i\varepsilon\zeta}}\Big) \exp(-i\omega t)\, dt \tag{2.6}$$

$$P_{\mathrm{R}} = \sqrt{\frac{\pi}{8}} \cdot \frac{w_{\mathrm{pump}}}{\lambda} \cdot \frac{1}{\sin\beta} \cdot \frac{n}{k} \cdot \frac{dn}{dT} \tag{2.7}$$

$$\zeta = \frac{z}{z_{\mathrm{R}}}, \quad \varepsilon = \frac{w_{\mathrm{pump}}^2}{2\, w_{\mathrm{probe}}^2}, \quad \omega = \frac{f_{\mathrm{c}}}{f_{\mathrm{t}}} \tag{2.8}$$

The position (z) is scaled by the Rayleigh range as (ζ) and beam size as the relative ratio (ϵ) between pump (w_{pump}) and probe radius (w_{probe}). The modulation frequency (f_{c}) is also scaled to the thermal relaxation frequency (f_{t}). These are all factored into equation 2.6 which is then integrated until it converges. This result is linearly scaled by the photothermal response (P_{R}) which includes the crossing angle (β) and scales with thermal conductivity (k) and refractive index gradient $\frac{dn}{dT}$ terms.

The measured signal as a function of position for the 1064 nm pump is compared to the simulated values in figure 2.2. To determine the position of the maximum, the `curvefit` function found inside Python's scipy.optimize module [169] was used. It minimised the constant offset between the peak imaging stage position of the normalized numerical (equation 2.6) and measured dispersions. There appears to be good agreement for the calibration taken on 08/06/24 (black) with the numerical dispersion. The slight offset at lower imaging stage positions might indicate asymmetries in the system. If the pump size was 80% of the value, then the fit could be considerably improved. A more rigorous assessment of the dispersions position dependence would benefit from measurements past ≈ 62 mm where it sharply drops towards zero as the reimaging position approaches that from the crossing point. The data shown from 05/05/21 (pink) indicates a time, from a similar fit, where rough fitting of equation 2.6 indicates that the pump beam's waist

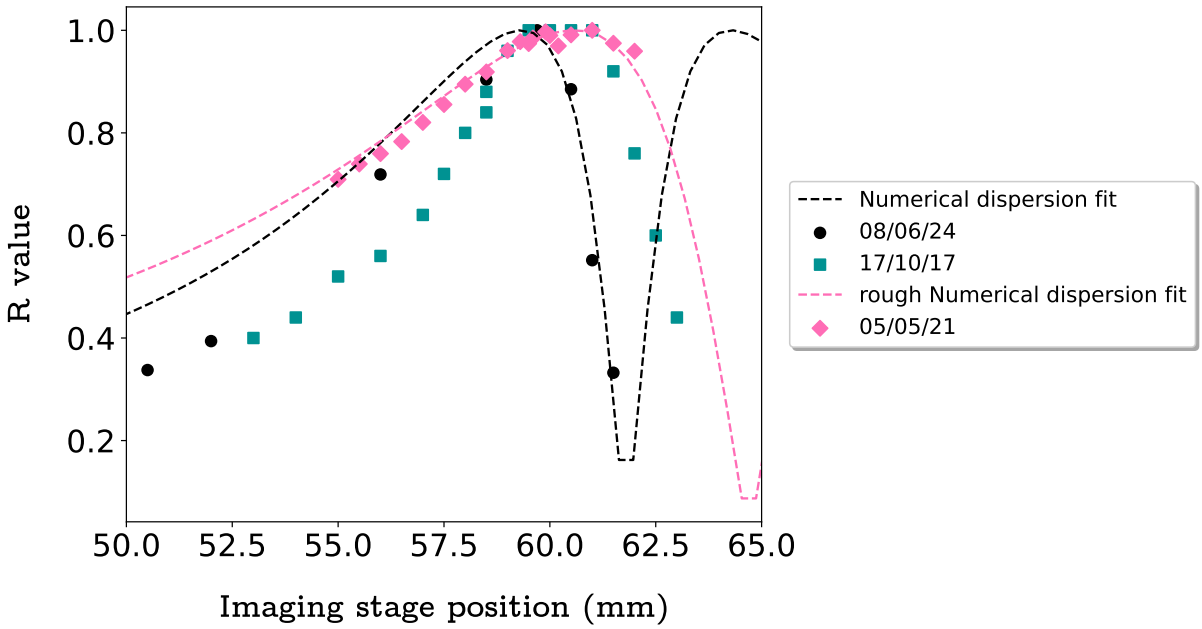

Figure 2.2: 1064 nm self-normalised butterfly curves which compares the measured data from different historical calibrations of the PCI setup to the dispersion formula.

could have been 50 % larger. As the plateau region is larger in the 05/05/21 fit, it is expected that the alignment here and therefore larger pump would make the system more resilient to unexpected changes in the target imaging stage position. This could be the result of positional drifts in either beam between measurements, driven by fast changes in the ambient lab temperature.

When measurements are made between different sample thicknesses ($d_{\mathrm{a}\to\mathrm{b}}$) and or refractive indices ($n_{\mathrm{a}\to\mathrm{b}}$) the optical distance between the interaction point and the interference maximum is shifted. To correct for this, the imaging stage position must be offset by the same amount ($\Delta z_{\mathrm{a}\to\mathrm{b}}$) using equation 2.9. This equation is a more generalised form of the waist shift expression shown in Nemoto [170].

$$\Delta z_{\mathrm{a}\to\mathrm{b}} = \left(1 - \frac{1}{n_{\mathrm{b}}}\right) d_{\mathrm{b}} - \left(1 - \frac{1}{n_{\mathrm{a}}}\right) d_{\mathrm{a}}. \tag{2.9}$$

2.3.2 Measurement and processing of the data

The PCI has a few distinct measurement regimes [168]. These are best distinguished by first considering how, from the measured samples coordinate frame, the crossing point is scanned through and across the sample in the XYZ axes shown in figure 2.1.

A scan through the Z-axis takes the form shown in figure 2.3. Given the angular offset of the probe beam in the plane spanned by the Y-Z axes, if the absorption is dominated by the coating then the induced refractive lensing and, therefore, imparted phase shift should drop off uniformly as the beam separation moves either side of the maximum during a z-axis scan. In reality, there is also a secondary signal maximum that arises due to interference effects produced by the Rayleigh ranges of different crossings having a shared maximum. This Z-axis scan is critical to finding the maximum signal for a calibration sample alongside adjustments to the imaging stage. The scan is also the standard way of measuring the point absorption of a target sample relative to a calibration.

In a standard measurement, the scan locations are randomly selected from the x-y surface as it runs close to parallel with the coatings surface. From the set of at least five points, a representative absorption measurement for each coating is given by the mean and standard deviation of this set. All plots shown in this chapter include this standard deviation as an error, representing the variation in absorption from point to point. For any measurement taken on the PCI an absolute error for the true absorption level is typically set at $\pm 20\,\%$. This was agnostic to the sample and the compound of different systematic errors. For example, errors on R due to the alignment drifting with thermal fluctuations in the environment may occur between the measurement of multiple points and samples. This was minimised through the routine measurement of the R-factor and repeating of sample measurements when it drifted by $\pm 20\,\%$. Also, for a range of samples compared with other similar PCI setups, the author noted that this recommended absolute error range captured variations in measured values. To minimise the potential systematic effect and improve the repeatability, the same PCI setup was (unless otherwise stated) used over the course of an absorption study. The suitability of evaluating the absorption error based on the $5-10$ spatially separated points compared to a map of $\geq 1000s$ is considered (see section 2.7.1). Mapping large optics such as the mirrors of gravitational wave detectors is crucial, as it allows point absorbers with significantly larger absorption than the uniform level to be identified. If not mitigated in gravitational wave detectors, these can affect the duty cycle (see section 1.6).

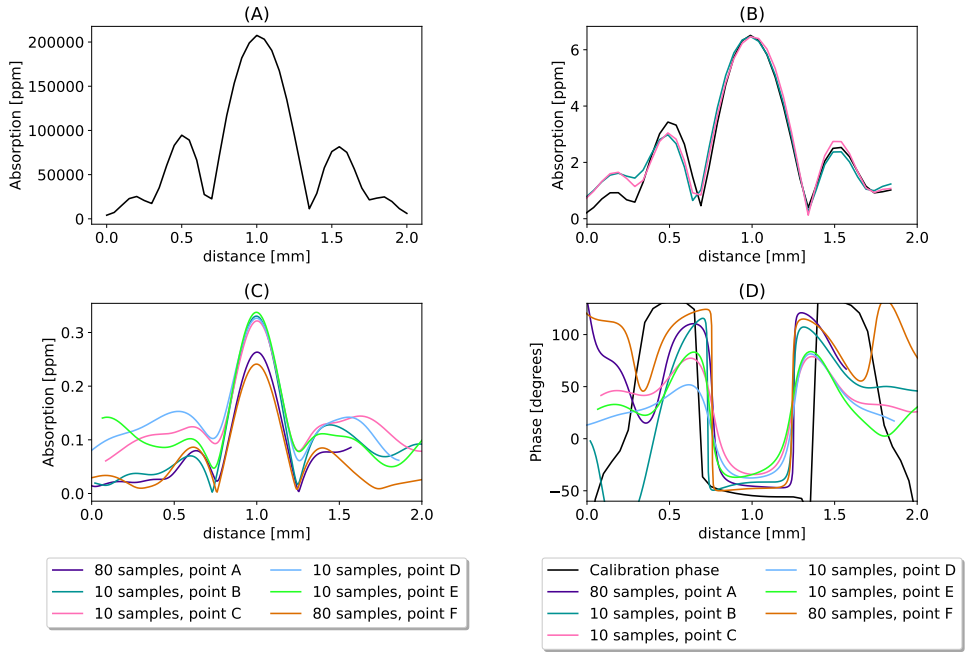

Figure 2.3: This figure shows different PCI z-scans through coated optics. The linearity of the position-dependent response holds across the different of orders of magnitude in peak coating absorption. (A) shows the level from the calibration sample, (B) the as deposited LMA HR stack TiO_2:SiO_2, (C) the same stack after a 600 °C heat treatment as described in section 2.7. Lastly, (D) shows the phase corresponding to the calibration scan and scans shown on (C).

The PCI absorption scans (see figure 2.3) will now be considered in more detail. Once the raw data is measured from a scan, a rolling median filter is applied to smooth the data [171] shown in (A-C). The phase plot (D) shows that around the central peak there is a distinct phase of $\approx -52\,^\circ$. This corresponds to the PCI's phase delay (time-domain) for heat to diffuse and the thermal lens to form. The theoretical phase can be calculated from the imaginary component of equation 2.6. For the PCI beam parameters used here, this value was agreed with the theory. When measuring the sample (B) there was a slight phase shift of $\pm 3\,^\circ$ between scans. This close agreement relative to the calibration is used as an indicator that the thermo-optical properties are behaving as expected and most importantly that the absorption scan is a good measurement. The phase of the low absorption scans (C) shown on (D) show a significantly larger shift in phase. This was identified to be an indication of optical scattering and will be further discussed in section 2.7.

2.4 Theory of gravitational wave detector mirror coatings

Research towards the development of coatings for gravitational wave detectors, is largely motivated from Levin's work highlighting the need to reduce the coating thermal noise (CTN) which significantly limits the performance of all current detectors in the frequency bands where they are most sensitive [89]. Direct measurements of the CTN have previously been correlated with the coating mechanical loss for a range of materials and in agreement with the theory [172] leading up to equation 1.5. For various amorphous thin film coatings, both of these properties have recently been further correlated with the local atomic order [173, 174, 175]. This local order was optically measured with an ellipsometer up to approximately 500 nm in a recent study [175]. This therefore may indicate a fundamental link between optical absorption and coating thermal noise. In parallel to this, there has been significant research into the optical properties (1064 nm) and their uniformity. This was necessitated by the need to minimise the loss of stored light-power in the optical cavity due to both scatter and absorption.

The first generation of LIGO detectors had coating stacks made of alternating layers of silica (SiO_2) and tantala (Ta_2O_5). A highly reflecting (HR) coating stack is a Bragg reflector, whereby a number (N) of refractive index contrasting bilayers will constructively interfere the light reflected from each interface, with a very high reflectivity possible only for a suitable number of layers. The overall reflectivity of the coating stack is the third crucial optical property, alongside absorption and scatter as it enables the optical cavities to build up the high operational power necessary for GW detection.

The CTN of aLIGO was significantly reduced by doping the tantala layers with titania [176]. As the thickness of the coating, through the summation of the layers, scales into the CTN as shown in equation 1.5, research has also focused on making them thinner. However, from an optical perspective, this must be balanced against the minimum thickness required to maintain the desired high reflectivity. A simplified reflection-transmission model was derived by Heavens [177] that serves as a good approximation. Provided that the deposited coating layers are consistent in refractive index and thickness. The reflected intensity is then approximated as

$$R_{2\mathrm{N}} = \left(\frac{n_{\mathrm{S}} \left(n_{\mathrm{ratio}}\right)^{2\mathrm{N}} - 1}{n_{\mathrm{S}} \left(n_{\mathrm{ratio}}\right)^{2\mathrm{N}} + 1} \right)^2 , \qquad R_{2\mathrm{N}+1} = \left(\frac{n_{\mathrm{H}}^2 \left(n_{\mathrm{ratio}}\right)^{2\mathrm{N}} - n_{\mathrm{S}}}{n_{\mathrm{H}}^2 \left(n_{\mathrm{ratio}}\right)^{2\mathrm{N}} + n_{\mathrm{S}}} \right)^2 \tag{2.10}$$

where the high index (n_{H}) and low index (n_{H}) layers are expressed as a contrast ratio ($n_{\mathrm{ratio}} = n_{\mathrm{H}}/n_{\mathrm{L}}$). These equations also account for the index of the substrate (n_{S}). The individual layer thickness, following from the Bragg design, is fixed at approximately a quarter wavelength (QWL) thick. For the benefit of reducing the CTN the total coating stack thickness should be minimised (see equation 1.5). It is desirable to have a high index contrast ratio. Taking a lossless Bragg reflector, the transmission (T) equivalent to reflectance ($T = 1 - R$) is shown in figure 2.4 for a range of incremental bilayers and index contrasts. In reality, the aLIGO coatings are not exactly a QWL design, but instead they comprise of SiO_2 layers slightly thicker than a QWL optical thickness and TiO_2:Ta_2O_5 layers slightly thinner than a QWL optical thickness. Each layer pair thus still sums close to a $\lambda/2$ optical thickness. This is done to also provide suitable reflectivity at 532nm which is the operating wavelength for the arm length stabilisation system lasers of current detectors, but as a consequence also slightly improves the CTN [178, 179]

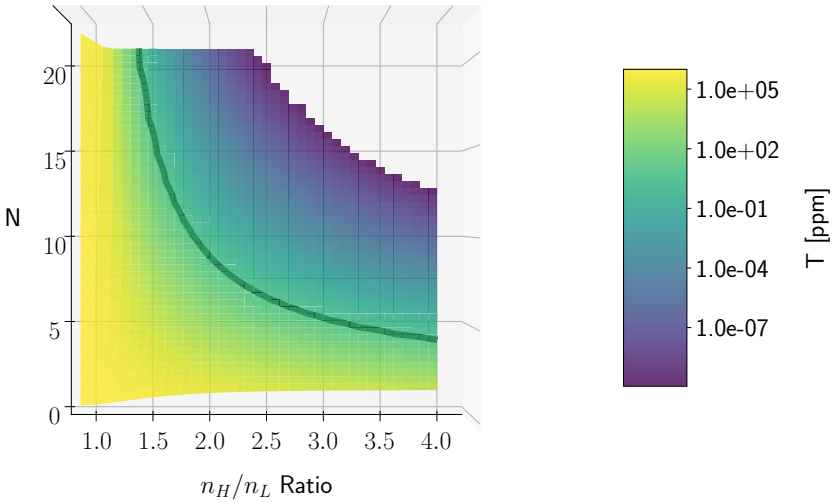

Figure 2.4: This plot shows the order of magnitudes of light (units of ppm) that is transmitted (T) through an ideal lossless Bragg reflector. The contour shows the combinations of contrast ratios ($n_{\mathrm{H}}/n_{\mathrm{L}}$) and number (N) of bilayers which could be used to achieve the current aLIGO transmission of 5 ppm [180].

The balance of different optical and mechanical losses may shift the traditional bilayer material pairings of future coatings to a multimaterial stack [91]. This balance often pushes low-loss materials with high absorption further back in the stack, where the electric field intensity is lowered: having passed through a few layers of lower-absorption albeit higher

loss materials. It is important then that the optical losses are considered across a range of candidates, and that combinations are also considered. In section 3.3, novel multimaterial stack designs for the ET-LF detector based on measurements will be proposed and discussed in detail.

2.5 Candidate coating materials for gravitational wave detector mirrors

With proposed future gravitational wave detectors operating at three distinct target temperatures of $10-20\,\mathrm{K}$, $123\,\mathrm{K}$, $293\,\mathrm{K}$ a wide range of materials are being studied as candidates for future coating stacks. This section will give wider context of the research behind each coating material considered, first for room temperature, then followed by those for cryogenic temperatures.

As the CTN is a limiting noise around the 100 Hz band in current room temp GW detectors, research has continued into other amorphous coating materials. Research for upgrades has in recent years largely focused on studying the feasibility of new amorphous materials like TiO_2:GeO_2 [101], TiO_2:SiO_2 [102], and SiN_X [181] to replace the current high-n material TiO_2:Ta_2O_5. SiN_X may also be of interest as a low-index material alongside high-index amorphous silicon (a-Si) layers. My own research into these candidate replacements is discussed in detail for TiO_2:SiO_2 in section 2.7 and TiO_2:GeO_2 in section 2.8.

A vast amount of research has also been undertaken into improving current TiO_2:Ta_2O_5 coatings by exploring deposition parameters and mitigating contaminants such as argon [182]. Also, Ta_2O_5 mixed instead with other metal oxides has been explored, but TiO_2 was found to be the best metal oxide for producing low CTN coatings [183]. Other prospective higher index materials have also been studied for their potential to improve detector performance, these include hafnia [184], zirconia [185] and niobia [175].

Amorphous silicon is also a very promising material for both room temperature and cryogenic detectors due to its very low mechanical loss and the ability to make thin coatings due to its comparatively high refractive index. However, the absorption has typically been too high for it to be used [186]. Recent studies have shown reductions in the absorption through different deposition parameters [187] and hydrogenation [188]. This process for materials like a-Si that have a high hydrogen affinity can notably, through structural relaxation, reduce both the absorption and mechanical losses.

The low index material counterparts for the coatings stacks will now be considered. In current aLiGO/adV mirrors, silica has a relatively small contributions to the CTN given its very low mechanical loss at room temperature [88] (evaluated through equation 1.5). For future cryogenic detectors, it should be noted that the mechanical loss (and therefore CTN) of silica can increase significantly at low temperatures (see section 3.2). Alumina however appears to show reduced CTN contributions, and so the optical absorption was studied here. To the benefit of the proposed ET-LF detector, very promising results for these are shown in section 3.3.

High index materials considered for future cryogenic detectors have shown improved properties compared to room temperature counterparts. In the case of TiO_2, a lower effective CTN has been observed at cryogenic temperatures, [189]. Also, notably, a-Si coatings have previously shown a 45% reduction in absorption from room temperature [186, 190]. Independent of the specific coating, it is expected that holding a mirror at cryogenic temperatures would allow an amorphous ice to form on top with a large NIR absorption coefficient. Although, this effect will not feature in any measurements presented here, it has recently been studied in the KAGRA detector [191, 192]. In future cryogenic detectors, it will require active mitigation [17, 193] to prevent any significant observing downtime [194].

Other coatings that are distinct mono-crystalline semiconductor materials have also been considered [195] due to their low mechanical losses compared to sputtered amorphous thin-film coatings. However, at the time of writing, these are currently limited by other parameters: with AlGaAs posing cost of scale challenges for the achievable diameter due its requirement for large substrate transfer [196] as opposed to direct deposition on the fused silica substrate and AlGaP requiring several orders of magnitude reduction to the absorption [197, 198].

There are many coating materials worth considering in isolation for any of their stand-out opto-mechanical properties. However, for use in the mirrors of gravitational wave detectors, each coating material used has to have low absorption and mechanical loss. To achieve this, a lot of research has focussed on fine-tuning the deposition and treatment parameters. These will now be discussed to contextualise the detailed measurement studies.

2.6 Effect of treatments and deposition on the absorption of thin-film optical coatings

This thesis will consider different key factors for minimizing the absorption of thin-film coatings. The first is the deposition method. The coatings deposited and measured in this thesis are considered to be homogeneous, isotropic and non-magnetic such that the refractive index ($\hat{n}(\lambda)$) and its components, shown in equation 2.1, are simply represented by scalar complex values for each wavelength (λ). There are many distinct methods for depositing coatings, but the preferred method for high-quality low optical and mechanical loss coatings for gravitational wave detectors has been ion beam sputtering (IBS). The layout of an IBS chamber is shown in figure 2.5. The coating is deposited by a stream of atoms sputtered from a chosen target. These atoms are liberated from the target with an Ar ion beam that is itself guided by electromagnetic controls. The liberated atoms will have a higher kinetic energy [17] than if deposited with similar physical vapour deposition techniques [199] which ensures a high packing density. This is because the high energy allows each atom to bond in a lower energy state that typically corresponds to shorter bond lengths. Depositing coatings with IBS has been shown to result in low optical and mechanical loss coatings for a range of materials [101, 102, 158]. In a-Si coatings produced via IBS, slower deposition rates were found previously to assist in producing lower absorption coatings [187].

With reference to figure 2.5, there are additional parameters which might affect the composition and properties of a deposited coating. Starting from the ion beam, the EM field which accelerates it, physical mask which guides it and angle of incidence on the target all can influence the properties of the final coating. The base environmental pressure of an IBS chamber will typically be set at $< 1 \times 10^{-6}$ mbar and the temperature of a substrate to be coated is known to reach values of $\approx 100\,^{\circ}$C during deposition without any external heating being applied. A gas inlet is also opened to allow elementary gases, such as oxygen, to be bled into the chamber and incorporated into the coating.

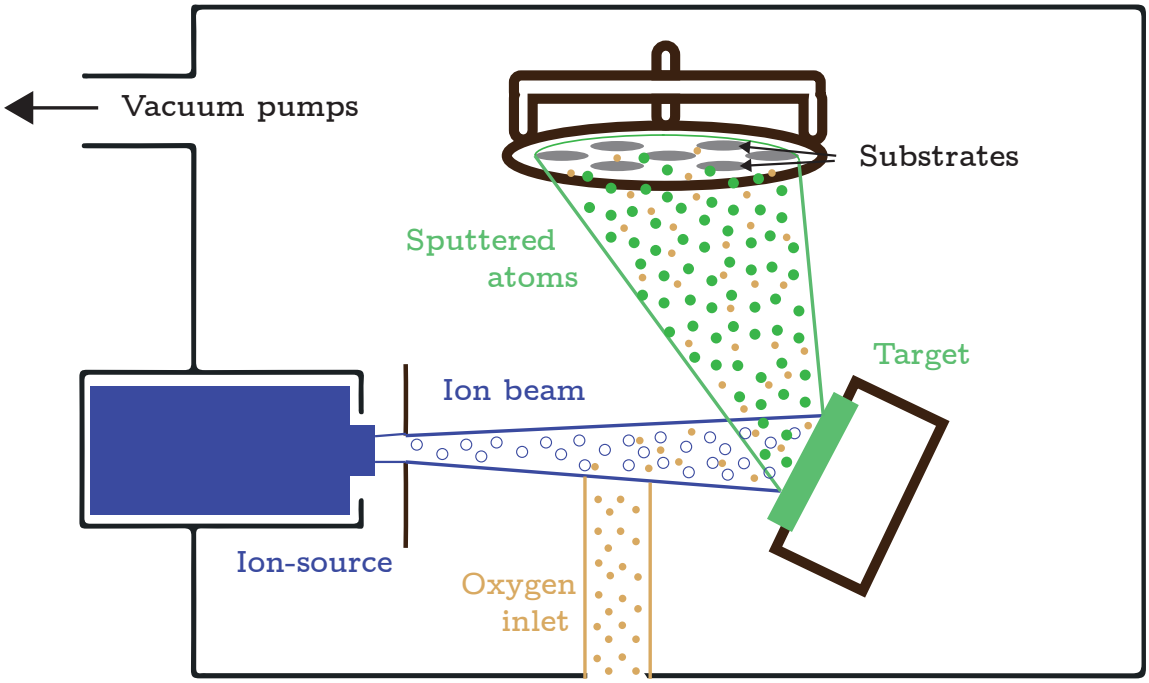

Figure 2.5: Layout of an ion beam sputtering chamber. This graphic was derived from R.Robie [106].

Studies have investigated the effect of elevated temperature deposition. Vajente *et al.* [200] showed that for Ta_2O_5 coatings deposited with either IBS or magnetron sputtering deposition, the mechanical properties were improved across a temperature range of $200 - 500\,°C$. A similar effect was observed also for a-Si deposited with electron beam evaporation [201]. Sub-stoichiometric (Oxygen-poor) deposition for oxides is expected to affect the optical absorption [202]. For deposition of Ta_2O_5 in an IBS chamber, when the level of oxygen backfilling was slightly increased the extinction was previously modelled and found to drastically drop by more than three orders of magnitude [203].

After deposition, coatings typically undergo thermal heat treatment/annealing to reduce their optical absorption [202] and mechanical loss. Both the temperature and duration of heat treatment are important parameters. In addition to improving stoichiometry, heat treatments have also been shown to reduce absorption through the correction of structural defects [204]. These improvements occur up until the crystallisation threshold, at which point clusters start to form, and the total extinction can increase: in a large part due to an increase in optical scatter observed for HfO_2 [205] and Ta_2O_5 [206]. Although, previous studies have shown that this crystallisation threshold temperature has been improved with the inclusion of co-deposited or significantly doped metal oxide titania [97, 102]. The effect of crystallisation on the absorption is not clear but will be considered in section

2.7 Absorption of Titania doped Silica

From this section onward, the rest of this chapter will focus on the experimental measurements made using the PCI setup at the University of Glasgow.

Titania doped silica (TiO_2:SiO_2) is one material of interest as a high index layer in GW detector's mirrors, as a potential replacement for the current titania doped tantala (TiO_2:Ta_2O_5) used in the aLIGO and Advanced Virgo detectors. The need for improved coatings is motivated by the need to reduce the CTN and enable the required improvements in detector sensitivity around 100 Hz for the Advanced LIGO+ and Advanced Virgo+ upgrades. TiO_2:SiO_2) was initially studied by Vajente, Menoni and others who found it could have promisingly low mechanical loss [207]. These initial studies were the inspiration for the project reported on in this thesis.

It was also important that the absorption of any coating upgrade, relative to aLIGO, was below the design limit of 0.5 ppm and ideally close to the level of the current aLIGO and adV mirrors of between $0.22 - 0.27$ ppm [144]. This section will discuss measurements made on TiO_2:SiO_2 coatings from four different batches of coatings, split between two commercial vendors. These batches are distinguished with the four distinct subheadings in table 2.1. Each row of this table features a coating from a separate deposition run alongside most of the key measured material properties.

The rest of this section will discuss the targeted and measured differences between the coatings. The first thing to note is that the measured Ti concentrations [%] were often different from the targeted values. The Ti concentrations of each coating (also called the doping level) is distinguished here as the cation ratio: between just Ti atoms and the total number of Ti + Si atoms.

2.7.1 Measurement of titania doped silica from FiveNine optics

The absorption measurements featured in this section were published (2023 PRL) [102] alongside other independent measurements into the coatings, which are credited here as further comparisons are made.

Targeted Ti conc. [%]	Ti conc. [%]	t_{SL} [nm]	T [°C]	n	t_{HR} [µm]	ρ [kg/m^3]	α [ppm]
			FiveNine Single layers				
40	46.2 ± 0.4	298	As dep.	1.77	10.83	2686 ± 50	Unknown
			450	1.75	11.56		
50	58.5 ± 0.5	274	As dep.	1.88	7.94	2889 ± 50	2.55 ±0.14
			450	1.86	8.63		
			750	1.88	7.94		
60	62.3 ± 0.5	272	As dep.	1.93	7.21	2967 ± 50	2.41 ±0.15
			450	1.92	7.54		
			500	1.91	7.56		
60	62.6 ± 0.5	256	As dep.	1.93	7.21	3022 ± 50	3.78±0.12
			450	1.91	7.56		
			600				2.32
			FiveNine HR coatings				
50	63.2 ± 2.0	Not applicable	As dep.	1.93	7.21	3303	7.58 ±0.48
			450				1.16 ±0.21
			550				1.90
			575				1.30
			600 *				1.71 ±0.08
			600 (prog.)				1.14
60	69.5 ± 1.7	Not applicable	As dep.	1.97	6.83	3443	6.03 ±0.47
			450				2.03
			500 (prog.)				1.36
			525 (prog.)				1.07 ±0.04
			550				0.88 ±0.05
			575				1.08 ±0.14
			600 (prog.) *				1.37 ±0.03
			600 +				0.84±0.09
			650				1.15 ±0.58
			850 (prog.) +				0.82 ±0.11
			LMA single layers				
69.5	62.2	561	As dep.	1.89	unknown	unknown	19.6
			450 +				8.30 ±0.64
			600 +				1.40 ±0.20
			LMA HR coatings				
69.5	62.2	Not applicable	As dep.	unknown	unknown	unknown	6.32 ±0.08
			450 +				1.39 ±0.09
			600 +				0.28 ±0.03

Table 2.1: Nominal and measured Ti-cation concentrations, t at 1064 nm at selected heat-treatment temperatures T_t, and ρ of the single layers, and t_{HR} required for $R \geq 99.9994\%$ (using $n_{SiO_2} = 1.45$). This table shows the discrepancy between target and measured Ti cation concentration expressed as a ratio Ti/(Ti + Si). Fits of the refractive index (n) and thickness (t) are also shown from transmission measurements made on single layers with extrapolations made to the HR stacks [102]. The absorption data as plotted throughout this section is also highlighted in this table for each measurement made.
* Indicates samples which were found to have defects after heat treatment.
+ Indicates samples which were heat treated at a slower ramp up rate of 50 °C/hr.

In order to find the optimal Ti concentrations [%] three distinct levels were targeted with the vendor FiveNine Optics [208]. The TiO_2:SiO_2 coatings were all deposited using IBS with Ti and SiO_2 targets; using argon as the sputtering ions /ion source and with the substrates held at $\approx 100\,^{\circ}C$ during deposition. The coating batch consisted of single layer depositions of three target titanium cation ratios and two HR multilayer stacks with two target ratios. Measurements by collaborators at Universitié de Montréal with Rutherford backscattering spectrometry (RBS) [209] on single layers and with elastic recoil detection with time of flight measurements on stacks, showed that the actual Ti cation percentage was higher than targeted: at most by up to 13%. As a result, coatings will be referred to here by their measured value (see table 2.1).

In order to compare the effects of heat treatment on the (1" diameter) absorption samples, direct heat treatments – in which the sample is taken from the as-deposited state to the temperature of interest – were preferred. Due to a limited number of samples, each one was typically quartered. To cut the samples, they first scored along the back with a diamond scribe before being physically snapped. This was suitable as all the samples were 1 mm thick. With four separate samples for each coating, these could be heat treated to the target temperature. Except where clarified, this heat treatment was direct from the as deposited state in and performed in a Carbolite [210] oven (CTF 12/65/550). This heat treatment typically featured a ramp up rate of $100\,^{\circ}C$/hr to the target temperature followed by a dwell time of 10 hours. Ideally, this would then follow a symmetric cooldown rate typically however the oven typically exhibited an exponential decay from the target temperature. Rapid temperatures changes can lead to the stress-induced destruction of thin-film coatings. A typical time of 10 hrs was given for the coatings to gradually cool through the $100 - 200\,^{\circ}C$ range and as a result no delaminated coatings were observed. The target heat treatment procedure followed for every coating is shown in table 2.1 and differed for a few samples as will be explained. In order to get a more fine sampling of the dependence of the absorption on the heat treatment temperature, some samples were progressively heat treated in small $25\,^{\circ}C$ increments.

Direct thermal noise measurements and mechanical loss measurements were carried out on coatings deposited at the same time as those produced for absorption measurements. These measurements of the 69.5 % HR stack (consisting of high-n QWL layers of 69.5% ti cation concentration TiO_2:SiO_2 and SiO_2 and low-n QWL of pure-SiO_2) showed (see figure 2.6) that a decrease in the effective mirror CTN with measurements correlated across two distinct experimental setups with increasing heat treatment temperature. For the 69.5 % TiO_2:SiO_2 and SiO_2 HR stack an optimal CTN was found to occur at around $850\,^{\circ}C$ (after

a distinctly longer hold time of 100 hr) to be 76 % of aLIGO. Discrepancies between the HR and the single layer coatings suggested, at the time, that this value could potentially have been further reduced to about 46 % of aLIGO if the coatings were deposited with state-of-the-art and low mechanical loss SiO_2 layers.

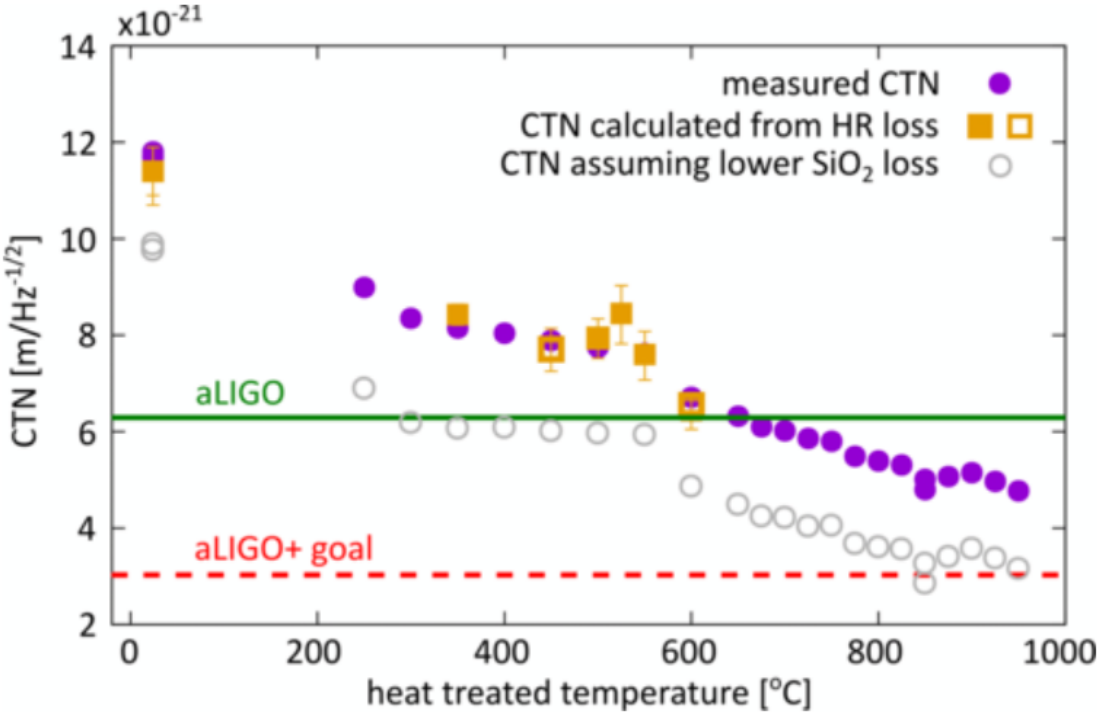

Figure 2.6: This figure is taken from [102]. This plot shows the CTN of the 69.5% ti cation concentration HR stack, measured through different techniques, at 100 Hz and scaled to the aLIGO end test mass beam size. Direct measurements by MIT (purple, solid points), and the CTN calculated from the coating mechanical loss (shown by yellow squares), are compared. The latter of which was recalculated for lower SiO_2 losses. The red, dashed line represents a reduction compared to aLIGO (green line), which is the CTN goal for the aLIGO+ upgrade.

The 69.5 % HR coating was also shown to have remarkably low scattering, that increased within the acceptable limits up to 850 °C and showing no observable defects up to 950 °C. In parallel to these measurements, there was strong interest in evaluating how the absorption likewise behaved with heat treatment temperature. Figure 2.7 shows the results of the (averaged point) absorption measurements of the 69.5 % TiO_2:SiO_2 HR stacks as a function of post-deposition heat treatment temperature. As first shown (see table 2.1), the absorption dropped significantly with increasing heat-treatment temperature, from 6.2 ppm as deposited down to 1.15 ppm at 650 °C. However, the sample At 600 °C had an absorption of 1.37 ppm. Closer inspection showed that there were defects (see figure 2.8 (a)-(e)). When the absorption was checked in proximity to these defected regions, there was not a clear increase in the absorption but a uniform increase across the coating. In order to better understand the effect that heat treatment rate had on both of these effects,

another identical sample was directly heat treated to 600 °C but with a slower ramp rate of 50 °C/hr. This sample, unlike the previous, seemed immaculate to the eye, though upon inspection with an optical microscope had a single small defect (see figure 2.8 (g)) on an otherwise pristine optic. The absorption level was significantly less at 0.84 ppm compared to the coating progressively annealed and with faster ramp rates of 100 °C/hr. As the CTN was improved after being held at a temperature of 850 °C for 100 hrs (by 24 %) in comparison to the 600 °C point, the absorption had to be checked. For the same sample, the slower ramp rate from above was followed up to 850 °C. The absorption reached a comparable level of 0.82 ppm.

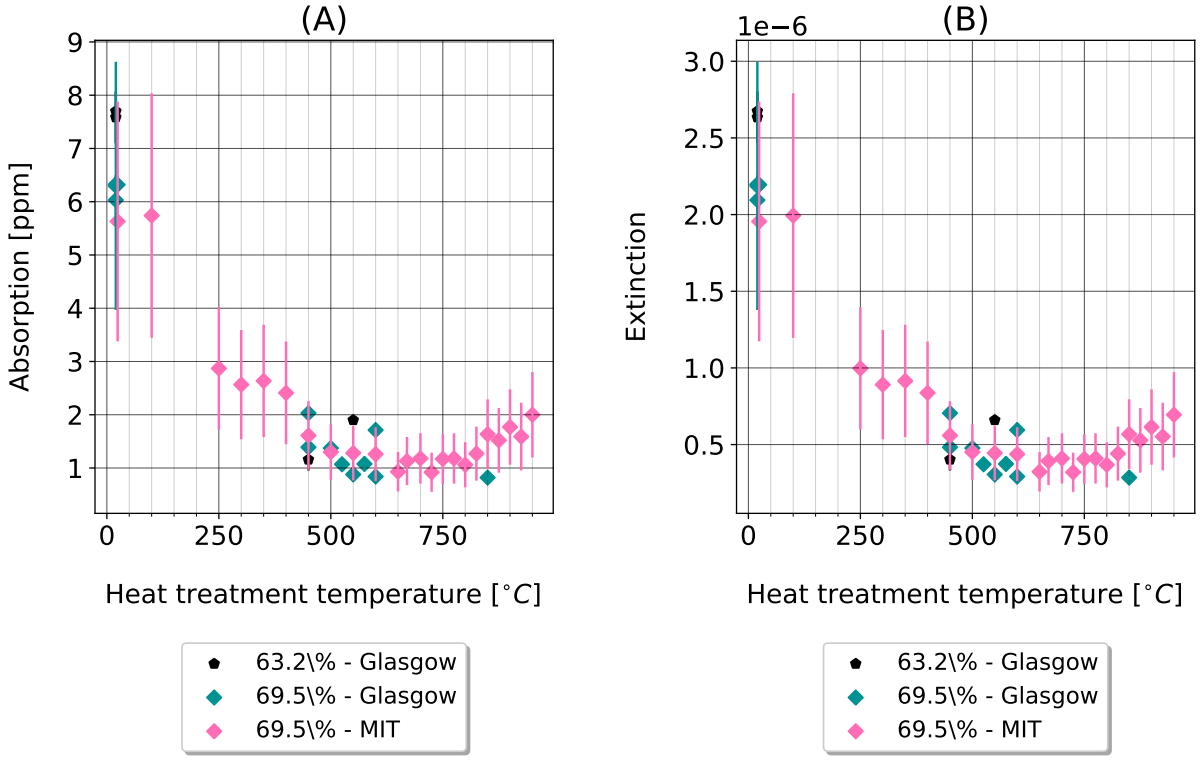

Figure 2.7: (A) the absorption of the two HR stacks with TiO_2:SiO_2 as the high index layers. (B) the evaluated extinction of the TiO_2:SiO_2 layers. The 850 °C 69.5 % Glasgow point is for the a sample that was heat treated at temperature for 100 hrs.

This shift in absolute terms for the absorption was also observed for the same batch of samples independently in a different optical setup at the Massachusetts Institute of Technology (MIT). At the time of writing, the full details of the MIT measurement procedure beyond the layout of the setup [100] has not been published by the group, but the principles are discussed in McGhee [156]. In short, the resonance frequency of a high-finesse cavity is dependent on the loss due to optical absorption. A relative measurement can be made if the cavity contains a sample of known absorption that can also be substituted in

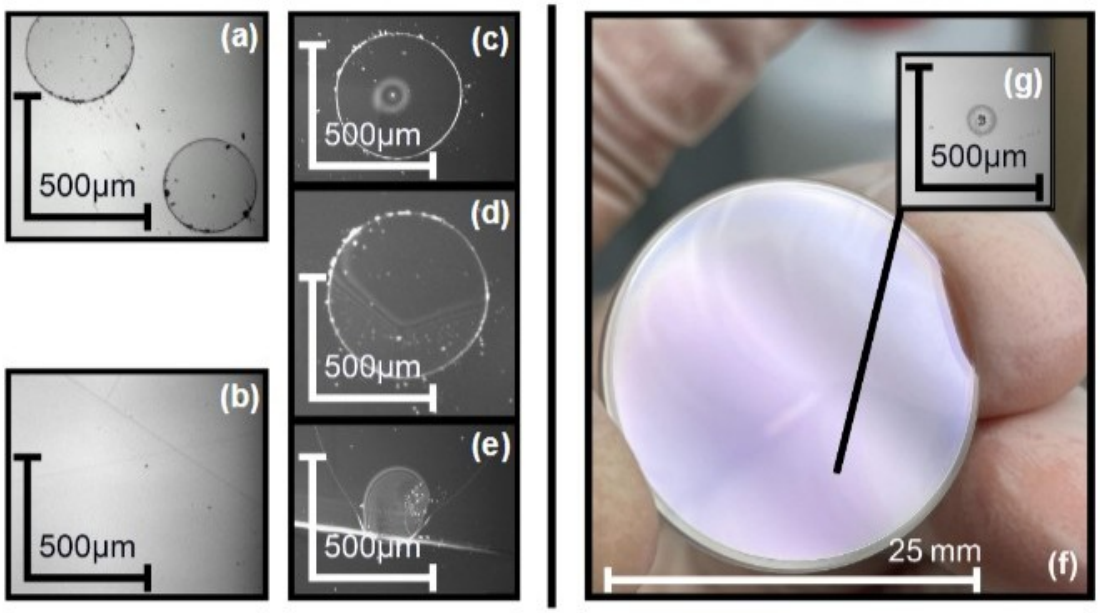

Figure 2.8: Optical microscope images of the 69.5 % samples that were heat treated to 600 °C.
(a)-(e) Microscope images of the defects formed on the sample that was progressively annealed from lower temperatures to 600 °C (see table 2.1 (*)). (f) Sample heat treated directly to 600 °C which only showed one small defect when viewed under the microscope (g).

place of the measurement sample. Given the higher error in the MIT data and the low measurement plateau, the true minimum absorption indicated could be anywhere between $650 - 800$ °C. Within the errors shown, the absorption from both setups and for each data point was in agreement.

For the 63.2 % TiO_2:SiO_2 stack as deposited, the uniformity was first investigated by mapping (see figure 2.9 (C)) the sample over a 2 mm × 7 mm rectangular region of the quartered 1" sample with a stepping resolution of 50 µm (close to the lateral resolution set by the PCI pump beam waist 35 µm). There were clearly small point absorbers on the coating that were measured to be within $50 - 150$ µm scale (in each axis). The absorption level of these reached the 500 ppm level for the given sampling resolution. In order to investigate the distribution in absorption, a histogram was taken (figure 2.9 (A)). The average value of this was evaluated to be 12.1 ppm. Then a cut-off threshold of 30 ppm was placed (red line) above which the point absorbers representing 2 % (as outliers) were ignored and the average of the absorption was re-evaluated as 7.7 ppm. As discussed in section 2.3.2, there is a phase threshold level within which absorption measurements are accepted. This was typically chosen to be ±10 degrees, as shown either side of 55 degrees (black lines) (figure 2.9 (B)). It was not clear from this map if a bad phase (outwith the range) correlated with an absorption outlier. After this, the sample was investigated

under a green light and there were clearly specks of dust on the surface. Repeat absorption scans were made across 5-10 discrete points, and the average level was remarkably similar at 7.6 ppm. Although this given sample was not investigated under a microscope at the time, other single layer coatings were checked as deposited and after heat treatments and appeared to show, unless otherwise stated, no visual indication of any surface defects. For the rest of the coatings, the decision was made to measure them with discrete points. The belief was that any high absorbing points due to point absorbers should statistically (for the low expected distribution) be unlikely and stand out.

For the 63.2 % TiO_2:SiO_2 stack, the as deposited absorption of 7.6 ppm was slightly higher and dropped to $\approx$ 1.16 ppm both for heat treatments to 450 °C and 600 °C. Compared to the 69.5 % this minimum value was 30 % higher. However, limited sampling of the (heat treatment) parameter space makes it difficult to properly resolve the minimum absorption. Also, given time constraints none of these samples were heated at a slower ramp rate so it is believed that the same absorption level as the 69.5 % could be reached. As described for the 69.5 %, one of the 600 °C samples, although annealed directly to the desired temperature this time, showed similar defects and a significantly higher yet uniform absorption of $\approx$ 1.71 ppm.

To understand the true extinction level of these materials and the difference between dopings all of these absorption values (fully shown in table 2.1) were converted to an expected extinction coefficients. These extinction values were for the high-index layer, following the assumption that the extinction of the TiO_2:SiO_2 layers is dominant over that of the SiO_2 layers. To test this, single layer (SL) coatings of approximately 63 % TiO_2:SiO_2 were investigated from the same batches in order to best determine the TiO_2:SiO_2 layer's true extinction coefficient due to absorption losses.

The single layer coatings across a narrow range of Ti concentrations ($58.5 - 62.6$ %) were also measured. The absorption levels as deposited were at a level of $2.4 - 2.55$ ppm. This increased to 3.78 ppm for the 62.6 % concentration coating. As this single layer had the closest absorption to the 63.2 % stack, it was heat treated to one of the optimum temperatures of 600 °C. Although, the absorption level only reached 2.32 ppm. It was interesting, therefore to investigate the extinction between the single layers and stacks for the $\approx$ 63 % TiO_2:SiO_2 coatings assuming the SiO_2 layers do not contribute to the extinction. The converted values are shown on figure 2.11. It appears, as deposited, that the extinction attributed to the TiO_2:SiO_2 layers in the HR stack is approximately double the value indicated by the single layers. However, after an annealing temperature of 600 °C the TiO_2:SiO_2 extinction estimated from the HR measurements appears to agree with the

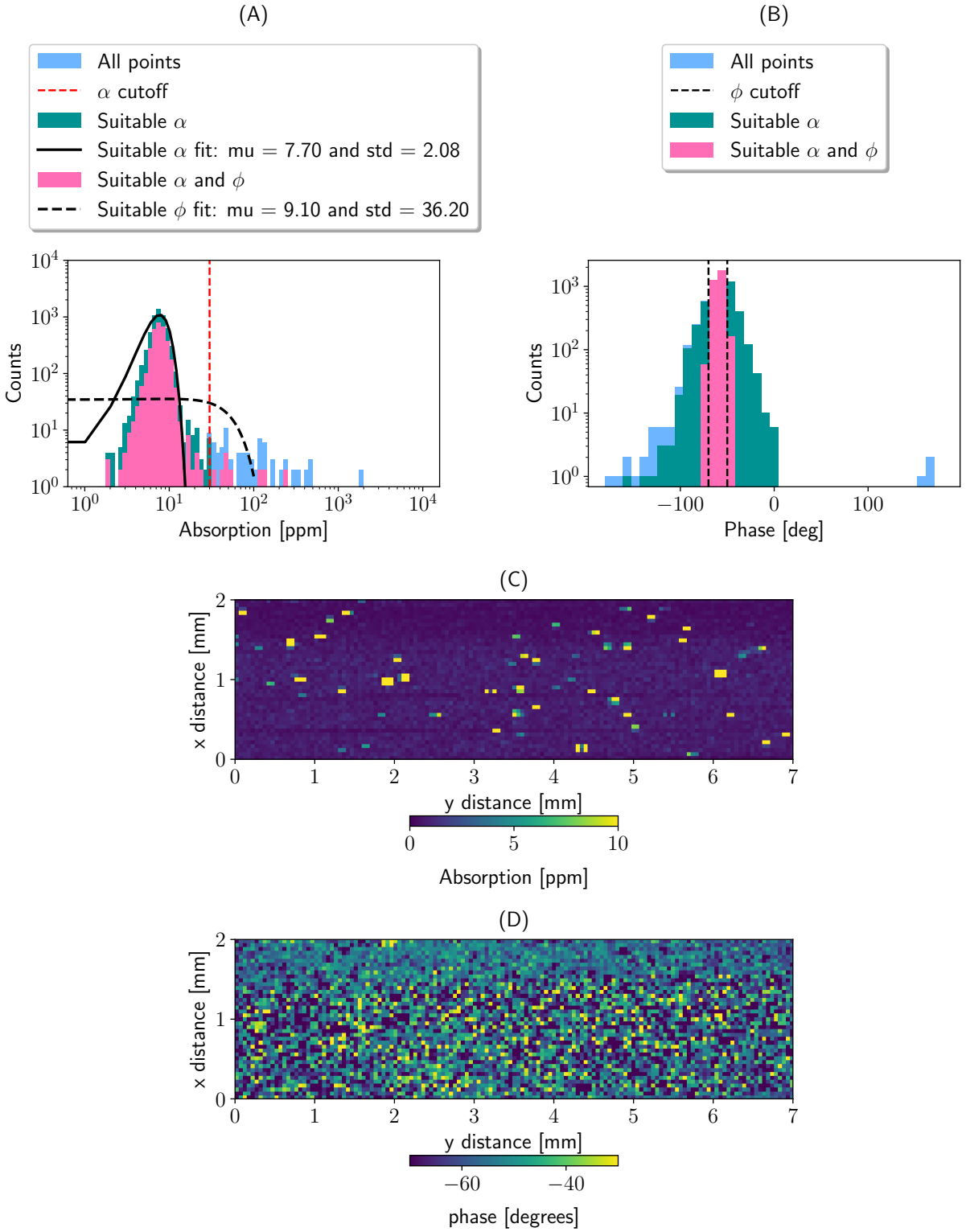

Figure 2.9: Absorption and phase map alongside an evaluated histogram for the TiO_2:SiO_2 63.2 % Ti ADP stack.

single layers. Although the data sample is limited, this indicates that either the extinction

of the TiO_2:SiO_2 was truly reduced more when included in a stack or that the model's assumption of silica having zero absorption as deposited in the stack is incorrect. The latter case would indicate that the silica may have worse stoichiometry or structural defects that are corrected with heat treatment.

From the extensive studies made on these coatings, they were found to be promising candidates for the mirrors of future gravitational wave detectors. To summarise, the optimal properties and improvements from as deposited coatings are as follows. The CTN level (shown in figure 2.6) reported although not at the 50 % of aLIGO target was close at 76 %. In the paper, the excess CTN was suggested to arise from the silica layers [102]. Although the silica layers did not appear to contribute to any excess absorption in the heat treated 63.2 % stack. They were possibly significantly contributing to the absorption as deposited.

The minimum absorption for directly measured stacks with a concentration of 69.5 % was found to be 0.82 ppm. This coincided with a slower ramp rate (50 °C/hr), longer anneal (100 hr) and defect free sample. These three conditions, for other samples, were also shown to improve the optical absorption. This absorption level, after improvement, of the HR stack fell short of the 0.5 ppm secondary target. However, through the preparation of further coatings and prolonged heat treatments and temperatures shown here, the target is expected to be reachable. In addition to these promisingly low absorption measurements, the absorption and both the scatter stayed low even after the coated stacks started to crystallise between 575−600 °C and up to the defect threshold of 950 °C . The scatter of the coating was measured for the 69.5 % with a total integrated scatter (TIS). As deposited, it was $\approx$ 2.8 ppm and increased to $\approx$ 5 ppm after the 850 °C. This is approximately half the value of current aLIGO test masses (9.5 ppm) [158].

The low absorption and scatter indicated that the true combined level of extinction is very low. This is surprising as recent literature has indicated that at the onset of crystallisation the both scattering and absorption should increase [205, 206]. However, it is possible that previous measurements did not fully distinguish between the optical losses of scatter from those due to absorption. Instead, the results shown here are in good agreement with the qualitative model of optical loss annealing provided by Wang [202]. They show that the changes in scattering and absorption are anti-correlated over crystallisation progression (with heat treatment). The TiO_2 studies and optical measurements near the visible range, predicted that mixing the TiO_2 film with additives could reduce the onset of crystallisation and the absorption level. For mixing with silica, the work presented here supports these predictions for the first time.

2.7.2 Measurement of titania doped silica from LMA

Following the promising results of the FiveNine the current GWD coating vendor Laboratoire des Matériaux Avancés [211] (LMA) elected to help expand the development of this material. Through their experience in making state-of-the-art low optical and mechanical loss coatings, it was expected that the deposition recipe could be improved on their end. The measurements that followed took place as part of a wider study that aimed to fine-tune the heat treatments procedure in order to mitigate defect formation. As part of this, the author focussed on investigating the absorption.

The coatings prepared by LMA (see table 2.1) consisted of both single layers and HR stacks. Although, targeted at 69.5 % for comparison to the optimal FiveNine coated stack, these all ended up being 62.2 % TiO_2:SiO_2. This turned out to be close to the 63.2 % TiO_2:SiO_2 from FiveNine and so suitable comparisons between the two could be made.

These coatings were also deposited using IBS with Ti and SiO_2 targets and using argon as the sputtering ion. The chamber pressure was 8×10^{-6} mBar and the substrates were held at nominally the same temperature 100 °C during deposition. These were all then heat treated with a ramp rate of 50 °C/hr, held at the target heat treatment temperature for 10 hours and cooled at the same targeted rate in the oven.

The total absorption for this stack was measured as deposited 6.32 ppm (see figure 2.3 (B)) and after 450 °C at 1.39 ppm. These were both slightly below the absorption of the FiveNine stacks after similar heat treatment levels. Then the coating was heat treated to 600 °C. However, when trying to measure in the PCI there was no clear absorption peak, a raw noise level of 0.9 ppm and a phase compared to the calibration ($\approx$ 55 degrees) that was close to zero. When inspecting the beam, there were multiple beams (derived from the pump) clustered around the probe, as shown on figure 2.10 (A). There was difficulty moving these away from the probes central axis and prior to the telescopic imaging stage's first lens. When tilting the sample by hand, these stray beams shifted drastically and so the decision was made to modify the sample mount and shift them away from the probes path. The modification (see bottom left of figure 2.10 (C)) involved a small plastic spacer followed by using a rapid set (low-outgassing) epoxy such that the optic was reintroduced to the mount, in-situ, the stray beams were angled downwards and away from the lenses central axis. However, there was still some background red light visible on the card and so a tight sub-mm aperture was centred on the probe before the lens. The effect of these modifications to the setup (shown on figure 2.10 (B))) was not only to give a well-defined

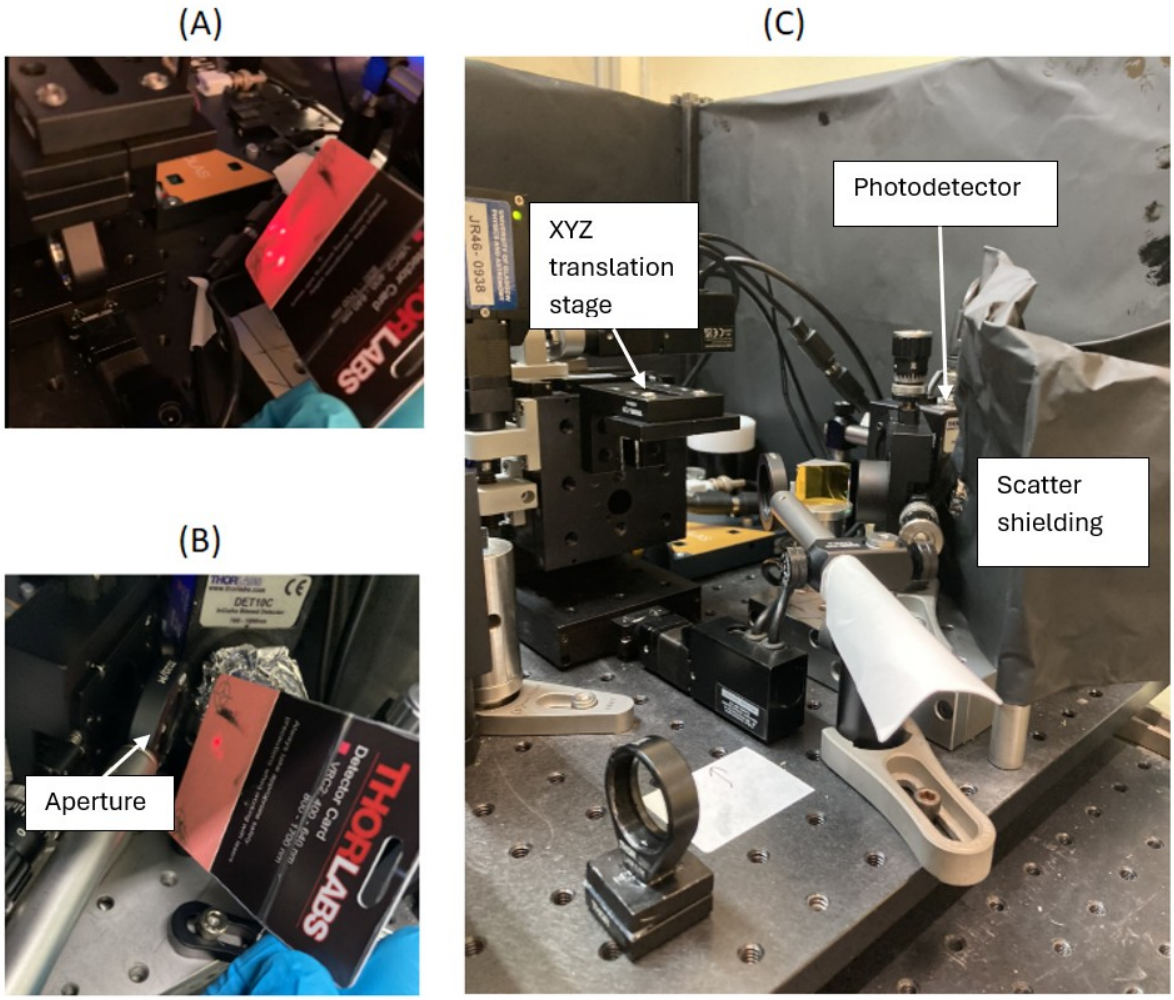

Figure 2.10: Improvements made to the PCI setup in order to reduce scattered light level. (A) Multiple reflections of the pump beam scattered along the path of the probe and towards the photodetector. (B) Reduction in scattered light through centring a tight sub-mm aperture around the probe. (C) Side on view of the PCI featuring the translation stage and black aluminium foil used to block stray light from a wide range of angles onto the photodetector.

probe beam as viewed on the NIR imaging card but give a clear absorption peak. The absorption was subsequently measured, over prolonged periods, with a well-defined peak resolvable on the coating surface. The average value measured was $0.28\,\text{ppm} \pm 0.03$. This is remarkably low.

The value equated to half of the $\approx 0.5\,\text{ppm}$ minimum absorption requirement and was, within error, equivalent to the level of the current aLIGO and adV mirrors of between $0.22 - 0.27\,\text{ppm}$ [144]. The measurement scans will now be discussed in more detail.

The individual PCI absorption scans taken across the surface of a 1" optic are shown in figure 2.3 (c). During these scans the pump laser was operating at its maximum available power (2.26 W) and the measurement was made over prolonged periods of approximately 10 hrs for point scans A & F and 1 hr for the rest of the scans. These 2 mm scans were stepped at a distance of 5 μm and corresponded to 80 and 10 measurements per step respectively. To the whole data series, a combination of median and averaging filter was applied. The scan levels for the shorter scans by comparison showed a ≈ 0.1 ppm background noise level. It appears that this also offset the peak by the same amount. As the phase shown on figure 2.3 (D) for each of these scans is closer to zero and away from the reference phase, it is expected that light from the pump (to which the phase is calibrated to zero) was hitting the photodiode. Due to the non-random noise, this created a background level which required increased median filtering to remove.

With these low absorption levels $0.28\,\text{ppm} \pm 0.03$ (include a safety margin) relative to the aLIGO target, it was interesting to also consider the LMA TiO_2:SiO_2 other properties. Using a coating from an identical run collaborators at MIT found the CTN had also slightly improved compared to the FiveNine coatings to around $\approx 72\,\%$ of current aLIGO levels. However, though both absorption, and CTN had been improved with these 62.2% Ti based LMA coatings, all the LMA coatings, regardless of heat treatment, whether they were single layers or full HR stacks, developed cracks, and sometimes blisters, when heat treated above 600 °C.

In order to understand the consistency of the extinction levels between single layers and stacks, the assumption that the silica layers contribute zero extinction (previously made for the FiveNine coatings). For as deposited measurements, figure 2.11 shows the comparative extinction levels of stacks and single layers with approximately the same doping concentration of 63 % and coming from both vendors.

The LMA single layer (SL) compared to the stack showed excess extinction attributed to the TiO_2:SiO_2 of 3.1×10^{-6} compared to 2.3×10^{-6} for the stack. The proportional excess extinction in the SL increased slightly after heat treatment with the SL giving 2.2×10^{-7} compare to the stack's 9×10^{-8}. This is an unexpected result. The coatings were expected to have the same deposition conditions. It is possible, assuming the TiO_2:SiO_2 layers dominate the absorption, that there is some inter-diffusion with the silica layers that acts to reduce its effective extinction in the stack.

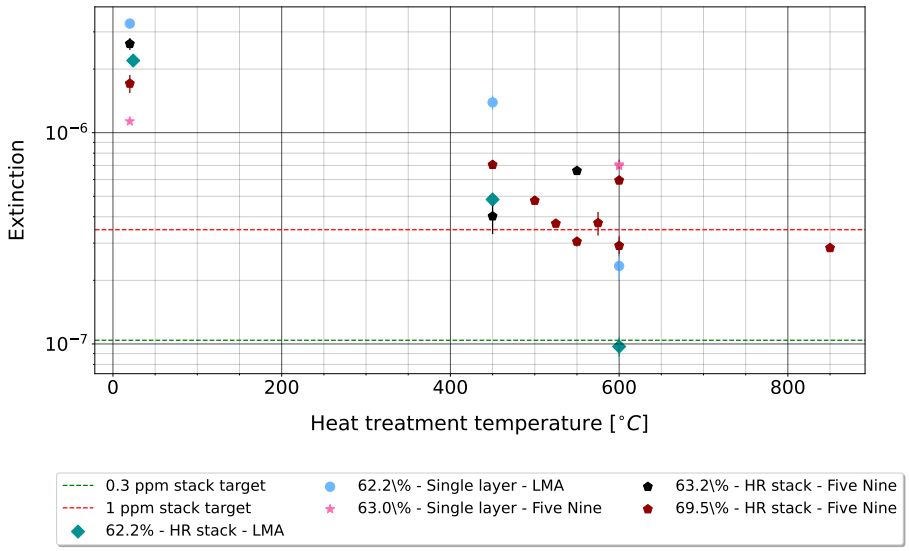

Figure 2.11: This plot shows the evaluated extinction coefficients for TiO_2:SiO_2 from both single layers and HR stacks where the low index bilayer pair is SiO_2. The SiO_2 layers in the stack evaluations are assumed to have values which don't contribute measurably to the measured stack absorption.

The lowest absorbing SL coatings from LMA and FiveNine were found to occur for the same 63 % doping and after the same heat treatment temperature of 600 °C. The evaluated extinction value for LMA was 2.2×10^{-7} compared to 7×10^{-7} for FiveNine. As for the 63 % LMA HR stack, the evaluated extinction at 600 °C for the TiO_2:SiO_2 layers was also as expected, considerably lower at 9×10^{-8} than the extinction value of 6×10^{-7} found for the lowest absorbing FiveNine stack (69.5 % Ti). Both coatings reached their optimal absorption with a slower ramp rate 50 °C/hr.

The work here gives strong experimental evidence on towards slow and prolonged heat treatments improving the extinction of thin-film coatings. Anneals that were 100 hours long were tested and favoured by a FiveNine sample and indicates given the substantial reductions with heat treatment that sub-stoichiometric correction and structural defects are limiting the extinction and therefore derived absorption of mixed titania films. Through further optimisation of the heat treatment parameters, the extinction of these thin-film coating is expected to further decrease.

The measurements shown here contribute to the scientific understanding of mixed titania films. With only a few TiO_2:SiO_2 studies, published to date, the comparison between different vendors and agreement in favoured annealing conditions indicates that absorption mitigation, to the extremely low level required for future GW detector mirrors, is being realised across multiple IBS deposition systems. The hope therefore is that with improved access to ultra-low absorption thin-film coatings that the underlying factors and theory

can be better understood. As future optical systems look to increase their power, the limit of tolerable absorption levels will continue to decrease. These systems may make use of thin-film coatings deposited in anti-reflective forms and so further progress to understand the effect of coating structure on extinction will be of future interest. The work here for the LMA coatings indicates that the same TiO_2:SiO_2 coating when deposited in stack had a significantly lower extinction. This was a surprising result that indicates either inconsistencies between the deposition runs or inter-diffusion with the SiO_2 at the top of the HR stack.

As a result of research contained in this section, alongside the extensive efforts of collaborators, TiO_2:SiO_2 is actively being considered as material for use in future Virgo detectors. Future research will help clarify to what extent this is an optimal coating material to match the increasing power and sensitivity of precise optical measurement systems.

2.8 Absorption of Titania doped Germania

Titania doped germania TiO_2:GeO_2 is another primary candidate of interest, alongside TiO_2:SiO_2 as a replacement for the current titania doped tantala TiO_2:Ta_2O_5 found in aLIGO and Virgo detectors [101]. The co-deposition of TiO_2 with the target cation ratio (described in section 2.7) is done in order to increase the refractive index: allowing the coating to be used as high-index layer counterpart to low index silica. This section will present measurements made on TiO_2:GeO_2 batches received from two different vendors. A batch received from Cutting Edge Coatings (CEC) [212] and the batch from Extreme Performance in Optical Coatings EPOC (new large area IBS facility in Scotland [213, 214]). All of these coatings and their absorption results are detailed in table 2.2.

The CEC coatings were deposited using IBS at a range of different TiO_2 doping concentration with properties (see table 2.2). For each single layer coating, the target doping cation ratio was informed from previous work [101] and measured with RBS. The thickness and index of these were determined by spectrophotometer measurements. A CEC HR coating was also produced with 27 bilayers where the lower index layers were SiO_2. Each layer was targetted to be close to a quarter-wave optical thickness at 1064 nm. The Ti doping concentration for the TiO_2:GeO_2 layers in stack was at 42.9 %. This was targeted as it was one of the most promising of the concentrations in account of low-mechanical loss, resistance to crystallisation and refractive index identified by a previous study [101].

Ti conc. [%]	T [°C]	t_{SL} [nm]	n	α [ppm]	κ $\times 10^{-6}$
			CEC Single layers		
42.9	As dep.	499	1.88	7.4 ± 0.5	1.2 ± 0.1
52.1	As dep.	498	1.95	5.3 ± 0.1	0.9 ± 0.01
72.5	As dep.	498	2.13	7.3 ± 0.2	1.2 ± 0.04
			EPOC Single layer		
48.7	As dep.	500	1.85	3.2 ± 1	0.54 ± 0.2

Ti conc. [%]	T [°C]	$t_{TiO2:GeO2}$ QWL [nm]	$\alpha_{TiO2:GeO2}$ [ppm]	$\kappa_{TiO2:GeO2}$ $\times 10^{-6}$
		CEC HR coating		
42	As dep.	138	20 ± 0.8	6.7 ± 0.3
		EPOC HR coating		
48.7	As dep.	141	11.8 ± 0.2	4 ± 0.2
48.7	600 (10 hours)	141	1.5 ± 0.3	0.33 ± 0.07
48.7	600 (100 hours)	141	0.5 ± 0.1	0.11 ± 0.02

Table 2.2: Table summarising the key properties for all the TiO_2:GeO_2 coatings alongside their measured absorption.

For the EPOC coatings, the TiO_2:GeO_2 was deposited using IBS with the substrates placed towards the edge of the sputtered ion plume. The single layers were deposited onto JGS glass [215] and a Ti conc. of 48.7 % was achieved. For these runs, the doping ratio was targetted to closely align with previous promising TiO_2:GeO_2 samples in the CEC and other studies [101]. The HR stack were deposited on Corning 7980 [216] with a low base pressure in the chamber of $5 - 8 \times 10^{-8}$ mbar. The stack comprised of 51 quarter wavelength layers at 1064 nm (alternating between TiO_2:GeO_2 and SiO_2) with a half-wavelength cap layer on top.

The optical absorption measurements presented here are summarised in table 2.2. These were made in parallel to those in a paper in preparation [217]. The paper features some single layer measurements from Markosyan [218] for some of the equivalent coatings (with cation ratios of 42.9 %, 52.1 % & 72.5 %). These measurements are shown here on figure 2.14 for iterative heat treatments made up to temperatures of 700°C. The heat treatments were ramped up at 50°C/hr, the dwell time at temperature was ten hours and the targeted ramp down rate was 50°C/hr.

Alongside this paper, the study here investigated single layer coatings, from the same deposition batches as [217], ADP and found that absorption measured in the Glasgow setup for each doping was between $24 - 35$ % less than the aforementioned study. As these coatings were measured at different times (months before) the shift could in part be attributed to the coatings in the parallel study absorbing water from the atmosphere prior to measurement. However, previous observations have suggested that this would have tracked with the coating turning cloudy or hazy. As this was not observed, the discrepancy likely indicates the compound of different systematic errors between the two PCI systems. Further comparative measurements of distinct and heat treated samples would reveal if this effect was intrinsic to this particular coating itself. For the three distinct concentrations' extinction levels up to around 12×10^{-7} were measured as deposited. The 52 % gave the lowest extinction of 9×10^{-7} , and no clear trend with doping concentration was observed. Based on the proportional improvements with heat treatment shown in the parallel study, these extinction levels after heat treatment between $300 - 400$°C are expected to reach from 6×10^{-7} down to 2×10^{-7} for the 52 % coating.

Given time constrains, the priorities shifted to measuring the coatings deposited by EPOC. The as deposited measurements of the single layer coating are shown on figure 2.12. They showed an absorption profile differing from the standard profile that would be expected from a sample dominated solely by absorption from a coating (see figure 2.3). The JGS glass substrate used here is known to have higher bulk absorption than many Corning or Suprasil 313 glasses conventionally used for these types of measurement [215, 216, 219], and so the significant substrate contribution was expected. In an attempt to isolate contribution to the absorption signal from the coating alone, multiple absorption measurements were taken with the sample flipped around, such that the coating was on the rear-face (backward) with respect to the incoming lasers. The absorption of the coating facing backward was shown to be lower, which agreed with the reduced power reaching the coating in account of the air-substrate and substrate-coating interfaces. As for the coating facing forward, the coating absorption was approximated by subtracting off half off the bulk. For all three of the scans this bulk contribution was found to be 3.2 ppm. Due to the bulk contributions the single layer coating was not processed any

further, because the bulk absorption was not expected to reduce after heat-treatment. As a result, the resolution of any improvements to the coating's absorption would be limited by the bulk absorption. It was clear, however, that the absorption from the EPOC vendor showed improvements as deposited with an extinction of $5.4 \pm 2.0 \times 10^{-7}$ compared to the 52.1 % CEC coatings value of $9 \pm \times 10^{-7}$.

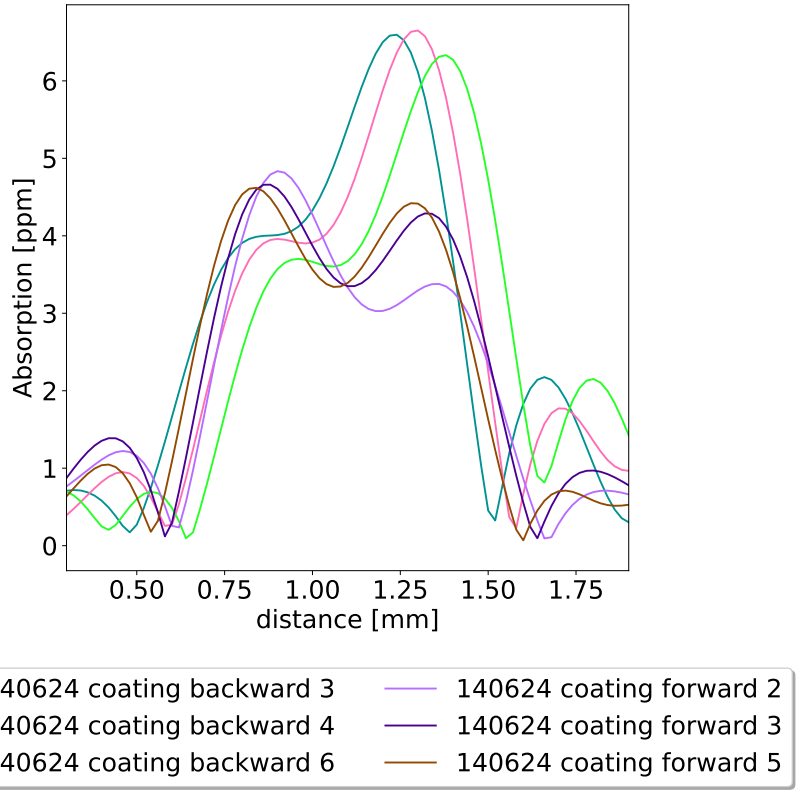

Figure 2.12: This plot shows the absorption scans of a TiO_2:GeO_2 EPOC single layer coating on JGS silica glass. The scan direction is in the z-axis as shown on figure 2.1 and for different coated samples on figure 2.3.

The interest then moved onto studying the EPOC HR stack. As deposited the absorption was 11.8 ± 0.2 ppm. This was approximately half the value of what was measured on the CEC HR stack (with 42.9 % Ti doping) at 20 ± 0.8 ppm. With distinct absorption improvements shown for the CEC single layers compared to as deposited in the parallel study [217], the EPOC HR stack was heat treated. Following absorption results from this and other previous TiO_2:GeO_2 studies[101, 217], and using the heat treatment ramping procedures for TiO_2:SiO_2 (see table 2.1), the coating was heat treated to 600°C (see table 2.2) with a ramp up rate of 50 °C/hr and down with a 10 hr hold time, followed by a ramp down rate of 50 °C/hr. The absorption reduced by a factor of eight down to 1.5 ± 0.2 ppm. The PCI scans for which are shown in figure 2.13. The small value and error from the point z-scan measurements indicated that there were unlikely point defects on the coating surface. To check for these, the sample was further inspected under a microscope. Although there were small defects, no large scale blistering was observed where it was previously

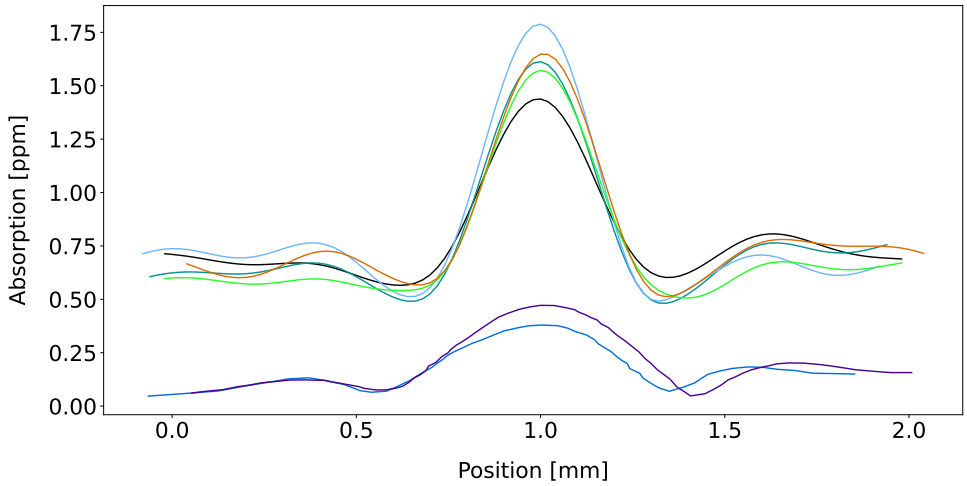

Figure 2.13: This figure shows different PCI z-scans through TiO_2:GeO_2 deposited by EPOC. The peak of the scans give the absorption level of the coating. The two distinct lines at the bottom represent the improvement in absorption after the coating was heat treated at 600°C for 100 hours beyond the initial 10 hours

known to be problematic for other TiO_2:GeO_2 based coatings [217, 220]. As other samples produced from a different EPOC deposition run with a higher base pressure did observe this, the mitigation was attributed to a reduction in the H_2O partial pressure on the coating during deposition [221].

With significant improvements expected to thin-film absorption after long duration anneals and previously observed for TiO_2:GeO_2 [217], the HR stack was annealed for a further 100 hour (dwell time) at 600°C and subsequently measured in the PCI. Given downtime in the Glasgow setup, the measurements were made at the University of Strathclyde. Previous cross-checks made between the setups showed that the absorption was consistent within a margin of 20 %. The absorption scans (bottom of figure 2.13) showed that the level dropped to 0.5 ± 0.1 ppm. This brings this HR coating within the aLIGO targets and close to the 0.27 ppm achieved by LMA for the current LIGO mirrors [144] that instead use Ta_2O_5:TiO_2 as the high-index layer. Some point z-scans gave a comparatively high but still low absorption of 0.9 ppm. These were attributed to small, microscopic surface defects, which were observed by eye and subsequently wiped off with cleaning solution. Ongoing research into numerous equivalent TiO_2:GeO_2 HR stacks, produced by other vendors has also suggested that after this heat treatment, the coating thermal noise levels of such an HR coating would be significantly lower than that of the current LIGO mirrors [101, 217]. CTN levels of around $60 - 70$ % of aLIGO have already been verified from many such TiO_2:GeO_2 stacks [156]. The low absorption level measured from this EPOC HR coating is amongst the lowest ever recorded for a stack of these materials, and is an important result for verifying the feasibility of TiO_2:GeO_2 coatings.

Throughout these measurements, the crystallisation was checked by collaborators at Strathclyde. The crystallisation state is typically undesired, as it indicates that the scattering from the coating would typically be too high and above the level of aLIGO test masses (9.5 ppm) [158]. To measure the crystalline structure grazing incidence X-ray diffraction (GIXRD) were performed using a PANalytical X'Pert PRO diffractometer [222].

All the single layer and HR samples were amorphous as deposited up to 10 hours. However, after the HR stack was heat treated for 100 hours it appeared to be partially crystallised [214]. The parallel study of CEC [217] showed that the surfaces of the coating stacks start to blister at 300°C and that the biggest proportional reductions in the absorption as indicated by measurements in the MIT optical cavity setup referenced in section 2.7 occurred after the same final heat treatment with a 100 hr dwell time at 600°C.

To better understand the source of the absorption, all measured absorption values were converted to (thickness-independent) extinction values. For the HR stack sample, an assumption was made that the TiO_2:GeO_2 layers dominated the absorption and that the SiO_2 layers in the stack did not contribute at all. This included data provided for the equivalent CEC samples by Markosyan [218] but heat treated with a fine resolution. Starting with the EPOC HR stack, it notably showed after the optimal heat treatment (100 hr dwell at 600°C) an expected TiO_2:GeO_2 extinction level of 1.1×10^{-7} that was $\approx \times 3$ better than the CEC single layers optimally heat treated (10 hr dwell at $300-400$°C). As deposited, the expected extinction of the TiO_2:GeO_2 from the stack layers was considerably higher by a factor of between $\times 5.5$ and 6.5 for both the CEC and EPOC coatings. As discussed for a similar observation in FiveNine's TiO_2:SiO_2 coatings (see section 2.7.1) this effect indicates that as deposited both the TiO_2:GeO_2 and SiO_2 layers were perhaps deposited oxygen-poor. The models cannot account for any as-deposited sub-stoichiometry (of either material) and as such the as deposited TiO_2:GeO_2 results are expected to be an upper bound on the real value. It is entirely possible, for TiO_2:GeO_2 films, that extinctions of less than $\sim 1\times10^{-7}$ are achievable.

Further clarity could be gained with the evaluation of the residual silica extinction and from measurements of the absorption of silica single layer samples sourced from the same vendor deposited in the same chamber under close to the same conditions. Additional measurements could be used alongside this, such as X-ray photoelectron spectroscopy to better understand if the coating composition in single layer or HR form is the same. To this end, a range of different number of layer thick AR coatings would be more effective in sampling any extinction discrepancy between materials layers across the coatings total thickness.

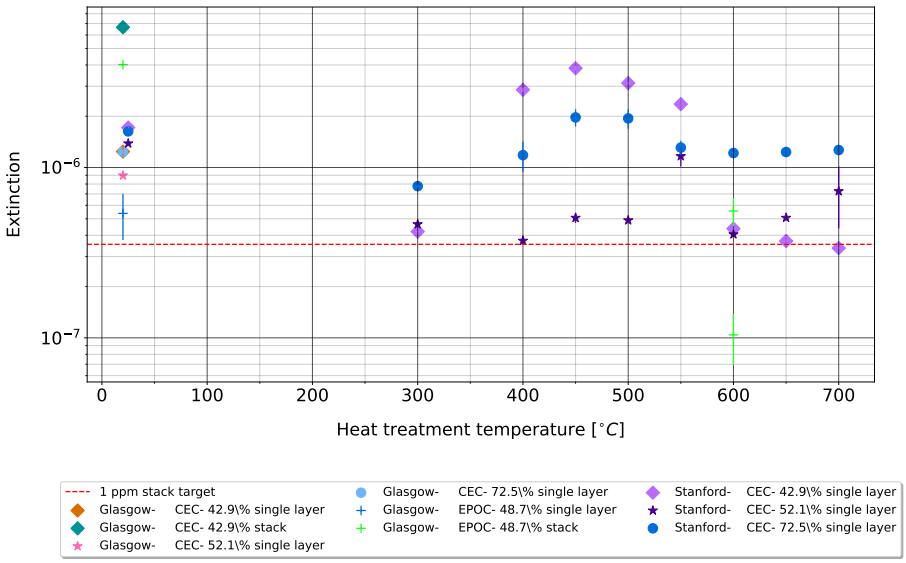

Figure 2.14: This plot shows the evaluated extinction coefficients for TiO_2:GeO_2 from both single layers and HR stacks, where the low index bilayer pair is SiO_2. The SiO_2 layers in the stack evaluations are assumed to have values which don't contribute measurably to the measured stack absorption.

The measurements shown here (in parallel to the TiO_2:SiO_2 studies) are some of the first comparative absorption studies between different vendors for mixed titania thin-films. In order to reach extremely low absorption for both TiO_2:GeO_2 and TiO_2:SiO_2 IBS deposition systems are clearly a good technique. Longer duration heat treatments were also shown here to substantially lower the absorption. Through standardisation of deposition and heat treatments, future studies that follow this work will hopefully continue to reduce and better understand the factors limiting the absorption.

Where the absorption reached an extremely low-level the scattering was expected to increase as the thin-films started to crystallise after the 100 hour mark. The parallel study indicated that the CEC coatings had a scatter level after equivalent heat treatments that was six times higher than the current level of aLIGO mirror coatings at ≈ 65 ppm. Provided that these results carried to the EPOC coatings (expected from their partial crystallisation) then these measurements in addition to the TiO_2:SiO_2 studies (section 2.7.1) would further support the qualitative model of absorption and scattering change with heat treatment proposed by Wang [202].

2.9 Absorption of germania coatings

The samples measured here were intended to be additional titania doped germania coatings of a range of different doping concentrations from 0% through to 100% to compare to the measurements presented in section 2.8. However, when measured independently, only trace titania concentrations of ≤ 0.3 at.% was detected across the coatings. The explanation given by the vendor Helia Photonics [223] was the vapour pressures for both titania and germania were not accurately set. As a result, the coating will be considered instead as near pure germania coating. The measurements will not directly benefit current room temperature gravitational wave detectors. However, the material, conditioned on its mechanical loss could be a viable option for detectors that chose to operate their mirrors at cryogenic temperatures. As a result, the material was investigated as an alternative for silica, silica: halfnia and alumina as discussed here. To this end, studying the absorption and better understanding the factors affecting the extinction of germania will provide useful comparison data for another coating materials and deposition methods. The measurements presented in this section made by the author, along with measurements made by collaborators (D Diksha, Maastricht University) - was published in mid-2024 [147].

The properties of germania will now be considered in comparison to silica. It shares a similar atomic order with silica. Improvements to the medium range order of germania, through annealing, have been shown to reduce the mechanical loss to 1×10^{-4} . This was structural improvement was also observed for silica [224] although it has been calculated to a level as low as $\approx 1.25 \times 10^{-5}$ [97]. The similar atomic structure results in a similar density and therefore a refractive index of (n$\approx$ 1.6 at 1064 nm) which is close to that of silica. This expectation follows from the Clausius-Mossotti relation [225]. Though the refractive index of pure GeO_2 is perhaps too low for it to serve as a high index material (hence the necessity to dope with TiO_2, in the context of GW HR mirrors, this value would allow it to serve as a low index material.

The germania coatings measured here were deposited by Helia Photonics [223] on SiO_2 substrates (Corning 7979 and 7980) [216] that were 25.4 mm in diameter and ranged from 1 mm thick (7979) 3 mm thick (7980). The deposition method of plasma ion-assisted electron beam evaporation was similar to IBS as described in section 2.4 [199]. A germanium target was used (99.999% purity Ge) and the deposition rate was approximately 3 Å/s. Before deposition started, the chamber was evacuated to 2×10^{-6} mbar pressure. During deposition, this reached 1.4×10^{-4} mbar as oxygen atoms were introduced alongside inert Ar by bleeding them into the chamber. The substrates were also maintained here

Run	Heat Treatment [°C]	k (1550 nm) $\times 10^{-5}$
1	As dep.	1.6 ± 0.11 *
		1.7 ± 0.2
1	150	1.52 ± 0.15
1	200	1.22 ± 0.15
1	225	0.86 ± 0.15
1	275	0.74 ± 0.15
1	300	0.68 ± 0.15
1	325	0.68 ± 0.15
1	400	1.10 ± 0.32
1	500	3.78 ± 2.19
2	As dep.	3.90 ± 0.07 *
		2.00 ± 0.40
2	150	1.83 ± 0.28
2	200	1.84 ± 0.28
2	225	1.17 ± 0.31
2	250	1.12 ± 0.17
2	275	1.45 ± 0.19
3	As dep.	3.00 ± 0.06 *
		2.73 ± 0.08
3	150	1.39 ± 0.07
3	200	0.96 ± 0.10
3	225	0.84 ± 0.19
3	250	0.82 ± 0.08
3	275	0.66 ± 0.07
3	300	0.85 ± 0.05
3	325	0.94 ± 0.18

Run	Thickness [nm]	n(1064 nm)	k(1064 nm) $\times 10^{-5}$	n(1550 nm)
1	533 ±7	1.6 ±0.02	0.81 ±0.04∗	1.6 ±0.02
2	584 ±10	1.58 ±0.02	0.47 ±0.07∗	1.57 ±0.02
3	459 ±5	1.62 ±0.02	4.6 ±0.13∗	1.61 ±0.02

Table 2.3: Optical measurements of the thickness, index and extinction at 1064 nm and 1550 nm for different heat treatment temperatures.
*: indicated measurements made by the author in the photothermal common-path interferometer at Glasgow. The rest of the data was measured, approximately one year later, at the University of Maastricht by D. Diksha.

at 100 °C. In addition to this, each coating had a Ar concentration of $(0.5 - 0.7)$ at.%. The measured properties of each coating germania coating alongside the heat treatment temperature are shown in table 2.3, with additional properties such as trace titanium concentrations shown in the recent publication [147].

There were three coatings deposited, each with a separate run of the same deposition method. The coatings were then measured first as deposited on the Glasgow PCI system as shown by the 20 °C points on figure 2.15. Then, on a separate PCI, the as deposited measurements were repeated one year later. For runs 1 and 3 shown on the figure, the measurements agreed both to within 10 %. However, for run 2 the remeasured extinction was a factor of two less. The expectation was that the GeO_2 coating would increase

in absorption due to the adsorption of water whilst kept in air, throughout the long duration of the study. However, the measurements do not support this. The thickness, alongside index, was measured over a large area in a Cary 5000 spectrophotometer [226], the measured values did not capture potential non-uniformities in thickness, over the smaller sampling size of approximately 70 µm in the PCI. From this same logic, the extinction evaluated from run 1 and 3 is expected to be accurate and indicative either of the material's extinction remaining the same and or the setups being consistent within the level reported. However, it is entirely possible that the reverse case might be true for both.

The ADP measurements were also made on the Glasgow PCI at 1064 nm. However, despite the accuracy of measured points being high, there was no sample specific correlation. It is clear though that, specifically on samples from runs 1 and 2, there was a considerable correlation with wavelength: with the lowest ADP 1064 nm extinction being ≈ 33 % of the lowest 1550 nm measurement. Despite the extinction values being the best at 1064 nm the rest of the study was continued at 1550 nm in the year that followed: on the Maastricht PCI system which only had 1550 nm as the Glasgow PCI system was down for optical realignment.

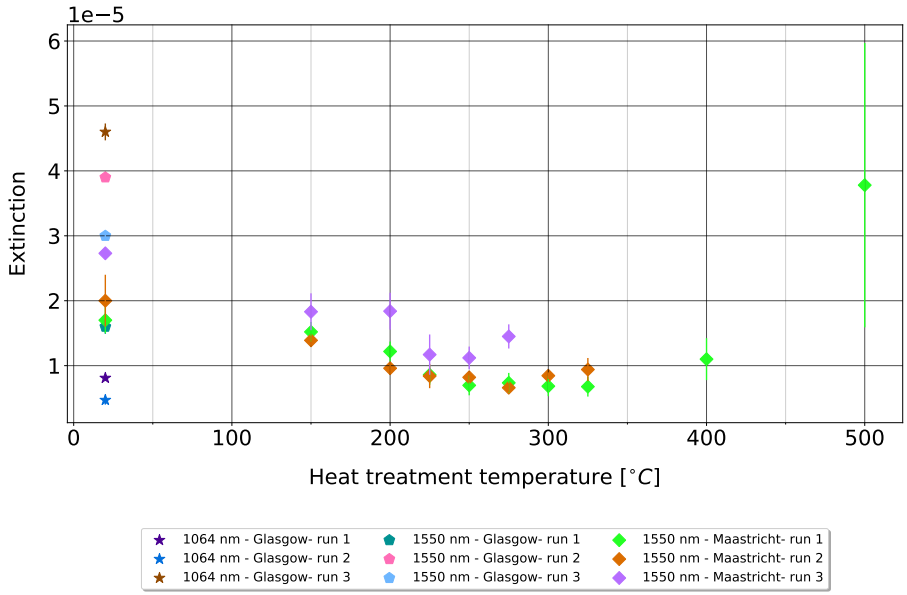

Figure 2.15: This plot shows the evaluated extinction coefficients for GeO_2 from single layers. The Maastricht values were measured by D. Diksha approximately one year after the Glasgow measurements were taken.

A heat treatment study was launched to progressively anneal each sample until an absorption/extinction minimum was identified. The minimum extinction value for each sample (see table 2.3) was found to occur at a similar temperature. For run 1 this was 325 °C, run 2 (275 °C) and run 2 (250 °C). It was expected that at heat treatments on towards the transition temperature of the coating from an amorphous to crystalline state that the

absorption would start to increase [97, 227]. The sample from run 1 was heat treated up to 500°C and although the absorption had clearly increased beyond 325°C, there were no signs of crystallisation from Raman spectroscopic measurements shown in the publication [147]. However, the sample from run 2 showed signs of crystallising to quartz GeO_2 at 325°C, with an absorption that decreased up to this point. The distinct crystallization state of a single layer coating deposited and heat treated under nominally the same conditions could be due to the trace Ti doping, that was known to vary between the runs. Although it is possible for the Ti atoms to be sites of crystallisation their concentration for samples from run 1 and run 2 could not be distinguished outwith the 0.2 at.% error on the RBS measurement technique.

A recent study by Vajente [101] found that a pure GeO_2 coating crystallised beyond 325°C and at 550°C. If the coating was a quarter wavelength thick, then the low-point in the extinction of this was 7×10^{-7} after the same anneal threshold of 500°C. The systematic study of the extinction here showed extinction values that were likely above the measurement of Vajente *et al.* [101]. When comparing this to SiO_2 alongside the mechanical loss values and reduced crystallisation temperature, there does not appear to be a clear pathway for pure GeO_2 coatings to be implemented into GW detectors. However, building on this work, further studies of GeO_2 might reveal a clear dependence of the absorption on the impurity concentration of Ti and the possibly co-correlated crystallisation threshold.

2.10 Comparison of extinction values measured

In addition to the detailed absorption studies presented other measurements were made on alumina (see section 3.3), perovskite coatings (see appendix 6), silica and tantala.

The lowest measured extinction of each coating studied here is shown on figure 2.16 alongside the values published from other studies and those expected from private communications. These values cover three orders of magnitude in range. All the high-index materials measured here had lower minimum extinctions compared to those from the low-index materials. Compared to expected values, the germania and alumina measured here are believed to have an order of magnitude improvement potential. Absorption of thin-

film coatings at the ppm-level measured is expected to be due to the sub-stoichiometric nature that arises from the specific deposition environment. This was supported strongly by this, work, which provides some of the first comparison studies of extinction (due to absorption) between multiple vendors.

The gold standard for thin film coating absorption at 1064 nm is that of the HR stack deposited by LMA on the aLIGO mirrors (0.27ppm [144]). This is comparable to the total absorption of the lowest published bulk absorption for silica that is a standard size of 3 mm thick. This difference in thickness implies that the best extinction due to absorption of a thick-substrate is approximately three orders of magnitude lower. In the absence of a clear theory to explain a fundamental limit between the extinction of amorphous materials in thin-films compared to thick substrates, it is believed that the extinction values of thin-film coatings will continue to be reduced.

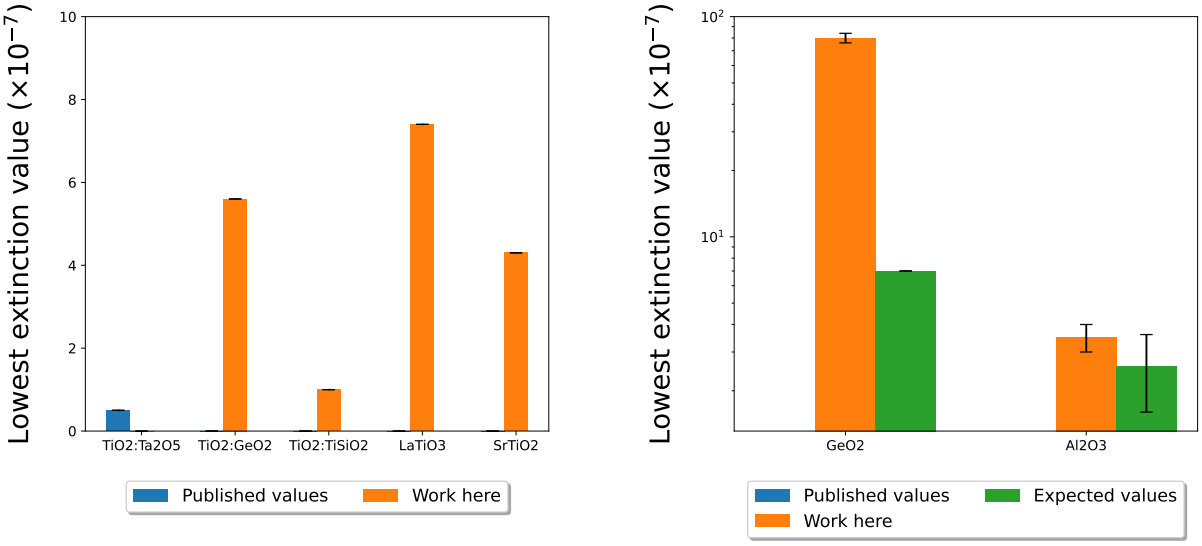

Figure 2.16: This figure shows the lowest measured extinction values for thin-film materials discussed in this chapter. This figure summarises the lowest values measured here, published in other works and expected values from projections and or private communications as explained for each material throughout chapter 2.

2.11 Conclusion

The discrete measurements presented in this chapter indicate a clear improvement in the absorption of select thin-film coatings.

HR stack coatings of TiO_2:SiO_2 produced by FiveNine were found to have $0.8 - 0.84$ ppm absorption after a heat treatment with a slow ramp rate of 50 °C/hr to 600°C with a dwell time of 10 hrs and a similar level after the same ramp rate but to 850°C and with a dwell time of 100 hrs. This work, along with parallel studies of the coating mechanical loss and thermal noise, showed that these coatings had significant potential for use in future detectors or detector upgrades, and inspired further coating development work by LMA. The LMA coatings characterised by the author showed an even lower absorption of 0.3 ppm, well below the target for the A+ detector and very close to the 0.26 ppm absorption observed for the current aLIGO / Adv Virgo coatings.

It is interesting to note that the best mechanical loss/thermal noise performance was found after the coatings had crystallised. Usually crystallisation of amorphous coatings is avoided as the optical losses due to scatter are expected to increase significantly. However, while the scattering of the FiveNine coatings did increase on crystallisation, it remained low, reaching 5 ppm at 850°C. This is lower than the scattering measured on the current aLIGO coatings in their fully amorphous state. As the absorption also remained low, this is potentially on the contrary to the anti-correlation proposed by the theory [202] and could allow this coating material, if repeated, to reach the lowest total extinction (i.e. summation of absorption and scatter losses) value. This level if pushed down could enable thin-film coatings (beyond the gold standard aLIGO HR stacks [144]) to push the capabilities of high finesse Fabry-Pérot cavities, potentially also benefiting applications beyond gravitational wave detectors, such as optical atomic clocks and precision length metrology.

Overall, the absorption studies presented here alongside the parallel studies the coating thermal noise properties [102, 156] show that TiO_2:SiO_2-SiO_2 coatings offer a clear improvement over the TiO_2:Ta_2O_5-SiO_2 coatings found in current aLIGO detectors with a CTN that is $\approx 72\,\%$ of current aLIGO levels and an absorption value of 0.28 that meets the absorption target. As a result of these studies, the coating is actively being researched for possible use in future upgrades to the Virgo GW detector test-masses, and remains a potential back-up material for the A+ detector.

Another high index material which was considered was TiO_2:GeO_2. As a result of extensive research across the the LIGO scientific collaboration, this coating has been chosen as the baseline coating design for the upcoming test-mass upgrades in the Advanced LIGO detectors - although at the time of writing a final solution has not been arrived at. This was backed by the extensive research into the coating, which showed that the CTN improved upon current levels [101, 156].However, previously the absorption produced by HR stacks

incorporating this material were found to be too high at, around the few-ppm level [218]. This is beyond what would be tolerable in aLIGO. In the past, a CEC HR coating run was, however, able to produce sub-ppm absorption levels after heat treatment, but only in a very small region of a surface otherwise covered with macroscopic blisters and cracks [217]. The work here has shown that the absorption of a HR IBS coating of TiO_2:GeO_2 and SiO_2 can reach 0.5 ppm with no macroscopic defects. This exceptionally low-value reached after a precise long and gradual annealing procedure, if replicated, for other coatings has the potential to push down the level of thin-film absorptions for other titania and oxide films. In the following weeks and months since the measurements of the EPOC HR stack design achieving 0.5 ppm absorption, colleagues at the current GWD mirror manufacturer LMA have been fine-tuning recipes in their own coater. They are now achieving great successes with sub-ppm absorption and defect free coatings. The prospects for this material have never seemed higher. Though at the time of writing, recipe and heat treatment procedure that consistently produces low-scattering is still to be determined.

As for low index materials, pure-GeO_2 layers showed a low absorption, but they were not better than pure SiO_2 in terms of absorption and mechanical loss. As a result, they are not expected to be implemented in the mirrors of future room-temperature detectors.

To the benefit of gravitational wave detectors the systematic studies of both low and high-index materials suitable for HR coatings stacks indicate a clear improvement in absorption for annealing temperatures that exceed that of the substrate during deposition. Further analysis of the elemental composition and bonding after different heat treatment steps or by annealing in different inert gases might allow the dominant absorber in thin-film extinction of amorphous coatings to be identified and mitigated: therefore pushing them below the 10^{-7} level. For the oxide coatings studied here, stoichiometric effects, although reduced, might still have been the limiting factor.

In the future, it is expected that lasers tuneable to high powers across this NIR range could be implemented into photothermal measurement techniques such as the PCI to identify any distinct low absorption bands. An example of such a laser is the C-Wave GTR by HÜBNER Photonics [228] which has already been shown to output across wide areas of this range with at least 1.5 W. With this power level, it is expected that ppm-level absorption levels could soon be measured across a broad near-infrared (NIR) spectral range. However, the calibration would have to be a lot more involved as tuning the laser frequency is expected to change the shape of the output laser mode and without using an aperture this would change the measured signal independent of the absorption. If achieved, this increased data might reveal empirical relations that correlate between other amorphous

materials and with other properties such as the mechanical loss. With sufficiently detailed deposition and treatment parameters there would be scope for a materials database such as the Materials Project [229] to openly track such efforts in reducing the absorption of thin-film amorphous coatings and in the process enable us to discover new low extinction coating materials.

Chapter 3

Measurement and design of alumina coatings suitable for ET-LF

3.1 Introduction

Looking further ahead to future cryogenic-temperature detectors (2030s), there is a critical need to study new materials. The current coatings used in gravitational wave detectors are typically not suitable as their mechanical loss value is too high at cryogenic temperatures [92, 93, 94]. Since the targeted silicon substrates are not transparent at 1064 nm (the laser wavelength used in current detectors), the use of either 1550 nm or 2000 nm is planned for cryogenic detectors with silicon mirrors. Therefore the optical absorption measurements will need to be carried out at these wavelengths. At the low-ppm absorption level of interest, it is not known how the absorption level varies across this spectral range and so precise measurements should be made at distinct wavelengths. Reducing the absorption of coatings below the 5 ppm limit for cryogenic detectors such as ET-LF will reduce the total heat load and allow the detectors to stably operate with their test-masses at the required temperature of $10 - 20$ K.

A previous study at the University of Glasgow into the cryogenic mechanical loss of alumina (Al_2O_3) coatings identified Al_2O_3 as a promising low-index coating material [106]. Here, to extend this previous work and further evaluate the suitability of alumina, the optical absorption of these alumina coatings was studied. Absorption measurements were made at wavelengths of 1064 nm and 1550 nm, using samples from the same coating runs as the previous study. The effect of post-deposition heat treatment at temperatures up to 850 °C on the optical absorption was investigated. The measurements presented represent some of the lowest absorption values ever measured for alumina (Al_2O_3) coatings.

These measurements were used to design novel multi-material coatings for ET-LF mirror substrates. Through comparison to other proposed designs, the designs which feature alumina as low-index layers are shown to have the best theoretical thermal noise and an extremely low absorption level. As a result, the coating designs presented here are expected to be the best candidate coatings for the ET-LF. To strengthen this claim, the designs were compared to optimal designs based on recent advancements in silicon nitride materials.

3.2 The motivation for alumina coatings

A promising alternative coating material for cryogenic GWD is amorphous alumina (Al_2O_3). The effective CTN was previously studied down to cryogenic temperatures through mechanical loss measurements by Robie [106]. This work indicated that coating stacks containing alumina as a low-index layer in place of silica might produce a lower CTN, due to the absence of a cryogenic loss peak in the alumina layers.

The refractive index of alumina deposited using a range of different techniques has been previously reported to be between $1.52 - 1.76$ at 632 nm [230]. Compared to this broad range, the index of any of the samples studied here was not expected to shift at 1550 nm outwith a few percent. This small wavelength dependence in the NIR range is highlighted for a distinct deposition technique in Kumar [231]. This index range is situated in the middle of the bounds of the currently used low-index layers (silica, $n \approx 1.45$) and high-index layers (titania-doped-tantala, $n \approx 2$) inside GWD mirror stacks. For this reason, alumina can be considered as either a high or low index layer. At room temperature, research into the former case showed that it contributed a mechanical loss higher than tantala Ta_2O_5 [232]. A further exploratory material study showed that this was also true when alumina was doped with Ta_2O_5 and compared to the current aLIGO high-index layer material (TiO_2:Ta_2O_5) ([183]. If paired with SiO_2 the resulting CTN would be high in account of the low bilayer index contrast and therefore thicker coating stack.

At the low temperatures of 20 K considered for ET-LF, silica is known to have a mechanical loss peak [120, 233, 234, 235, 236] which is $\approx 2 - 3$ orders of magnitude higher and would as a result dominate the coating thermal noise compared to its small contributions at room temperature. The work by Robie [106] (see figure 3.1) shows the mechanical loss of IBS alumina at cryogenic temperatures as being considerably better than IBS silica. It is promising though that this single run of alumina indicates improved mechanical loss

below 50 K. The biggest improvement occurs at ≈ 20 K where alumina gave a value of 3.6×10^{-4} compared to silica (deposited with IBS) value of 7.1×10^{-4}. This improvement by a factor of two was conditioned on a Young's modulus value that was estimated from the literature and used to estimate the mechanical loss of the coating material from the measured data. The intrinsic coating mechanical loss is inferred by scaling the measured loss of a coated sample by the ratio of the elastic energy stored inside the coating to the energy stored in the substrate. This energy ratio depends linearly on the Young's modulus of the coating. With the improved mechanical loss expected to coincide with the ET-LF operational temperature range of $10 - 20$ K, it was very interesting to extend the study and investigate the optical absorption.

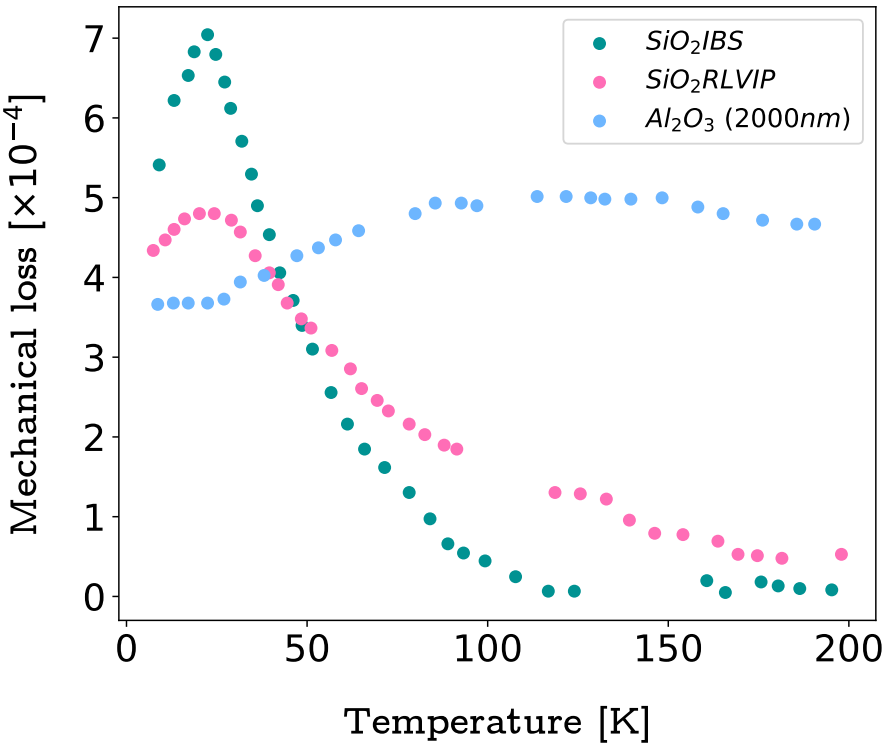

Figure 3.1: Data from Robie [106] which compares the thin-film mechanical loss of both silica and alumina. The alumina measurements were made after a post-deposition heat treatment to 600°C and a short dwell time of 1 hr.

The coatings considered here were deposited by ATF [237] using ion beam sputtering with an aluminium target, on samples present in the same deposition runs as the mechanical loss samples studied by Robie [106]. There was no active substrate heating during deposition, but temperatures up to 90 °C are likely to have been reached during the sputtering process. Two different coating thicknesses were deposited, to allow investigations of possible effects of thickness and stress on the mechanical loss. The two coatings were measured by the vendor to be 2020 ± 20 µm and 505 ± 8 nm thick. The Young's modulus of the films was estimated to be 200 GPa [106]. This value was taken from the upper range of known values for widely-studied pulsed reactive magnetron sputtering (RMS) deposition. This process has a similarly high deposition energy to IBS and is therefore likely to

be a fair comparison. Changes to the Young's modulus of an amorphous thin film as it is heat treated are strongly dependent on the degree to which the film is crystallised. As similarly heat treated coatings from both RMS and IBS have comparative crystallisation profiles, it is expected here that the initial Young's modulus before any heat treatments is comparable.

The mechanical loss studies showed that for post deposition heat treatment temperatures from $300-800°C$ with a short dwell time of 1 hr that there were no large changes between mechanical loss values [106].

3.3 Absorption measurements of alumina coatings

The coated substrates were quartered to provide multiple samples of each of the two coating thickness, which could separately be heat treated to allow any dependent trends in absorption to be distinguished. As the samples were 6 mm thick a Logitech 15 Model [238] saw was used to quarter the samples. Prior to cutting the samples were temporarily set in a fixed position (with heated wax) on a metal plate. To confirm that this had no effect on the absorption, samples were measured in the PCI before and after cutting and showed no difference.

For both the 0.5 and 2 μm coatings, individual quarter-disk samples were heat treated in a Carbolite annealing oven as described in section 2.7 to three distinct target temperatures; one to 400 °C, one to 600 °C and another one to 850 °C. The ramp up rate for these heat treatments was 100 °C/hr and the hold time at each target temperature was 10 hours. Then the cooldown was targeted likewise at 100 °C/hr with this rate slowing down below 250 °C as described in section 2.7. These heat treatment temperatures make the measured coatings comparable to those prepared for mechanical loss measurements by Robie [106]. However, higher dwell times of 10 hrs were chosen as it was believed in light of the other absorption studies presented in this thesis that these could only improve the optical absorption. In addition to this one sample was kept as deposited (ADP) as a spare.

The refractive index of a subset of the samples was measured. A sample was taken from each combination involving both thicknesses alongside the heat treatment temperatures of ADP and 600 °C. Measurements were then made on a PHOTON RT UV-VIS-MWIR Spectrophotometer device [239] at the University of Strathclyde. This device measured the reflectivity and transmissivity across the NIR region of interest. The measured transmission data for each coating is shown in figure 3.2.

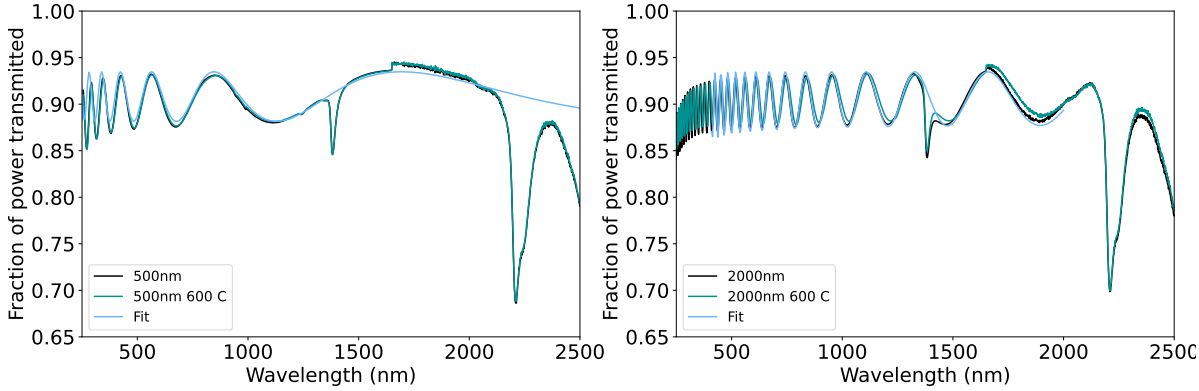

Figure 3.2: The measured and fitted transmission spectrum for the (Left) ≈ 500 nm and (Right) ≈ 2000 nm alumina single layer coatings.

Using the OptiChar software produced by OptiLayer GmbH [240] normal dispersion curves were fitted to the data (only shown for the as deposited) which allowed the thickness and wavelength dependent refractive index to be determined. Beyond 2000 nm the measured transmission drops drastically. This is expected to be due to water absorption – a common occurrence at these wavelengths – which is not captured in the model. As the PCI optical absorption measurements were made at the lower wavelengths of 1064 nm and 1550 nm this discrepancy is not considered any further. For the nominally targeted 500 nm coating, the thickness was measured to be 516 nm ADP and 520 nm at 600 °C. The fitted refractive index ADP at 1064 nm was 1.65 and at 1550 nm was 1.63. For the nominally targeted 2000 nm coating, the thickness increased from 2020 nm ADP to 2056 nm at 600 °C. Likewise, the index dropped ADP from 1.64 at 1064 nm to 1.63 at 1550 nm . The drop in refractive index across the wider NIR can be seen by the horizontal offset of the interference fringes on figure 3.2 (Right). For both the 500 nm and 2000 nm coating, this indicates that they have reduced in density. This, in line with other studies involving crystallography measurements [241] suggests that this alumina has shifted to have a more porous gamma phase structure.

The absorption of all of the samples was measured using the PCI at both 1064 nm and 1550 nm. The results were converted into extinction values by using the measured index values from above. The extinction results are shown on figure 3.3. At 1550 nm, in the as-deposited state, the 500 nm extinction was 3.6×10^{-6} and the 2000 nm extinction was

2.8×10^{-6}. At 1064 nm the extinction was lower and most noticeably for the 500 nm coating at $\approx 1.8 \times 10^{-6}$. Coatings were then heat treated to 400 °C and 600 °C. Aside from the 2000 nm thick coating, the extinction values reduced by up to 20 % from its ADP state with heat treatment. For the 500 nm-thick coating at 1550 nm the value was $\approx 3 \times 10^{-6}$ and at 1064 nm it was very low with a value of $\approx 1.3 \times 10^{-6}$.

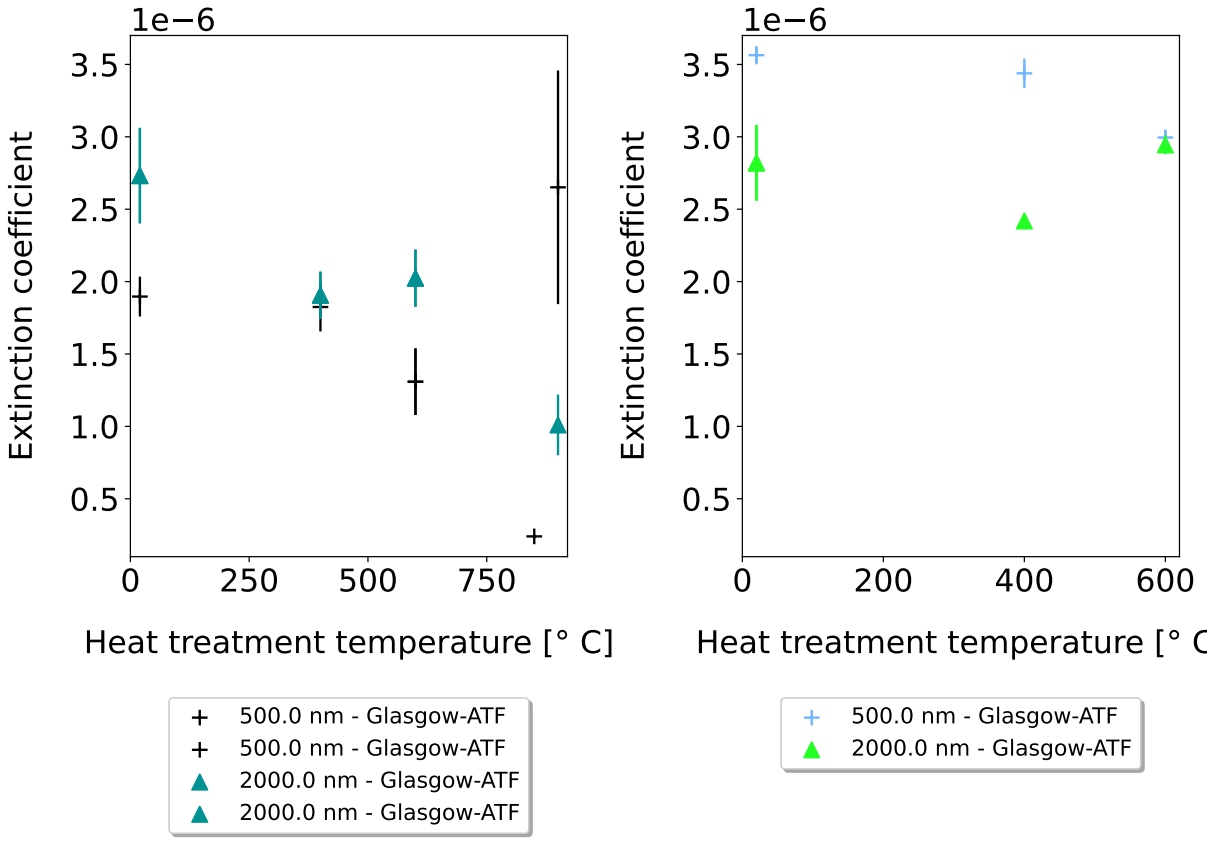

Figure 3.3: (Left): The extinction coefficient for Al_2O_3 at 1064 nm. (Right): The extinction coefficient at 1550 nm.

To understand if there was any wavelength dependence, the ratio of the extinction for each treated sample between the 1550 nm and 1064 nm values was evaluated (see figure 3.4). There was clearly an increased extinction for the thinner coatings at 1550 nm and after the heat treatments up to 600 °C. In other words, at 1064 nm the reduction in extinction with temperature was significantly more pronounced for the thinner 500 nm coatings by a factor of $\approx \times 2$. This is some of the first evidence towards thickness dependence and might hint at an underlying empirical relation that goes beyond alumina. A deeper study of this would require more samples and longer anneal times to see if anneal times beyond 10 hours affected the minimum reached. However, it was more critical for this first study to first identify the heat treatment temperature that gave the optimal absorption. As such, a sample of each thickness was therefore heat treated to 850 °C under the same ramping rate of 100 °C/hr.

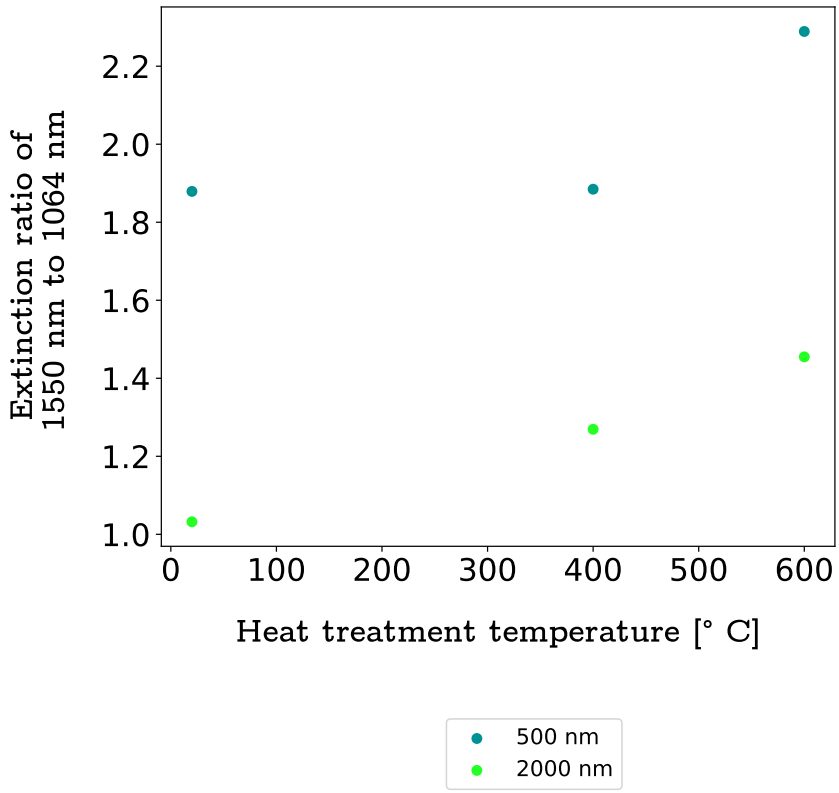

Figure 3.4: The extinction ratio of the 1550 nm compared to the 1064 nm for both thickness of alumina single layer coatings.

The thinner coating came out of the oven immaculate and with no defects observed under the microscope. However, surprisingly, the thicker coating became sparkly and milky, and on microscope inspection (see figure 3.5) small iridescent features were clearly present across the surface with a scale of around $20 - 50\,\mu m$. It was therefore interesting to check the crystallisation state of both coatings, as crystallisation could generally indicate a high optical scatter and an undesirable state for coatings in the mirrors of gravitational wave detectors. To check for crystallisation, grazing incidence X-ray diffraction (GIXRD) was used. A shallow incidence angle (θ) allows the thin-film surface to be probed. A broad around low angles would indicate an amorphous coating, whereas higher angles spikes in the intensity spectrum would indicate different crystallisation axes had formed [242]. At 850 °C both thicknesses appeared to be crystallised. For the thicker coating, the crystallisation was much more prominent for the thicker coating with sharp GIXRD spikes centred at 46 ° and 67 ° (see figure 3.6). As the thinner coating had a significantly lower peak intensity, it was believed to be only partially crystallised. This was a surprising result, as literature values indicate that the crystallisation point can be as high as 1200 °C [243]. Further measurements of the direct total integrated scatter could reveal if this scatter is a limiting factor for the implementation.

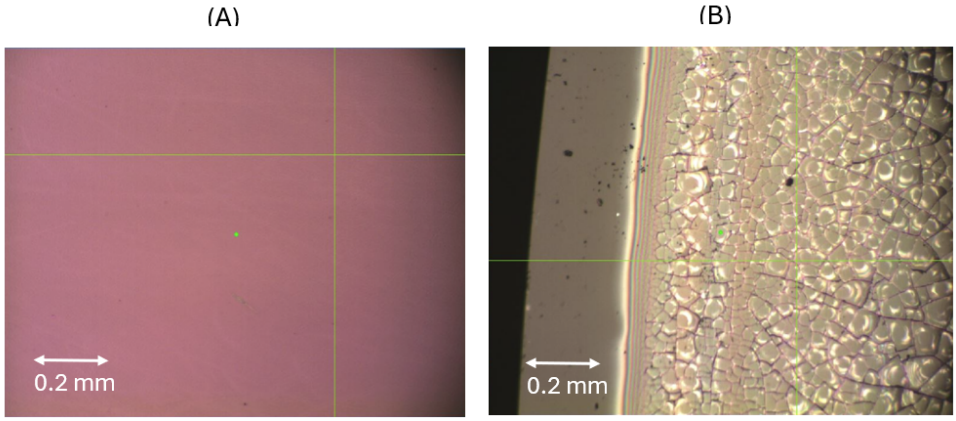

Figure 3.5: (A) shows the immaculate alumina coating as deposited. (B) Shows defects found on the alumina coating after the 850 °C heat treatment described in the text.

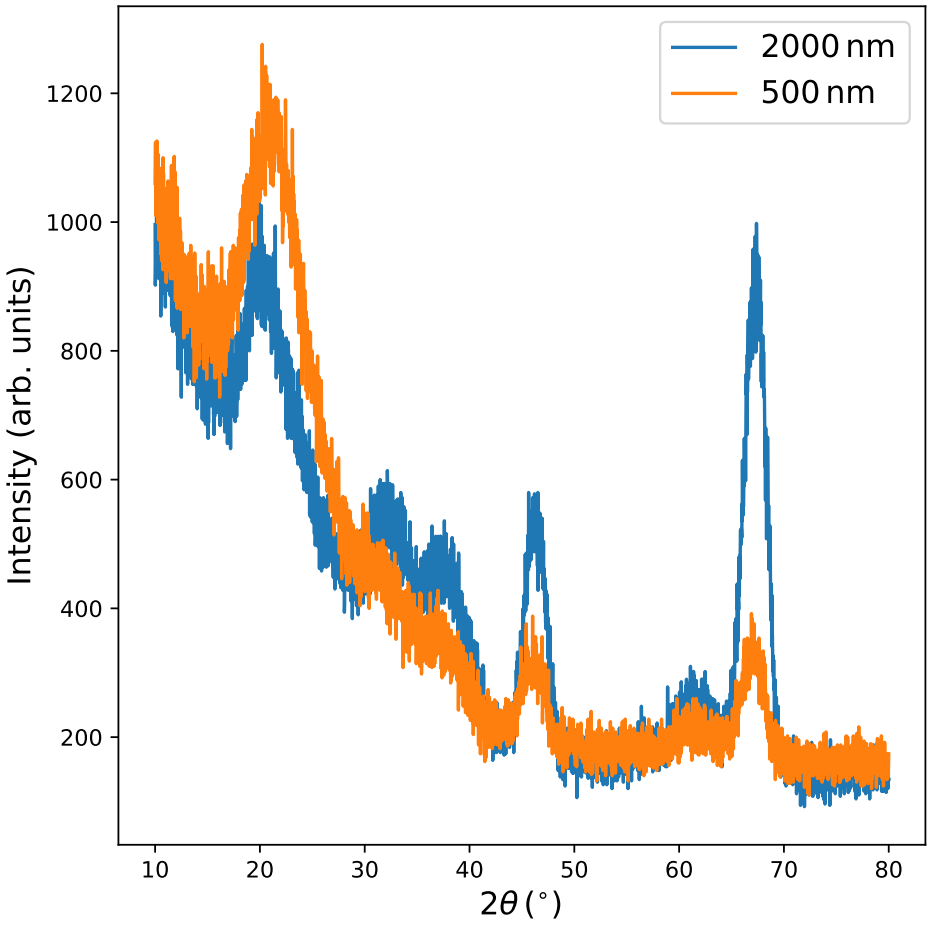

Figure 3.6: GIXRD diffractograms of alumina ADP and after annealing to 850 °C.

The absorption of the samples was then measured in the PCI. The thicker coating did not give a clear absorption signal due to the high scatter level from the surface. In contrast, the thinner coating gave a considerably reduced extinction at 1064 nm of 3.5×10^{-7}. In order to resolve the absorption minimum, the sample was further heat treated to 900 °C for 10 hours. The sample was then measured in the PCI and showed a significant increase

for the 500 nm coating by approximately a factor of ten from the 850 °C to 2.7×10^{-6}. In contrast, the thicker coating (although not measured at 850 °C) showed a distinctly lower value of extinction due to absorption of 1×10^{-6}. As the thickness of layer if implemented in a QWL HR stack (1550 nm) would be ≈ 240 nm the 500 nm results and minimum will be considered most applicable. Unfortunately, the sample was not further measured at the 1550 nm targeted for ET-LF (given downtime in the setup), and so the 75 % increase observed at lower heat treatment temperatures was used to scale this to give an expected 1550 nm extinction value of 6×10^{-7} for the 500 nm coating. This absorption value will now be compared to other thin-film coatings. It is also promising that the crystallisation was reduced with the thinner coating, and it is hoped that further studies could critically quantify the scatter level so that the coating could fully be assessed as a top-layer coating in an HR stack.

3.4 Comparison of alumina with other mirror coatings

The only other IBS alumina absorption measurements which have been published are those by Zhao [241]. For a comparable index of 1.67 and thickness of 460 nm, their as deposited IBS alumina was shown through X-ray diffraction measurements to be dominated by the amorphous phase. Notably, they observed microstructures on the surface and a significantly higher extinction than observed here by $\approx$ three orders of magnitude. However, the best comparative absorption value at 1064 nm that could be found for this coating material was ≈ 1 ppm for a 500 nm layer shared by Markosyan [218] after a 600 °C heat treatment for 10 hours. Although the refractive index, was not measured if the same value, of 1.65, used here is assumed, the extinction evaluates to be 2.6×10^{-7}. This value is ≈ 25 % lower than the value measured here of 3.5×10^{-7}. However, as the shared value had no absolute error nor specified refractive index it is not possible to further interpret the true extinction nor make a fair comparison. The expected value of 6×10^{-7} at 1550 nm projected from measurements made at 1064 nm for the 500 nm (heat treated to 850 °C) will now be considered first in respect to other coating materials (shown in table 3.1).

The current aLIGO coatings consist of a number of bilayers of low-index SiO_2 and high-index TiO_2:Ta_2O_5. The resulting multilayer stack has an absorption which is a factor of ≈ 4 below the 1 ppm absorption limit set for aLIGO[144]. This extremely low-absorption level was also measured for TiO_2:SiO_2 (see section 2.7). Both TiO_2:Ta_2O_5 and TiO_2:SiO_2 have a minimum extinction which is lower than alumina by up to a factor of ten. It

Table 3.1: The key coating and bulk substrate optical and mechanical properties required to evaluate the transmission, absorption, and Brownian noise of coated substrates.
This value is an expected value for SiO_2:TiO_2 carried from measured data for Ta_2O_5, as other material properties were similar.

Coating	n (1550 nm)	κ (1550 nm) $\times 10^{-6}$	T_κ, t_{dwell} [°C], [hrs]	ϕ (20 K) $\times 10^{-4}$	T_ϕ, t_{dwell} [°C], [hrs]	Y [GPa]	ν
SiO_2	1.45	0.1		7		70	0.19
SiO_2:HfO_2	1.91	4.0 [92]	400, 24	3.8	400, 24	180	0.19
Al_2O_3	1.65	0.6	850 , 10	3.6 [106]	300-600 , 1	200	0.24 [106]
SiN	2.68 [244]	12.1 [244]	not specified	0.58 [244]	not specified	96	0.23
Ta_2O_5	2.05 [92]	0.08 [92]		5.0		140	0.29 [245]
SiO_2:TiO_2	2.07 [92]	0.1		not specified		140	0.29 [245]
a-Si	3.48	12.2 [187]	400, 1	0.18 [96]	300-450, -	147	0.22

Bulk	n (1550 nm)	k (1550 nm) $\times 10^{-6}$	Y [GPa]	ν
SiO_2	1.45	1×10^{-10}	72	0.22
c-Si	3.47	1×10^{-9}	166	0.22 [125]

is promising that the minimum absorption of TiO_2:SiO_2 occurred alongside Al_2O_3 after a 850 °C heat treatment. Coating designs which incorporated both would be expected to have a distinct absorption minimum at this temperature. With the ET-LF limit also currently set at a higher level of 5 ppm it is interesting to evaluate first the effect of substituting the low-index SiO_2 layers with Al_2O_3 layers, which have lower mechanical loss and may therefore be expected to reduce the thermal noise.

Compared to Al_2O_3 the extinction level of SiO_2 is approximately $\times 6$ lower. However, as shown in figure 3.1 the loss of Al_2O_3 is a factor of two lower than SiO_2 at temperatures around 20 K where the ET-LF detector is planned to operate. The lower loss of Al_2O_3could potentially provide thermal noise improvements. However, since the refractive index of Al_2O_3 is higher than that of SiO_2, thicker layers (and perhaps more bilayers) would be required to obtain the same reflectivity, increasing the total coating thickness and therefore tending to increase the coating thermal noise. Careful trade-off studies of the thermal noise and optical absorption are therefore needed to assess the suitability of using AL_2O_3 as a low-index coating material in place of SiO_2. It should be noted that at 20 K, the higher index coatings of Ta_2O_5 likewise have a mechanical loss peak of 5×10^{-4}. As the cryogenic loss of TiO_2:SiO_2 has not yet been studied, it can not be considered further as a substitute for Ta_2O_5.

To allow an initial evaluation of the performance of Al_2O_3, it can be substituted for SiO_2 in the simulated aLIGO ETM coating design. To accommodate for the increased wavelength of 1550 nm proposed for use in ET-LF (compared to 1064 nm in aLIGO), the thickness of all layers was increased proportionally to maintain a quarter-wavelength optical thickness design. The absorption value worked out to be 2.7 ppm which is still within the 5 ppm limit. The coating therefore is suitable at least from an absorption perspective from this quick substitution. To build on this design, other state-of-the-art coating materials need to first be considered.

Recent research has drastically improved the low-mechanical loss of SiN to 0.58×10^{-4} at 20 k. Despite this low and promising value there are a few distinct challenges to overcome with this material. Firstly, the extinction of the coatings is considerably higher than other coatings described by an order of magnitude of $\approx 1 \times 10^{-5}$. Also, the deposition technique was fine-tuned but for Chemical Vapor Deposition (CVD) instead of IBS (the standard for the rest of the coatings discussed). Further studies have tried to reduce the extinction, in part, through the use of IBS but the extinction (all be it) at 1064 nm was only a factor of two less [246]. As the refractive index between the two studies, from the latter to the former, varied from 2 to 2.68 the deposited coatings and their density is clearly different. Alongside the distinct CVD deposition and unspecified heat treatments, it is hard to project the SiN with low-mechanical loss values into designs. However, it is possible that it can survive high 900°C heat treatments without crystallisation and so it will be considered later on in designs alongside Al_2O_3, which survived all the same.

Another promising material but with an even higher index ($n = 3.48$) is a-Si (previously discussed in section 2.5). Its promise for future coating designs largely lies, similar to SiN, in this high index contrast (for any bilayer) alongside its extremely low mechanical loss 0.18×10^{-4}. The next section will delve into more details here as specific designs are optimised to account for parallel improvements in the thermal noise. Unfortunately, its extinction is approximately 2 orders of magnitude higher than other coatings described at 1×10^{-5} such that when it is substituted for Ta_2O_5 in the aLIGO design it gives an absorption of 7.7 ppm: above the limit set for ET-LF.

One of the main coating designs, which will become of interest, features only Al_2O_3 and a-Si. The absorption of an 8 bilayer (suitable for ET-LF) stack was evaluated to be 8.6 ppm at the top of both curves (see figure 3.7). The pink curve shows how the total coating absorption would improve with reductions from the previously measured

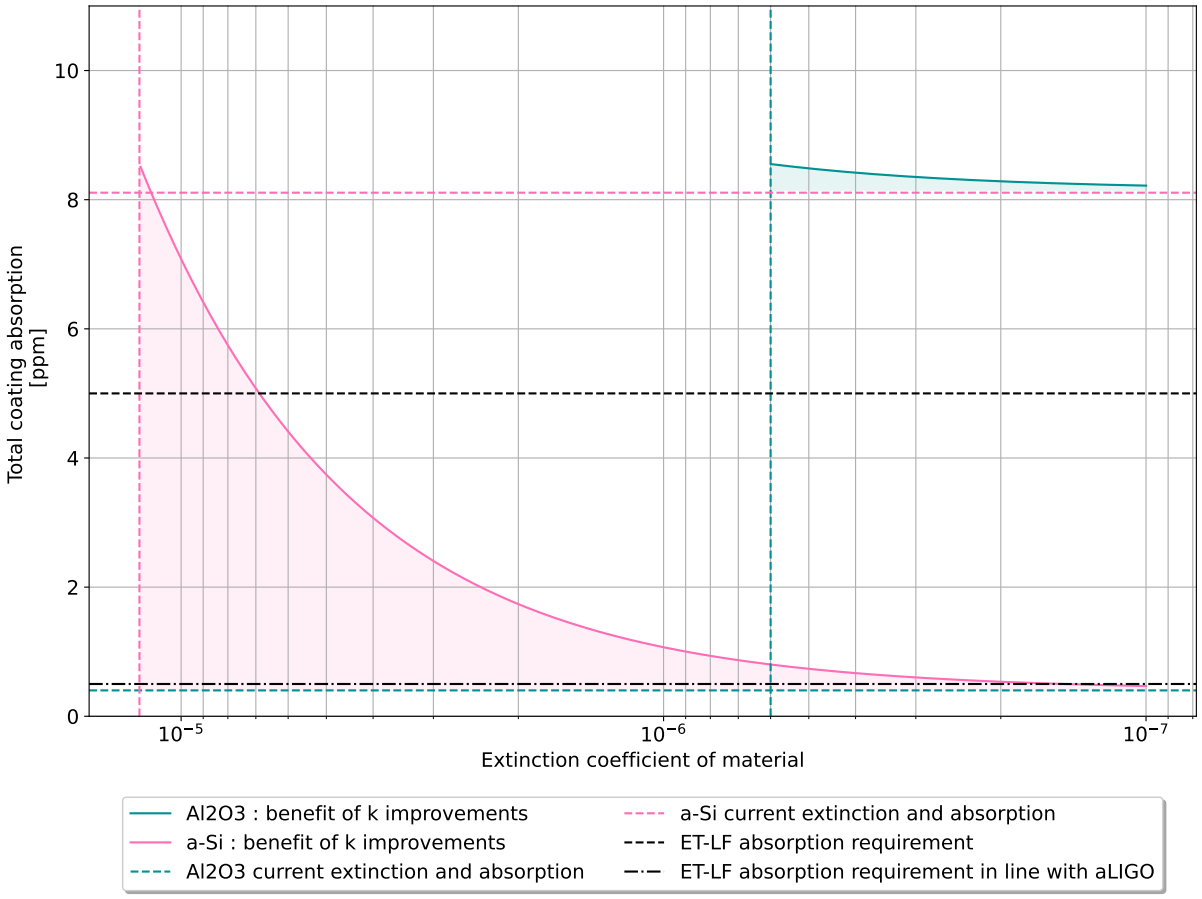

Figure 3.7: The reductions required in the extinction coefficients in order for a a-Si:Al_2O_3 to reach the target absorption for ET-LF.

extinction coefficient (vertical dashed pink line) with the Al_2O_3 layer extinction remaining fixed. The blue curve shows same but for improvements to Al_2O_3 with a fixed extinction coefficient for the a-Si layers. This plot allows one to visualise how future improvements in the absorption of either of the materials will affect the total absorption of an HR stack.

Reducing the extinction of a-Si by 40 % from 12×10^{-6} to 7×10^{-6} would allow the design to reach the 5 ppm target of ET-LF. Previous measurements of a-Si have indicated that absorption reduced by 45% from room temperature [186, 190] and so this might already be possible with current coatings, pending further measurement. Beyond this and in order to reach a 0.5 ppm target 3.7 the extinction of a-Si would need to be reduced to at least 0.8×10^{-6} and by a total factor of fifteen. In this Bragg mirror design, the absorption contributions between each layer, for a given bilayer pair, contribute in equal proportions to the total. The effect of this is that even if the extinction contributions of each layer in a dual-material design are different, a scalar improvement to both of 50%, for example, would be reflected by a 50% reduction in the total absorption. If the a-Si was improved by the minimum amount, then both a-Si and Al_2O_3 would contribute approximately 0.5 ppm to a total of 1 ppm. After which comparably modest reductions

in the extinction of Al_2O_3 by 80 % from 6×10^{-6} to 1×10^{-7} would lower the additional reduction required for a-Si to 20 % for a total factor of twenty. In summary, Al_2O_3 already meets the ET-LF requirements for this bilayer stack design. However, in order to further push the absorption of the HR stack to 0.5 ppm to reduce the total heat load on the test-masses, the extinction of a-Si would need to be improved by a factor of twenty and Al_2O_3, from the measured value, by a factor of five. These factors have not previously been considered and so with the clear visual guide now given by 3.7 future research efforts can be proportionally allocated.

Where lots of research has previously gone into reducing this absorption a-Si towards the value of 1×10^{-5} [187] only this single detailed study which followed from previous mechanical loss measurements Al_2O_3 has been reported. As a result, IBS deposited Al_2O_3 is expected to be a promising low-index material for future cryogenic gravitational wave detectors. To further investigate the suitability of these coating materials, the next section will design novel coatings with a focus on integrating Al_2O_3 into the designs.

3.5 Coating designs for ET-LF based on alumina measurements

In this section, various possibilities for incorporating alumina layers into HR coating stack designs are investigated, making use of the optical absorption measurements in the previous section along with the mechanical loss measurements made by Robie. Due to the low cryogenic mechanical loss of Al_2O_3 relative to the loss peak in SiO_2 at 20 K, Al_2O_3 will be incorporated as a low index layer for these mirror coating designs. The coating stacks indexed throughout the discussion (from a to i), specific materials and layer structures investigated here were chosen at first to meet before surpassing the ET-LF detector's target thermal noise and optical properties.

The specified target for CTN_{Detector} of the ET-LF detector is $\approx 3.6 \times 10^{-21}\,\text{m}/\sqrt{\text{Hz}}$ at 10 K [92]. This is evaluated at a frequency of 10 Hz is chosen here to evaluate the noise, as ET-LFs target sensitivity will require the lowest noise floor in the surrounding region of a few Hz to a few tens of Hz. To compare this level to the rest of the amplitude spectral density levels shown through this thesis (see figure 6.5) the value should be scaled by

the arm length (through equation 1.1). In the case of ET-LF, the length of 10 km would give a noise level of $\approx 3.6 \times 10^{-25}/\sqrt{\text{Hz}}$. For the target operational temperature of 20 K, the target will be proportionally set here with the multiplication of $\times\sqrt{\frac{20}{10}} = \times 1.41$ (that follows from equation 1.4) to give $5.1 \times 10^{-21}\,\text{m}/\sqrt{\text{Hz}}$ ($\approx 5.1 \times 10^{-25}/\sqrt{\text{Hz}}$).

Design (a) *18 bilayer stack of silica and tantala.*
The standard HR coating design used for current aLIGO GWD test masses is a Bragg reflector, consisting of alternating layers of higher and lower index materials, as described in section 2.4. The structure of this design is shown in figure 3.8 A CTN of $\approx 6.3 \times 10^{-21}\,\text{m}/\sqrt{\text{Hz}}$ and absorption of 0.5 ppm was evaluated for the ETM. The total Brownian detector noise (CTN_{Detector}) was evaluated from the ETM and ITM contributions (through equation 1.7) and shown in figure 3.9 (B). The CTN_{Detector} for this design is $1.1 \times 10^{-20}\,\text{m}/\sqrt{\text{Hz}}$. This is a factor of two larger than the limit of $5.1 \times 10^{-21}\,\text{m}/\sqrt{\text{Hz}}$ and would likely limit the detectors' sensitivity around the frequency 10 Hz (see ET-LF noise breakdown on figure 3.11).

From an optical perspective, the specifications for ET-LF includes a transmission value of 7000 ppm and 6 ppm respectively for the ITM and ETM, as initially set out in the 2011 conceptual design study [125]. For the ITM, a higher transmission is required to let light into and out of the arm. The upper threshold for the ETM absorption is set at 5 ppm, but preferably this would be closer to the sub-ppm of current detectors in order to reduce the heat load on the mirror, as discussed in section 1.7. Furthermore, as this low level is currently achievable with current designs, 0.27 ppm and so it is important to still consider this as a secondary lower limit.

The design process used throughout this section in order to meet the ET-LF requirements will now be introduced for an arbitrary coating. Starting with the ETM coating, the number of bilayers was chosen to yield the target reflectivity (through equation 2.10) and transmissivity (assuming at first a lossless model of $T = 1 - R$). Then accounting for the losses (see appendix C.1) if the absorption was too high, a series of lower absorbing cap layers were added to the front. In the case of the mostly used low absorbing TiO_2:SiO_2 and SiO_2 cap-layers, this was evaluated to reduce by approximately 50% the dual-material absorption baseline. This is an example of the so-called 'multi-material' coating design approach [90, 198] (introduced in section 2.4). This design pushes materials with lower mechanical loss but higher absorption levels, away from the high incident powers at the front of the coating, towards the lower part of the stack.

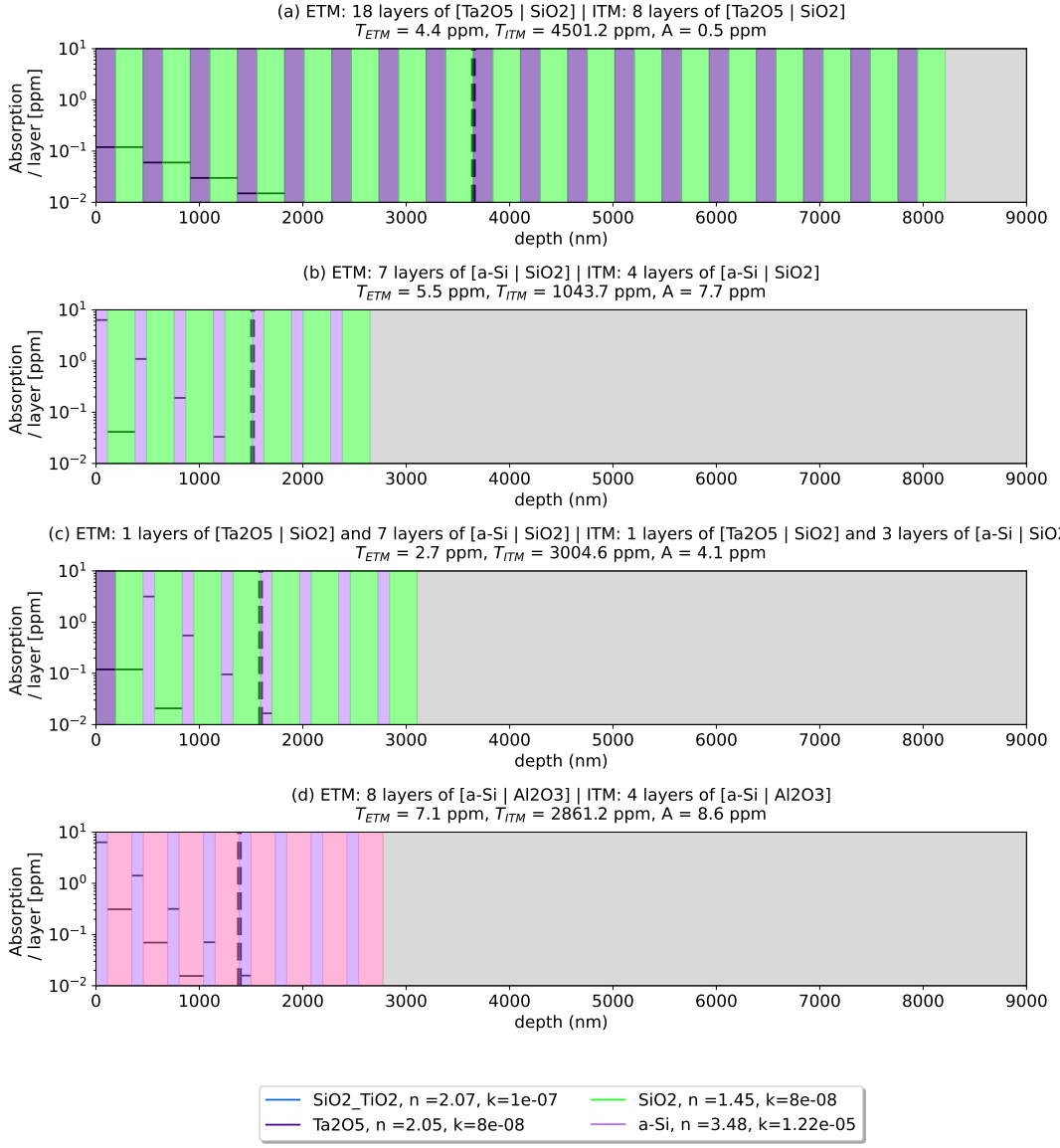

Figure 3.8: Coating designs for the ETM and ITM (ending at vertical dashed line) of ET-LF based on which meet the transmission and absorption thresholds. The materials and designs shown here are inspired largely from the designs of mirror coatings in current detectors. Different coating materials are distinguished by colour (legend) and the silicon substrate used here is shown here (grey). For all the coating designs, the absorption in each layer is shown with a standardised ppm-scale (horizontal black lines).

After these cap layers are added, a number of original layers were removed from the back to maintain the transmissivity. To convert these ETM designs to ITM designs, layers are removed from the back to increase the transmission without increasing the absorption. As a result of using the same materials, these ETM and ITM designs will be referred to here as being symmetric and the absorption will be quoted only for the ETM. This is because the absorption difference was less than 1 % different. For both the ETM and ITM, the transmissivity values were allowed to exceed 30% of the ET-LF targets because a less than 3% shift in the refractive index contrast of the bilayers could recover the difference. For two-material designs, this clearly follows from the reflectivity equation 2.10.

The other eight ETM and ITM coatings stack designs indexed from (b-i) will now be introduced. Each design topology is described and the structure is shown in figure 3.8. The extra layers required to go from an ITM to an ETM design follow after the dashed vertical black line. Alongside the number of layers, the figure also shows the transmission and absorption of each stack, evaluated through the extinction to absorption model (see appendix C.1). The absorption contribution of each layer is shown with a horizontal black line until they are below 0.01 ppm and considered to have negligible contributions to the total.

In parallel to this figure, the Brownian coating thermal noise (CTN) for each ETM and ITM stack is shown on figure 3.9 (A) with a distinctly coloured bar. The CTN values were evaluated using the material properties from table 3.1 passed through equation 1.5. The total Brownian detector noise was then evaluated for select coating design combinations for the ETMs and ITMs on figure 3.9 (B) compared to the required $5.1 \times 10^{-21}\,\mathrm{m}/\sqrt{\mathrm{Hz}}$ limit for ET-LF (at 20 K). Lastly, the absorption for these chosen ETMs and ITMs is shown in figure 3.9 (C) compared to the required 5 ppm.

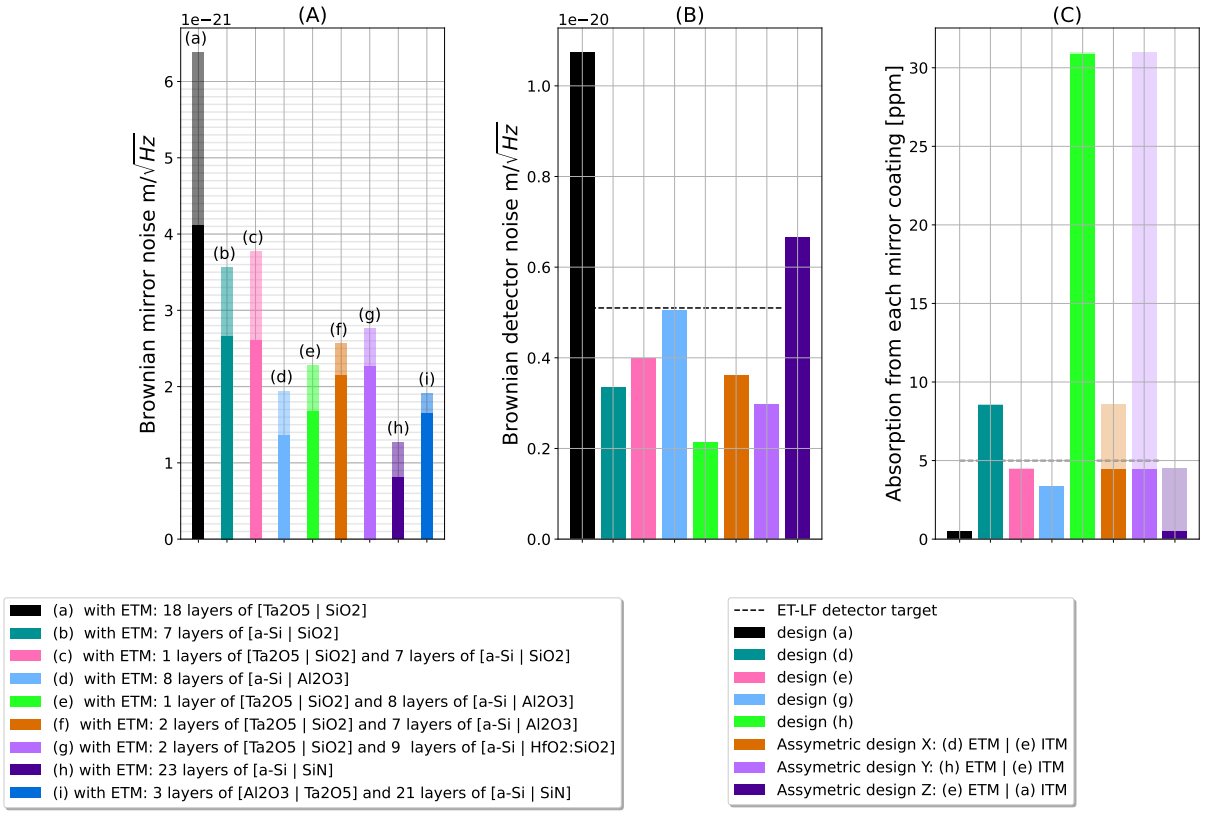

Figure 3.9: (A) Coating Brownian noise for each coating mirror design for the ETM and ITM. (B) The total Brownian detector noise for the ITM and ETM design pairs. All of these thermal noise values were evaluated for a temperature of 20 K and a frequency of 10 Hz. The properties of the materials involved at this temperature are shown in table 3.1. (C) the expected absorption contributions are also shown for the ET and ITM design pairs.

Design (b) *7 bilayer stack of silica and amorphous-silicon*
To try and reach the ET-LF noise requirement, the high-index layers are swapped for amorphous silicon. The effect of this high index (first discussed in section 2.4) is to approximately half the geometric thickness of the coatings with an index ($n < 2$). The benefit of this follow from the CTN's thickness dependence, summed for each layer, as shown in equation 1.5. For this coating design, the thickness dropped drastically from design (a)'s 8.2 µm to 2.7 µm. This is a massive 67 % reduction in the total ETM coating thickness that is approximately matched in the ITM coating. The total detector noise dropped to $6.3 \times 10^{-21}\,\mathrm{m}/\sqrt{\mathrm{Hz}}$ which is still above the target and only represents a value which is 43 % less than that of design (a). Following the equation 1.5, the reason that this reduction does not follow is that the silica layer's geometrical thickness is considerably more, such that they occupy 70 % of the stack's total thickness and so further limit the Brownian noise (in account of their high mechanical loss). As for the absorption, the coating was 50 % above the target with a value of 7.7 ppm and so it is not suitable for ET-LF.

Design (c) *multi-material stack. (Top) 1 bilayers of silica and tantala followed by (Bottom) 7 bilayers of silica and amorphous silicon.*
Through the addition of a cap layer, the absorption of this was approximately and as expected, halved compared to (b) to a value of 4.1 ppm. This value is below the design limit but increased the detector CTN noise to $7 \times 10^{-21}\,\mathrm{m}/\sqrt{\mathrm{Hz}}$ and so it is still not viable for ET-LF.

Design (d) *8 bilayer stack of alumina and amorphous silicon.*
Inspired from design (b), Al_2O_3 with a lower mechanical loss was substituted in for the SiO_2 layers. For the ETM the total thickness was low at 2.8μm and the CTN dropped accordingly to $1.9 \times 10^{-21}\,\mathrm{m}/\sqrt{\mathrm{Hz}}$ alongside the detector CTN to $3.3 \times 10^{-21}\,\mathrm{m}/\sqrt{\mathrm{Hz}}$. This represents a significant improvement and to a level that is 35 % below the target of $5.1 \times 10^{-21}\,\mathrm{m}/\sqrt{\mathrm{Hz}}$ (shown with a cyan bar on figure 3.9 (B)). However, the absorption level was 8.6 ppm and so the applicability of the design, based on currently measured extinction values, is limited. The improvements required for the design to be viable (described in section 3.4) are largely attributed to a-Si.

Design (e) *multi-material stack. (Top) 1 bilayer of silica and tantala followed by (Bottom) 8 bilayers of alumina and amorphous silicon.*
The structure of the designs that follow from here onwards will be shown on a distinct figure 3.10, with the same layout and features as described for figure 3.8.

Following the noise improvements of design (d), this design made use of a cap layer (similar to design (c)) to approximately half the absorption to 4.5 ppm and within the acceptable limit of 5 ppm (shown with a pink bar on figure 3.9 (C)). The higher mechanical loss of the cap layer increased the detector CTN to $4 \times 10^{-21}\,\mathrm{m}/\sqrt{\mathrm{Hz}}$ but this was still within the limit (by 20 %). The design therefore is a suitable candidate coating for both the ITM and ETM mirrors of ET-LF.

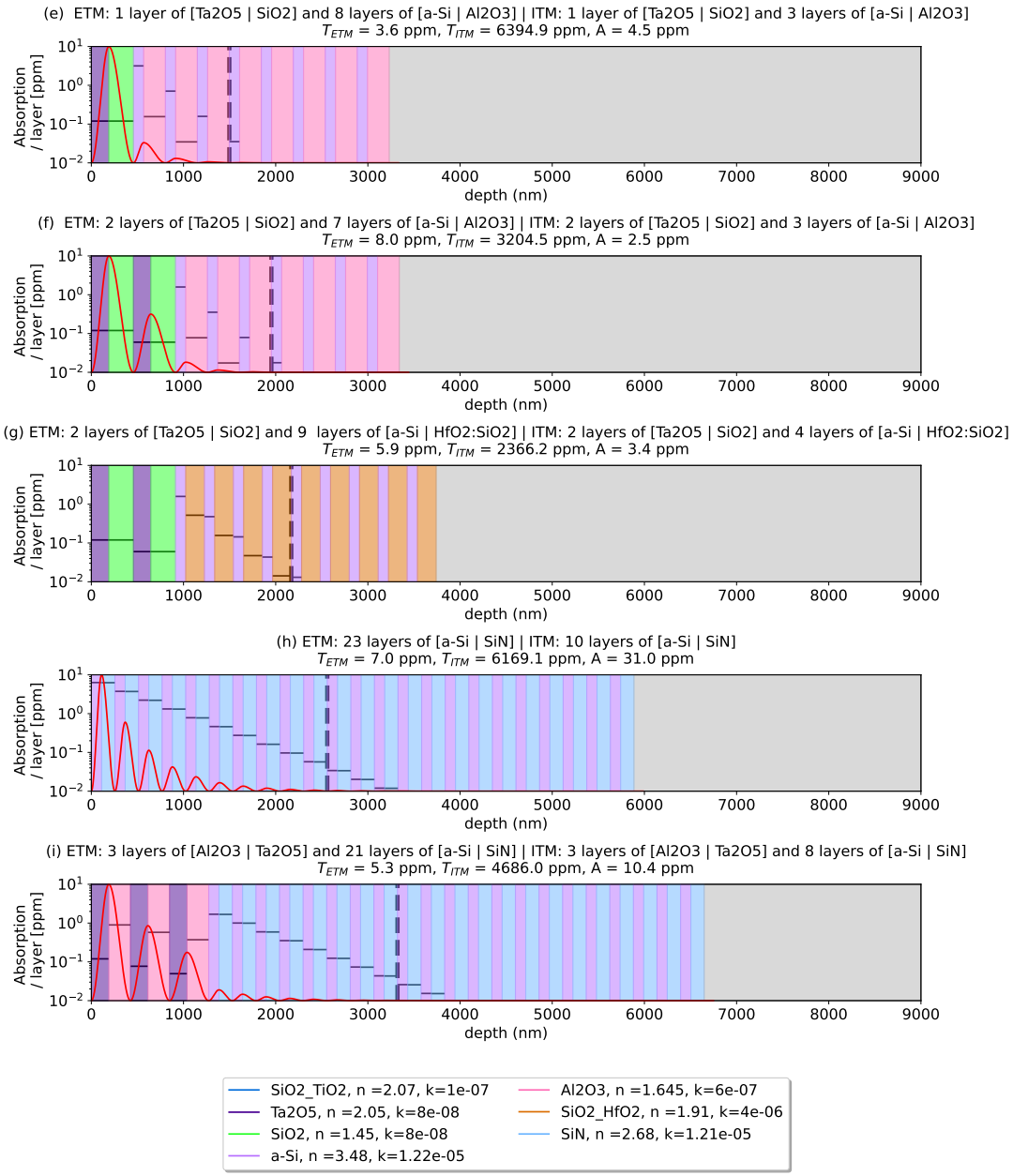

Figure 3.10: Candidate coating designs for the ETM and ITM (ending at vertical dashed line) of ET-LF which meet the transmission and absorption thresholds. The different coating materials are distinguished by colour (legend) and the silicon substrate used here is shown here (grey). For all of the coating designs the absorption in each layer is shown with a standardised ppm-scale (horizontal black lines). The Electric field intensity normalised of the first peak (red line) highlights the additional drop in power found through the use of a-Si and Al_2O_3 bilayers.

Design (f) *multi-material stack. (Top) 2 bilayers of silica and tantala followed by (Bottom) 7 bilayers of alumina and amorphous silicon.*
To further explore the current potential of absorption improvements, another cap layer is added with this design to reduce the electric field intensity (power entering into the layers, as shown with red lines on figure 3.10). This absorption dropped to 2.5 ppm which in the context of ET-LF if considered for the ITM (compared to design (e)) could reduce the heat load from coating absorption by ≈ 50 mW. Compared to other heat load terms (see table 1.1) this could significantly reduce the total heat load and go a long way towards the stable operation of the detector. Of course, this has to be balanced with the detector CTN increase to $4.7 \times 10^{-21}\,\mathrm{m}/\sqrt{\mathrm{Hz}}$. However, as the ETM has no substrate absorption, the higher absorbing and lower noise designs could be considered separately for this mirror to the effect of the same equivalent heat load. Compared to the symmetric ITM and ETM choices considered thus far, this equates to a detector CTN of $4.4 \times 10^{-21}\,\mathrm{m}/\sqrt{\mathrm{Hz}}$ with the use of design (e) on the ETM and $4.1 \times 10^{-21}\,\mathrm{m}/\sqrt{\mathrm{Hz}}$ for the use of design (d). The equivalent increase in the heat load following from the cavity power of 18 kW (see equation 1.14) and absorptions previously stated for the ETM would be 40 mW and 100 mW respectively.

Design (g) *multi-material stack. (Top) 2 bilayers of silica and tantala followed by (Bottom) 9 bilayers of silica-doped-hafnia and amorphous silicon.*
The only comparable coating design study which has been made in the context of ET-LF is that by Craig [92]. This work proposed a multi-material design with SiO_2:HfO_2 as the low-index layer to pair with a-Si in the bottom of the stack. In front of which, a two low absorbing cap bilayers of silica and TiO_2:Ta_2O_5 (used likewise for design (f) here) was placed. Compared to the 20 K chosen here, the CTN value for the design was reported for ET-LF if it operated 10 K instead. Recalculating this, the CTN for the ETM is $2.8 \times 10^{-21}\,\mathrm{m}/\sqrt{\mathrm{Hz}}$ and for the detector as a whole is $5.1 \times 10^{-21}\,\mathrm{m}/\sqrt{\mathrm{Hz}}$ which is equivalent to the set target (likely set originally by this design). Compared to this, the multi-material alumina design (e) proposed here, has a CTN which is 28 % lower and which, given the small changes in mechanical loss of these materials, should give an equivalent improvement at 10 K. The reason for the worse theoretical performance of the previously proposed SiO_2:HfO_2 design follows mostly from its mechanical loss being 40 % higher than Al_2O_3.

As for the absorption, it is slightly more at 4.5 ppm (for design (e)) compared to 3.4 ppm due to the higher power transmitted through a single cap layer instead and through to the high absorbing a-Si layers. Although, the double cap layer Al_2O_3 design has a lower absorption. This is because the extinction of SiO_2:HfO_2 considerably higher by a factor of ten 4×10^{-6} compared to Al_2O_3.

To start to consider the impact of the detector CTN more deeply, the total noise curve as it stands for ET-LF is shown in figure 3.11 (at 10 K with the conversion as discussed at the start of this section). The rest of the noises (introduced in section 1.4) shown in this plot were calculated [245] from pre-set detector specifications originally stated in initial ET design report [125]. Above 10 Hz, aside from the broadband quantum primary limit, the CTN detector noises are expected to set a secondary and fundamental limit. At frequencies, especially between $10-20$ Hz, the design (e) proposed here based on alumina materials offers an approximately 3 % reduction from the baseline (g) to the total detector noise (when added in quadrature).

Improvements beyond this could be expected if the quantum noise floor and cavity power of the detector was set differently. Therefore, it is important to look now for further improvements, even if their contributions to the current design (when added in quadrature with the other theoretical noise levels) is not as clear. The baseline for comparison will now be considered here as design (e) with its detector CTN of $4 \times 10^{-21}\,\mathrm{m}/\sqrt{\mathrm{Hz}}$ at 20 K (equivalent to $2.8 \times 10^{-21}\,\mathrm{m}/\sqrt{\mathrm{Hz}}$ at 10 K) and absorption of 4.5 ppm.

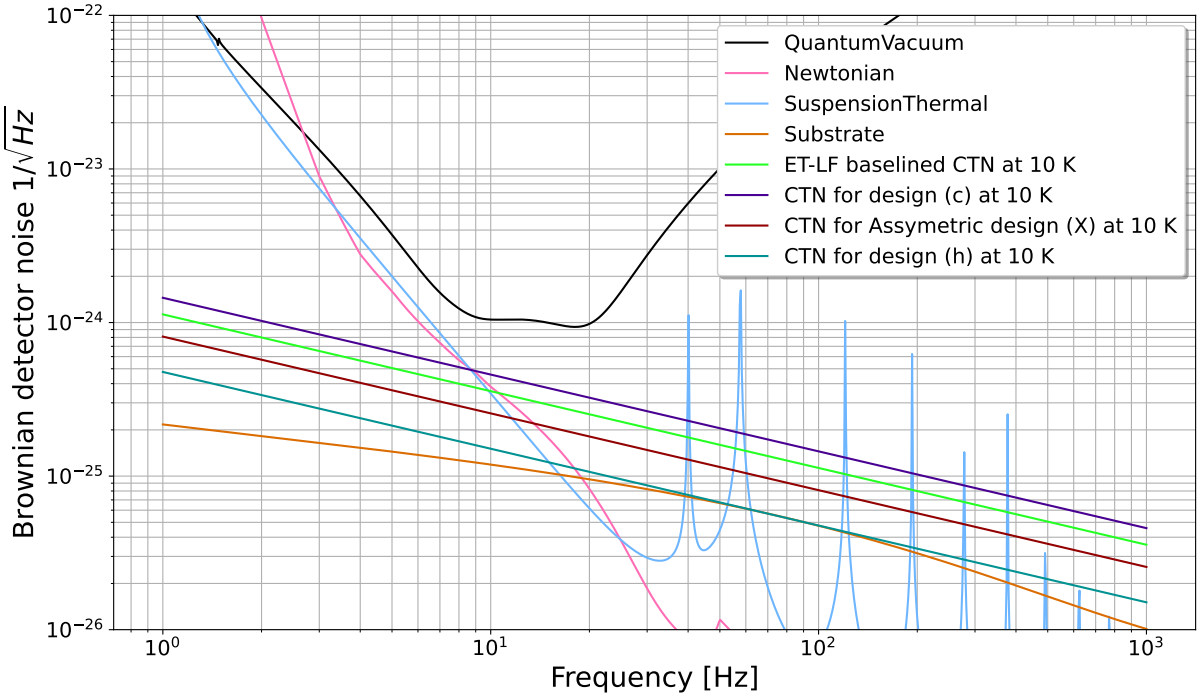

Figure 3.11: Evaluated CTN performance of select designs compared to the ET-LF CTN baseline and other prominent noise sources.

Design (h) *23 bilayer stack of silicon nitride and amorphous silicon.*
This design follows the progression from (b) and (d) of substituting materials with lower mechanical loss into bilayer pairings with the high-index a-Si. Although, the thickness increases by a factor of two compared to design (d) (which used alumina) the CTN reduced by $\approx 40\,\%$ for the of the ETM from $2 \times 10^{-21}\,\mathrm{m}/\sqrt{\mathrm{Hz}}$ to $1.25 \times 10^{-21}\,\mathrm{m}/\sqrt{\mathrm{Hz}}$ and for the detector from $3.3 \times 10^{-21}\,\mathrm{m}/\sqrt{\mathrm{Hz}}$ to $2 \times 10^{-21}\,\mathrm{m}/\sqrt{\mathrm{Hz}}$ (shown with a green bar on figure 3.9 (B)).

Although, this is extremely low, this value is not expected to be physically reproducible on the short term. This is because the SiN was deposited with a CVD based technique, as opposed to IBS [244]. IBS is known to be distinct in its ability to produce both low absorption, scatter and mechanical loss coatings. For this reason, all other coatings both measured here and used in current detectors use coatings deposited by IBS. Therefore, it's not guaranteed that the work of can be replicated with IBS.

The other challenge facing this design is that the lowest measured extinction level for both SiN and a-Si is at least a factor of forty above the measured values for the other coatings here of Al_2O_3, TiO_2:SiO_2 and others, as shown in table 3.1. This would result in an absorption level that is a factor of six beyond the limit of 5 ppm and up to 31 ppm. Following the absorption discussion for Al_2O_3 and a-Si (in relation to figure 3.7) given the equivalent extinction of both materials, this could be realised with a minimum factor of three reduction for one (from the 15.5 ppm contribution) and a reduction in excess of ten for the other. Otherwise, the extinction of each would have to be improved by the factor of six to reach the 5 ppm level.

Design (i) *multi-material stack. (Top) 3 bilayers of alumina and tantala followed by (Bottom) 21 bilayers of silica-doped-hafnia and amorphous silicon.*
To see if this absorption level could be considerably reduced for design (h), cap layers were added to the front. In order to preserve the mechanical-loss Al_2O_3 and Ta_2O_5 cap layers were chosen. Although, given the lower refractive index contrast, three bilayers were required to reduce the absorption. The value reached for this design was 10.4 ppm which is a factor of two higher than the limit set for ET-LF.

However, compared to the new baseline design (e) the detector CTN was only 12 % better at $3.5 \times 10^{-21}\,\mathrm{m}/\sqrt{\mathrm{Hz}}$ compared to $4 \times 10^{-21}\,\mathrm{m}/\sqrt{\mathrm{Hz}}$. As the absorption for design (e) was 60 % better at 4.5 ppm, it will remain as the new baseline for a symmetric combination of ITM and ETM mirror coatings.

It is expected once better estimate values are known for the other heat load terms from substrate absorption (most notably in the ITM) to ambient heat load that radiates from the warm environment in proximity to the test-masses that outwith 5 ppm, a range of different coating absorption limits could be acceptable. In a similar sense to how multi-material designs improved upon the absorption and therefore thermal noise, asymmetric coating designs first proposed here could through higher-absorbing and low thermal noise ETM coatings (through its considerably lower substrate contributions) enable the use of higher thermal noise coatings on the ITM which have been shown to already have an absorption down to sub-ppm level. Following this reasoning, three asymmetric combinations will now be proposed for the ET-LF detector which make use of the ITM and ETM designs proposed here. All of these designs will make use of the new baseline design (e): single silica and tantala bilayer on top of eight bilayers of Al_2O_3 and a-Si.

Asymmetric detector design (X) *ETM: design (d) | ITM: design (e)*
By accepting a modestly higher ETM coating heat load following equation 1.14 (with a cavity power of 18 kW) of approximately 80 mW the total detector CTN could be reduced from $4 \times 10^{-21}\,\mathrm{m}/\sqrt{\mathrm{Hz}}$ to $3.5 \times 10^{-21}\,\mathrm{m}/\sqrt{\mathrm{Hz}}$ (shown by the orange line on 3.9 (B)).

Asymmetric detector design (Y) *ETM: design (h) | ITM: design (e)*
By accepting a drastically higher ETM coating heat load due to the use of design (h) of 540 mW the total detector CTN could be reduced further from $4 \times 10^{-21}\,\mathrm{m}/\sqrt{\mathrm{Hz}}$ to $3 \times 10^{-21}\,\mathrm{m}/\sqrt{\mathrm{Hz}}$ (shown by the lilac line on figure 3.9 (B)). However, as this heat load would likely be significantly larger than other terms and so would not be suitable for ET-LF.

Asymmetric detector design (Z) *ETM: design (e) | ITM: design (a)*
This design focuses instead on drastically reducing the ITM absorption by using design (a) where the absorption was calculated here as 0.5 ppm (shown by the purple line on figure 3.9 (C)) but if it follows closer to the aLIGO produced coating could be down to 0.27 ppm [144]. This would equate to a trace coating contribution to the ITM heat load of 5 mW which is expected to be considerably less than the substrate and ambient terms. However, this design as shown is not viable with the detector CTN increased above the $5 \times 10^{-21}\,\mathrm{m}/\sqrt{\mathrm{Hz}}$ limit to $6.5 \times 10^{-21}\,\mathrm{m}/\sqrt{\mathrm{Hz}}$ (shown by the purple line on figure 3.9 (B)).

With a revision of this detector design and change of design (a) to four bilayers of SiO_2 and Ta_2O_5 followed by just two bilayers of a-Si and Al_2O_3 the theoretical properties improved. The absorption reduced below 1 ppm and the noise reached the $5 \times 10^{-21}\,\mathrm{m}/\sqrt{\mathrm{Hz}}$ limit. Therefore, making use of the Al_2O_3 materials studied here it is possible that both the currently required detector CTN can be achieved and that the sub-ppm absorbing coatings (for the ITM) can be achieved.

3.6 Conclusion

One potential replacement for the low-index SiO_2 coating layers in the test-masses of future gravitational wave detectors was previously identified as Al_2O_3. Its suitability from a mechanical loss perspective at cryogenic temperatures was previously supported by measurements from Robie [106]. From the same IBS coating run, measurements of the absorption at both 1064 nm and 1550 nm were made in an attempt to fully qualify the material for use in cryogenic detectors. After heat treating a sample at 850 °C with a ramp rate of 100 °C/hr and dwell time of 10 hrs the extinction achieved was extremely low at 3.5×10^{-7} at 1064 nm. As this value it was within the uncertainties of another stated low-value [218], it stands as one of the two lowest measurements ever reported for this thin-film material. Given the increasing trends with temperature across the heat treatments (by just under a factor of two) the value at 1550 nm was expected 6×10^{-7} and so this was chosen to evaluate the total absorption for coating designs feature throughout this chapter.

This value is within a factor of five of the known extinction of silica (see table 3.1) which in combination with its lower mechanical loss value (50 % less at 20 K) indicate that it is likely the best substitute for the low-index silica layers for coatings in cryogenic gravitational wave detectors. This is very promising, especially in consideration of the limited number of studies published on this material [106, 241].

With an operational ET-LF currently targeted at 10 years away, there is clearly scope to further improve these values and establish a safety margin for both the Brownian noise contributions and absorption. This safety margin is crucial, as theoretical projections of small-scale lab measurements are limited in their extension. Experimentally validating the projections here will require considerable and time-consuming efforts in research and development for upscaling the optics, annealing procedures, and then simply in cooling them down to the $10-20$ K environment required for close to in-situ ET-LF testing. There

is also currently a large uncertainty in the expected heat loads in ET-LF from both the ambient environment and substrate, as discussed in section 1.7. Given the ETM's higher reflectivity its trace substrate contributions, shown in table 1.1, for the same coating absorption it is expected to have a lower total heat load.

To account for these variances, it is important to widen the scope of target ET-LF coating absorption levels, both below and above the current 5 ppm target. In doing so, other coating designs and materials were considered here. The CTN of coatings featuring both Al_2O_3 and SiN at cryogenic temperatures were modelled for the first time and shown to have the potential to significantly improve compared to current projections. This work has provided strong evidence that a low CTN and absorption ET-LF cryogenic coating can be achieved. This thesis also shows that Al_2O_3 and TiO_2:SiO_2 found their minimum absorption values after the same heat treatment temperature of 850 °C whilst both being partially crystallised and so future design revisions and cryogenic measurements of TiO_2:SiO_2 could support the design of multi-material stacks tailored for target heat treatment temperature. The realisation of a viable ET-LF coating solution was reached with current measurements in the literature and with key measurements contained in this chapter. Given the limited research into the mechanical loss and absorption of the alumina presented, there is promise that these can be further improved. In the future, further coatings should be prepared using IBS and the Young modulus and mechanical loss should first be checked as deposited. Heat treatment studies should look to improve find the optimal heat treatment temperature parameters: beyond the $800 - 850$°C for loss and absorption samples and dwell times of $1 - 10$ hrs respectively. These heat treatments will start to get more standardised as different coatings are optimised as stacks and potentially multi-materials towards implementations in future detectors.

As a result of these Al_2O_3 measurements, it was interesting to evaluate novel coating designs for future mirrors of gravitational wave detectors such as ET-LF (at 20 K). An asymmetric coating detector design (Z) was proposed here for the first time. This showed that the coating heat load on the ITM mirror could be mitigated if a higher noise multi-material ITM coating was used: derived from the lower absorption levels of currently used and widely researched coatings. This design was specified to ensure that the other requirements were met and that the total detector CTN was below the requirement set here of $5\times10^{-21}\,\mathrm{m}/\sqrt{\mathrm{Hz}}$ that was scaled proportionally (with temperature $\times\sqrt{\frac{20}{10}} = \times 1.41$ from equation 1.4) from the previously set baseline of $\approx 3.6 \times 10^{-21}\,\mathrm{m}/\sqrt{Hz}$ [92].

Aside from this, an optimal symmetric design (e) was found here, which consisted (for the ETM) of a single silica and tantala bilayer on top of 8 bilayers of alumina and amorphous silicon. This design had a detector displacement CTN of $4 \times 10^{-21}\,\mathrm{m}/\sqrt{\mathrm{Hz}}$. This was 20 % better than the previous detector baseline of $5 \times 10^{-21}\,\mathrm{m}/\sqrt{\mathrm{Hz}}$. In account of the detector length (10 km), the detector CTN noise level would be $4 \times 10^{-25}\,/\sqrt{\mathrm{Hz}}$ at 20 K and $2.8 \times 10^{-25}\,/\sqrt{\mathrm{Hz}}$. This is approximately 50 % better than what would be achieved if the aLIGO coating was used $6.2 \times 10^{-25}\,/\sqrt{\mathrm{Hz}}$. Also, the aLIGO detector (length 4 km) CTN at RT is $8 \times 10^{-24}\,/\sqrt{\mathrm{Hz}}$. [92]. Compared to this, the detector CTN of ET-LF for design (e) proposed here is a factor of at least twenty lower (20 K). As the expected quantum vacuum noise source $1 \times 10^{-24}\,/\sqrt{\mathrm{Hz}}$ (10 K) the ET-LF CTN detector noise is expected to now be considerably reduced by a factor of three (10 K).

With a range of viable ET-LF coating designs, proposed that incorporate a range of different compatible coatings, it is more likely now that the full detector sensitivity improvement of ET-LF of $\times 10^3$ compared to current detectors will be realised in the 1–10 Hz frequency band. Considering the improvements to the baseline offered here alongside the dominant ET-LF quantum noise, the total detector noise (through quadrature addition) could be further reduced by 3 % between $10 - 20$ Hz, to increase the sensitive volume that scales with the cube of the sensitive distance (see section 1.5) by a further 10 %. This improvement would crucially occur where the detector is most sensitive. As a result of this work, the ET-LF could, when operational, detect known young pulsars [247], make the first detections of a Galactic type Ia supernova [248]. In addition to this, with a wider frequency range, inspirals will be observed for a longer time leading up to the final merger event.

Chapter 4

Theory and transmission measurements of mono-crystalline silicon's absorption

4.1 Introduction

This chapter will cover optical measurements made to determine the near infrared absorption of mono-crystalline silicon. The silicon substrates measured here are small-scale representative samples of materials, much smaller than the large substrates proposed for the mirrors of next-generation GW detectors. The measurements will crucially provide a calibration absorption reference for the distinct setups introduced in chapter 6. To first provide context for the absorption measurements section 4.2 will introduce the underlying theory; section 4.3, the different growth methods used to produce crystalline silicon and lastly section 4.4 will show how different foreign atoms couple through and impact the absorption. Following this, the measurement technique, fitting routine and absorption results for the transmission setup will be discussed section 4.5.

4.2 Absorption theory for bulk mono-crystalline silicon

At room temperature (RT), mono-crystalline silicon has two distinct absorption bandgaps where the energy corresponds to that required to excite an electron interband and create a free carrier: from the valence to conduction bands [249]. The direct bandgap is at energies equivalent to a photon wavelength $\approx 350\,\text{nm}$ and the indirect one is at lower energy, corresponding to $\approx 1100\,\text{nm}$. Indirect transitions are assisted here by phonons. For wavelengths below this indirect bandgap, there are therefore high intrinsic absorption coefficients. Moving above the bandgap, from $950 - 1300\,\text{nm}$, studies have been able to isolate this interband absorption coefficient of silicon and shown that it drastically drops off with both increases in wavelength and reductions in temperature [250, 251, 252]. At 1300 nm and RT, this equates to $23\,\text{ppm}/\text{cm}$. When extrapolated, as shown on figure 4.1, to the higher wavelength candidate of 1550 nm for future GW detectors, it should be considerably less than $1\,\text{ppm}/\text{cm}$. This is considerably less than the level indicated by previous measurements and the targets set for future GWDs. If there are sufficient impurities, as shown in studies where sulphur was intentionally implanted [253], then there could also exist localised sub-band defect states that contribute to the discrepancy in theoretical and measured absorption.

By comparison with the RT absorption measured for high-purity silicon at approximately, $3\,\text{ppm}/\text{cm}$ the interband absorption is not expected to be a significant factor for silicon optics in future GWDs. Instead, the intraband absorption, of electrons excited within bands, is expected to dominate. The main contributor to this, from $1 - 200\,\mu\text{m}$ [256], is the free carrier absorption (FCA). This is the energy lost during the free carrier oscillation imparted by light, as it is absorbed and mostly re-emitted in transmission through the silicon. At RT, the thermal energy acts to liberate nearly all the free carriers from the dominant donor or acceptor concentration. The interdependence of photon energy, carrier energy and the scattering source, be it a phonon or impurity, all determine the time-scales and level of absorption [257]. The Drude model [258] is the standard model for describing the theoretical FCA at RT

$$\alpha_{\text{FCA}_{\text{Drude}}} = n_{\text{e}}\sigma_{\text{e}} + n_{\text{h}}\sigma_{\text{h}} \quad \text{where} \quad \sigma_{\text{carrier}} = \left(\frac{q^3\lambda^2}{4\pi^2 c^3 \epsilon_0 \nu \cdot m^{*2}_{\text{carrier}} \mu_{\text{carrier}}} \right). \tag{4.1}$$

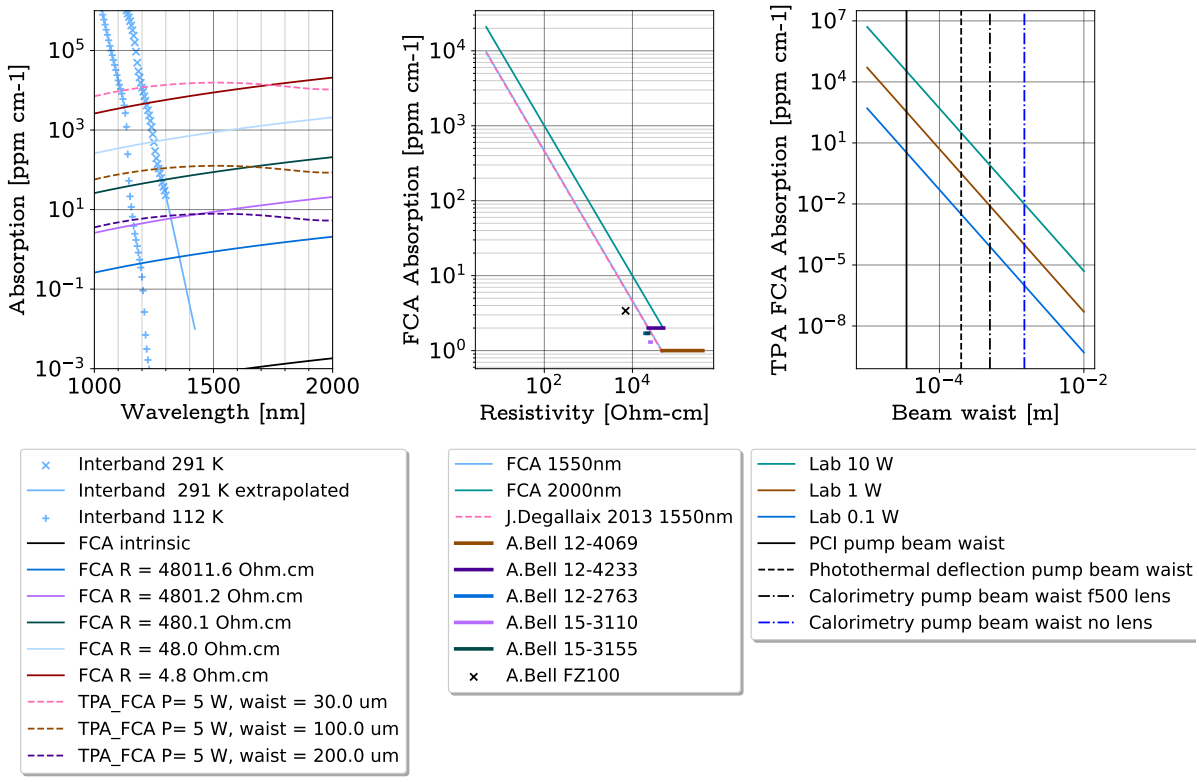

Figure 4.1: This figure shows all the expected absorption contributions for silicon of different resistivity values and illuminated by light over a range of both intensity and wavelength.
(A) This combines the expected absorption from the three distinct mechanisms discussed in this section across the parameter space relevant for c-Si, its measurement and proposed use in future GWD. The interband absorption shows a negligible NIR level from the RT extrapolations. The level is expected to reduce even further at cryogenic temperatures, as indicated by the second trend at 112 K absorption. The FCA show a significant decrease for purity levels approaching the intrinsic limit.
(B) This plot shows a comparison of FCA equations 4.2 and 4.4. Additional data is also shown from J.Degallaix [254] and A.Bell [255].
(C) This plot shows the two-photon FCA dependence on beam intensity over a range of beam parameter spaces relevant to the various experimental setups highlighted in the plot used throughout this thesis and further discussed in section 6.2.

which sums together the separate products from the electron (e) and hole (h) carriers' density (n) and cross-section (σ). The electronic charge is given by (q), permittivity of free space (ϵ_0), refractive index (ν), the conductivity effective mass of each carrier (m^*_{carrier}) and carrier mobility (μ_{carrier}). For n-type c-Si, at wavelengths of 1550 nm and donor electron free carrier densities (n_e) down to 10^{-15} cm^{-3} the Drude model is in close agreement [259] with the empirical Green formula [260]

$$\alpha_{\mathrm{FCA_{Green}}} = 2.6 \times 10^{-18} n_{\mathrm{e}} \lambda^3 + 2.7 \times 10^{-18} n_{\mathrm{h}} \lambda^2. \tag{4.2}$$

It is desirable for the mirrors of gravitational wave detectors for the absorption and therefore doping to be as low as possible. Low doping implies high purity and silicon which is by definition close to its intrinsic state. The established electrical activity of n-type c-Si means that a sample with resistivity (R) should give through the conversion

$$n_e = \frac{1}{R \mu_e q} \tag{4.3}$$

a doping level that is similar to the more detailed evaluation found in the American Society for Testing and Materials (ASTM) standard [261] and therefore an accurate indication of the FCA. Degallaix [254] established this at a wavelength of 2000 nm with an empirical relation of resistivity, over the range of $0.17 - 10,000\,\Omega \cdot \mathrm{cm}$, with the FCA

$$\alpha_{\mathrm{FCA_{empirical}}} = (0.0454 \pm 0.0007) \frac{1}{R}. \tag{4.4}$$

Equations 4.2 and 4.4 are shown on figure 4.1 alongside measurements made previously by A. Bell [255]. The agreement of these measurements indicate that all doping atoms are electrically active in high-purity silicon with a resistivity up to $10,000\,\Omega \cdot \mathrm{cm}$. To the best of the author's knowledge, no empirical relation has been established at different NIR wavelengths; for p-type c-Si where the carrier concentration is dominated by that from holes (n_h); for lower carrier concentrations or at lower temperatures. Any combination of these changes could be expected for silicon optics in future GWD and so in the absence of a clear theory, it is important to measure and push the boundaries of the current one [262].

To motivate measurements over this different parameter space, the expected difference in the through coupling to FCA will be considered independently for each parameter. Firstly, considering the extension to p-type silicon, the FCA is expected to be lower with the disappearance of a wide absorption band centred on 2300 nm [263]. In the case of n-type silicon with high resistivity values ($>$ few k $\cdot$cm) it is not clear whether measured absorption is dominated by FCA as previous data, shown on figure 4.1, has suggested a

deviation from the empirical equation 4.4. Therefore, it is possible that some impurities are not electrically active, and their contributions to the absorption may carry complexities that exist beyond the standard Drude model. This model predicts that intrinsic silicon with carrier concentration $\approx 10^{-10}\,\mathrm{cm}^{-3}$ [251, 264] should have an absorption of $< 0.1\,\mathrm{ppm\,cm}^{-1}$, at 1550 nm as shown on figure 4.1. This is an order of magnitude lower than the best absorption measurements made $< 1\,\mathrm{ppm\,cm}^{-1}$ [255]. The resistivity measurements, through the four point probe method (described later in section 6.8.2, carried a large error. This range ($\approx 40 - 400\,\mathrm{k}\ \cdot \mathrm{cm}$ indicated that the absorption was likely in excess, by up to a factor of 10, of what was expected from the doping level. In addition to the absorption from the silicon bulk, impurities contaminated on the surface have been reported to cause a high overall absorption in excess of that which was expected from the measured carrier or resistivity values [265].

It was previously expected that at the low temperatures, particularly the $10 - 20\,\mathrm{K}$ target of ET, that there would not be thermal energy to liberate the free carriers. It was expected then that the carrier concentration would start to effectively freeze-out of existence and the otherwise dominant FCA would disappear. However, for low resistivity samples ($< 0.5\,\Omega \cdot \mathrm{cm}$) independent studies have measured below room temperature an increase in resistivity [266] and and absorption which approximately remained constant [263]. This trend continued for moderate resistivity values of a single p-type sample, at $100\,\Omega \cdot \mathrm{cm}$ where the absorption was consistent between calorimetric measurements of absorption at both RT and 6 K [262]. In this study, through an independent measurement, the free carrier concentration was observed to decrease. Given these results, it is clear that further measurements and potentially revisions to the theory are required.

Another interband absorption mechanism which can generate free carriers is the two-photon absorption (TPA) process with coefficient (β). The theoretical model of the absorption contributions will now be evaluated. For TPA to occur, it requires the close spatial-temporal proximity of two simultaneously absorbed photons. The probability of this scales linearly with intensity I_{pump} and carries into the TPA absorption (α_{TPA})

$$\alpha_{\mathrm{TPA}} = \beta \cdot I_{\mathrm{pump}}, \quad \text{where} \quad \mathrm{I}_{\mathrm{pump}} = \frac{\mathrm{P}_{\mathrm{pump}}}{\pi \mathrm{w}_{\mathrm{pump}}^2}. \tag{4.5}$$

The total energy removed from the pump beam per unit volume per unit time is obtained by multiplying α_{TPA} again by the intensity. This is then converted to the carrier generation rate (G) by dividing by the photon energy ($\hbar\omega$)

$$G = \beta \cdot \frac{I_{\text{pump}}^2}{\hbar\omega}. \tag{4.6}$$

There could also be some linear contributions to the free carrier generation through the sub-band absorption. However, these are not considered here. Another study has considered these, but for the case where the linear absorption is expected to be dominated by sub-band defect effects [267].

As the generated free carriers (Δn_{e}) have a limited lifetime (τ_{carrier}) there is a recombination rate $R = \frac{\Delta n_{\text{e}}}{\tau_{\text{carrier}}}$. For measurement times (t) where ($t >> \tau_{\text{carrier}}$) the steady-state free carrier electron concentration can be approximated by equating the generation and recombination terms such that the electron carrier floor (n_{e_0}) is offset by

$$n_{\text{e}} = n_{\text{e}_0} + \Delta n_{\text{e}} \quad \text{where} \quad \Delta n_{\text{e}} = \beta \cdot \frac{I_{\text{pump}}^2}{\hbar\omega} \cdot \tau_{\text{carrier}}. \tag{4.7}$$

This TPA absorption is an approximation of the full effect. A full treatment should consider how the generated free carriers across at least a 2D space are diffused out and generated non-uniformly in line with the beam's intensity profile [267]. Another variable to consider is that the carrier lifetime will increase for high purity silicon.

Then, the additional absorption can be evaluated through equations 4.1 and 4.7. It is expected, given the low intensities, that TPA or the induced FCA will not be significant for future detectors [77] (see figure 4.1 (C)). However, absorption measurements made previously at Glasgow [10, 268] and in section 6.8 have shown that the TPA need to be decoupled from low ppm-level absorption measurements when small laser beams and moderate intensities ($>1\,\text{MW}/m^{-2}$) are used. The relevant beam parameters for each absorption setup used to measure silicon and the levels of expected two-photon induced FCA are shown on figure 4.1.

4.3 Different growth techniques for monocrystalline silicon

The production process for monocrystalline silicon starts with the feedstock of silica (SiO_2) rich sands, which is converted to polycrystalline silicon through a high temperature reduction process. At this point it still contains a large amount, at around 2%, of impurities of metals and dopings which will be generally classified from here on as foreign atoms (FAs). The silicon is then converted to an electronic-grade through a separate reaction process. Here, it is combined with hydrogen chloride at elevated temperatures to form an intermediate silicon molecule, which is then processed through a series of fractional distillation and decomposition processes to recover polycrystalline silicon with drastically reduced FA concentrations, down to the parts-per-billion (ppb) level [269]. The metallic and boron FAs, for example, are largely removed here as halide by-products [270]. To get monocrystalline silicon, the most common next step, with a 95 % market share [271], is the Czochralski (CZ) crystal pulling method. The key features of this process, are shown to the left of figure 4.2. The polycrystalline silicon is placed as a feedstock in a large silica crucible and brought just above its melting point of 1420 °C with graphite heaters. A seed crystal, with a set crystal axis, is then lowered to touch the top of the melt and slowly pulled out with silicon feedstock solidifying beneath as a continuation of the seed crystal. The extracted silicon's tapered cylinder is referred from here on as the boule. Beyond the FAs from the initial feedstock, additional FAs can be introduced during this process: such as large amounts of oxygen from the silica, carbon from the graphite and metals from contamination in the crucible.

One notable advancement to this technique is the Magnetic-field-induced Czochralski (MCZ) method. Electromagnetic coils are added around the crucible to allow different orientations of magnetic fields [271] (see figure 4.2 (A)) to interact, through the Lorentz force, with the silicon: enabled by the metallic like conductivity in its molten state [272]. This can crucially mitigate melt convections which would otherwise distribute oxygen amongst other impurities, for example, arising from the crucible and across the diameter of the boule [270, 272].

The rest of the silicon growth market is largely made up by the Float Zone (FZ) method. As shown on in the middle of figure 4.2 (B) the seed is fused to the bottom of the supported feedstock. The radio-frequency induction heater is then moved up alongside the molten zone to propagate a continuous crystal orientation from the seed to the top. The impurities are likewise pushed up through the melt to the top, where they can be

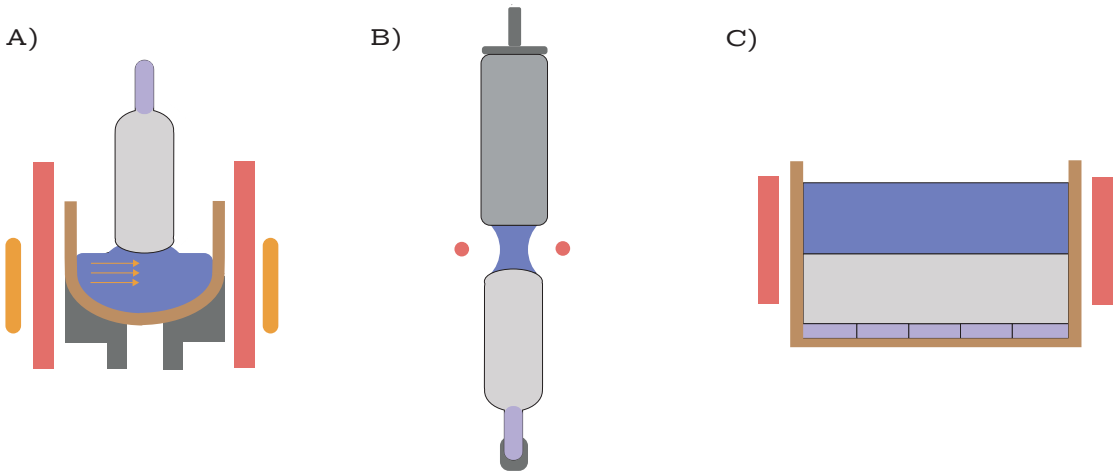

Figure 4.2: Plots (A-C) show 2D cross-sections of the key features found in three distinct mono-crystalline silicon growth techniques. Each of these converts either solid silicon feedstock (dark grey) or its molten form (blue) ideally to mono-crystalline silicon material with higher purity (light grey) that aligns to the crystal axis of the initial growth seed/s (light purple).
A) The CZ method notably has a contact crucible (brown) and heaters (red). With the addition of electrostatic coils (orange) around the crucible the method becomes MCZ. An example of the induced magnetic field lines in the horizontal plane is shown by the (orange) arrows.
B) The FZ method moves the melting zone through the solid feedstock.
C) The DS technique with its multiple seeds shown at the bottom of the crucible.

largely cut off [271]. The ability to repeat this process, particularly without the need for a contact crucible, allows it to achieve the highest purity levels with resistivities reported at $\approx 100\,\mathrm{k}\ \cdot \mathrm{cm}$ [273]. However, the size is physically limited to a diameter of 20 cm due to the effects of surface tension during growth.

A third technique which can produce large and potentially pure silicon is the directional solidification (DS) technique shown to the right of figure 4.2. The placement of seeds at the bottom of a crucible which is subsequently filled with feedstock allows, with careful control of the heaters, the crystal to be re-solidified from the seed upwards [274]. The technique's potential and limitation centres on its use of multiple seeds, for which it is commonly referred to as quasi-monocrystalline. The multiple seeds allow for larger growth volumes, close to that required for silicon test masses. However, the multiple seeds can also lead to distributed bulk defects, multi-crystallization sites and high FA levels through contamination. The absorption of silicon and its limitations will be considered alongside measurements made in chapter 5 for DS and chapter 6 for MCZ.

4.4 Role of foreign atoms in optical absorption

Foreign atoms (FAs) are those others than the intrinsic silicon atoms. Within this classification there are two categories which will be distinguished here. Dopants will be in reference to atoms which typically have either one more or less electron valance than the intrinsic silicon atoms. When incorporated, they substitute a silicon atom and are readily ionised by the thermal energy, as shallow donors, at RT to create free carriers. These free carriers absorb as described in section 4.2. These are typically introduced intentionally to achieve the desired resistivity. However, for gravitational wave detectors, undoped and high resistivity silicon will be required. The comparative concentration of dopant atoms in order of the silicon increasing resistivity and application will now be distinguished. Silicon with dopant concentration of 1 ppma is commonly used for photovoltaics and < 10 ppta for semiconductors [275]. For gravitational wave detectors, the target < 10 ppta (through equation 4.3) equates to a resistivity of $> 10\,\mathrm{k\Omega \cdot cm}$ and a baseline FCA absorption (through equation 4.2) of $< 1\,\mathrm{ppm\,cm^{-1}}$. This target is within the requirements for the silicon substrates of all future test masses (see table 1.1). However, as discussed after the measurements of quasi-monolithic silicon (see section 5.5), a higher absorption and therefore lower resistivity may be suitable for some of the silicon mirror substrates.

Contaminants (or impurities), on the other hand, are those generally speaking unintentionally introduced FAs that originate from either the feedstock or the growth medium. The incorporation of particular impurities is determined by their segregation coefficient as the ratio of the impurities in the solid compared to the liquid state [276], which further depends on atomic solubility and size. This process is explained in detail by Yang [272]. For simplicity here, the segregation value of CZ silicon will determine the impurity concentration in its magnitude and variation with depth along the axis of growth. Oxygen impurities alongside carbon, boron, and phosphorus have high segregation values when the boule is close to melting point and so will be incorporated in high concentrations. Aside from the known dopants, the directly incorporated oxygen and carbon contaminants are not shallow donors and so will not create free carriers at RT.

In the case of oxygen, it is incorporated interstitially between silicon's lattice structure. Oxygen in this state, can have a high diffusion rate and, as a result, a high probability of bonding with other oxygen atoms to form complex oxygen clusters. These clusters act as shallow donors in a similar sense to the substitutional dopants. Their concentration will therefore carry into that of the free carriers as a result. As the generation rate of

these oxygen clusters is strongly dependent on temperature (see figure 5.6 (B)) they are catagorised as thermal donors. The effect of these will be investigated in detail in section 5.3. For other growth methods, beyond CZ, the efforts to reduce these through reduction to the interstitial oxygen concentration will be considered.

In CZ, FAs with lower segregation values will be incorporated considerably less, albeit more so towards the end of the pulled boule [272]. The incorporation of dopants and large amounts of oxygen is likely the reason industry CZ does not exceed a resistivity of $50\,\Omega{\cdot}\mathrm{cm}$ [257]. From equation 4.4 this resistivity equates to an optical absorption of approximately 900 ppm/cm. This resistivity and absorption level is comparable to the ($65\,\Omega \cdot \mathrm{cm}$) and (6600 ppm/cm evaluated in section 5.3 for CZ silicon due to thermal donors. This was evaluated using the lowest known interstitial oxygen concentration 20 ppma subject to a 100 °C/hr (rise and fall) heat treatment (see table 5.1). It is expected therefore that the lowest resistivity and therefore absorption is set in CZ by these free carriers from thermalised oxygen donors. For each type of silicon introduced here the size, typical FA concentrations (main doping, O, C), resistivity and projected absorption level are shown in table 4.1.

The table includes FA concentrations in units relative to the silicon atoms ($[x]_\mathrm{a}$) in units of parts per million atoms [*ppma*], as opposed to absolute concentration ($[x]_\mathrm{c}$) in units of [$atoms \cdot cm^{-3}$], with the conversion [282]

$$[x]_\mathrm{a} \approx \frac{[x]_\mathrm{c}}{5 \times 10^{16}} \quad [\mathrm{ppma}]. \tag{4.8}$$

The units of this can easily be converted to, for example, parts per trillion atoms [*ppta*] with the correct order of magnitude scaling.

For MCZ, notably in the case where the field is aligned in the horizontal axis shown on figure 4.2, the flow of oxygen from the crucible and resulting incorporation is considerably reduced [283]. Only oxygen impurities are expected to vary, as a function of diameter [284]. This correlated with previously measured variations in the optical absorption [284, 285]. Low absorption of approximately 3 ppm /cm has already been demonstrated by A. Markosyan & A. Bell [285]. However, significant radial and longitudinal variations in absorption have been shown throughout the boule. At different ends of a boule this periodically oscillated, as a function of radius, up to and back from $3-15$ ppm /cm. At the

Table 4.1: Overview of the current monocrystalline silicon substrate materials and their measured absorption limits. Due to limitations in available data, the columns and individual O, C, N concentrations are generally taken from independent sources. The overall combination is therefore an idealized target.

Silicon Type	Max Diameter [cm]	α_{1550} [ppm/cm]
Czochralski (CZ)	45 [277]	-
Magnetic Czochralski (MCZ)	30	20
Advanced Magnetic Czochralski (a-MCZ)	20 [278]	20
Float Zone (FZ)	20 [279]	3.4 [280]
Quasi Cast (G8 batch)	40 [276]	$\leq 1 \times 10^5$
Sapphire	30 [281]	≤ 50 [281]
ET-LF ITM Target	45	1 to 5
ET-LF ETM Target	45	200

Silicon Type	O_i	C_s [ppma]	N_i	Factors Limiting Absorption
Czochralski (CZ)	20 [272]	200	200	contaminants & doping
Magnetic Czochralski (MCZ)	5	-	-	oxygen
Advanced Magnetic Czochralski (a-MCZ)	<5 [278]	0.5	0.5	not known
Float Zone (FZ)	0.2 [272]			purity of feedstock
Quasi Cast (G8 batch)	>2	6	0.1	contaminants & defects
ET-LF Target		not set		unknown

centre of this boule, this range increased to $25 - 625\,\mathrm{ppm/cm}$ [285]. Further reductions to the oxygen concentration through an advanced MCZ (a-MCZ) technique [278] might reduce the absorption due to thermalised oxygen donors. The distribution of oxygen as such is discussed further on in section 6.8.

FZ techniques generally have lower and more homogenous distributions of both contaminants and dopants. This is attributed to the absence of a contact crucible, gradual heating and specific techniques which can improve the doping uniformity [257]. The absorption of high resistivity FZ silicon has been previously measured at $1\,\mathrm{ppm\,cm^{-1}}$ [285]. This is comparable to the MCZ above.

As for boule size, 30 cm diameter CZ boules are standardized in industry and 45 cm has previously been explored [283, 286]. For CZ or MCZ, it is not clear that there will be continued industrial development of 45 cm and beyond, which would align with scheduled construction of future cryogenic GW detectors. In the case of FZ, 20 cm is the industry standard [287]. This is considerably less than the target test mass diameter for all proposed cryogenic detectors (see section 1.5) of 45 cm alongside the 80 cm proposed for the cryogenic CE2 detector. There is currently no discussions regarding scaling the diameter of FZ. As silicon boules grown with MCZ have shown regions of sufficiently low absorption and as the technique has previously been considered for upscaling to 45 cm this a promising growth technique for future detectors. In order to investigate the radial absorption variation of a new a-MCZ silicon, in this thesis, measurements were made (later on in section 6.8).

On the other hand, from the scale notably targeted for CE2 silicon (see table 1.1), DS silicon is the only one which has the current potential to meet the size requirements. Absorption measurements discussed in section 5.2 show that its value is higher than the target, but within what was expected from the doping level of the feedstock material. Beyond this, the promise of the technique is shown through the discussion on ways to further reduce the oxygen and carbon concentration. If this technique, for example, were to be repeated with high resistivity FZ or MCZ feedstock, then the absorption value should be considerably lower.

4.5 Transmission measurements of silicon

The absorption in the NIR wavelength ($1550 - 2000\,\mathrm{nm}$) range of high-resistivity silicon has previously been measured to $\approx 1\,\mathrm{ppm\,cm^{-1}}$. For the benefit of GW detectors operating in this wavelength range, it is important to focus on getting absorption values which are transferable. Relative absorption techniques, can reach the required absorption sensitivities, as discussed later in section 6.2. This section contains measurements made on low-resistivity silicon using an absolute transmission setup. Whilst this technique is not capable of measuring the target low absorption levels it can, in part, provide the scaling factor required for the relative absorption techniques.

To arrive at the correct technique it is important to consider the transmission regime of the sample, as it is distinct from the coating layers discussed in section 2.2. All silicon samples measured throughout this thesis (shown later in table 6.2) have thicknesses (d) greater than 1 cm and so are considerably thicker relative to both the NIR wavelengths and coatings, as previously discussed. As a result, for the small angles greater than 10 degrees, used here, the multiple internal beam reflections did not spatially overlap within the diamter of the beams and interfere.

In this incoherent case, the total light reflected is that from the front surface combined with the infinite sum of the contributions from the back. The initial front surface reflection factor for p-polarised light, relevant for all the light sources used throughout this thesis, for the refractive boundary between air (n_a) and substrate (n_b) is

$$R_\mathrm{ab} = \frac{\hat{n_\mathrm{b}}^2 \cos\theta_0 - \left[\hat{n_\mathrm{b}}^2 - \sin^2\theta_0\right]^{1/2}}{\hat{n_\mathrm{b}}^2 \cos\theta_0 + \left[\hat{n_\mathrm{b}}^2 - \sin^2\theta_0\right]^{1/2}}. \tag{4.9}$$

To evaluate the contribution of any subsequent light rays the reductions in power due to transmission must be considered. The power of each beam that exits on the reflected side will be reduced by the transmission factor of the light entering and exiting the substrate $(1 - R_\mathrm{ab})^2$. The number of reflections experienced by each beam prior to it exiting the sample will now be considered. In the case $n = 1$, the exit beam has only internally reflected once. This increases to three reflections for $n = 2$ and so for the n^th internal beam this $\approx R_\mathrm{ab}^{2n-1}$. The substrate absorption factor due to the exit beam having traversed a total distance of $2n \times d_\mathrm{app}$ is $(e^{-2n\alpha \cdot d_\mathrm{app}})$. Combining all these terms together gives the total fractional power of the light which exists for the n^th internal beam

$$R_n = (1 - R_\mathrm{ab})^2 R_\mathrm{ab} e^{-2\alpha \cdot d_\mathrm{app}} [R_\mathrm{ab}^2 e^{-2\alpha \cdot d_\mathrm{app}}]^{(n-1)}. \tag{4.10}$$

To evaluate the total power for the internally reflected beams, an infinite sum of R_n can be made, starting from $n = 1$. From the substitution $1/(1 - Z) = 1 + z + z^2$ as shown by Tanner [288] the total reflection (R), accounting for the initial R_ab, converges to

$$R = R_{\mathrm{ab}} + \frac{R_{\mathrm{ab}}\left(1 - R_{\mathrm{ab}}\right)^2 \cdot e^{-2\alpha \cdot d_{\mathrm{app}}}}{1 - R_{\mathrm{ab}}^2 \cdot e^{-2\alpha \cdot d_{\mathrm{app}}}}, \tag{4.11}$$

$$T = \frac{\left(1 - R_{\mathrm{ab}}\right)^2 \cdot e^{-2\alpha \cdot d_{\mathrm{app}}}}{1 - R_{\mathrm{ab}}^2 \cdot e^{-2\alpha \cdot d_{\mathrm{app}}}}. \tag{4.12}$$

The total transmission (T) could likewise be derived by expressing the n^{th} transmitted beam in a similar form to equation 4.10. The apparent thickness (d_{app}) used throughout these equations is the change in optical path due to the refracted angle (θ_1) that the beam takes through the sample

$$d_{\mathrm{app}} = \frac{d}{\cos\theta_1} \tag{4.13}$$

$$\theta_1 = \arcsin\frac{n_{\mathrm{a}}}{\sin\theta_0 n_{\mathrm{b}}}. \tag{4.14}$$

A simple approach to evaluating the absorption in this incoherent regime is to tilt the sample, in the plane parallel to both the beam and the optical bench, towards the Brewster angle. Evaluating equation 4.9 at this angle gives the minimum reflectivity, which coincides with the maximum transmission. Taking power measurements relative to the input, around these extrema and fitting (equation 4.11 or 4.12) the absorption can be determined. This method, was previously reported for a range of millimetre thick materials to be accurate down to $2.3\%\,\mathrm{cm}^{-1}$ [289] when fitting instead to the reflected data. The limiting factors were noted as being the surface parallelism, surface imperfections and notably instrumental noise. Although the silicon samples measured here had low absorptions, the physical thickness, on the centimetre scale, allowed for a considerable portion of the light to be absorbed, and so instead the transmitted data was measured and fitted against equation 4.12 in this work.

The optical setup constructed to enable these measurements is shown in figure 4.3. Thorlabs S425C power meters [290] were chosen as their thermal sensing heads could tolerate the high power of up to 1 W used here during measurement. Their sensitivity was also independent of small $\pm 5^\circ$ offsets. Within this range, angular uncertainties could be expec-

ted: in the movement of the power meters between measurement positions that followed from changing input beam angles. The power meters also provided a large aperture, which ensured that the first few parallel beam passings representing effectively the total transmitted beam power was captured.

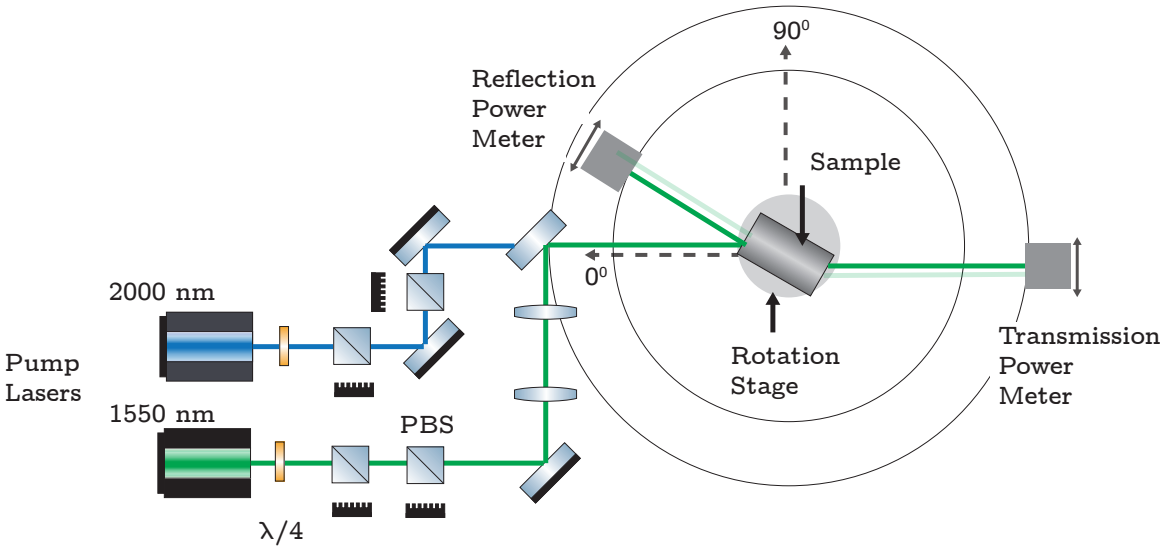

Figure 4.3: Layout of the transmission measurement setup.

The fractional power absorbed is determined by first measuring the transmission over a range of beam incidence: crucially up towards the Brewster angle, where the transmission value is distinctly non-linear with angle, as shown on the left of figure 4.4. The array of measured transmission (T) data is then fitted, carrying the associated power meter error of $\pm 3\%$, against the theoretical transmission given from equation 4.9 and 4.12. Python's scipy.optimize.curve_fit function [169] was used here to find the absorption value, which produced the best fit to the data.

The absorption samples measured here are called AB1 and AB2. The data and fitted models for each sample are shown in figure 4.4. For AB2, the fitted absorption value was $[7.0 \pm 0.4]\,\%/\text{cm}$ and for AB1 the value was $[4.6 \pm 0.8]\,\%/\text{cm}$. For AB1 the accuracy is limited, with a relative error of 18%, due to the limited number of points sampled. Sample AB2 will provide an absorption value from which measurements in the photothermal deflection setup (see section 6.3) can be relatively scaled. In this sense, AB2 is referred to as a calibration sample.

It is worth noting here that the samples measured here are in a high absorption regime, where the fractional absorbed power (A), scaled to d_{app}, deviated from being linear with the absorption coefficient (α) (see the right of figure 4.5) for different angles and thicknesses. This is because the total power absorbed starts to saturate. For this reason, a

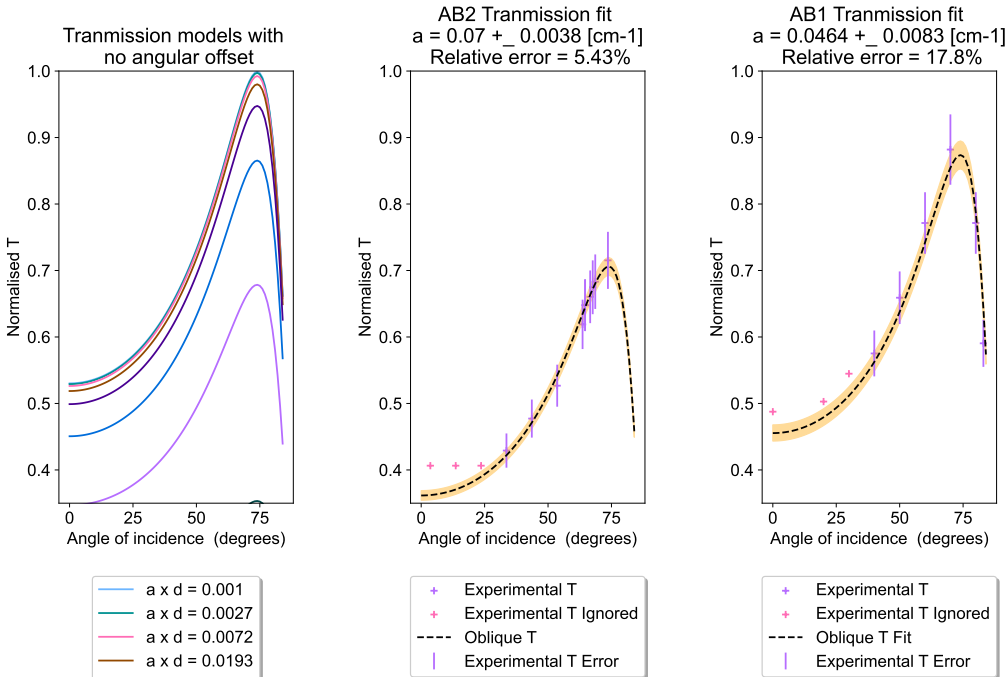

Figure 4.4: Fitted absorption for AB2 (Right) and AB1 (Middle) calibration samples compared to the thickness independent absorption depth plot (Left). Both the (Middle) and the (Right) plots show the extremes of the error on the absorption: propagated through as an orange error bar around the optimal transmission fit.

distinct approach from the fitting here of evaluating the absorption ($\alpha = \frac{A}{d_{\text{app}}} = \frac{1-R-T}{d_{\text{app}}}$) would underestimate the absorption coefficient. The technique shown here adjusts for these non-linearities and provides an accurate measurement of the optical absorption of thick optical substrates. Building on previous work [289], the measurement and fitting routine developed here provided accurate absorption measurement for thick (∼cm scale) silicon down to an extinction (evaluated through equation 2.2) of 8.6×10^{-9}. Beyond the measurements here, this technique is expected to be useful for measuring the average absorption (∼cm scale) of optical substrates in the extinction regime $10^{-10} - 10^{-7}$. The upper limit is set due to the absorption saturation described, and the lower limit is projected from the accuracy of a similar technique's limit, on thinner (∼mm scale) samples [289].

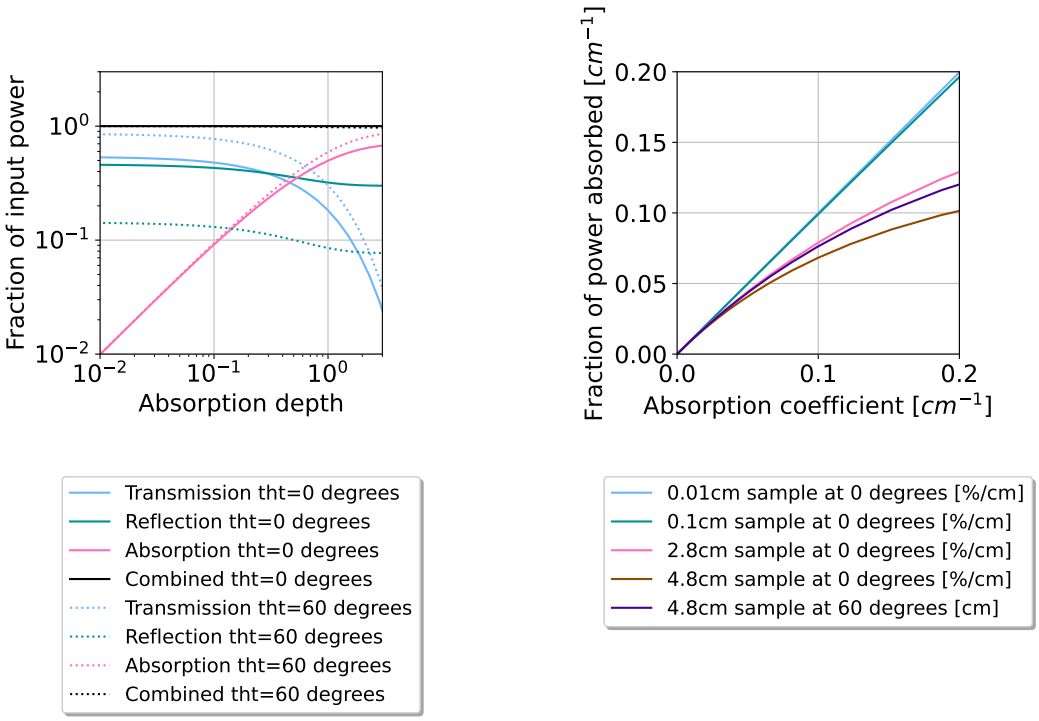

Figure 4.5: Saturation of absorbed powers for silicon in the high-absorption regime. Independent of sample thickness, the recovered absorbed power starts to plateau as the absorption depth (αd_{app}) approaches 100%. At 10% there is ≈10% reduction in the absorbed power away from the linear relation at low depths. There is also a clear coupling with the input angle, as higher angles allow for a higher fraction of light to be transmitted and absorbed.

4.6 Conclusion

To first provide context for these absorption measurements, this chapter gave a comprehensive overview of the different absorption mechanisms that could arise in silicon: at the lower intensities of interest for gravitational wave detectors. In parallel, the growth methods were considered alongside the coupling of different foreign atoms into the material. This discussion highlights critical contaminants and absorbing factors and, as work continues in the field to drastically reduce the total head load on test masses, will serve as a guide to finding and improving the best silicon growth methods.

Chapter 5

Optical absorption of quasi-mono-crystalline silicon

5.1 Introduction

This chapter reports on a study investigating the possible use of quasi-monocrystalline silicon, grown by directional solidification (see section 4.3), as a GW detector mirror substrate. The major advantage of this material is that it is already available in the large sizes required to meet the dimension and mass requirements of future cryogenic GWDs (e.g. for ET-LF diameters of 40-50 cm are being considered, with a mass of up to 200 kg). This absorption study was part of a collaborative project with Leibniz-Institut für Kristallzüchtung (IKZ) Berlin and Hamburg University, in which the mechanical loss and optical absorption of quasi-monocrystalline silicon were studied alongside detailed measurements of the structure of the material and the impurities present in the samples. The author carried out optical absorption measurements as part of this study, and co-authored a paper presenting the results of the study [276].

5.2 PCI measurements of quasi-monocrystalline silicon

The quasi-monocrystalline silicon studied here was from an ingot initially grown to have a low-resistivity suitable for solar cell applications. The material was p-doped with boron and had a measured resistivity of $0.9\,\Omega\cdot\mathrm{cm}$, and so it was expected, through equation 4.4, to have a high absorption of $\approx 10\,\%/\mathrm{cm}$. The optical studies aimed to first check this and then to correlate any excess absorption with FAs or defects. In parallel, mechanical loss measurements were carried out to test whether this distinct growth method could yield suitably low loss material.

Several samples were cut out from parts of a $195\times19\times220\,\mathrm{mm}^3$ ingot. The sample used for optical absorption studies had dimensions $40\times12\times12\,\mathrm{mm}^3$. Another sample cut from the same ingot and in proximity was further processed into a thin disc that was 50 mm in diameter by 5 mm thick. The geometry of the disc was beneficial for the mechanical loss measurements that followed for the sample. The location of this sample is shown alongside the absorption sample in figure 5.1. The cuts were made such that two flat edge from each sample were aligned to the 100 crystalline axis.

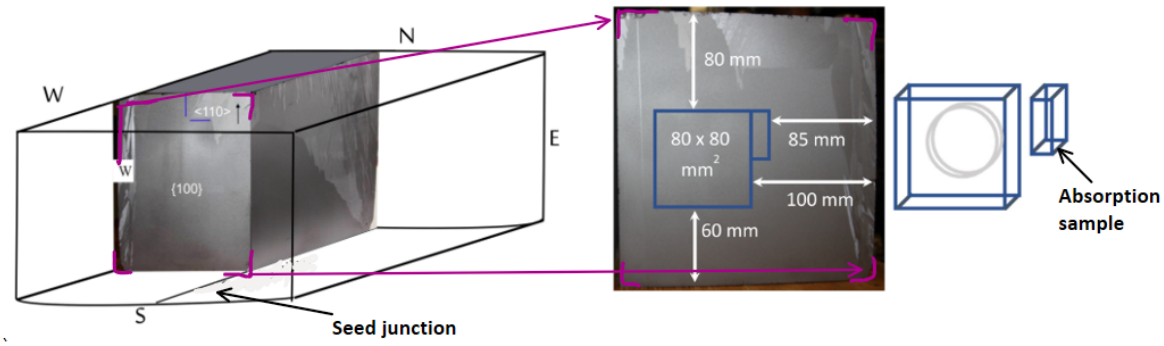

Figure 5.1: Photo of the 1/4 of the quasi-monolithic ingot on the left followed by the magnified photo on the right of the vertical cut along the 100 crystalline axis. The source position on this face for the cylindrical sample cut (5 mm thick and cut from a larger cuboid is shown. Next to this sample, the source of the absorption sample is shown. The different shades of grey, present on the larger ingot and away from the samples discussed, are regions where the silicon has a different crystalline axis.

As addressed in the paper [276], the mechanical loss of the substrate can in itself contribute to the mirror's Brownian thermal noise. The mechanical loss measurements from the paper are shown compared to those of float zone silicon in figure 5.2. The loss was shown to be similar across a number of vibrational modes. There are slight differences between the compared frequencies as although the float zone sample had the same dimensions, its crystalline axis was instead 111.

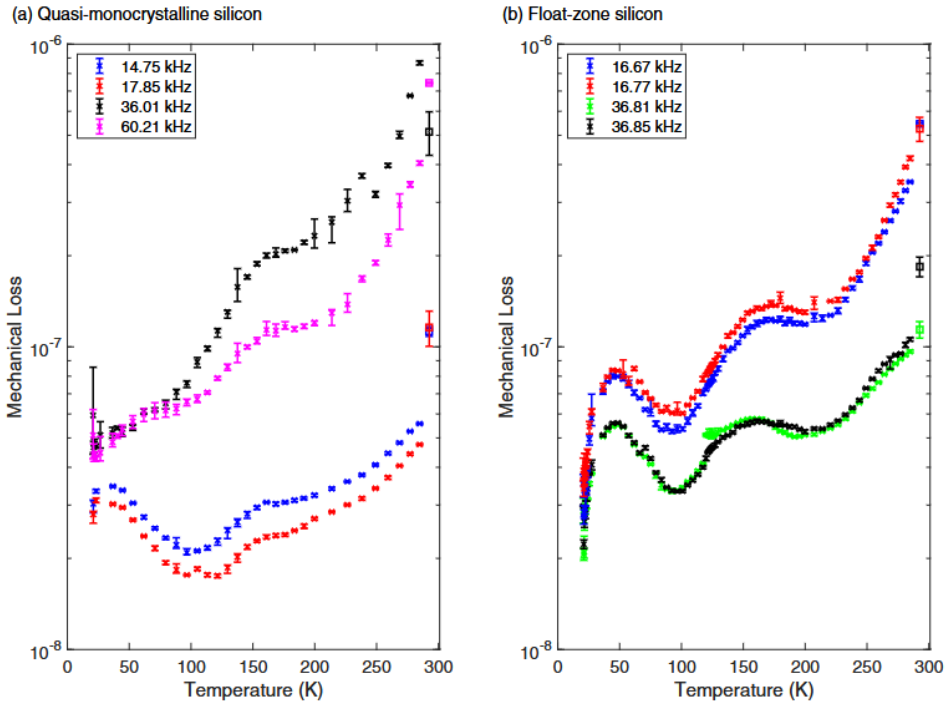

Figure 5.2: Mechanical loss as a function of temperature, from 4 to 300 K, of the 50.8-mm-diameter × 5-mm-thick QM disk (left) and FZ disk (right) samples. This figure is taken from [276].

The mechanical loss for every mode is below 10^{-6} at room temperature. Down towards the cryogenic temperatures of interest for gravitational wave detectors from 123 K and below, and all the mechanical losses measured were below 2×10^{-7}. At 123 K and 20 K of interest for Voyager and ET-LF the mechanical loss of the lowest measured quasi-mono mode was 1.8×10^{-8} and 2.6×10^{-8} respectively. These values were both within a factor of two of the minimum values measured for the float zone sample. This is a promising result suggesting that the quasi-monocrystalline growth process produces silicon comparable, in thermal noise terms, to the best, highest purity single-crystalline silicon available.

The expected absorption was first evaluated using the resistivity value of $0.9\,\Omega \cdot \mathrm{cm}$ provided by the vendor. Using the same conversion detailed in section 6.8.2 for the Okmetic silicon this was calculated to give a absorption of $15\,\%\mathrm{cm}^{-1}$. An average absorption was then measured at 1550 nm with the transmission setup described in section to be, $[23 \pm 1]\,\%\mathrm{cm}^{-1}$. This discrepancy will be discussed later in this chapter.

This measurement was fitted across a range of input beam angles from 5 to 40 degrees. Across this range, the input pump power was kept at 740 mW and the transmission increased slightly up from 150 mW to 180 mW. The small 12 mm thickness of the sample limited the input angle, as clipping effects appeared above input angles of 50 degrees. This was expected as for the length of the sample the lateral distance traversed in passing through the sample for this angle would have equalled $\approx 75\,\%$ of this thickness of the sample. The beam size was also the same as set for the deflection setup at 560 µm (described later in section 6.3) and so only linear absorption contributions, as expected, were observed at higher powers.

The spatial profile of the absorption at 1550 nm was then measured using the PCI technique (described in section 2.3), with a 1310 nm probe laser. This method was suitable as the silicon was known to be very highly absorbing, and an operational pump power of 600 mW was expected to be low enough to measure in a regime where no non-linear optical effects were observed. The setup also provided fine translation over the 2D plane of the sample surface. This allowed for independent scans to be made through different points of the sample's surface and bulk as a result. In total, five scans were made. These are all shown in figure 5.4.

In order to measure the PCI signal for bulk silicon, the setup was first aligned with a surface calibration sample (see section 2.3) and then calibrated with a bulk calibration sample. This sample was bulk SCHOTT glass #12 [291]. The associated R-value was measured at the centre of the substrate to be 0.286 for an absorption value of 10.5 %/cm. The silicon sample was then measured likewise. To correct the measured absorption, a scalar correction was made in two stages. The first scalar correction was due to the differing thermo-optic optical properties of used SCHOTT glass calibration relative to silica. The company Stanford Photothermal Solutions specified this as 0.74 based on proprietary measurements. The second part was evaluated through the relative theoretical bulk dispersion due to the different thermo-optic properties of silicon relative to silica. Compared to surface dispersion, bulk, takes a slightly different form with the denominator of the fraction in equation 2.6 taken as the square root. [163]. The dispersion signals (see figure 5.3 (a)) are evaluated at room temperature, using the conductivity of crystalline silicon is 138 W/(m.k) and amorphous silica is taken as 1.44 W/(m.k) [292]. The refractive index gradient for crystalline silicon is also different at $18\times10^{-5}\,K^{-1}$ compared to $1\times10^{-5}\,K^{-1}$.

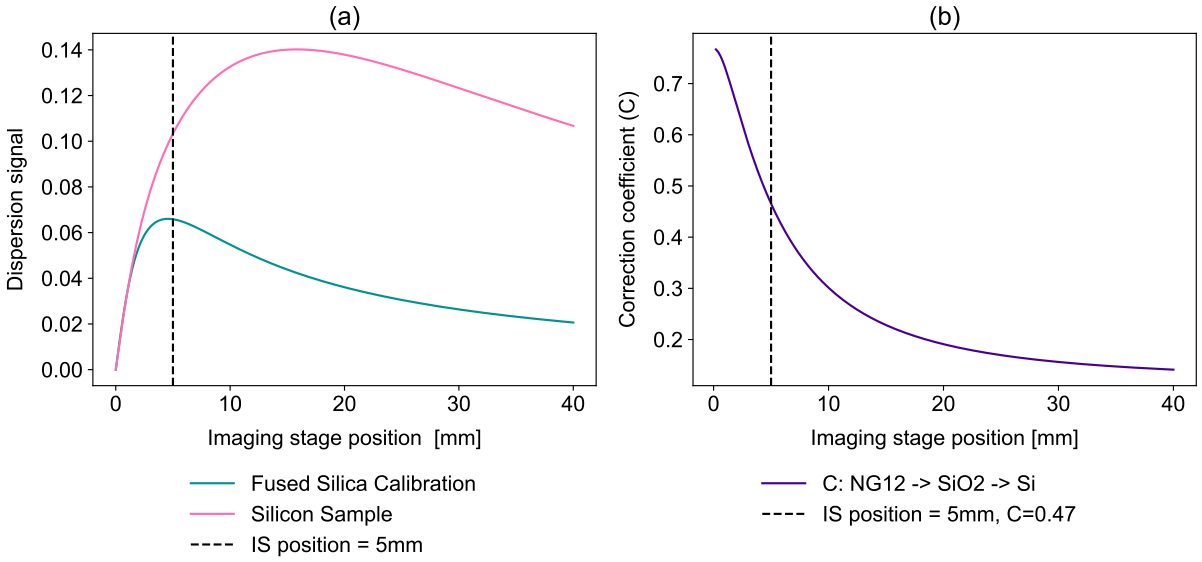

Figure 5.3: Theoretical correction coefficient (C) for scaling absorption signals from the surface calibration sample through to bulk silicon in the PCI across a range of imaging stage positions. This coefficient is the product of two parts. The first part in scaling from surface to bulk absorption contributes a factor of 0.73. The second part is given by taking the ratio of the bulk silica to silicon dispersion. For a range of imaging stage positions the total product is shown on the right. At the imaging stage of 5 mm, $C = 0.47$.

At an imaging stage position of 5 mm (see figure 5.3 (a)) which corresponds to the maximum position previously chosen for the surface calibration sample, the dispersion scaling from measuring a silicon sample relative to silica calibration is evaluated as 0.64. In order to get the total absorption correction factor, this correction is multiplied by the first scaling factor of 0.74 to give $C = 0.47$ at the chosen imaging stage position. It is possible that the correction factor could be increased as shown on the right of figure 5.3 up towards a maximum of 0.74 at lower imaging stage positions. However, as sensitivity was not a limit for this high-absorbing silicon sample the imaging stage effective position was not adjusted. The only adjustments that were made to the imaging stage were to mitigate the changes in optical path length through equation 2.9 when shifting to measure both the bulk calibration and silicon sample.

Three different 'line-scan' measurements were made along the length of the sample from different starting positions on the front face, producing parallel scans of the absorption throughout the sample. The absorption results are shown in figure 5.4(a). The vertical dashed lines mark the position of the front and back surfaces of the sample corresponding to measurement position 3 (where the surfaces were at slightly different locations for each of the three measurement positions).

All three line-scans through the sample show an absorption peak near the front surface of the sample (i.e. at a depth of around 10-15 mm in the figure), where the absorption appears to be approximately 15 %/cm on average. The absorption decreases to a relatively flat plateau throughout the rest of the sample. To confirm that the absorption peak near the front surface was a genuine feature of the sample, the sample was turned around and two more line scans were measured - shown in figure 5.4(b). These measurements now showed the absorption peak at the back of the sample, confirming that the peak was intrinsic to the sample and not an artifact of the measurement technique.

Non-linear optical absorption effects considered here arise in silicon both through two-photon absorption and its additional free carriers as described by equations 4.5 and 4.7. To test whether there was a significant non-linear component to the measured absorption signal, some measurements were repeated using two different 1550 nm pump laser powers of ≈300 mW and ≈840 mW, in addition to the ≈600 mW used for the majority of the measurements. The measured absorption did not change with the pump power, indicating that there was not a significant contribution to the absorption signal from non-linear effects. The non-linear absorption of silicon was investigated further on in section 6.8.3.

Figures 5.4(c) and (d) show the phase measurements at each point in the sample, corresponding to the absorption measurements in the plots above. The horizontal red line represents the expected phase for crystalline silicon in the PCI apparatus. Analysis of all the line-scans shows that the lower-absorption part of the sample, from a depth of $25 - 50$ mm in figure 5.4(a), has an average absorption of $[7.1 \pm 2.6]$ %/cm. The absorption averaged across the total length of all scans was 8.9 %/cm. Due to the limited number of scans and a large variance in the data here is some uncertainty in the true variance of the absorption in account of the whole samples volume. Further work, with similar samples, should consider 3D mapping and fitting of discrete absorption levels (shown for a different photothermal measurement setup and sample in figure 6.16).

The average value of 8.9 %/cm is ≈ 60 % less than the $[23 \pm 1]$ %cm^{-1} what was calculated from the direct transmission measurements. The discrepancy between these two optical measurements is possibly due to an under-sampling of the sample by the PCI as it had a considerably smaller sampling area by a factor of($\approx \times 250$). However, it is also possible that the silica to Schott glass empirical correction factor of 0.74 specified by Stanford photothermal solutions was based on measurements where the effective dispersions were different. This could follow from changes to the imaging stage position and beam sizes: of both the pump and probe.

It is, therefore, believed that the transmission setups average value of $[23 \pm 1]\,\%\mathrm{cm}^{-1}$ is more representative of this silicon sample. However, the PCI measurement's value is largely shown by its spatial characterisation of the absorption along the length of the samples. In between both these average values, the absorption value of $15\,\%\mathrm{cm}^{-1}$ expected from the resistivity, $0.9\,\Omega \cdot \mathrm{cm}$ was found. However, as the resistivity value was taken, by the vendor, from an unspecified location on the larger ingot it is not clear if it is representative exactly of the region from which the absorption sample was taken.

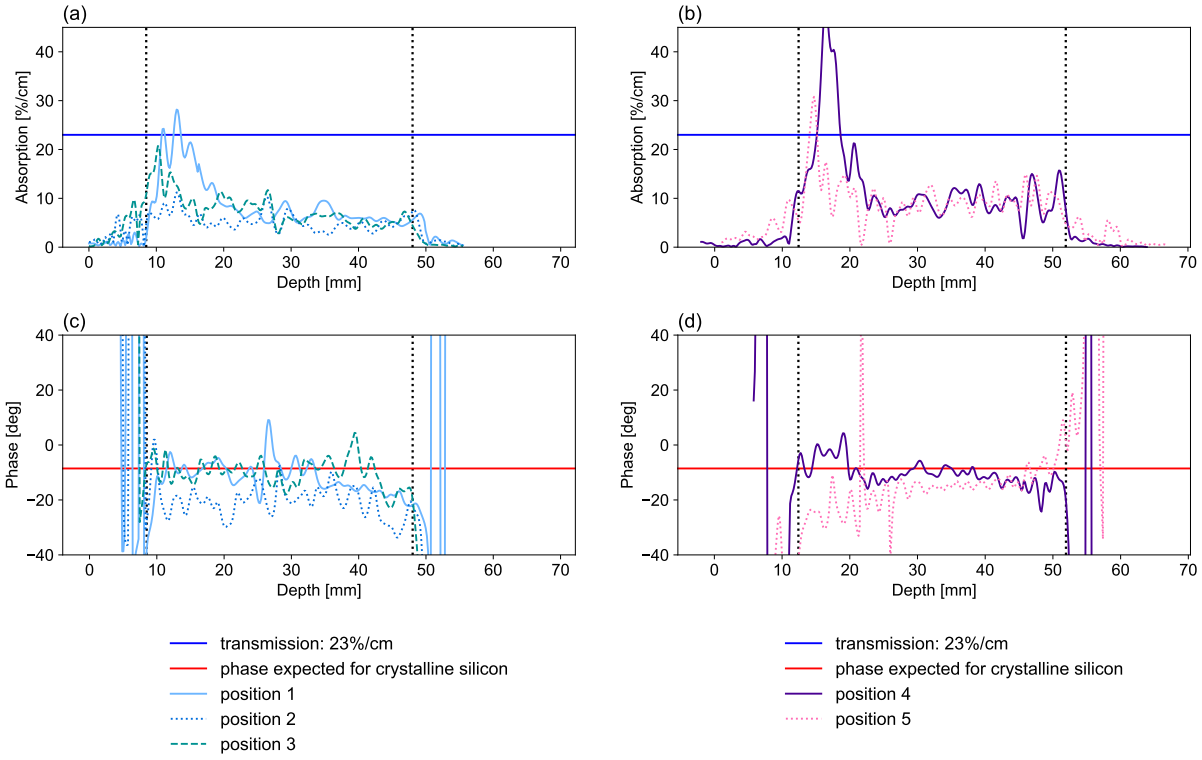

Figure 5.4: PCI measurements of the 40-mm-long small QM cuboid sample measured from different directions but shown independent of this (a) Optical absorption measured at three different positions indicated by the different colours and line styles. (b) Optical absorption scans at two positions when measured from the backside of the sample. Panels (c) and (d) show the corresponding phase signals of those measurements. Outside the sample, the signal is meaningless: while the absorption signal becomes approximately zero, the phase shows large oscillations. The frontside scans (a) start from the side which was located closer to the top of the ingot.

5.3 Evaluation of absorption due to thermal donors

To investigate the excess absorption at the front of the sample, the impurities were characterized by IKZ using a range of optical techniques, as fully described in the paper detailing all the results of this quasi-monocrystalline silicon study [276]. Interstitial oxygen can contribute to the optical absorption through an increase in free carrier contributions due to

thermal oxygen donors. The interstitial oxygen was measured for the quasi-mono silicon through a Fourier transform infrared spectroscopy (FTIR) process. This process identifies the oxygen concentration by first probing the strength of molecular absorption lines across a broadband IR spectrum. These measurements were performed with a Bruker IFS 66 V instrument under vacuum and the results are shown in figure 5.5.

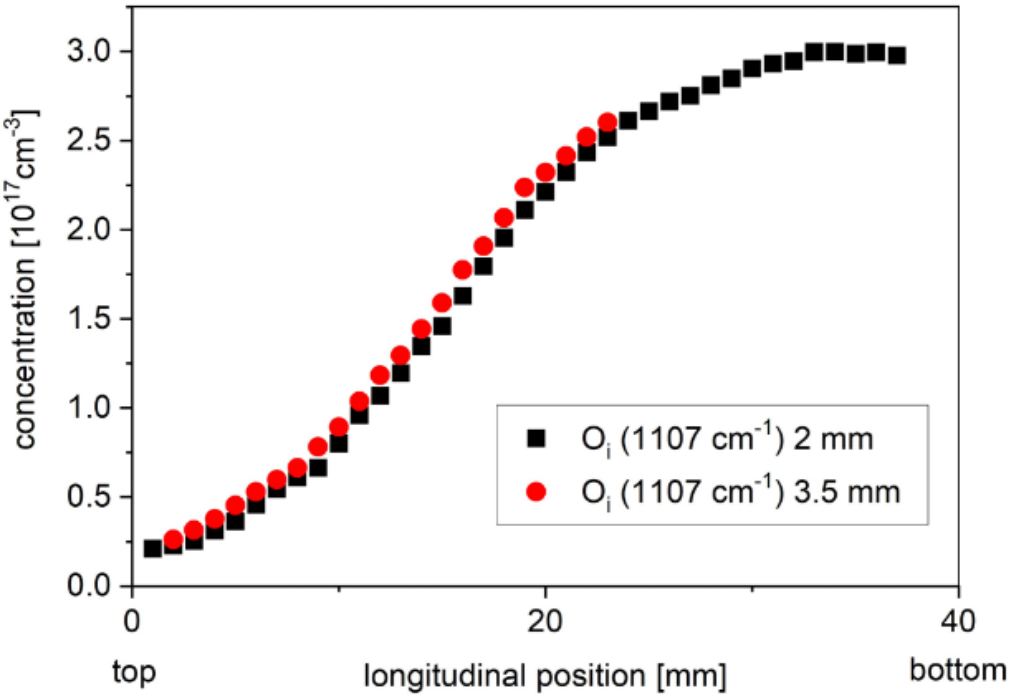

Figure 5.5: FTIR measurement of the interstitial oxygen along the length of the quasi-mono absorption sample. The measurement was repeated with two different apertures used in the FTIR setup. The results from aperture diameters of 2 mm are shown in black and 3.5 mm in red. This plot is taken from [276].

The concentration units discussed here will be converted from those shown in the plot into -ppma units through equation 4.8. Over the front 10 mm of the sample the oxygen concentration is 1 ppma. Towards the back of the sample, which faced towards the bottom of the growth chamber, the trend as shown increased towards 6 ppma. The scanning direction is the same as shown for the absorption plot on the left of figure 5.4. It is clear that both are trending in opposite directions.

Previous measurements have shown that for Czochralski silicon, the thermal donor rates generated (introduced in section 4.4) amongst depending on the temperature scales with the fourth power of the interstitial oxygen concentration [293]. Therefore, It was expected, after the quasi-mono silicon was heated to the melting point of silicon 1420 °C and cooled back down and uniformly so, over the scale of the sample, that a distinctly higher concentration of optically absorbing thermal donors would be found at the back of

the sample. This overlap was expected, as the diffusivity of interstitial oxygen in silicon within the range of donor formation temperature range was between $10^{-12}\,\mathrm{cm^2 s^{-1}}$ at 800 °C to $10^{-18}\,\mathrm{cm^2 s^{-1}}$ at 400 °C [294]. This equates to short diffusion lengths relative to sample size and over the expected time at temperature an expected optical absorption gradient due to thermal donors that would be opposite of what was observed.

A theoretical concentration of thermal donor concentration will now be evaluated for the top and bottom of the sample, starting from the interstitial oxygen concentrations of 1 ppma at the top and 6 ppma at the bottom. The evaluated thermal donor concentrations are shown alongside the expected increases in free carrier absorption in table 5.1. The data shown is evaluated through a process shown in figure 5.6 and detailed below.

The expected thermal donor generation rates (R) were first extrapolated from rates measured on CZ silicon by Londos *et al.* from post-growth heat treatments [293]. The only difference between the silicon, used was that the substitutional carbon concentration of the Quasi-mono was at least a factor of ten higher at 10 ppma, as measured in the FTIR. This higher level is expected to suppress R, and so it is possible that the values shown here are an overestimate. To extrapolate R to the lower interstitial oxygen concentrations measured here, from $10-30$ ppma, a power law of the form $R = 10^{a_0}\, n_i^{a_1}$ was fitted. The coefficients for each temperature are shown in table 5.1 and the plots on figure 5.6 (A). The R-value was then calculated for each interstitial oxygen concentration on the table, after it had been scaled from units of ppma to $\mathrm{cm^{-3}}$ using equation 4.8. These were best fitted (see figure 5.6 (B)) with a quadratic equation.

After this, in the absence of a known temperature profile, the silicon during its growth was assumed to uniformly progress through a steady temperature increase and decrease towards and away from the maximum temperature. These trends were used to construct a temperature profile with time and therefore, using the previous fit, $R(t)$'s as functions of time (t). It was these R functions that were further integrated to give total thermal donors generated using the Trapezium rule for integration [295] as implemented in python's `trapezoid` function from the scipy.integrate package [169]. The exact temperature gradients shown across both figure 5.6 (C) and table 5.1 are i). 200 °C/hr and ii) 100 °C/hr. Towards the front of the sample, the absorption (see figure 5.4) is notably higher and compared to the highest expected free carrier generation from oxygen acting in isolation it is ≈ 4 orders of magnitude higher. It is important to consider what other effects could augment the thermal donor generation rate and potentially explain the higher optical absorption measured towards the front.

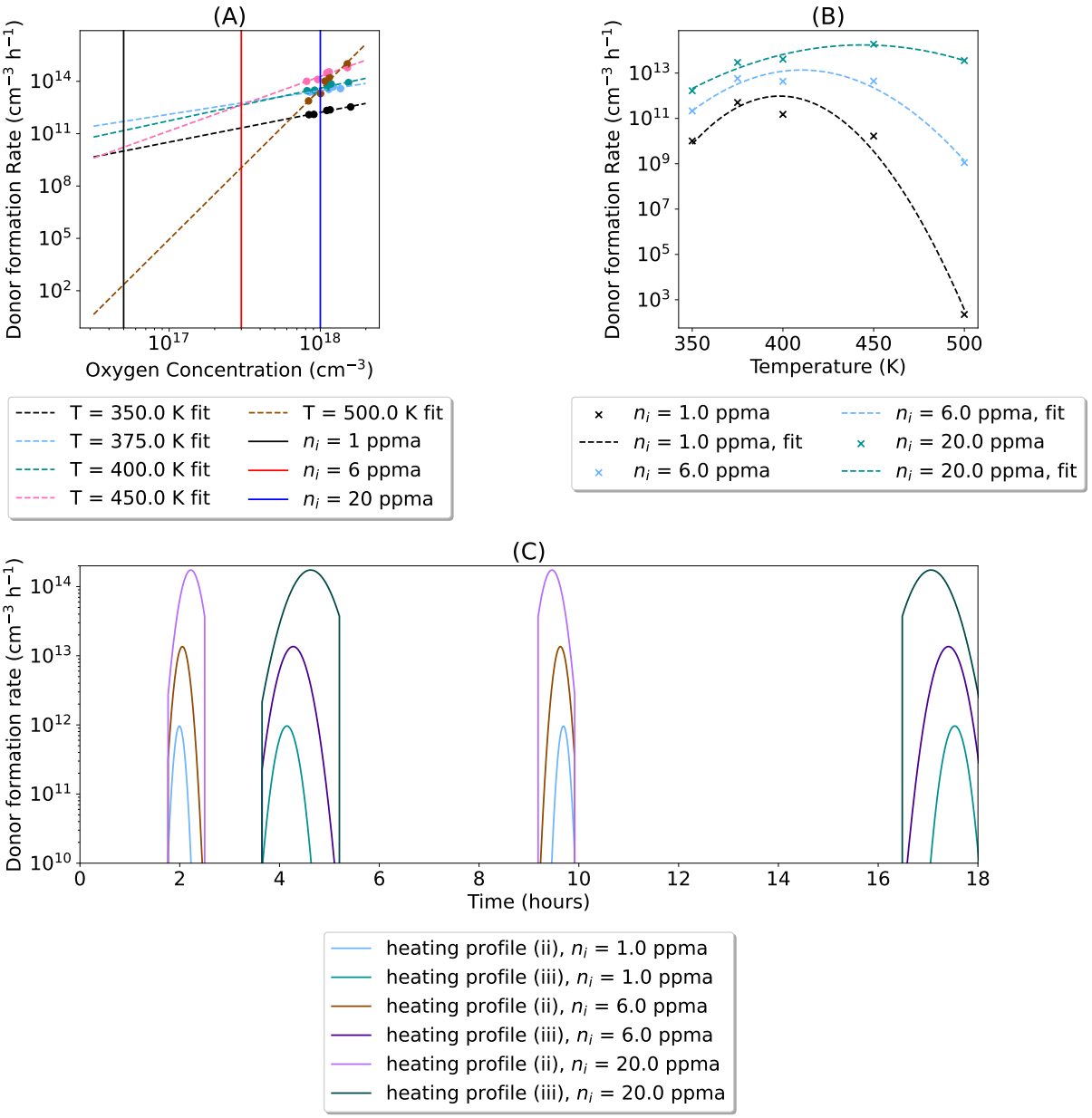

Figure 5.6: These plots show the theoretical evaluation for the thermal donors generated rate for the measured range of interstitial oxygen ($1-6$ ppma) and a high level for CZ (20 ppma). (A) The expected generation extrapolated from empirical data in the $10-30$ ppma range measured for CZ silicon [293]. For each of the five fixed temperatures, the evaluated generation rate is shown in table 5.1. For each concentration, the generation rate is then evaluated and shown in plot (B). As a function of temperature, these are fitted. Then plot (C) shows the thermal donor generation rate for each concentration due to the two temperature profiles starting at room temperature and ramping up to approximately 1000 °C at rates of i). 200 °C/hr and ii). 100 °C/hr.

Table 5.1: Excess absorption expected for different silicon growth temperatures and associated thermal donor generation rates.

Temperature [°C]	Power law fit coefficients (a_0, a_1) for $R = 10^{a_0}\, n_i^{a_1}$ [cm^{-3}/hr]
350	$a_0 = -18.4, \quad a_1 = 1.70$
375	$a_0 = -11.0, \quad a_1 = 1.36$
400	$a_0 = -20, \quad a_1 = 1.87$
450	$a_0 = -41.8, \quad a_1 = 3.12$
500	$a_0 = -141, \quad a_1 = 8.61$

n_i [ppma]	Polynomial fit coefficients (b_0, b_1, b_2) for $R = 10^{b_0+b_1T+b_2T^2}$ [cm^{-3}/hr]
1	$b_0 = -132, \quad b_1 = 0.72, \quad b_2 = -0.0009$
6	$b_0 = -70, \quad b_1 = 0.41, \quad b_2 = -0.0005$
20	$b_0 = -29, \quad b_1 = 0.19, \quad b_2 = -0.0002$

n_i [ppma]	Ramping rate [°C/hr]	Donors generated [cm^{-3}]	Excess FCA [ppm]
1	i). 200	3.7×10^{11}	0.9
1	ii). 100	7.8×10^{11}	1.9
6	i). 200	7.1×10^{12}	17
6	ii). 100	1.5×10^{13}	36
20	i). 200	1.3×10^{14}	320
20	ii). 100	2.8×10^{14}	660

5.4 Discussion of silicon carbide inclusions

The substitutional carbon was measured in the same FTIR setup and appeared to have a homogenous distribution of 10 ppma throughout the sample. In itself this was not expected to directly affect the absorption. However, this carbon concentration exceeded the solubility limit 9 ppma of molten silicon and was anticipated to be a source of particulate inclusions in the bulk material. In particular, SiC particles were expected to form.

To investigate if there were any SiC, the sample was placed under an optical microscope. In the front 10 mm of the sample that was positioned further away from the seed shown in figure 5.1, large inclusions which appeared to be $\approx 100\,\mu\mathrm{m}$ in diameter were found. The SiC inclusions were not expected to be a direct source of free carriers and therefore

additional absorption by themselves. However, through the creation of local defects around which oxygen would precipitate there could have been a drastic increase in the thermal donor generation rate. This could explain the higher optical absorption found in the front 10 mm of the sample.

The paper [276] goes into more detail on the SiC formation process. Although it is not clear why the SiC preferentially formed further away from the seed it is more important to consider the methods of mitigating SiC inclusions all together. The methods proposed for this include an improved mixing of the melt and a reduced carbon context which is expected to have the biggest impact. However, should the inclusions not so easily be mitigated, further joint absorption and FTIR may be required to better understand them. Alongside this, thermal annealing studies could provide a method to either mitigate or enhance the donor states and therefore better understand their origins.

5.5 Discussion of results

The optical absorption of the test sample of quasi-monocrystalline silicon was found to be much higher than the value of $\leq 5-10\,\text{ppm cm}^{-1}$ that is generally thought to be required for a gravitational wave detector test masses. However, it should be noted that in reality there are different requirements for the input test masses (ITMs), which are required to transmit light into the detector arm cavities, and the end test masses (ETMs), which are designed to be more highly reflective and to transmit very little light. A higher absorption material can therefore be tolerated in the ETMs (see table 4.1) than in the ITMs. The ITM reflectivity is approximately 99.5%, compared to the ETMs 99.9995%. This means there is approximately a factor of 200 less laser power within the ETM than there is in the ITM and so the absorption can be proportionally larger to keep the total absorbed power equal. If the absorption of the ITM is $< 5\,\text{ppm}$ based on the design report [125] then this gives an acceptable absorption range of $200-1000\,\text{ppm}$ for the ETM. The upper limit is approximately a factor of one hundred less than the absorption measured for quasi-mono silicon, which was measured here optically to be in the range of 9-23 % cm^{-1}.

It is interesting to note that the material was specifically boron doped to a low resistivity of 0.9Ωcm for intended application inside optically absorbing solar cells. As a result, it was not grown with a specific target of minimising impurities that could cause optical absorption around 1550 nm. The level of absorption matched the expectations from the doping level. It is expected, therefore, that the use of a higher purity silicon feedstock

would prevent the free carrier absorption due to doping concentration from being a limiting factor. The potential for excess absorption due to thermal donor generation was investigated to see if it could explain the discrepancy in absorption measured through the different methods. However, the value estimated based on FTIR measurements of the interstitial oxygen concentration was several orders of magnitude below the value expected. This evaluation should be considered for all future studies looking to correlate oxygen concentration with low optical absorption in the NIR.

Reduction of the impurity levels as measured directly and indirectly throughout this section would require a series of improvements to the growth process. First, to minimize their concentration, the material of the crucible could be changed from the oxygen-rich quartz to a high-purity fused silica. In particular, to reduce carbon and oxygen impurities the hot zone, positioned as the boundary between solid and liquid silicon (figure 4.2) could be redesigned. Also, as gas species containing carbon and oxygen are produced in the process, improvements must be made to evacuate these from the chamber. This could be achieved by improved flow of the inert Ar over the top of the melt [296].

5.6 Conclusion

Quasi-monocrystalline silicon, as shown in the paper [276], has a very low mechanical loss, comparable to the best float zone silicon and capable of meeting the thermal noise requirements of future gravitational wave detectors. In addition to this, the material is already available at a large enough scale (1151 mm wide by 390 mm tall) required for future detector mirrors as shown (between table 1.1 and section 1.5). As a result of this work, Quasi-monocrystalline silicon is of significant interest for future detectors.

The optical absorption of the material studied here was too high for use in a GW detector, as was expected from the doping concentration, but it seems likely that the use of pure feedstock and some development of the growth process may allow the absorption to be decreased to the point where this material could be used for an ETM mirror. Reducing the absorption enough to allow the material to be used for an ITM mirror is likely to be significantly more challenging. However, an intriguing possibility suggests itself from this work - the use of differently sized mirrors for the ETM and ITM [297]. This concept would

allow the benefits of higher mass and larger diameter to be gained from the ETMs, while using purer silicon, only available in smaller diameters, for the ITMs. While significant trade-offs and design optimisations would be required, this concept may be a useful way forward towards the realisation of silicon-based cryogenic gravitational wave detectors.

As future quasi-monolithic like silicon is developed, it is expected that in conjunction with the purity that the main problems facing its applicability, as described, will be minimising the areas in which it deviates from a single crystal through dislocation edges propagated in part from the seed junction. In a similar sense to the SiC inclusions found here, the dislocations could be sites for local increases in absorption. It is critical, therefore, that absorption measurements, as presented here, are carried out as part of future studies.

The work in this chapter investigated the NIR optical absorption of a new type of silicon called quasi-monolithic for the first time. A good agreement was found between the studies made with a photothermal measurement technique, transmission measurements, and resistivity calculations. Excess absorptions in the sample were investigated further, and correlations were found between the high excess absorbing region and the independently identified areas of SiC inclusions. The methods by which these could contribute to the absorption was discussed alongside the need for continued measurements as the silicon growth method develops, both in purity and scale, in the future.

Chapter 6

Photothermal measurements of the absorption of mono-crystalline silicon

6.1 Introduction

Reducing the absorption of silicon optics is critical to minimise the thermal distortion and heat load of future cryogenic gravitational wave detectors test-mass mirrors: if it is chosen as the bulk substrate material (sections 1.6 -1.7). In particular, as the large silicon optics summarised in table 4.1 are equivalent, if not larger, than currently available growth techniques, it is important to consider how the absorption might vary throughout. Over short resolutions, localised impurity clusters may be more distinguishable, whereas over long resolutions longitudinal, radial or tangential trends in the cylindrical boule may be observed. This chapter will cover optical measurements made to map the near infrared absorption of mono-crystalline silicon. To achieve the required spatial resolution a modified measurement technique distinct to laser transmission measurements (section 4.5) and calorimetry (as detailed later in chapter 7) was implemented. This technique can generally be classified under the category of photothermal deflection. The theory and utility of this particular technique will first be established (section 6.2) before the setup at Glasgow is introduced (section 6.3). After this, the details of work performed to improve the alignment and sensitivity will be shown along with measurements of silicon samples. After which, an investigation into the radial absorption of a new silicon is presented in section 6.8.

6.2 Theory of photothermal deflection applied to silicon optics

The target absorption sensitivity level for absorption measurement of high-resistivity silicon samples should aim for the ∼ppm/cm level of sensitivity. This is in line with the lowest measurements made of ≈ 1 ppm on FZ silicon and the target values for large scale silicon mirror substrates (see table 1.1). Although, this sensitivity level was not reached in the Glasgow setup (discussed later in section 6.4), the level was sufficient to spatially map a range of silicon samples and otherwise improve measurement and analysis capabilities. From the outset of this research, the PCI setup (discussed in chapters 2 and 3), was not ideal as its high laser intensities were expected to impede the measurement of low-absorbing silicon. Although the PCI pump beam size could in principle have been adjusted, the time to recalibrate between the different beam sizes was expected to take too long. Furthermore, this time spent would have gone against the need to run this study in parallel to the thin-film absorption studies (chapters 2 & 3). Without an otherwise routine recalibration, the large pump beam waists would have limited the spatial resolution and reduced the absorption sensitivity following equation 2.6. As a result of this, a new technique that was better suited to measuring the bulk absorption of silicon was implemented.

Photothermal deflection (PTD) is a measurement technique which makes use of thermal distortion effects: first introduced in this thesis as a challenge faced by GW detectors (see section 1.6). This technique can be used to measure the absorption and refractive index coefficient of most materials across the EM spectrum. The thermo-optic distortion, effectively a lens, arises from the temperature gradients induced by an absorbed laser. In PTD, it is these gradients that are measured. Power is absorbed from a high power 'pump' laser beam as it is transmitted through the sample. This scales linearly into the induced distortion. A secondary probe beam that is smaller in radius passes in close-proximity, and as a result of the index distortion is deflected from its optical axis. To make a relative measurement of intrinsic absorption in a similar sense to the PCI requires finding a regime of specific optical, geometrical and material properties whereby over many orders of magnitude a linear mapping from the absorption is distinct and measurable.

The particular type of PTD setup utilised here is best characterized as collinear. There are two distinct types of deflection that a beam can experience in moving through a thermo-refractive field. Parallel deflection is an offset that can occur when a beam moves through a symmetric thermo-refractive index field. On the other hand, angular deflection

arises from asymmetric field. Both of these deflections and additional sources of origin are considered by Dickmann *et al.*[298]. This setup will focus in particular on measuring angular deflections. Consider a uniformly absorbing thick-substrate. This would have a cylindrical-symmetric temperature gradient such that a finite probe offset in the y-axis, perpendicular to the crossing, would experience a uniform angular deflection. In order to help support the measurements made in the lab, a theoretical form of the angular deflection will now be derived.

To describe the collinear PTD, the temperature field will first be considered. The absorbing sample will be approximated as having have infinite radial extent and uniform starting temperature, such that on the timescale of heating the geometrical boundaries have no effect. A Gaussian pump beam is focused to a radius (r_{pump}) in the sample and pulsed as a square wave with an angular modulation frequency (w). On this timescale, set by the pulse frequency, if the diffusion length (λ_{T}) is such that, $\lambda_{\mathrm{T}} << r_{\mathrm{pump}}$ then the induced refractive index gradient profile will match the Gaussian extent of the beam. In section 6.3 the limitations of this assumption are discussed.

$$\lambda_{\mathrm{T}} = \sqrt{\frac{k}{\rho C \pi f}}. \tag{6.1}$$

The lens is then probed by a secondary Gaussian beam. This beam has a waist (r_{probe}) and separation (x_1) from the pump's peak intensity in the x-axis. As a result, the probe beam will experience an angular deflection (φ_β) [299, 300]:

$$\varphi_{\beta_{\lambda_T \ll r_0}} = \frac{-\beta \cdot \alpha \cdot P \cdot D}{\sqrt{2\pi} \cdot n \cdot \kappa \cdot \omega \cdot \sin(\theta_{\mathrm{cross}})} g(\mathrm{x}_1) \tag{6.2}$$

$$g(x_1) = i \left(-\frac{8x_1}{r_{\mathrm{pump}}^3} \right) \exp\left(\frac{-2{x_1}^2}{r_{\mathrm{pump}}^2} \right). \tag{6.3}$$

Aside from the absorption (α), the relevant material properties are refractive index coefficient (β), density (ρ_{p}) and specific heat capacity per unit mass (c_{p}). The last two scale the thermal conductivity (κ) to give the thermal coefficient ($D = \frac{\kappa}{\rho_{\mathrm{p}} \cdot c_{\mathrm{p}}}$) which is passed into equation 6.2. These input parameters also scale into equation 6.1.

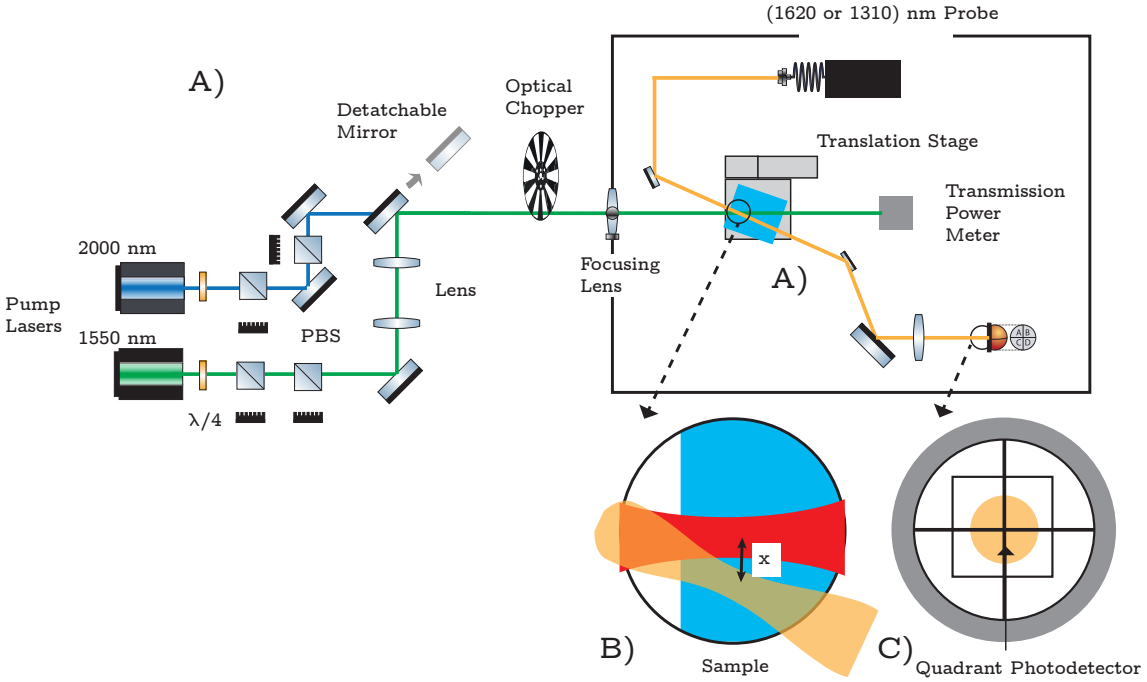

Figure 6.1: Layout of the Photothermal deflection setup that is operational at two CW pump wavelengths. (A) Shows the overall layout of the setup. Every component is described in the main text of this section. (B) Shows the crossing point of the pump and probe beam with a separation (x). The incoming angle of the probe here is approximated. (C) The target probe beam size relative to the sensitive quadrant photodiode area is shown.

For thermal timescales described above at room temperature, the ratio of these terms favourably produces a large thermo-optic distortion for silicon that is $\times 20$ larger compared to silica. The angle, as approximately shown in figure 6.1, gives a normalised interaction length ($\sin(\theta_{\text{cross}})$). This acts at desired small angles to reduce the depth resolution, but also increase the deflection signal. Aside from the interaction length, all these terms are contained within the combined geometric term ($g(x)$). This geometric term favours a pump waist which is comparable to the pump. The complex term indicates the 90 degree measured phase offset, as the maximum deflection signal occurs just as the pump beam is switched off.

This angular deflection will scale with the distance (d) along the path of the output beam to offset the centre, by ($\Delta x_2 = d \times \varphi_\beta$). In the case of semiconductors such as silicon, there can also be parallel deflection due to induced free carrier dispersion. This dispersion arises from refractive index changes due to the same induced free carriers that augment

the FCA as discussed in section 4.2. To prevent this from being an issue, across a range of powers, a lens of focal length (f) was placed before the detector such that the angular displacement was converted to a new detector offset ($\Delta x_2 \approx f \times \varphi_\beta$) and the effect of any parallel deflection and accumulated offset, up to the lens, was minimised.

To measure this distance, a quadrant photodiode (QPD) detector was used, as proposed in Jackson *et al.* [301]. This converted the incident beam into a static (V_{DC}) which was equivalent to the power and an alternating voltage (V_{AC}) which carries the deflection signal. For the calibration sample used here (with absorption of 7% cm^{-1}) the expected angular deflection was evaluated by passing the parameters (see table 6.1) into equation 6.2. The geometric term (equation 6.3 was maximised by sampling over a range of beam offsets (x_1). With all of this considered and the pump power set at 1 W a small and proportional deflection value of $\approx 1.2 \times 10^{-7}$ was expected based on the theory.

Table 6.1: These tables compare the measured absorption level to the theoretical values, which were evaluated using the stated setup parameters and c-Si properties.

Setup parameter	**Value**
Wavelength (λ)	1.55×10^{-6} m
Modulation Frequency (ω)	547 rad.s^{-1}
Pump Beam Waist (w_{pump})	550×10^{-6} m
Probe Beam Waist (w_{probe})	200×10^{-6} m
Focal Length of Lens (f_{lens})	0.15 m
Distance to QPD ($d_{\mathrm{cross->QPD}}$)	0.7 m
Input Crossing angle ($\theta_{\mathrm{input}_{\mathrm{min}}}$)	6 °
Input Crossing angle ($\theta_{\mathrm{input}_{\mathrm{max}}}$)	30 °
Internal Crossing angle (θ_{min})	1.7 °
Internal Crossing angle (θ_{max})	8.3 °

c-Si Property	**Value**
Refractive Index (n_{Si})	3.48
Thermal-Optic Coefficient (β_{Si})	1.94×10^{-4} K^{-1}
Thermal Diffusivity (D_{Si})	87×10^{-6} m^2.s^{-1}
Thermal Conductivity (κ_{Si})	1.25×10^{2} W.m^{-1}.K^{-1}

Calibration factors	**Value**
Theoretical (R_T)	$(1 - 4.2) \times 10^{-2}$
Measured (R)	$2{\times}10^{-2}$

Given the focal length of the QPD lens was ~ 0.15 m the deflected distance (17 nm) was considerably smaller than the refocussed gaussian waist (r_{measure}) of the probe beam. In this regime, the signal measured on the QPD could be approximated as [301]

$$\frac{V_{\mathrm{AC}}}{V_{\mathrm{DC}}} \approx \frac{4}{\sqrt{2\pi}} \frac{\Delta x_2}{\mathrm{r}_{\mathrm{measure}}}. \tag{6.4}$$

As the probe beam is refocussed by the lens, its size relative to the first focus point was given by

$$r_{\mathrm{measure}} = \frac{f \times r_{\mathrm{probe}} n}{d}. \tag{6.5}$$

By substituting equation 6.5 into 6.4 and accounting for the index of air ($n = 1$), the theoretical deflection measured by the QPD was

$$\frac{V_{\mathrm{AC}}}{V_{\mathrm{DC}}} \approx \frac{4 \times d \times \varphi_\beta}{\sqrt{2\pi} \times r_{\mathrm{probe}}}. \tag{6.6}$$

For the calibration sample, this evaluated to a signal of 6×10^{-4} . The expected signal will now be evaluated for a sample with the low absorption of 1 ppm cm^{-1}, that is considerably below the target of mirrors of future gravitational wave detectors (as low as 5 ppm for CE2Silicon). The pump power, available in the lab, was set at 5 W and the deflection angle was calculated to be $\approx 2 \times 10^{-11}$, the QPD offset was 3×10^{-12} m and the signal $\frac{V_{\mathrm{AC}}}{V_{\mathrm{DC}}} \approx 1 \times 10^{-7}$. In order to detect low signals of this range the QPD differential channel carrying the V_{AC} was passed as the input signal to a lock-in amplifier. Alongside this, the modulation signal, carrying both the signature phase and frequency, was passed as an input such that the SNR of the signal could be increased.

Through the combination of equations 6.2 and 6.6 it is clear that the power absorbed linearly scales through to give a theoretical measured signal. At high intensities (used in section 6.8.3) the measured absorption was not linear (see figure 6.14) and so equation 6.6 was converted into an empirical form. The linear absorption is substituted with a 2^{nd} order polynomial parameterised on the power of the pump beam to account for the two photon absorption (TPA) effects

$$\frac{V_{\mathrm{AC}}}{V_{\mathrm{DC}}} = \left(\alpha_0 + \alpha_1 P + \alpha_2 P^2\right) P \cdot R. \tag{6.7}$$

All of the other terms are grouped into the calibration factor (R). Prior to the measurement of a target sample, a measurement of a high absorbing calibration sample, at low powers, in the linear regime where α_0 is known allows, through rearrangement, the R-factor $[W^{-1}]$ to be determined. To validate the PTD setup (described in section 6.3) the R-factor was measured and compared to the value expected from equation 6.6. The theoretical value had to be normalised to both the power and absorption dependency (that linearly couple to the deflection signal through from equation 6.2). There is a good agreement (see table 6.1) with both values close to 2×10^{-2}. This agreement is only limited by the error in the theoretical value. This is due to uncertainty in the exact crossing angle used at the time of measurement.

Following this, measurements of target samples were made across a range of powers and the linear absorption isolated. This power fitting and isolation of the linear term is crucial for estimating the absorption values expected at the lower operational intensities to be found in future cryogenic silicon gravitational wave detectors.

6.3 Design of the photothermal deflection setup at Glasgow

The finalised configuration for the setup is shown both on the diagram shown in figure 6.1 and the labelled photograph in figure 6.2. The particular optical components chosen will now be described from the source lasers through to the measurement plane. A 1550 nm pump laser was from the CEFL - KILO range by Keopsys [302] was chosen as it matched the wavelength of the baseline ET-LF detector. Although, 2 µm was also of interest for gravitational wave detectors the representative laser was not used due to technical issues. The chosen 1550 nm laser was capable of emitting up to 10 W. To ensure a high pump power throughput the sample and minimise reflections, if operated at large incidence angles, the polarisation state was chosen to have a high-purity of type “p”. To get this polarisation, the random output of the source light was first linearized with a quarter-waveplate. After this, the purity of a polarisation state in the p-plane was maximised up to the sample through the use of multiple polarising beam splitters (PBS). By further propagating the transmitted light from the PBS’ the highest extinction of “s” type relative to “p” was ensured. After this, the polarisation was maintained up to the sample through the use of gold mirrors.

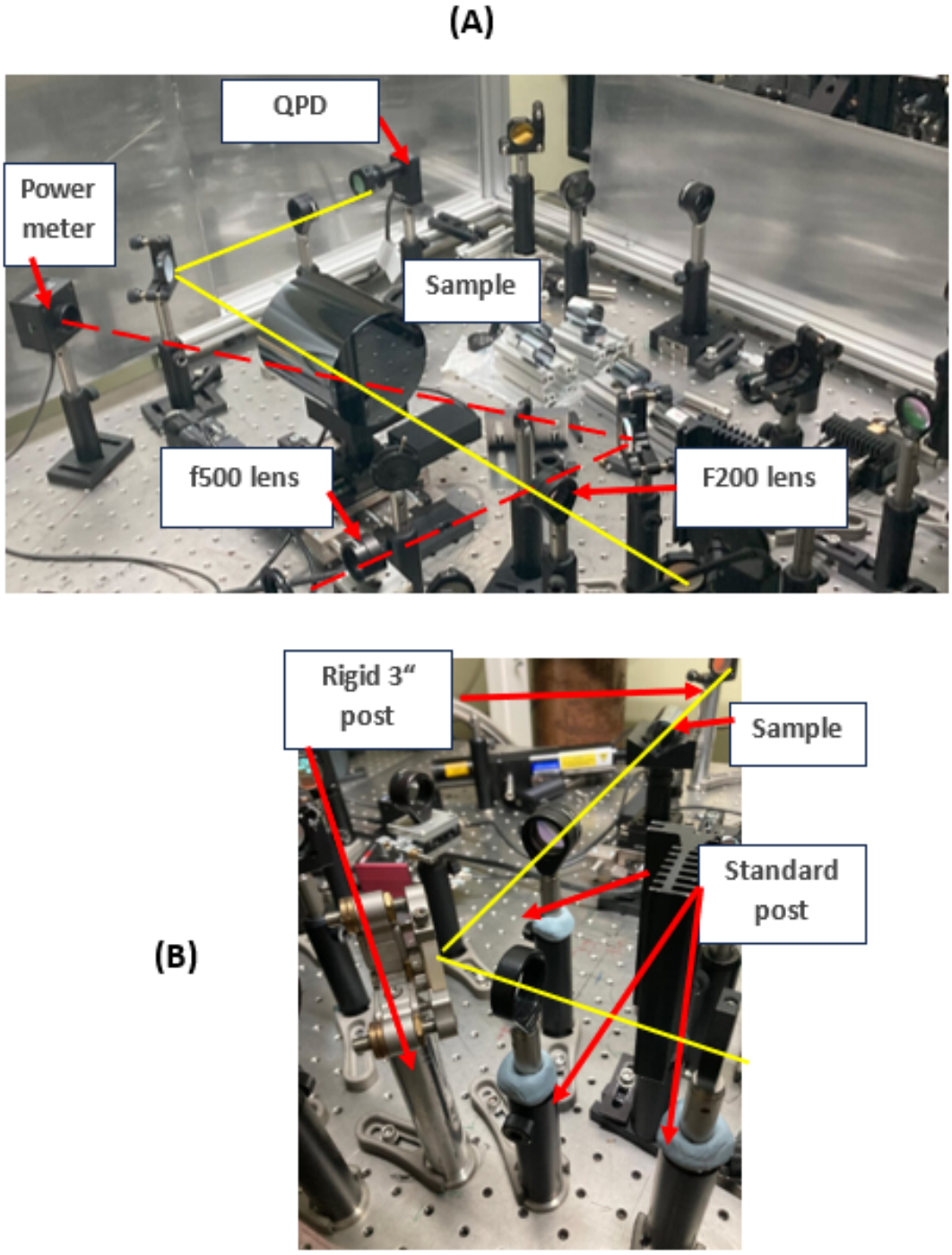

Figure 6.2: Photos of the Glasgow PTD setup. (A) shows the path of the two laser beams through the sample and up to their detection points. The probe which was closer to the sample normal (yellow line) and the pump was incident at a large angle (red line) (A) Shows the overall layout of the setup. (B) shows the rigid beam posts which were substituted in to reduce the vertical noise floor of the probe as measured on the QPD.

Instead of an internal pump-modulation from the laser source the work here made use of an optical chopper. Given the finite diameter of the pump (d), it was important to ensure that the rise and fall of the modulated signal was sharp. The crossing time can be scaled to the chopping period to give a normalised response time. This response corresponds to the pumps transmitted pump powers shift: away from the idealized step function.

$$\frac{t_{\text{cross}}}{T} = \frac{dn_{\text{blades}}}{2\pi r_{\text{chopper}}} \tag{6.8}$$

From the available commercial off the shelf chopper wheels, the MC1F10 was chosen from Thorlabs. For a Gaussian diameter of 1 mm the maximum inner radius of 8.5 mm and small number of blades (10), this equated to a normalised response time of 0.2. For 20%, compared to the duty cycle of 50% this means that the power transmission in account of the matched fall time was only truly maximised for $\approx 20\%$ of the on-cycle. This was evaluated after the measurements were made, and so the absence of a sharp response suggests that the absolute deflection would have been further shifted from the model described above. However, the expectation for relative measurements of interest here is that the normalised power time series and therefore relative deflection due to different linear absorption would still have been independent of power. An improvement to this would have been to choose a mechanical chopper with two blades, such that the power would have been truly maximised for $\approx 85\%$ of the on-cycle.

Following the parameters in equations 6.2 to 6.6 in order to achieve the desired absorption sensitivity, a low modulation frequency (f) was preferred so that a significant deflection signal was built up over the on-period. However, the frequency could not be too low, as the position sensitive QPD readout would otherwise be limited by vibrations: coupled proportionally from the $1/f$ seismic noise. For the measurements made in this chapter, this value was typically set at 87 Hz. In addition to this, the sensitivity spatial resolution of sub-mm required a small Gaussian extent of the pump. In retrospect, the value chosen of 550 µm was of the same order of size as the thermal diffusion length which was later evaluated to be 560 µm, (through equation 6.1).

The suitability of the model in describing the setup was further evaluated here (beyond to table 6.1) with further measurements of the R-factor up to high frequencies of 850 Hz where the diffusion length would be smaller than the Gaussian extent. In the frequency range $300 - 850$ Hz there was a strong agreement between the measured data and the expected data for input crossing angle of approximately 6 degrees (see figure 6.3). However, at the low frequencies used throughout this chapter (87 Hz), the measured value was only 40 % of what was predicted by the theory. Due to this, alongside the lengthened response time, the theory as exactly described (section 6.2) at the measurement frequency should not be considered for predicting the absolute absorption of a measurement. Instead, it is expected that given the side by side comparison expressed in Bukshtab [300] with respect to the opposite thermal diffusion limited regime where $\lambda_{\text{T}} >> r_{\text{pump}}$ that the effect of this will be to simply augment the calibration factor R and higher order absorption

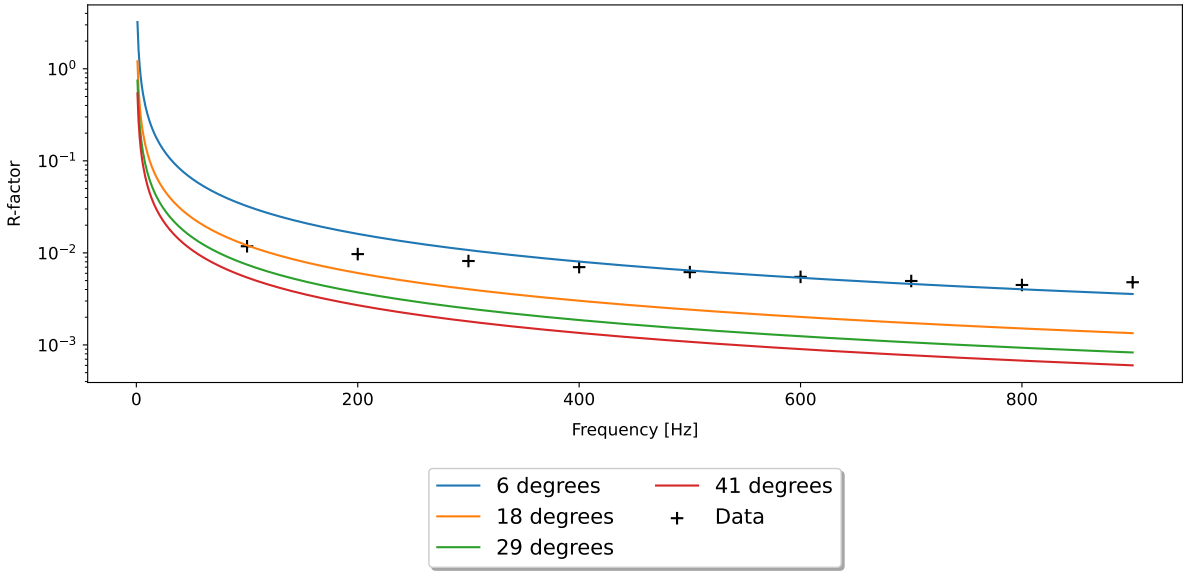

Figure 6.3: Measured calibration factor (R) for the PTD setup compared to the theory for a range of different input angles. The plot shows that the input separation angle for the beams was approximately 6 degrees, as this gave the closest agreement between theory and measured data at high frequencies.

terms as shown in equation 6.7. Fundamentally, the setup's ability to relatively determine the absorption is not expected to change. Additional efforts that were made to set the parameters of the system will now be considered. Although their impact on the measured deflection signal is now not as clear, they are still expected to have contributed to the R-factor as shown in Bukshtab [300].

Following from Brewster's equation, the Gaussian extent of the pump waist can be converted to a sampling depth (d_s) in account of its refraction through the sample. Following the small angle approximation, this is given by

$$d_s = \frac{\omega_{\text{pump}}}{\tan\theta_{\text{internal}}} \text{ and} \tag{6.9}$$

$$\theta_{\text{internal}} = \arcsin\left(\frac{n_{\text{air}}\sin\left(\theta_{\text{input}}\right)}{n_{\text{silicon}}}\right). \tag{6.10}$$

For silicon, this results in a low depth resolution for PTD maps. On figure 6.4 the scan resolution for a pump beam of radius 550 µm and input crossing angle $\theta_{\text{input}} = 40$ degrees is shown as 2 mm.

The size of the probe and pump beam at the crossing point can both affect the R factor. For measurements here of cm-thick silicon, there will be a slight change in path length of the beams when crossed at the front surface compared to the back surface. To prevent this coupling considerably to the measured signal, it was ensured that the beams were not highly divergent either side of the crossing point. The choice was therefore made to focus both the pump and probe beam to a well-defined and centred point on the sample. This was done with a total of four lenses between each laser source and the sample, using the following alignment procedure. The first collimated the source, the second acted as a reverse beam expander to contract the beam and allow the fourth lens to place each focus at a well-defined position. This position was the translated in a 2D plane through the sample with a 2-axis motorised stage.

The relative pitch angle of the beams leading up to the sample was another critical parameter. For the setup and length of samples considered (see table 6.2) it was expected that a pitch angle of < 0.2 degrees was required. This ensured that at the back of a sample of (length 5 cm) that an increase in beam separation would not shift the absorption beyond 5% and create a false absorption trend. This was best achieved here through setting up the probe beam first and centring it on kinematic mounted mirrors with a sub-mm pinhole aperture mounted on a moveable post to the same optical height. Over the long > 50 cm distances extended from the mirrors either side of the probe relative to the aperture, the angle could be constrained to less than 0.1 degrees with respect to the bench. This was likewise repeated for the pump, with additional kinematic mirrors used prior to accurately set the crossing height to give the maximum signal in account of the probe and beam separation. A large distance > 30 cm was also preferred from the last mirror to the crossing point for the pump, as this allowed for quick and precise beam height adjustments, given the mirror's fine pitch control of $\ll 0.5°$/revolution. The high index of silicon here proportionally reduced any internal angles, which helped to minimize this effect. However, it also limited the range of crossing angles achievable in the horizontal plane.

In order to better visualize and decide on the best input beam crossing angle and angle of the sample surface with respect to the fixed probe beam, a visual tool was created using the ipywidgets python package [303]. It was expected as shown on figure 6.4 that where the pump was closer to the sample's surface normal that there would be a false increase in absorption and therefore, gradient appearing throughout the sample. These were the result of the first internal reflection, carrying a significant power in account of the sample's low intrinsic absorption and high index contrast with respect to air. As a result, for all the measurements that follow, the sample surface normal was rotated closer towards the probe.

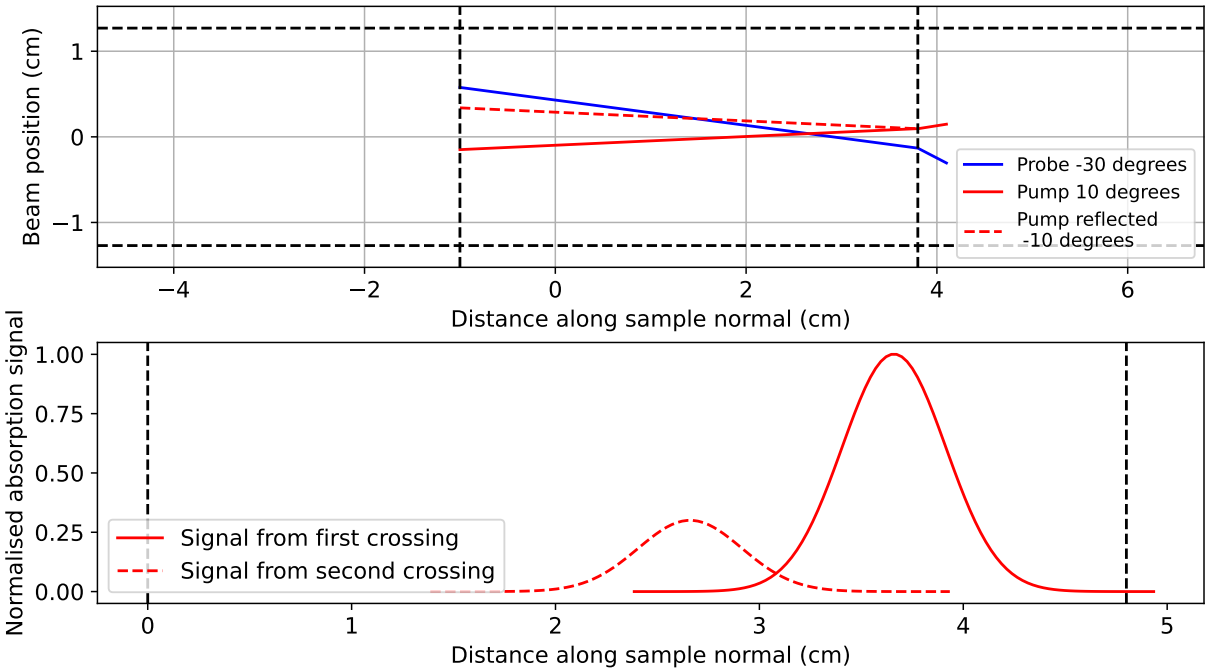

Figure 6.4: (TOP) Example of the small internal angles of a crossed probe, pump and reflected beam through a sample 4.8 cm thick. (BOTTOM) Absorption depth resolution shown at a particular crossing point. The effect of a reflected pump beam and comparative signal contributions are shown.

The probe beam parameters set in order to maximise the signal will now be considered. The probes wavelength [304] was chosen to be close to the maximum spectral response of the InGaAs QPD [305]. In order to maximise the response, the focussed beam size was set such that there was not a considerable amount of clipping over the 0.045mm thick quadrant boundary or with the 3 mm width of the sensing area.

The driving current and therefore output power of the probe was set such that the induced QPD SUM voltage was between $4-8$ V and considerably less the saturation point of 10 V. To ensure that saturation is not reached when measuring a more transparent sample relative to calibration, the transmitted power was set with a low absorbing silicon sample.

6.4 Noise hunting on the photothermal deflection setup

In attempting to measure low absorption (ppm-level) samples in the Glasgow PTD setup, the sensitivity limit was reached on multiple occasions. This section will detail the methods used to reduce the noise in the setup and in doing so support future efforts in measuring the lowest absorption silicon samples.

The noise of the PTD system's signal on the V_{AC} (differential QPD vertical readout) scaled by V_{DC} will now be compared. The units chosen were the amplitude spectral density (ASD) form with units $[1/\mathrm{Hz}^{\frac{1}{2}}]$. This representation of noise was introduced in the context of gravitational wave detector limiting noises in section 1.3.3. The noise was initially measured through a Stanford SR780 [306] signal analyser in units of $[\mathrm{dB}/\mathrm{Hz}^{\frac{1}{2}}]$ and converted to ASD form to give, over a range of operational probe currents. With the pump switched off, a deflection noise floor of $(0.35 - 1.1) \times 10^{-5}$ $[1/\mathrm{Hz}^{\frac{1}{2}}]$ was measured. This range is shown (black dashed line) on figure 6.5.

$$N\ [1/\mathrm{Hz}^{\frac{1}{2}}] = 10^{N_{dB}/20}. \tag{6.11}$$

This was compared to a measurable signal (through equation 6.7) for a pump power of 2.5 W and using the measured R-factor of 0.02. Assuming the absorption contributions are linear, the expected linear absorption coefficient to get an equivalent signal that matches the minimum of the measured noise 3.6×10^{-6} $[1/\mathrm{Hz}^{\frac{1}{2}}]$ was $50\,\mathrm{ppm\,cm^{-1}}$. In order to convert the noise signal measured by the lock-in to units $[1/\mathrm{Hz}^{\frac{1}{2}}]$, it had to be scaled by the square root of the equivalent noise bandwidth (ENBW)

$$\sqrt{\mathrm{ENBW}} = \sqrt{\frac{4}{64} \cdot \frac{1}{t_{\mathrm{constant}}}} \tag{6.12}$$

where the factor $(\frac{4}{64})$ comes from the chosen slope setting for the lock-in filter (24 dB/oct) [307] and the time constant (t_{constant}) was set at 0.1 s so that the $\sqrt{\mathrm{ENBW}}$ was evaluated to 0.8.

Compared to the target absorption level of $1\,\mathrm{ppm\,cm^{-1}}$, this noise was at least a factor of 50 too high. To reduce the noise, two changes were considered. The first was to reduce the seismic noise that coupled to the probe through different resonant modes of the posts. Long, post heights (≈ 10 cm) were used for compatibility with minimum stage heights. Without correction measures, the coupling of seismic noise was expected to affect the height of the beam relative to the QPD's centre of the QPD's surface. To investigate this, the spectrum analyser was operated whilst different posts (used by mirrors on the probe beam's path) were tapped by hand. It was found that the standard post connected to

the first kinematic steering mirror for the probe (positioned on the bottom left of figure 6.2 (B)) when tapped created a noise floor approximately three times above the other posts (shown on the figure). As a result, this post was swapped out for a 3 inch monolithic aluminium post.

The noise level was then remeasured, but with a MOKU:lab spectrum analyser [308] for ease of exporting the data across a wide spectrum. In addition to this, the noise was amplified by a pre-gain amplifier positioned before the input into the MOKU device. The noise was measured in units of [dBm/Hz] and converted through

$$N\ [1/\mathrm{Hz}^{\frac{1}{2}}] = \sqrt{R \times 10^{N_{\mathrm{dBm}}/10} \times 1 \times 10^{-3}} \tag{6.13}$$

in account of the input impedance ($R = 1\,M \cdot \Omega$) used by the Moku-amplifier to scale the noise power into a voltage. The scan #10 for the probe operated at a current of 71 mA and measured with a QPD sum voltage of 5.6 V (see figure 6.5 (A)) around 87 Hz was marginally the best operating current with a noise level of 9×10^{-7} $[1/\mathrm{Hz}^{\frac{1}{2}}]$ compared to scans #5 and #40 which were at 1.5×10^{-6} $[1/\mathrm{Hz}^{\frac{1}{2}}]$. Taking this higher level, the minimum improvement was a factor of 50 % lower than the noise level measured before the post swap. Following the same measurement conditions described previously through the lock-in, this was expected to set the measurable absorption level at 25 ppm cm^{-1}. This noise was confirmed (see blue line in figure 6.5 (A)).

To continue to reduce this level, the standard post connected to the second kinematic steering mirror for the probe (positioned on the top right of figure 6.2 (B)) alongside the one to which the probe laser was mounted were also swapped out for 3 inch monolithic aluminium posts.

For scan #78 compared to #77 (see figure 6.5 (B)), both for the probe operating at 309 mA, the noise although improved was distinctly higher due at 6×10^{-7} $[1/\mathrm{Hz}^{\frac{1}{2}}]$ compared to 3×10^{-7} $[1/\mathrm{Hz}^{\frac{1}{2}}]$. As the only difference was the operation of a loud scroll pump (see chapter 6) separated by the seismic isolation of the optical bench, it was clear that the coupled seismic noise could still be a limiting factor. With this scroll pump switched off, other scans #64 and #65 were made to check the effect of different operational currents. In particular, scan #65 showed that the operational current of 209 mA and quieter lab environment led to a reduced noise level of 8×10^{-8} $[1/\mathrm{Hz}^{\frac{1}{2}}]$ at 87 Hz. At 2.5 W of pump power, this was expected to give a measurable absorption level of ≈ 1 ppm cm^{-1}.

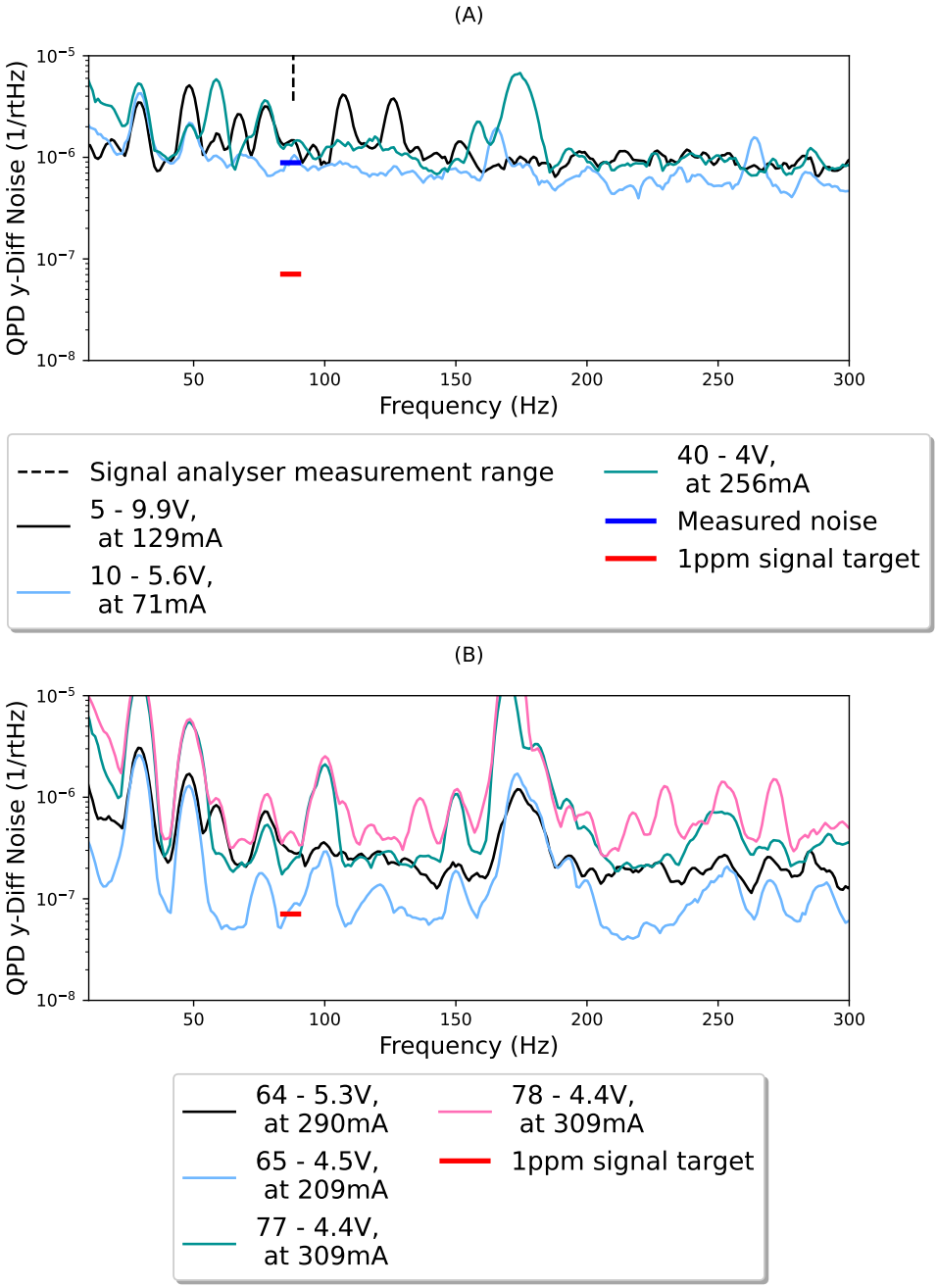

Figure 6.5: This plot show a range of different noise curves measured from the differential y channel from the quadrant photodiode. The separate plots (A) through to (B) show the different noise floors after improvements described in the text. The spectral noise measurements are shown across a wide frequency range of $10-300\,\mathrm{Hz}$. The measured and targeted lock-in signal or noise levels are shown with short horizontal lines centred on the frequency of interest ($87\,\mathrm{Hz}$).

Due to time limitations, it was not possible to directly measure this absorption level through the lock-in amplifier. However, it is believed that the PTD system and improvement as described would be capable of measuring the lowest known absorption levels of bulk silicon materials $\approx 1\,\mathrm{ppm\,cm^{-1}}$ (see red line in figure 6.5 (B). Further improvements, should consider lowering the height of the optical path to reduce the amplitude of seismic coupling, swapping all the posts for monolithic posts and assessing the probes optimum current point, for minimal jitter noise, in isolation first.

With both of these suspected noise sources mitigated the ideal PTD system would be Shot noise limited such that the signal-to-noise ratio of the effective absorption could be reduced not only over a long lock-in time constant (0.1 s) here but over many independent samples (N): over which the noise is uncorrelated.

$$SNR \propto \sqrt{N \cdot t_{\text{constant}}} \tag{6.14}$$

In reality, there are a range of other potential noise sources which are best distinguished between intrinsic and extrinsic origins with respect to the setup. The noise sources studied for the PCI and its Lock-in detection scheme by Alexandrovski [163] are expected to largely carry into the PTD setup as described here.

6.5 Measurement of the calibration samples

The AB1 and AB2 samples (see table 6.2) were the chosen calibration samples. These were monocrystalline CZ samples with a high and expected doping alongside absorption profile. They were independently characterised with the transmission setup as discussed in section 4.5. By independently measuring the samples in the PTD set up the confidence in the relative measurement process could be assured. The transmission measurements gave an absorption scaling of from AB1 to AB2 of 1.51±18 %. Averaging all the PTD scans without making further corrections gave a comparative scaling of 1.53±8.7 %.

Starting from the null hypothesis, the assumption that these absorption ratios represent the same physical, allows us to combine the errors to get an error of ±20 % to reflect the confidence in the PTD setup. In determining an absolute error on any absorption measurement presented here, this ±20 % was expected to carry and be the dominant factor.

Table 6.2: This table shows all the absorption measurements made at room temperature for silicon samples throughout this chapter and wider thesis. The first table is for the cylindrical samples of diameter (D) and length (L). The second table is for cuboid samples with height (H), width (W) and length (L).
* Value provided by vendor or collaborator.

Sample	**Type**	**D [mm] × L [mm]**	α [% cm^{-1}]
AB1	CZ	25 × 28	4.6
AB2	CZ	25 × 48	7
AB12 [111]	CZ	75 × 38	0.68
AB15	CZ	100 × 98	0.45

Sample	**Type**	**H [mm] × W [mm] × L [mm]**	**R** [$\Omega \cdot$ **cm**]	α [**ppm** cm^{-1}]	O_i [**ppma**]
AB-Quasi	DS	12 × 14 × 40	0.9 *	230,000	0.25-3 *
Okmetic #1	a-MCZ	10 × 60 × 60	1090	Not measured	4
Okmetic #3	a-MCZ	10 × 50 × 50	4400 *	31	4
Okmetic #4	a-MCZ	10 × 50 × 50	4400 *	41	4
Okmetic #5	a-MCZ	10 × 50 × 50	4400 *	120	4
Okmetic #6	a-MCZ	10 × 50 × 50	4400 *	79	4

6.6 Impact of spatially varying absorption

Different silicon growth methods are expected to have spatially varying absorption profiles. This follows from direct research [285] and indirect [309], based on the foreign atom spatial concentration profiles over the boules (discussed in section 4.4).Given the scale of the proposed mirror substrates for future gravitational wave detectors (see section 1.5) it is important to understand the optical absorption across the boule. It will therefore be necessary, given the current data, to map the absorption of silicon prior to its proposed implementation as a mirror substrate of future GW detectors.

Compared to point measurements or line scans, maps of the absorption through the bulk of a sample will help to identify and mitigate the source. Furthermore, for detectors such as Voyager which are interested in operating their test-masses at around 123 K maps could be critical to their operation due to the effect of thermo-refractive distortion. For a uniformly absorbing substrate, the impact of this effect is discussed in 1.6 and highlighted in figure 1.6. Prior to showing map measurements, this section will expand upon this by considering the effect and its dependence on spatial variation in more detail.

In current gravitational wave detectors, the test-mass substrate absorption without correction would impose a self-acting power limit on the main beam. Without active correction, this would limit the operational power of the interferometer. The limit is realised as the power of the beam is increased and the proportion of the beam that is scattered from the

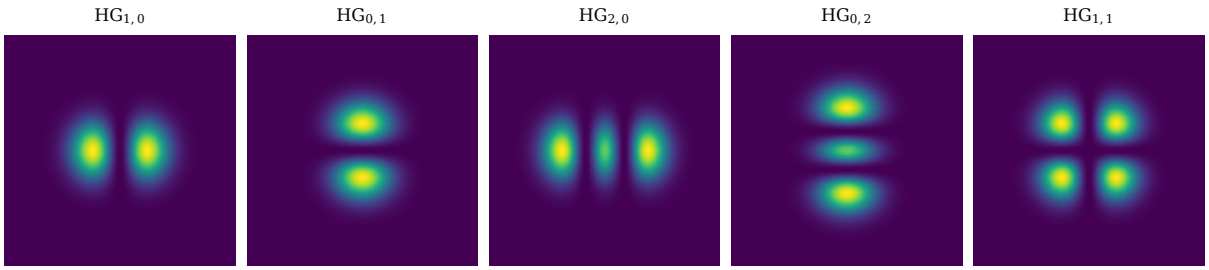

Figure 6.6: Orthogonal modes to the HG00 mode used by the interferometer's main beam. If temperature gradients due to a non-uniform absorption profile have significant spatial correlation with these modes then the stable operational power of the detector could be impacted.

lowest order Gaussian mode to a higher order is increased [54]. A detailed evaluation of the thermal compensation systems required to mitigate this is discussed by Brooks *et al* [127]. This work showed that for the silica substrates used in current detectors that in order for the wavefront distortion imparted from a uniformly absorbing substrate not to limit the operation that the distortion had to be decreased by a factor of twenty to 5.4 nm RMS.

Consider a radially asymmetric absorption profile that does not average out over the length of the substrate. For the same absorbed power and symmetric TCS, the spatial overlap of the distortion profile with the intensity of the interferometers Hermite–Gaussian HG00 beam would be reduced. It is this reduction that would scatter more light into higher order modes and lower the limit of tolerable absorption. The maximum scattering would therefore occur where the distortion profile was completely represented by higher order Gaussian modes (shown in figure 6.6) relative to the axially symmetric TEM00 of the main beam. The true absorption profile that would lead to each of these, if implemented, in the test mass mirrors of current gravitational wave detectors would follow from steeper absorption gradients due to the effective Gaussian sampling of the absorption profile from the intensity profile of the interferometer beam. The effects of thermal diffusion also act to minimise the lensing effects and effectively further smooth out the effects of any potential steep absorption profiles. A detailed analysis of distortion was beyond the scope of this work. Future developments should consider this in two parts, based on the availability of current research and software.

The first part of evaluating the distortion due to the absorption should consider the substrate heating and distortion equations set out in the theory by Vinet [310]. This was recently implemented into python `Finesse 3` module version 3.0a29 [311] for radially symmetric absorption profiles described by Bessel functions. In this model, these are fitted as spatially varying input light fields, but with a uniform absorption to achieve the

same effective distribution of absorbed power. To instead evaluate the distortion due to a radially asymmetric absorption profile, suitable derivations should be made from the thermal equations set out by Vinet [310]. With a suitable distortion profile, the resulting scattering of light and adjusted limit to the tolerable absorbed power should follow from the equations set out in Brooks [127]. These equations evaluate the spatial overlap of the main interferometer beam with that of the induced distortion by solving a 2D integral.

The possibility of a non-uniform distortion profile given existing measurements (discussed in section 4.4) creates a requirement for a future TCS to spatially compensate for it. Furthermore, if the resultant distortion profile is also significantly asymmetric compared to current detectors and does not balance over the depth of the substrate, then the actuation of the counteracting TCS would need to be increased in both complexity and heating power. However, this might lead to an increased total heat load applied to the test-mass. As a result of this, the targeted operational temperatures of these detectors, as focussed for the lower-temperature ET-LF in section 1.7, could be at odds with the cooling power available due to radiative cooling to the surrounding environment and required for the targeted operational parameters.

Following this reasoning, it is important to consider reducing not only the absorption but ensuring that the silicon mirror chosen from a grown substrate does not have any significant spatial variations in the absorption. On the short range, small clustered defects considerably smaller than the beam would be detrimental due to high absorption and scatter. Also, high variation that appears over the radius but not necessarily starting at the centre would be detrimental. Only through the development of mapping techniques and future scaling up in parallel to the growth of larger substrates can the effect of absorption and its spatial variation be minimised. Sufficient characterisation in advance of cryogenic detectors which choose to operate at the temperature of 123 K would allow them to mitigate the residual absorption with their TCS systems.

6.7 Mapping the absorption of silicon samples of low resistivity

The rest of this chapter will now consider the absorption measurements made to map the absorption through a range of silicon samples.

Starting with low-resistivity silicon samples this section will assess the mapping capabilities of the photothermal deflection setup. The process typically followed scanning a 2D plane and then either rotating the sample 90 degrees around its centre or offsetting the plane before repeating the scan. These scans were then combined to give a 3D absorption map. As discussed, this allowed spatial trends to be identified in different silicon samples.

The AB1 and AB2 calibration samples as measured in transmission in section 4.5 and linearly scanned with the PTD in section 6.3 were measured first and shown in figure 6.7. The black and blue regions towards the front and back of the scans represent the absorption and phase shift as the measurement regions gradually moves off the sample. Towards the edge and bottom, there are clear absorption spikes for both samples that do not correlate with either the simultaneously measured phase or probe power. It is expected, therefore, that this was a true increase in absorption but due to the pump beam clipping the edge. There are additional striped features which can be noticed along the length of the scans, and in particular relative to the mean value along the length of AB1. A uniform absorption profile along the length of the sample that was independent of the rotation of the scanning plane would lead to a high spatial correlation. By evaluating the correlation, any distinct trends could be observed. The simplest way to check this for two scans of the same size was to take the differential and normalises this to the average. For the case of AB1 and AB2 as shown in figure 6.8 no clear linear trends were observed between either the lateral or longitudinal components of the samples. However, for the AB1 sample the striped features along the longitudinal axis still appeared quite prominent as shown on figure 6.8 (A).

The PTD technique was used to map the absorption of the QM sample, as shown in figure 6.9. Compared to the previous average estimate from the PCI measurements, studied in section 5.2, the value measured by PTD is approximately 37 % higher at 11.3 %cm^{-1}. The power entering into the sample was only, 64 mW and so the measured absorption was expected to be linear with power. The FCA due to induced TPA contributions shown by the right-hand plot in figure 4.1 was five orders of magnitude below this and so not expected to contribute. This discrepancy is expected to arise from the relative errors between the setups, and perhaps as the setup was not otherwise tested when measuring relative to a calibration sample that had a lower absorption.

This section will now consider the measurements made on large low-resistivity silicon samples. The first sample that will be considered is AB12. It was procured from Spanoptic and had a distinct crystalline silicon axis of [111]. At the time of measurement, the choice was made to take distinct 1D line scans by starting the scans at a radial distance of 25mm

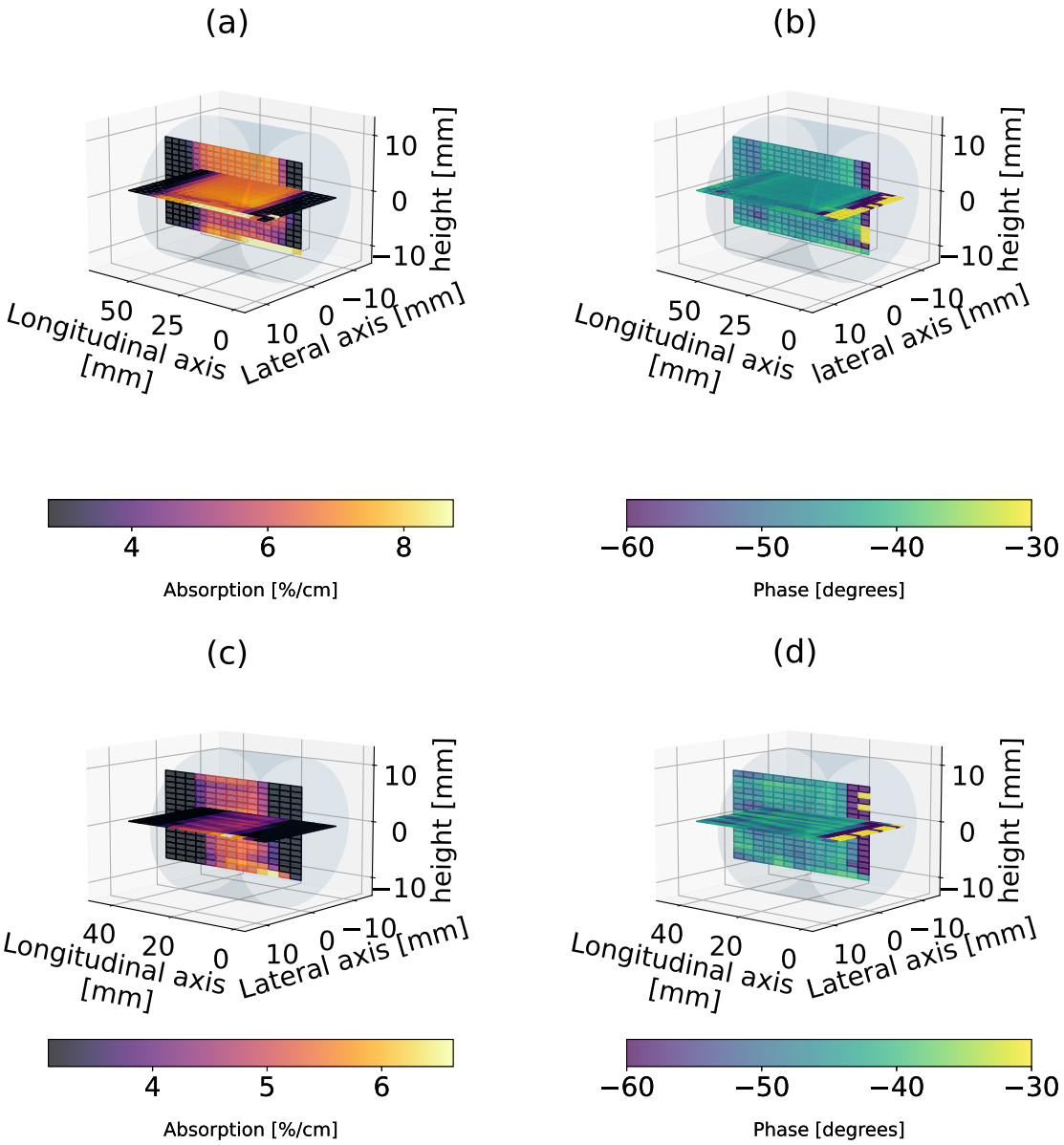

Figure 6.7: 3D Spatial profile of the absorption across the high absorbing calibration samples. (TOP) shows the high and uniform absorption of the AB2 sample on the left and position matched phase on the right. (BOTTOM) shows the AB1 sample and its increased spatial variation alongside changes in the phase.

from the centre and rotating the sample in increments of 45 degrees through to a total of 360 degrees. The result of this is shown on figure 6.10. Comparing the averages, across the cylindrical area and the sample appears to have a uniform absorption. The absorption averaged across all the scans was 6800 ppm cm^{-1}.

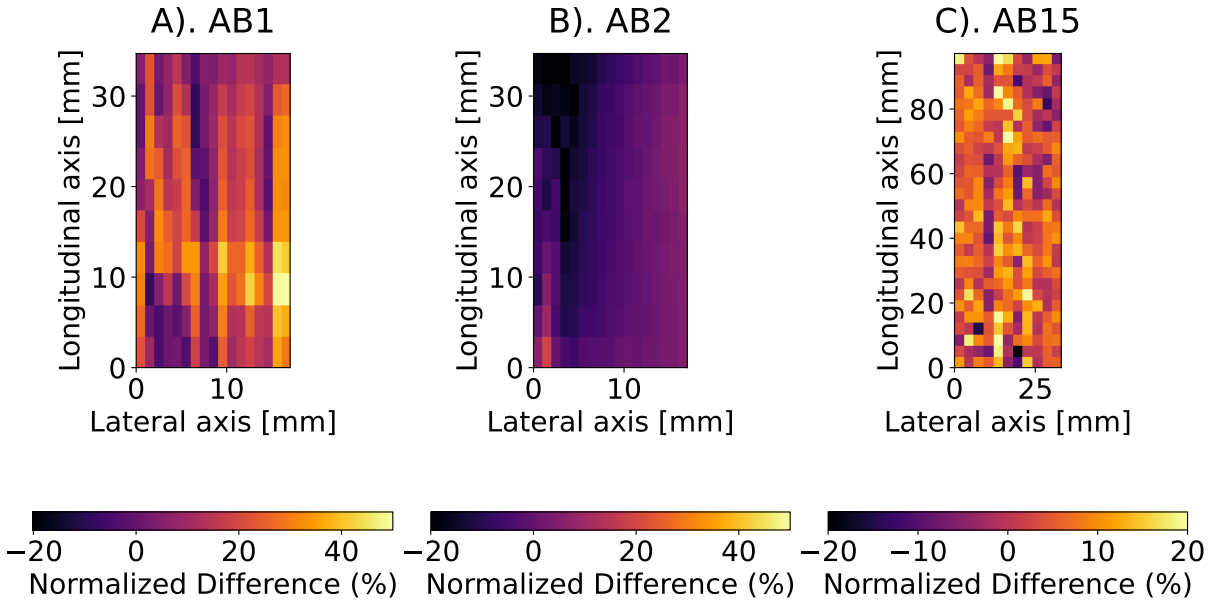

Figure 6.8: Normalised difference between the 2D scan

The most interesting 3D absorption maps were taken of a low-resistivity sample and large 10 mm diameter (AB15) as shown in figure 6.11. The trends observed in this sample show a slight increase towards the top and a significant increase along the length of the sample, along the length with an increase of approximately 30 % after the first 20 mm. The overall average therefore is 4500 ppm cm^{-1}. Above this, in regions distributed physically by several -mms are local clusters of absorption reaching up to 7000 ppm cm^{-1}. This clustering is an indication of higher absorbing defects. The linear correlation check made on AB1 and AB2 was repeated for AB15 as shown in figure 6.8 (C) and no trend was observed between the longitudinal or lateral axes of the rotated scans.

Over the size of the AB12 and AB15 samples measured here, which are comparable to the proposed Gaussian beam diameter of future detectors at $\approx$ 12 cm there was no significant spatial variation observed. Given the limited knowledge of these samples in their history and unknown location from the boule of larger silicon ingots, this result is not surprising. Beyond this, in order to know if significant variation effectively occurs across large pieces silicon, it was important to characterise samples from a range of positions inside a silicon boule. This mapping will be continued in section 6.8 from radially separated samples cut thin a disc of high-resistivity silicon.

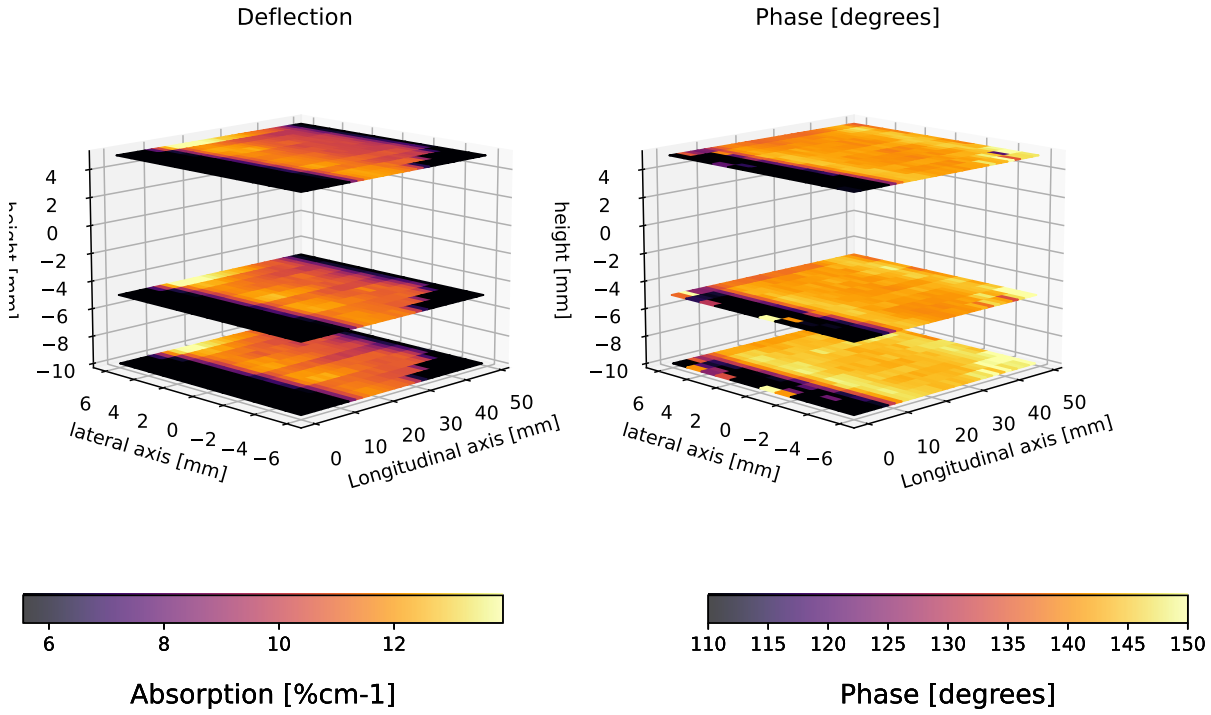

Figure 6.9: 3D Spatial profile of the absorption across the QM sample.

6.8 Measurements of a-MCZ silicon samples

This section will detail absorption measurements made on silicon samples that were grown by the silicon vendor Okmetic using their advanced MCZ growth technique. The applicability of MCZ silicon (as discussed in sections 4.4 and 6.6) for the substrates of future detectors depends on the reduction in spatially varying absorption levels both radially and longitudinally due to thermalised oxygen donors. However, if this can be done, the MCZ technique may provide a pathway to producing test masses meeting both the size and absorption requirements for future GW detectors. It was therefore of interest to study material produced using the Okmetic advanced MCZ (a-MCZ) technique, which is believed to reduced oxygen content.

The a-MCZ sample was manufactured in 2022 and cut as a 14 mm slice from a larger boule that was 215 mm in diameter. The oxygen content was expected to be below the 5 ppma minimum level for MCZ (see table 4.1) and the resistivity was targeted at 4.4 kΩ.cm (P-type). Further communications with the Okmetic company revealed that the sample was taken from approximately 40 mm from the seed end of the boule [312]. The resistivity measured by the company for this silicon started to drop, from 4.4 kΩ.cm, past the 400 mm mark and approach 2.5 kΩ.cm. As for the oxygen content it was specified for the silicon disc provided as 4 ppma as quantified by the ASTM F121-83 standard [313]. This also decreased away from the seed end and reached 2.5 ppma just before the 1 m mark at the

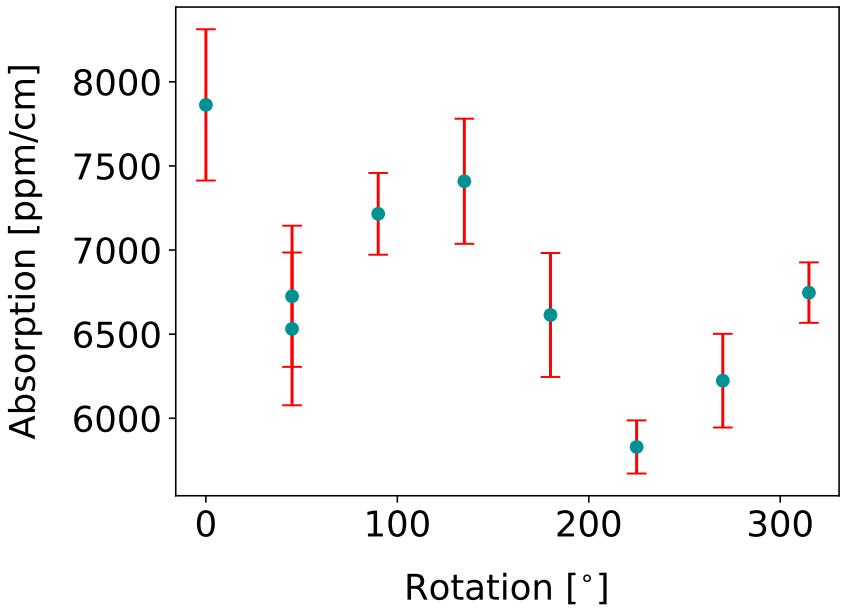

Figure 6.10: 3D Spatial profile of the absorption across the AB12 sample.

end of the cylindrical region of the boule. Based on these numbers, the absorption of the disc due to thermalised oxygen donors (see section 5.3) could be at the level of 10 ppm level. However, exact values would require knowledge of the silicon boule's temperature as a function time during growth.

The cut disc arrived unprocessed from Okmetic. The process to prepare the sample will now be described in the following subsection.

6.8.1 Cutting and polishing procedure for crystalline silicon

Within the context of this study, this polishing procedure was only followed for the Okmetic samples and the ET-pathfinder silicon (introduced later in section 7.8). For the Okmetic disc described above, it was further cut up in order to get smaller optics that would be compatible with the PTD measurement setup. The layout of the resulting subsample is shown alongside its ID number on figure 6.12.

The requested polishing properties necessary for low-loss optical measurements will now be discussed alongside the justification for each. The samples were polished in the final steps with a Col-k slurry [314]. This slurry is a colloidal silica slurry that can be tailored in its particulate and chemistry. A minuscule particulate size down to the nm-scale can

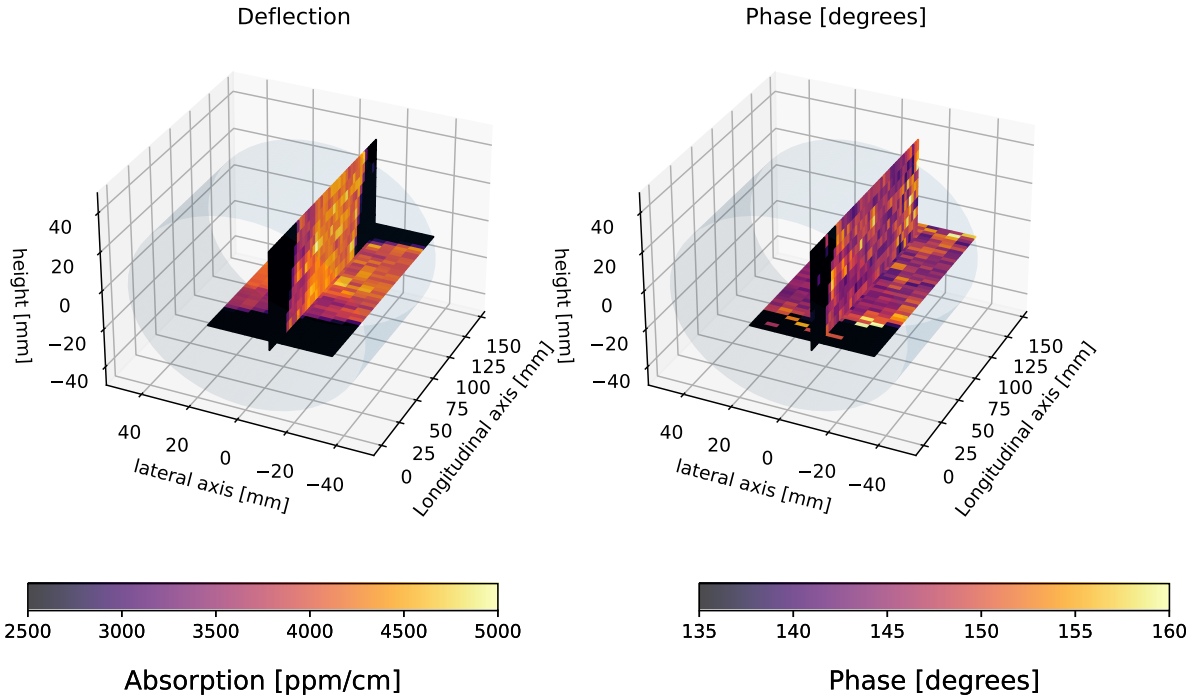

Figure 6.11: 3D Spatial profile of the absorption across the AB15 sample.

notably be reached, this allowed the roughness of both faces to be specified by Crystran to $< 0.5\,\text{nm}$. At this level, the surface losses due to Rayleigh scattering will not affect the measurement. In addition to this, a flatness of less than 1200 nm was achieved over a circular aperture of 80 %. For the PTD applications here, having the clear aperture was the most important aspect in order to allow measurements to be made through the entire sample. Although, the flatness was within orders of magnitude of what is acceptable for PTD it was standard practice for the group at Glasgow to maintain this polishing procedure and therefore flatness to ensure the samples are compatible with other optical tests.

6.8.2 Estimating the absorption through resistivity measurements

As established in section 4.2, resistivity is a suitable indicator for the dominant FCA and NIR absorption of all c-Si, except for the highest purity samples. To measure the resistivity on the surface of silicon, the four-point probe method (see figure 6.13) was used to recover it as a linear factor in a simple ohm-law expression. By measuring the voltage drop (V) and current (I) applied across the measurements heads, pressed into the surface, a value for surface resistivity (ρ_{surface}) was determined [315].

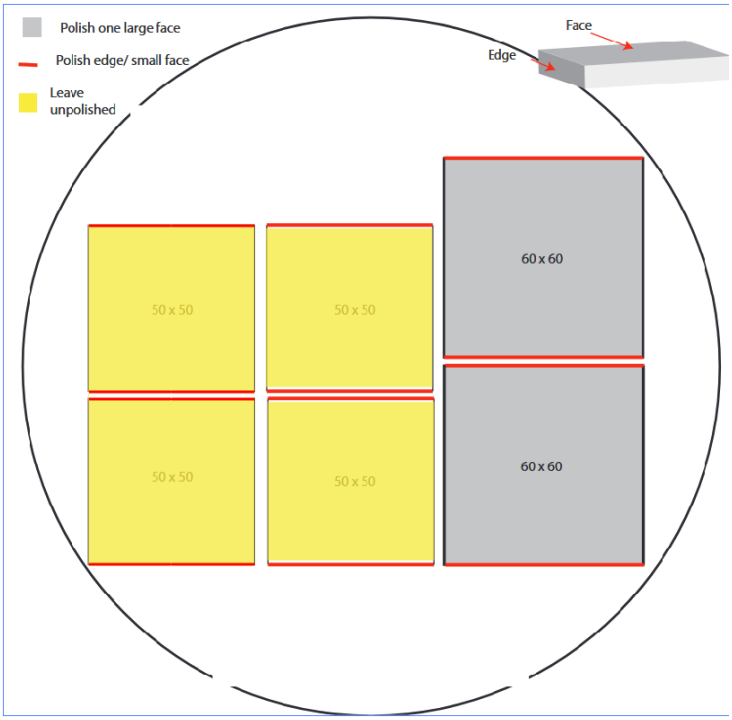

Figure 6.12: Layout of the cut and polished Okmetic sub-samples processed from the larger disc by Crystran Ltd.

For the Okmetic samples, introduced in section 6.8, the surface resistivity was measured for sample #1 using the four-point probe method. The bulk resistivity (R) was then calculated using scale corrections: where the sample is approximated as having both infinite thickness and surface area [316].

$$R = 2\pi s \rho_{\text{surface}} \quad \text{where} \quad \rho_{\text{surface}} = \frac{V}{I} \tag{6.15}$$

The infinite boundary assumptions were valid as the probe head spacing (s) was 0.1 cm and considerably smaller than the geometrical dimensions of the Okmetic silicon sample #1 as shown in table 6.2 for the surface area (60 mm by 60 mm) and the thickness of 10mm. For 10 mA applied current, the voltage drop at the centre and edge was 17.4 V and 16.96 V. This equated to a resistivity of 1.07 k .cm and 1.08 k .cm which was approximately 75 % lower than the value of 4 kΩ.cm measured by the Okmetic company who manufactured the silicon. Through equations (4.2 and 4.3)the resistivity value measured here equated to approximately 135 ppm/cm for the measurements here and 31 ppm/cm for those by Okmetic.

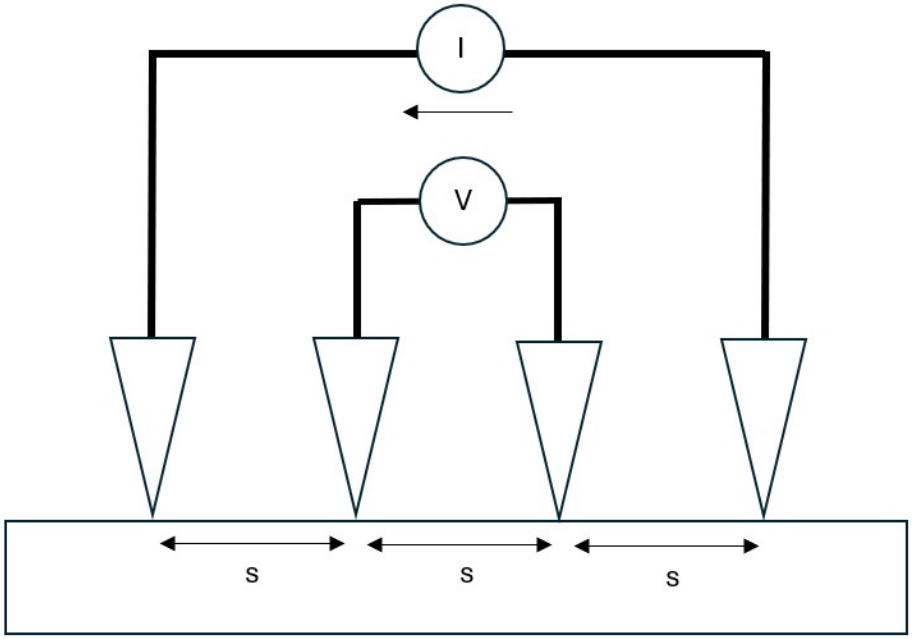

Figure 6.13: Schematic of the four-point probe method used to measure the resistivity.

The limits of the four-point probe measurements of high-resistivity samples are expected to largely be due to poor electrical contacting between the probes and the sample. However, research has shown the potential for improved accuracy through spectral impedance analysis. Although, the applicability of these improvements may be limited in measurement throughput due to the required thin-film deposition onto samples. The measurement process also damages the silicon surface [270] and so may be incompatible with other optical measurements.

6.8.3 Power dependent absorption of a-MCZ

To improve the understanding of the true absorption level and its variance across the different samples measurements made in a similar setup with A. Markosyan, whilst on a short placement at Stanford University, will be discussed.

The PTD setup used by A.Markosyan can be derived from the same theory as presented in section 6.2. The notable differences in the setup were that the pump beam's wavelength of 2000 nm, Gaussian waist at its focus point of 113 µm and a chopping frequency of 400 Hz. The calibration sample used was a 0.89 %cm^{-1} sample that had been absolutely calibrated

with a calorimetric technique. Using this sample, the calibration factor R was evaluated from equation 6.7. At pump powers measured up to 0.4 W, this R-factor was independent of power and so the equation simplified to be linear with power and when rearranged gave $R = 0.156$. This was $\sim 10\times$ larger than the value measured in the Glasgow setup.

Okmetic sample #3 was then placed on the stage, before the crossing was scanned through and located at the centre of the sample. From the known resistivity range evaluated in section 6.8.2, the linear absorption was expected to be between 31.0 ppm cm^{-1} and 135 ppm cm^{-1} respectively. The sample was first measured at 0.34 W equivalent to the low beam intensity of 8.1 MW/m^{-2}. The total absorption signal was evaluated through a re-arrangement of equation 6.7 by normalising the signal $V_{\mathrm{AC}}/V_{\mathrm{DC}}$ to the power and R-factor above. The total absorption was 14 ppm cm^{-1}. The pump power was then increased to a maximum of 3.82 W ($\approx 11\times$ higher), but the absorption only increased to 69 ppm cm^{-1}. As the absorption increased by a smaller factor ($\approx 5\times$ higher) it was clear that it had a non-linear power dependency. To mitigate these, the total absorption was sampled across a range of power values between this minimum and maximum. Although the maximum was a hard limit for this laser, the minimum point, adjusted directly from the laser driver, was set to avoid an increased noise and instability at lower laser powers.

In order to determine the true α_{FCA} value from the equivalent linear term α_0 in equation 6.7, the non-linear terms with power had to be fitted and subtracted in account of their power dependence. The coefficients of which were fitted with an optimisation routine provided by Python's `curvefit` found inside the scipy.optimize package [169]. The fit was evaluated with no bounds set on the values and with an absolute error of 5% passed from the power meter to each absorption value.

The empirical polynomial fit as stated previously (equation 6.7) and verified for linear absorptions (a_0) was

$$\frac{V_{\mathrm{AC}}}{V_{\mathrm{DC}}} = \left(\alpha_0 + \alpha_1 P + \alpha_2 P^2\right) P \cdot R. \tag{6.16}$$

This polynomial fit is shown on the left of figure 6.14 but with the power values along the x-axis scaled by the beam area ($\pi \times r_{beam}$) to give intensity. The absorption coefficients as stated in equation 6.16 are fitted (see table 6.3).

Fit	a_0 [ppm cm^{-1}]	a_1 [ppm cm^{-1} · W^{-1}]	a_2 [ppm cm^{-1} · W^{-2}]
Low intensity	19.9 ± 0.9	-9.7 ± 1.4	5.2 ± 0.4
High intensity	5 ± 0.6	-4.9 ± 1.8	16 ± 0.9

Table 6.3: Fit of the absorption coefficients for the polynomial equation 6.16 for Okmetic sample #3 measured over both low and high intensity ranges.

The physical origin of each coefficient with respect to the fitted lines (shown in figure 6.14):

- a_0 is the linear absorption (green line).
- a_1 is proportional to the free carrier dispersion (blue line). It is expected to be a negative coefficient, following from the two photon absorption term given in equation 4.5.
- a_2 is proportional to the induced free carrier absorption (purple line).

The fitting and physical significance of these will now be considered. At lower powers, there is evidently not as good a fit, given the large proportional separation between the points and the fitted polynomial. It was believed that this error could be attributed to a combination of not leaving enough time for the laser to stabilise after each adjustment and any drift in power over the time it was measured (minutes) before the absorption measurement was taken. The a_1 coefficient is expected to be proportional to the TPA absorption coefficient, which (β) fitted from measurements by Bristow *et al* [317] was 4×10^{-10} cm^{-1} · W^{-1} at 2000 nm. Taking the fitted coefficient here, of -10 ppm cm^{-1} · W^{-1} and scaling it by the beam area, the TPA is calculated simply here as a value that is two orders of magnitude less than the known value. The large discrepancy is expected as the index profile of the TPA is small compared to the beam size as shown by Dickmann *et al.*[298]. Beyond gravitational wave detectors, further studies into the carrier lifetime may benefit from connecting the 2$^{\text{nd}}$ order absorption term to the free carrier absorption induced by equation 4.7 and its spatial distribution.

The effect of a reduced beam size on the signal was checked to ensure that the empirical relation holds across a broader range of beam intensities. After the measurements described below, the setup was recalibrated with a shorter focal length lens. This resulted in a beam size of 56 µm and a calibration factor of 0.116. On the right of figure 6.14 the effect of the higher intensities is to significantly increase the non-linear terms. The fit shows a significantly increased 2$^{\text{nd}}$ order coefficient by a factor of three. Although, the crossing point and therefore linear absorption was sampled from a different position on realignment, the ratio of linear to non-linear components decreased by a factor of 10 at the maximum power of 3.78 W. This reduction means that the effect of errors on the fit

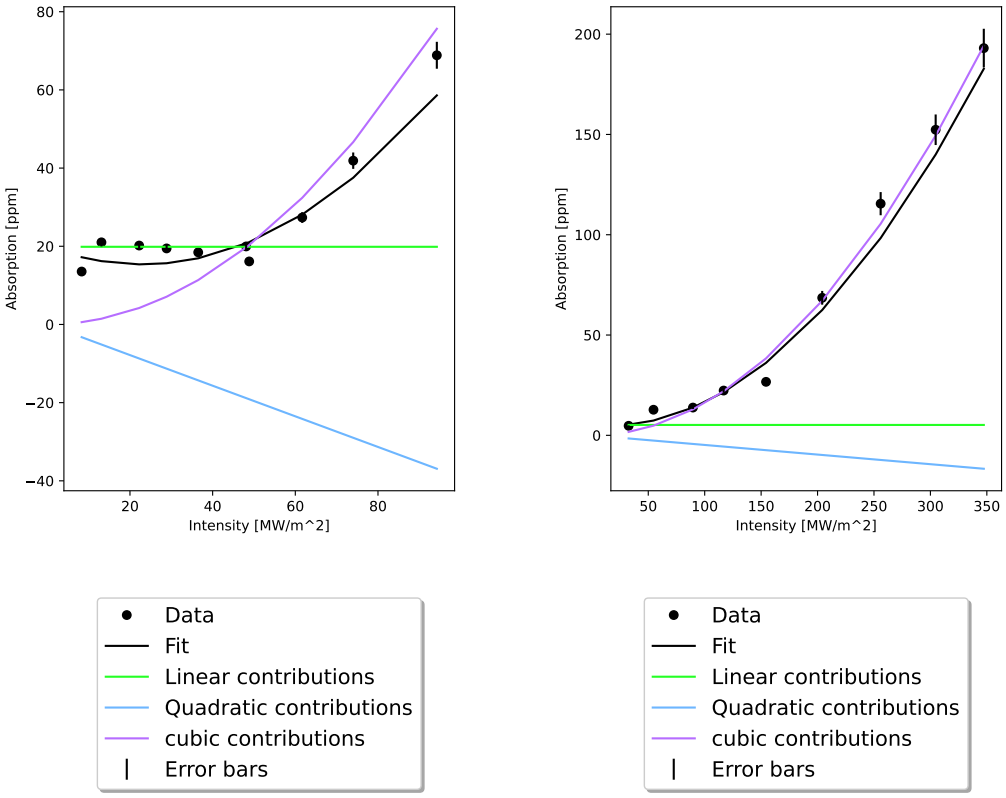

Figure 6.14: Plot showing the absorption coefficients fitted with the polynomial equation 6.16 for a-MCZ sample #3 for different incident beam sizes. (Left) is the low intensity regime and (right) is the high intensity regime.

would limit the use of this configuration in providing an accurate measure of the linear absorption. This highlights the need to measure low absorbing silicon samples at lower intensities where possible. In fact, similar studies by Bell [280] operated in the intensity regime of $1 - 10\,\mathrm{MW/m^{-2}}$ compared to the minimum intensity of $20\,\mathrm{MW/m^{-2}}$ used here.

For the first power dependent absorption measurements made over the lower intensity range, at 3.78 W the absorption contributions from the linear term were evaluated as $20\,\mathrm{ppm\,cm^{-1}}$ and the non-linear coefficients combined to give $38.7\,\mathrm{ppm\,cm^{-1}}$. Where this linear component may vary throughout the sample, the non-linear terms should not. Through a rearrangement of equation 6.14, the linear free carrier absorption could therefore be evaluated at every point inside the sample by subtracting these terms away. After

this, the Okmetic samples were scanned. The measured and isolated linear absorption from each scan is shown on the left of figure 6.15. Across each scan whole scans, the change in absorption or gradient through the length of the sample was typically either distinctly positive or negative.

Starting with the highest absorption peak, sample #5 peaked at the front surface with an absorption of $310\,\mathrm{ppm\,cm^{-1}}$ before dropping to and back up to $70\,\mathrm{ppm\,cm^{-1}}$. For sample #6, the absorption from the opposite direction steadily decreased from $230\,\mathrm{ppm\,cm^{-1}}$ to $30\,\mathrm{ppm\,cm^{-1}}$. For sample #4 the absorption decreased with a similar trend but from $90\,\mathrm{ppm\,cm^{-1}}$ to $10\,\mathrm{ppm\,cm^{-1}}$. Sample #3 back from the front direction decreased from $50\,\mathrm{ppm\,cm^{-1}}$ to $30\,\mathrm{ppm\,cm^{-1}}$.

In order to compare these results to the resistivity values, the latter had to first be converted into comparable absorption values. From measurements made in the lab on a separate and larger face polished sample shaded (grey) in figure 6.12 the absorption was estimated to be $135\,\mathrm{ppm\,cm^{-1}}$. In comparison, the resistivity specified by Okmetic was $31\,\mathrm{ppm\,cm^{-1}}$. The resistivity measurements are sampled over the volume of the sample through which the current flows. As the exact scale of this area is not clear nor are the resistivity measurements from the same measured origin points on the disc they are not directly compared here. To provide a more representative comparison from the optical measurements the absorption for each samples scan was averaged across the 5 cm length using the Trapezium rule for integration [295]. In the same order as shown before, the average absorption for the samples was $120\,\mathrm{ppm\,cm^{-1}}$ for #5, $79\,\mathrm{ppm\,cm^{-1}}$ for #6, $41\,\mathrm{ppm\,cm^{-1}}$ for #4 and lastly $31\,\mathrm{ppm\,cm^{-1}}$ for #3. These averaged measurements are within the range indicated by the resistivity. The increase in averaged absorption from sample #3 to #5 by a factor four, if the latter corresponded to the bottom left sample (see figure 6.12), could correspond to a higher thermo-optic distortion of a Gaussian beam incident on the centre of the full disc.

Compared to MCZ measurements [285] (discussed in section 4.4) the absorption level was not the lowest by and by a factor of 10. However, if the FCA absorption expected from doping level (assumed to be uniform based on homogeneous measurements of MCZ [309]) is subtracted (through the use of purer feedstock in the future) then the absorption, for example at the back, of sample #3 should approach the targeted $1-10\,\mathrm{ppm\,cm^{-1}}$ level. In addition to this, what is really promising about this silicon is the lower range of spatial-variation particularly compared to the $25-625\,\mathrm{ppm\,cm^{-1}}$ measured previously for MCZ

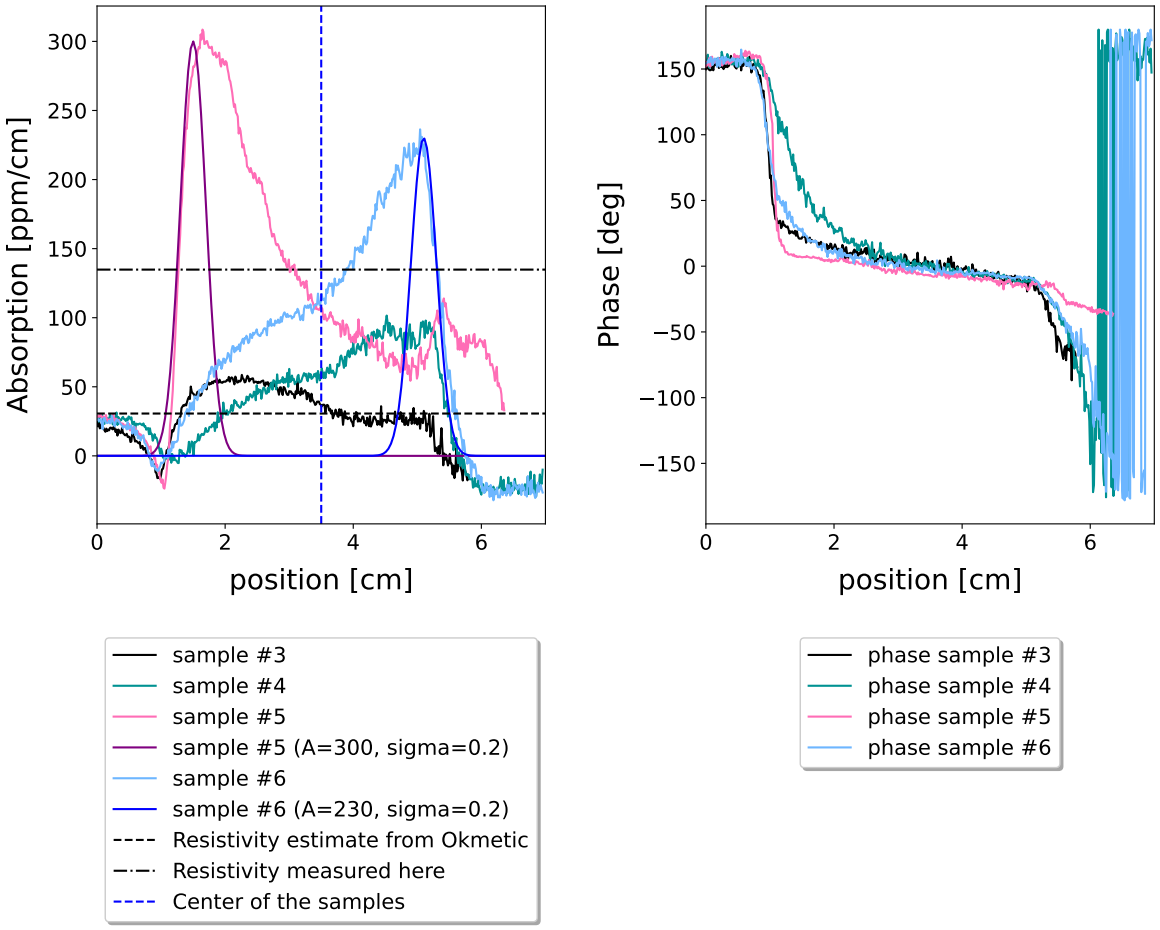

Figure 6.15: PTD z-scans of the isolated linear absorption component and phase for a-MCZ samples #3 through to #6. The expected absorption due to resistivity provided by the company (dashed) and measured (dot-dashed black) are shown. The 200 µm resolution of the PTD is shown with the overlayed gaussian distributions.

[285, 318]. Beyond the doping level discussed above, if this excess absorption is due to thermalised oxygen donors then heat treatment studies as shown by Markosyan [284] could considerably reduce their concentration by a heat treatment process that involves both rapid annealing and cooling.

Aside from the local range and small amplitude noise, some scanned samples showed a sharp changes in the millimetre scale. To consider these, the sampling depth of the setup was first evaluated through equation 6.9. With the input crossing angle $\theta_{\text{input}} = 10$ degrees was 0.2 cm. This sampling depth was checked against the slope of the front and back of the scans by fitting a Gaussian curve, as shown overlapped on the scans for both samples #5 and #6 in figure 6.15. The fitting confirmed that the sampling depth through the standard deviation of the Gaussian fit was approximately 0.2 cm. It is believed that the PTD absorption scan is equivalent to the convolution of a Gaussian function (whose width

is set by the sampling depth) with the true absorption function. In order to test this, a step function representation of the expected absorption was created with a chosen six distinct levels was created in Python. This function was then convolved with a Gaussian using the `FFTconvolve` function from scipy.signal package [169] to give an empirical fit of the absorption. This fit was optimised using the scipy.optimize package [169] to adjust the separation (in cm) and height of the levels (in ppm/cm). The fitting of the true absorption levels is shown for sample #4 on the right of figure 6.15. With six distinct and arbitrary absorption levels (pink), including the zero either side, the fitted absorption appears to be a good fit in consideration of the convoluted trace (cyan) compared to the data (black markers).

It is expected that further improvements could be made to this fitting, such as increasing the step size equal to be equal to the integer number (n) of independent samples calculated from rounding up the length of the sample divided by the sampling depth. With this theory confirmed, it is interesting to consider the significance of any features that appear to be the same size if not smaller than the sampling depth.

In particular, any sharp features such as seen on the front of sample number #5 are of interest as there is clearly a high absorption, near to the surface, that would not be acceptable for any silicon optic implemented in future detectors. To estimate the depth of this relative to the sampling depth, another arbitrary 6 level step representation of the absorption was fitted (left on figure 6.16). Although the fitted line (cyan) does not have the best agreement around the 2 mm and 5 mm positions, it is believed that an increase to n steps would provide a better fit. For this sample, it is clear that the absorption is significantly increased and close to the resolvable peak at 1 cm depth into the sample. A high surface absorption relative smaller than the sampling depth was not distinguished. However, it is important to check and fit for this to ensure suitable mitigation can be made of surface absorption. This was observed previously by Bell [10] and required surface etching in order to mitigate the high absorbing area.

Prior to applying an optical coating to any silicon substrate and integrating it into a gravitational wave detector, its absorption should be mapped with a low sampling depth in order to check, as was done here, that it's not limited by a region of high surface absorption. In parallel to this, further surface absorption measurements of small-representative samples would benefit future calorimetric and PTD studies at cryogenic temperatures. This is because these studies are expected to have a considerably reduced (if not zero) sampling depth resolution.

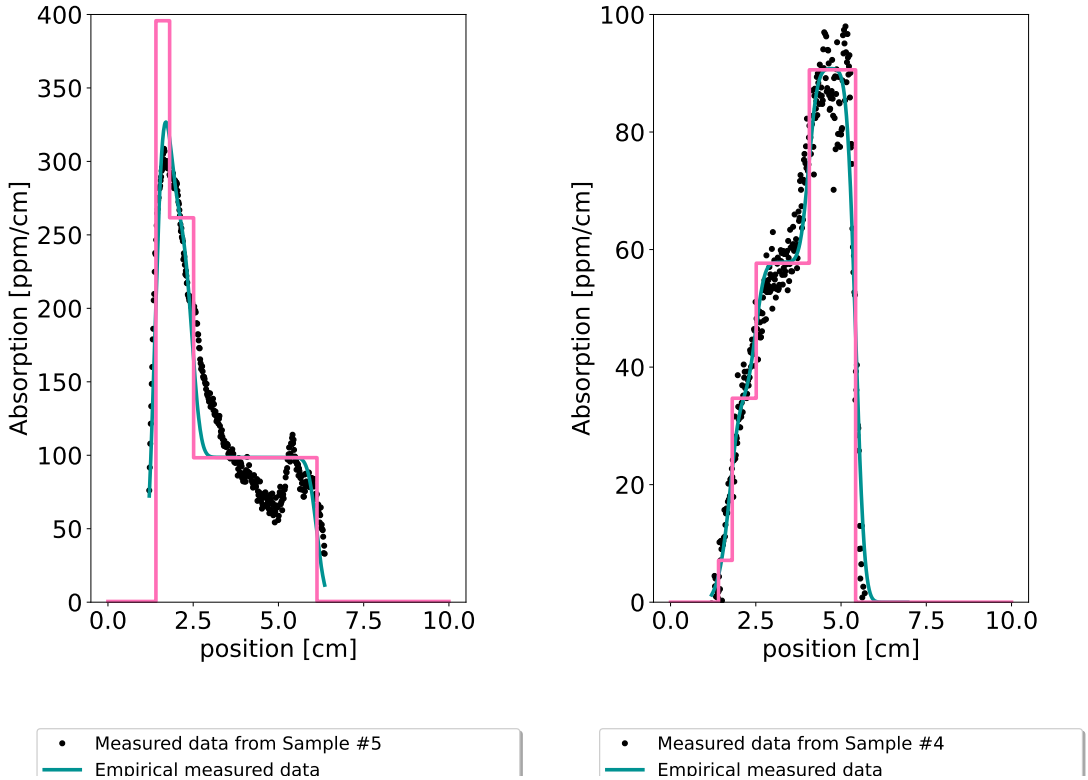

Figure 6.16: Plot of the fitted absorption profile (cyan) convolved with a discretised representation of the absorption profile (pink).

6.9 Conclusion

This chapter investigated for the first time the spatial profile of the absorption for a new type of silicon. The silicon was grown by Okmetic and known as advanced MCZ (a-MCZ) silicon. The absorption was found to be as low as the value 31 ppm cm^{-1} that was predicted from the resistivity measurements made by Okmetic. The absorption levels beyond this were expected to be excess and due to thermalised oxygen donors. It is believed that further studies could through the extension of the model (devised in section 5.3) and application of the thermal donor annihilation heat treatment steps investigated by Markosyan [284] help mitigate the effect of oxygen on the optical absorption of MCZ. However, it is easier to mitigate the precursor to the thermal donors (interstitial oxygen) and so future MCZ silicon research when scaling for applicability to the substrates of gravitational wave detectors should consider the production improvements followed by Okmetic. Although, in the case of a-MCZ, these are part of a proprietary process, it is expected that significant increases to the crucible material's purity and magnetic field strength may prevent oxygen incorporating into the silicon during growth.

To support this work and further push the capabilities of mapping optical materials this chapter expanded on an existing PTD setup at Glasgow and verified its performance compared to optical transmission measurements made in section 4.5. The performance and functionality of the setup was further explored through the description and quantitative calibration against a theoretical model.

For applications beyond gravitational waves, this technique could provide valuable information of the donor states and electrical activity of large crystalline substrate materials. In particular, the ability to probe deep into samples might allow for characterisation of indirect dopant and defect concentrations straight after the boule has been grown: given the minimal sample cutting and treatment required.

Chapter 7

Calorimetric measurements of the absorption of crystalline silicon

7.1 Introduction

The absorption of high-resistivity silicon ($> 1000\,\Omega \cdot \mathrm{cm}$) in the $10 - 20\,\mathrm{K}$ range where it is expected to be operated as a test mass substrate material for the ET-LF gravitational wave detector, has not previously been measured. In attempt to measure absorption of samples with this equivalently low-purity level, this chapter will detail work carried out to set up an optical calorimetric technique at Glasgow. This will be followed by measurements of three silicon samples each with progressively higher purity and grown with a different technique. Prior to these measurements, this chapter will first consider the suitability of current calorimetry techniques for determining the optical absorption of silicon down to the range of $10 - 20\,\mathrm{K}$. Afterwards, in consideration of the prototyping and range of different sample geometries (-cm scale) a new calorimetric measurement setup will be described.

7.2 Absorption of silicon at cryogenic temperatures

Previous studies, have measured mono-crystalline silicon across a range of both sample purities and temperature. Samples with resistivities ranging from $2 - 100\,\Omega \cdot \mathrm{cm}$ have previously shown the same absorption from RT down to as low as 6 K [262]. However, data was only published for a single sample. Further studies by contrast for different types of silicon and at both 1550 nm and 2000 nm have shown an increase in absorption down towards 60 K. This increase for MCZ was a factor of four from $3\,\mathrm{ppm\,cm^{-1}}$ to $12\,\mathrm{ppm\,cm^{-1}}$ at 100 K. As for FZ, the measured increase was 50 % from $6\,\mathrm{ppm\,cm^{-1}}$ to $9\,\mathrm{ppm\,cm^{-1}}$ [319].

The theory of absorption as set out in section 4.2, at room temperature, shows that the free carrier absorption, dominant in the near infrared and at low intensities, is linearly proportional to the free carrier concentration. However, other measurements have shown a decrease in free carrier concentration, at low temperatures, that did not track with the independently measured absorption level [262]. It is interesting to note that in contrast, independent measurements of silicon in a distinctly different amorphous thin-film form have shown a decrease of a factor of 2-3 down to 100 K [285]. Other studies of sapphire crystals, down to 6 K, found no temperature dependence. The absorption was high at $\approx 90\,\mathrm{ppm\,cm^{-1}}$ and expected to be affected by impurities or defects [320].

Compared to the measurements of crystalline silicon discussed above and measured here in chapters 2 and 6, this chapter will report on direct measurements of the absorption with calorimetry. As a result, the determination of the absorption value does not generally depend on knowledge of the specific heat, thermal conductivity and thermo-refractive index of the material. In the photothermal based techniques, knowledge of these material properties is effectively gained as the factor (R) from the measurement of a calibration sample. When this technique is implemented to measure silicon at cryogenic temperatures the sensitivity drops drastically as the strength of the thermal lens (from which the absorption is scaled) is reduced significantly due to the increase in the thermal conductivity of silicon at low temperatures. As a result, recent measurements showed significant error in the absorption for high-resistivity silicon at 60 K [319] and an inability to measure down to the $10 - 20$ K where the ET-LF mirrors will be operated. In addition to this, photothermal deflection (PTD) would require the inclusion of an absorption calibration sample in order to re-evaluate R at every temperature. As a result, a calorimetric technique is considered here.

7.3 Theoretical model of an optical calorimeter for silicon materials

Calorimetry is the measurement of a sample's temperature changes in response to an applied heat. In contrast to PTD, the sensitivity of a calorimeter increases as the specific heat capacity drops and so at cryogenic temperatures approaching 20 K, relative to RT, the calorimeter is expected to have a significantly increased sensitivity. The other advantages of calorimetry are described by Roshanzadeh [321] and will be considered throughout this chapter. For distinct monolithic optical materials, calorimetric measurements of a sample of mass (m_{sample}) across a range of temperatures can be used to determine the heat capacity ($c_{\text{sample}} = \frac{C_{\text{sample}}}{m_{\text{sample}}}$) or applied heating power (Q). To determine these, the thermal model of the sample (S) will be considered in vacuum and inside a cryostat. The sample is mounted onto a platform (P) that has a temperature (T_P) and conductive thermal resistance (R_{SP}). The sample is then surrounded by radiation shielding (V) that is at temperature (T_V). A vacuum environment will be created such that heat will only be transferred through conduction (Q_{SP}) and radiation (Q_{SV}).

The other bodies that are not considered for this model but are physically present in the cryostat chamber will be discussed. A temperature sensor of mass is placed on to the sample with a strong thermal connection R_{ST} (where $R_{ST} << R_{SP}$). The mass (m_{sample}) is also sufficiently low enough that the sensor does not contribute its own thermal mass ($C_{\text{sensor}} << C_{\text{sample}}$). The model will only consider the single thermal body of the sample during measurement. The required number of dimensions for the model can be set by considering the thermal diffusion length (λ_{T}) relative to the silicon sample's geometrical scale.

$$\begin{aligned} \lambda_{\text{T}} &= \sqrt{\frac{k}{c\rho}}, \\ \tau_{\text{diff}} &= \frac{\Delta x^2}{\lambda_{\text{T}}} \end{aligned} \tag{7.1}$$

For the samples measured here, the maximum distance between the heating region and the edge of the sample $\Delta x \approx 0.05\,m$. For the temperature dependent properties of silicon (see figure A) the diffusion timescale ranges from 5 ms at 20 K, 74 ms at 123 K and lastly 270 ms at 300 K. Compared to targeted measurement timescales in the range of $1 - 100$ s

it assumed therefore that the silicon has a uniform change in temperature, due to heating, spatially across its extent. It is expected therefore that the temperature of the sample $\frac{dT_S}{dt}$ in such a system should be sufficiently described by a 1D ordinary differential equation of the form (ODE)

$$\frac{dT_S}{dt} \;=\; \frac{Q}{C} \;-\; \frac{1}{C\,R_{SP}}\big(T_S - T_P\big) \;-\; \frac{\sigma\,\epsilon\,A}{C}\,\big(T_S^4 - T_V^4\big). \tag{7.2}$$

The thermal masses of the platform (C_P) and radiation shield (C_V) are assumed to be large (where $C_P, C_V >> C_{\text{sample}}$) such that their own temperatures are approximately unchanged over the short measurement timescale (t). If the sample and radiation shielding is at a low-cryogenic temperature, then the heat lost due to radiation is expected to be low such that ODE simplifies to

$$\frac{dT_S}{dt} \;=\; \frac{Q}{C} \;-\; \frac{1}{\tau_{SP}}\big(T_S - T_P\big). \tag{7.3}$$

This expression solves to give the temperature response of the sample ($T_s(t)$) and for a large R_{SP} this further reduces to give a response that is linear with both heat applied and the temperature dependent thermal mass of the sample.

$$\begin{aligned} T_s(t) &= T_{S_0} \;+\; \frac{Q}{R_{SP}}\left[1 - e^{-\frac{t}{\tau_{SP}}}\right], \\ T_s(t) &\approx T_{S_0} \;+\; \frac{Q}{C}\,t \quad \text{for } \big(\frac{t}{\tau_{SP}} \ll 1\big). \end{aligned} \tag{7.4}$$

Independent of resistivity, the specific heat capacity (c) of crystalline silicon has been shown to follow the same trend with temperature [322] (see figure 6). If heating at 20 K compared to room temperature, the temperature increase rate ($\frac{dT_{\text{measured}}}{dt}$) would be $\approx \times 240$ higher for the same heat applied. Depending on the time constants associated to the thermal coupling of the silicon to the surrounding environment and the timescale of the measurement (t_{measure}) it is expected that only a proportion of the heat applied is expected to stay in the silicon. The responsivity of the silicon (X) will therefore act to reduce the measured ($\frac{dT_{\text{measured}}}{dt}$).

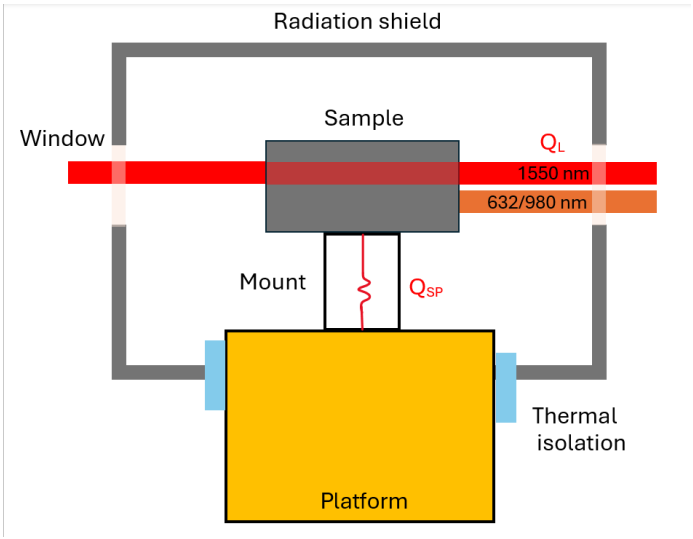

Figure 7.1: Diagram of the optical calorimeter setup. The sample is thermally connected through the conductive pathway of the mount and into the platform. There is also the radiative pathway from the sample to the radiation shielding. The 1550 nm measurement and 632.8/980 nm calibration beams are shown passing through the window/s and to the sample. The platform is thermally isolated (blue) from the radiation shield.

In order to minimise the heat lost to the surrounding, the ideal measurement environment will now be considered. The target absorption sensitivity was $1\,\mathrm{ppm\,cm^{-1}}$, which for a transmitted pump power of say $2.5\,W$ through a 4 cm thick sample equates to $10\,\mu\mathrm{W}$ of heating power. For the samples measured throughout this thesis, the mass of the samples were between $17 - 55\,\mathrm{g}$. As a result, the minimum expected temperature gradient (for sample mass 55 g and R=1) at $30\,K$ is $\approx 10\,\mu\mathrm{Ks^{-1}}$. Over 100 s this would equate to a 1 mK temperature increase.

For a chosen piece of silicon of mass, it is therefore possible with an accurate measurement of induced temperature change ($\mathrm{d}T$) to evaluate the recovered fraction (R) for the corresponding heating power (Q) also referred to here as the calorimetric response

$$R = \frac{cm\frac{\mathrm{d}T}{\mathrm{d}t}}{Q} \leq 1. \tag{7.5}$$

For the setup as described, this response should be independent of the chosen heating method. In the case of silicon, if the surface heating power is provided through optical absorption at a wavelength below the bandgap, then all of it will be absorbed in the surface. This known power is the calibration ($P_{\mathrm{calibration}}$). However, for NIR wavelengths between $(1550 - 2000)$nm in a region of relative transparency more light will propagate

through the silicon and so only a fraction of the relative power will be absorbed across the bulk of the sample (P_{bulk}). As the temperature change should be independent of the method of heating, it is possible to form a responsivity equivalence between both heating lasers.

$$R = \frac{cm\frac{\mathrm{d}T}{\mathrm{d}t}}{P_{calibration}} = \frac{cm\frac{\mathrm{d}T}{\mathrm{d}t}}{P_{laser} \times A_{1550}}, \qquad A_{1550} = \frac{\frac{cm\frac{\mathrm{d}T}{\mathrm{d}t}}{P_{laser}}}{\frac{cm\frac{\mathrm{d}T}{\mathrm{d}t}}{P_{Calibration}}} \tag{7.6}$$

This absorbance can be further scaled to give an absorption in account of the samples thickness (t_{sample})

$$\alpha = \frac{A_{1550} \times 10^6}{t_{\text{sample}}}\,[\text{ppm} \cdot \text{cm}^{-1}]. \tag{7.7}$$

A previous study used an electrical heater varnished onto the barrel to provide a known, electrical heating calibration [262] . Heating instead with a known optical power offers two benefits. With less internal wiring, the number of connections made to the sample was reduced, this also benefited the small size of the cryogenic chamber and samples.

7.4 Setup of a cryogenic optical calorimeter

The cryostat used was a Montana Instruments Cryostation S100 cryostat [324]. This is a closed-cycle cryostat, operating without requiring an intake of liquid helium or nitrogen. In principle, the platform (also called stage 2 see figure 7.3) can reach 4 K and the radiation shielding 28 K (stage 1) without any additional components or heat loads included in the cryostat. The cryostat by default adjusts the cooling power applied to the different components through a loop (controlling the cryocooler and compressor) in order to reach and stabilise at the targeted temperature. The physical extent of the platform is shown on figure 7.4 (A) and the coverage of the radiation shield around this and the sample is shown in figure 7.3.

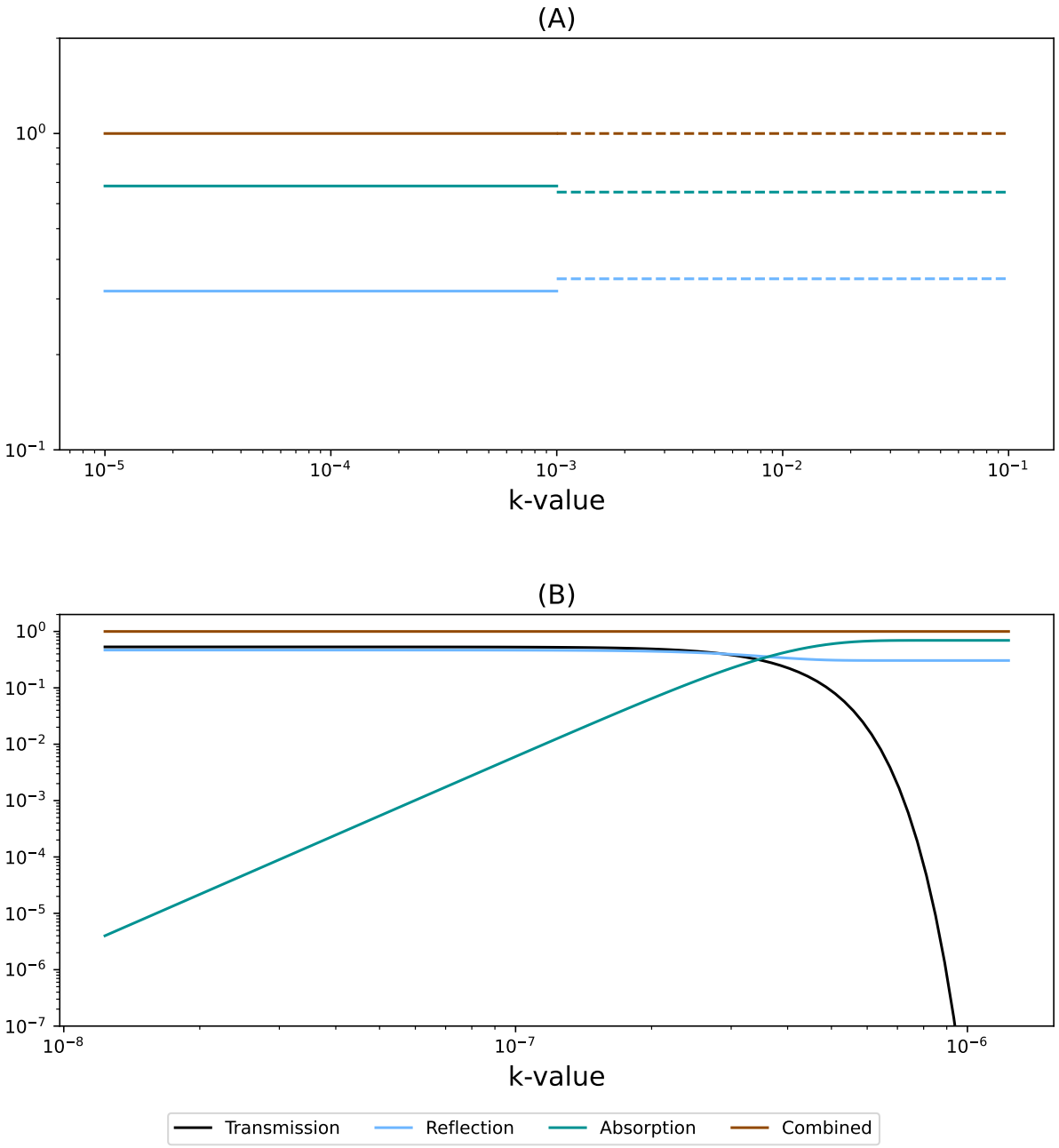

Figure 7.2: The normalised power for a p-polarised beam incident at 0 degrees onto a thick (4 cm) silicon sample. The lines on figure (A) shows the fixed absorption, transmission and reflection levels at 632.8 nm (dashed) (taken from known refractive index and extinction data [323]) and 980 nm. Figure (B) shows that the sample is in the transmissive regime across the extinction ranges expected here and that the total absorption is linear with the extinction.

Initial studies investigated the thermal isolation with the QM silicon sample in place. The sample was initially placed on a machined aluminium block such that it was close to the centre of the windows for both the radiation shields (1 ”) and vacuum housings (50 mm). The sample was mechanically held in place and DT-670 temperature sensors were attached to it with cryogenic varnish [325]. With the sample positioned, the cryostat chamber was sealed, before being evacuated with a scroll pump to 1×10^{-2} mBar followed

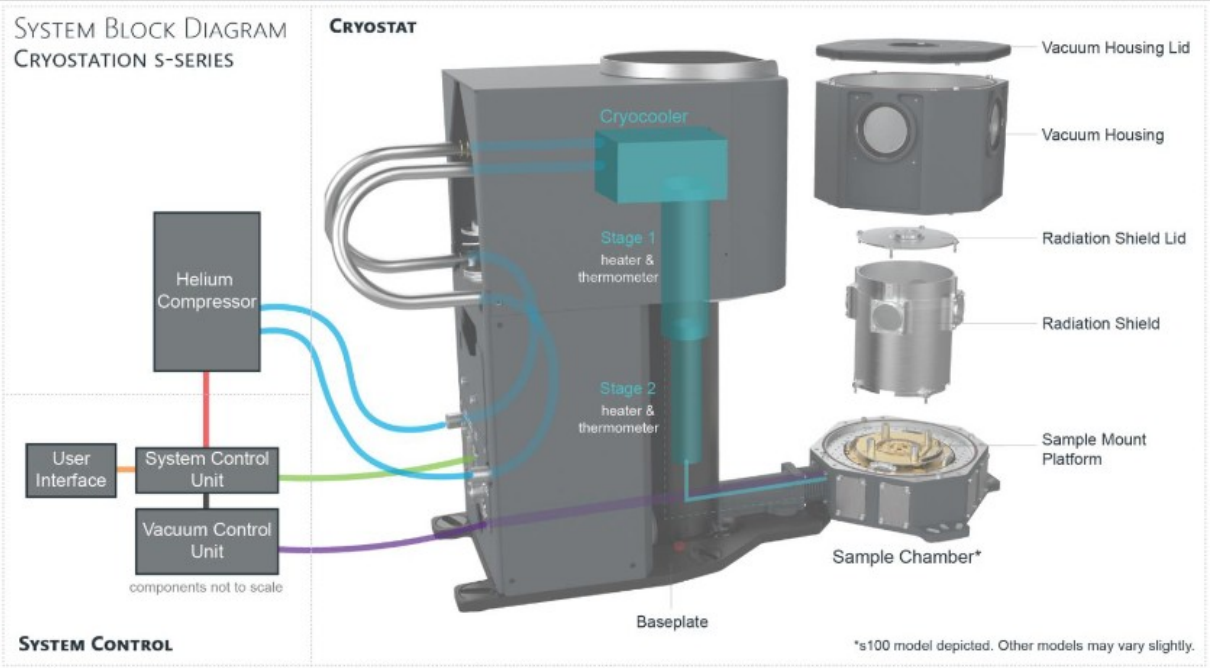

Figure 7.3: Layout of the Montana Cryostation S100 cryostat [324]. Stage 1 is thermally coupled to the radiation shield and stage 2 is coupled to the platform.

by a turbomolecular pump to reach 1×10^{-5} mBar. After this point, the cryostat was set to cool down from room temperature. Once it was close to the minimum temperature, the calibrated laser, initially a low power 3 mW 632.8 nm source was directed in towards the sample[1].

Initial studies investigated the thermal isolation of the sample. As target measurement samples had different geometries, it was important to consider a range of mounting solutions. The sample was first placed on a solid aluminium block (see figure 7.4 (A)) and with no direct isolation a baseline temperature of 23 K was reached. However, at this temperature there was evidently significant temperature cycling that would make it difficult to measure an average temperature gradient. The oscillation was expected to be as a result of an internal control sequence that was dynamically adjusted the cooling power depending on the platform's temperature. On a subsequent run, the isolation of the sample from the platform was significantly increased by varying the amount of thermal isolation with few-mm thick pieces of Teflon (PTFE) on either side of the sample. The baseline temperature reached was 27 K, but there was still temperature cycling.

1. The 632.8 nm source was initially folded down from a parallel and higher up optical axis. The second mirror that passes the beam into the cryostat is shown in figure 7.4 (C)

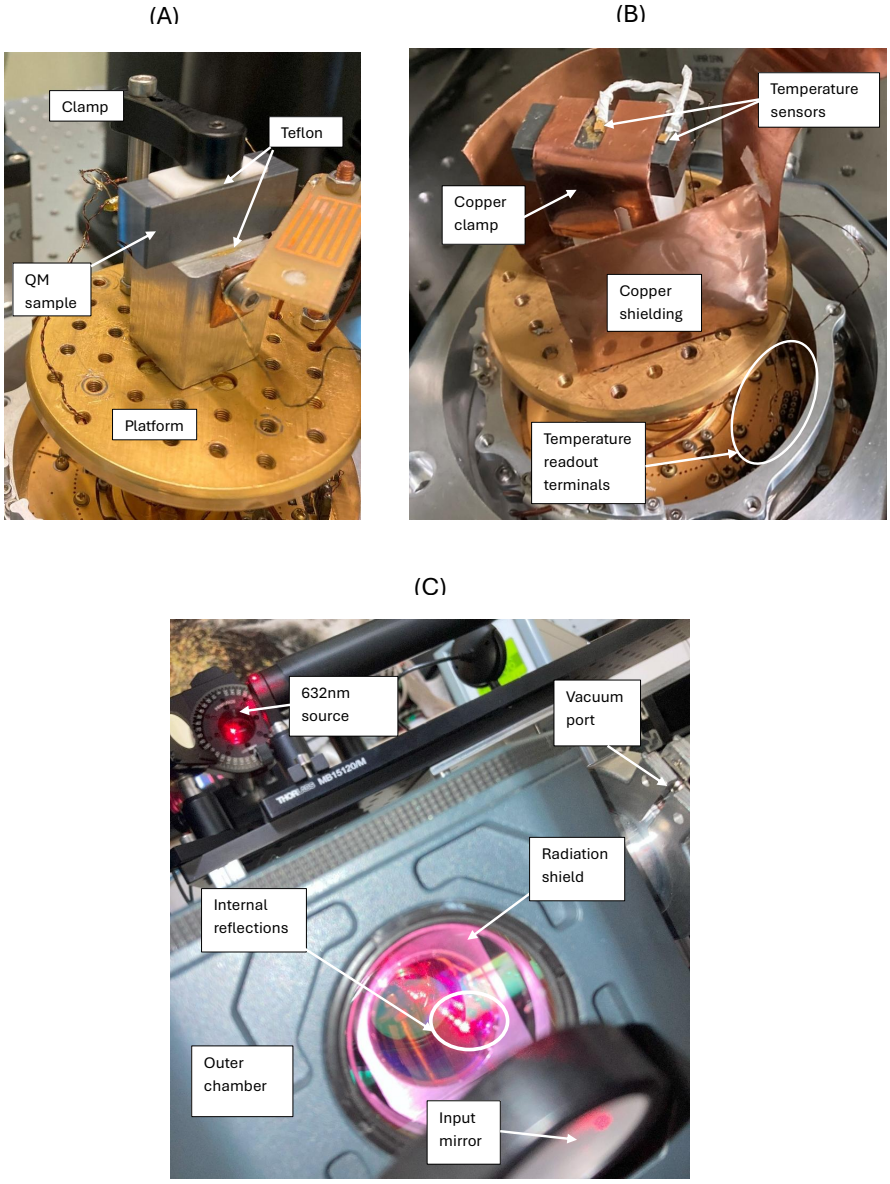

Figure 7.4: Calorimeter version 1 for measuring the QM sample. The copper shielding at the back (B) was rotated round during measurement such that the 1550 nm could pass from the sample and outside the cryostat without clipping.

The gradient response when heating with the calibration heating source (632.8 nm laser) was $\times 5$ larger and now represented 25% of the expected response. With this improvement, there was confidence that further isolation would shift the setup closer towards the simple linear calorimetric heating relation, where nearly all the heat that is put into the sample

essentially stayed (over the measurement duration). The temperature cycling was reduced, although still present, as the isolation was further improved (through the subsequent sections). Arising as a result of the cryostat's control sequence, this was later bypassed by manually fixing the cooling power prior to measurement windows.

7.5 Determining the accuracy of the optical calorimeter

The required absolute accuracy for the temperature sensors was set at the 50 mK level across the cryogenic temperature range ($10-123$ K). This is because at the low temperature of 10 K the rate of change of the specific heat capacity is extremely high and so would couple through, for this threshold, an absolute error of 1.7 % to any measurement of the heating power. In order to achieve this accuracy a range of calibrated sensors DT-670[2], cernox-1070 and cernox-1080 [326] were considered. The calculations performed in order to ensure their accuracy will now be discussed.

In a standard 2-wire sensor configuration, a current is passed through the wires and the voltage is measured. At a given temperature, the measured voltage will be proportional to the temperature dependent resistance value. The thin wires required for high thermal resistance would contribute a high electrical resistance and as a result could lead to high systematic offsets in the evaluated temperature [327]. To mitigate this and improve the accuracy, 4-wire sensing was used. The current was still delivered through the previous two wires (denoted $I+$ and $I-$). However, an additional pair of wires (denoted $V+$ and $V-$) carrying a low current ($\leq$ pA) were used to measure the voltage drop directly across the sensor and independent of this dominant offset.

All the sensors used were provided in a compact SD packaging and had a mass of 40 mg which is considerably less than that of the samples measured [328]. The packaging was gold-plated which was favourable for reducing the impact of any direct heating of the sensor through any stray light in the system. The sensors also had rigid anchor points for the electrical connections, which enabled them to easily be reattached without breaking[3].

---

2. In contrast, an uncalibrated DT-670 calibrated sensor has a significantly higher sensor (calibration) error of at least 250 mK from 2 K through to 300 K and so was not considered.
3. This was preferred over the smaller bare chip equivalent for each of these sensors, as their wired connections would require a lot of care to avoid breaking.

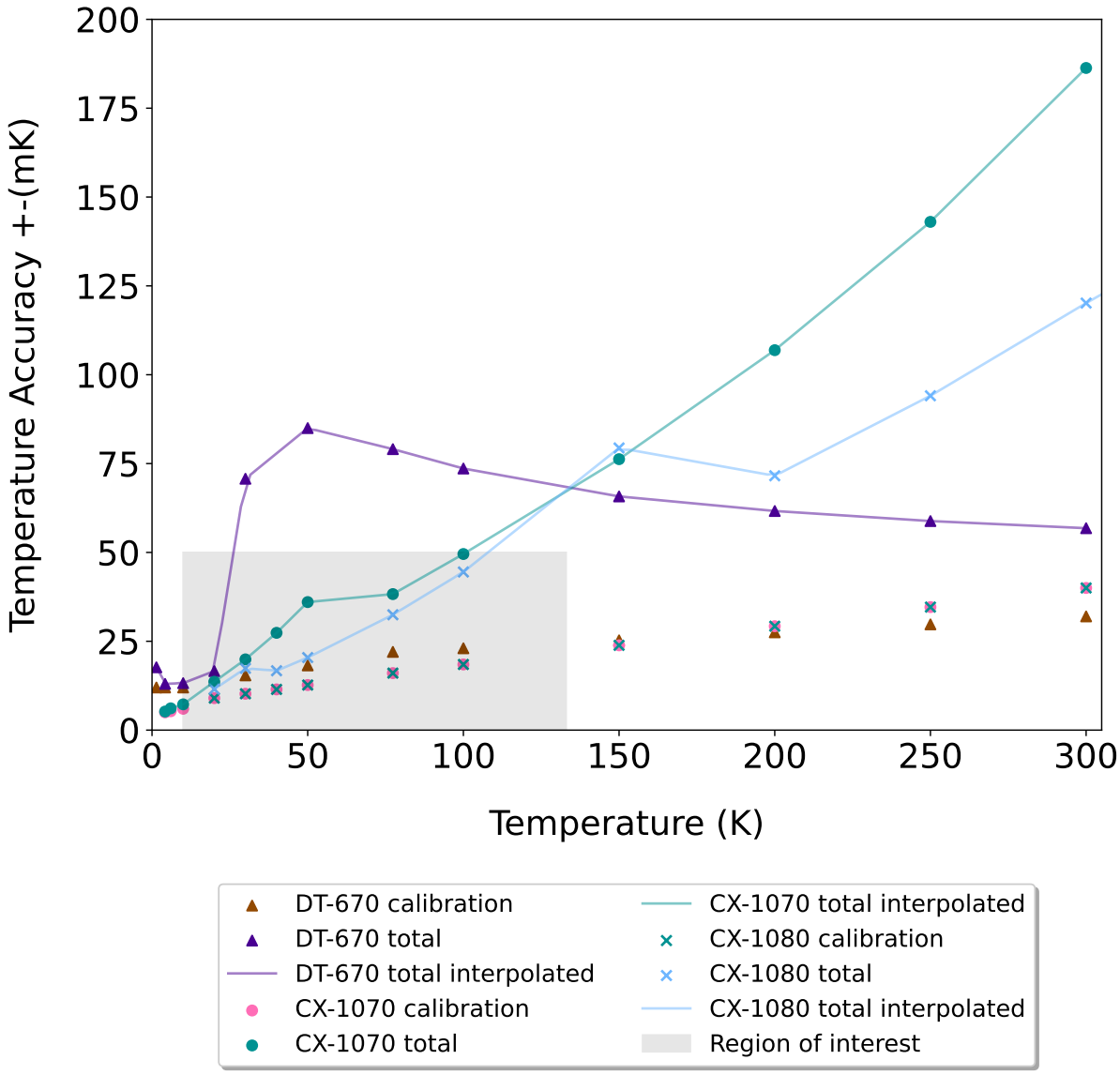

Figure 7.5: The accuracy of three distinct temperature sensors DT-670, CX-1070 and CX-1080 [326] is shown for the calibration alone and then when combined (in quadrature) with both the resolution and electronic errors evaluated in the main text for the Lake Shore 336 controller [329].

The total uncertainty in the absolute temperature (σ_{total}) has multiple factors, all of which typically vary with temperature. The accuracy of the calibration for the three sensors considered here are given in catalogue (appendix D) [327] and plotted for comparison on figure 7.5.

Across the temperature range from $10-70\,\text{K}$ the calibration accuracy of the Cernox sensors was approximately $6\,\text{mK}$ better than the DT-670 sensor. The sensors were connected through to a Lake Shore 336 controller [329]. This controller had a voltage resolution of $10\,\mu\text{V}$. For the DT-670 sensor, when scaled by the voltage to temperature responsivity the value steps from $20\,\text{K}$ to $30\,\text{K}$ to be $\approx 4\,\text{mK}$. It approximately stays at this level up

to room temperature. There is also electronic uncertainty ($\sigma_{electronic}$) to consider. This was evaluated for the DT-670 sensor by first taking the voltage uncertainty (percentage shown [329]) at distinct temperature steps and scaling it by the voltage to temperature responsivity data [327]. Again, following the significant drop in the responsivity from 20 K to 30 K there is an increase in the electronic error. At 30 K the value is 60 mK. This then peaks at 50 K at 60 mK before falling gradually down to 47 mK at room temperature. The combination of all these errors in quadrature gives the total measurement uncertainty

$$\sigma_{\text{total}} = \left(\sigma_{\text{calibration}} + \sigma_{\text{electronic}} + \sigma_{\text{resolution}}\right)^{0.5}. \tag{7.8}$$

The total uncertainty for the DT-670 sensors (see figure 7.5) was outwith the target precision of 50 mK (set at 10 K) from 30 K upwards. However, it had a low uncertainty of 60 mK from 123 K through to room temperature.

In order to reach improved accuracy at lower temperatures Cernox sensors were used. Their measurement resolution was converted to the temperature equivalent by scaling the resistivity by the resistivity to temperature ($R-T$) response [327] instead of the measured voltages. For the CX-1080 sensor this was evaluated to be 2 mK at 20 K and rose gradually to 20 mK at room temperature. The electronic uncertainty is then evaluated by scaling the uncertainty in by the same ($R-T$) response. As these are negative temperature coefficient sensors, their semiconductor materials drastically change their ($R-T$) response. As a result, the electronic uncertainty is considerably reduced[4]. At 30 K for the Cernox Sensors, electronic uncertainty is approximately a factor of four better at 15 mK. The total uncertainty for the Cernox sensors (see figure 7.5) stayed below the 50 mK (set at 10 K) from at least $10-100$ K. Above which the electronic error dominated such that at room temperature the total error for the CX-1080 was a factor of two higher than the DT-670. Therefore, for calorimetric measurements made across a wide range of temperatures, both sensors were considered. In fact, it was standard practice here to use two temperature sensors to mitigate absolute error in the measured temperature. These were interchanged at different points between the sensors discussed, depending on the temperature range of interest for a given measurement.

4. For example, the Cernox CX-1080 used drops from 6200 Ω to 130 Ω from 20 K to room temperature (a factor of sixty reduction). Over the same range, the DT-670. only drops its measured voltage (due to resistance) by a factor of three in comparison.

The heating power of a calorimeter which intentionally uses a resistive heating element (rather than a heating laser) would change with the resistivity at a given temperature. Independent knowledge of this resistivity would therefore be required to validate the heating power. When using an optical laser, uncertainty could arise from the excess light loss and/or scattering of light towards the temperature sensor, leading to direct heating of the sensor itself. For the 632.8 nm source initially used, there was uncertainty in knowing the transmission due to the cryostat optical feedthrough window having limited transmissivity. This was mitigated by measuring the value without the sample in place, removing the back windows before reinstating them and proceeding on to measure. The measured transmissivity was calculated for a single pass to be 25 % to the sample and a further 65 % passing onto be absorbed in account of the close to normal incidence reflection.

To minimise this systematic uncertainly, improve the optical throughput and reduce any internal reflections from the calibration the source was later swapped for a 980 nm at which wavelength the transmission of the windows was significantly improved. For this wavelength, the measured transmissivity was calculated for a single pass to be 87 % up to the sample and 65 % passing onto be absorbed. This represented a $\times 3.5$ increase in the absorbed power for a given input power and a significant reduction in concerns of secondary reflections.

7.6 Cryogenic measurements of the Quasi-monolithic samples

After the initial testing the setup was modified from figure 7.4 (A) to (B). The notable adjustments were a further increase in the isolation by placing the clamped sample on top of a 2 cm tall block of Teflon to try and further increase the thermal responsivity (R) from 0.25 and towards the value of one (expected for the ideal isolation described in section 7.3). In order to cool the sample down faster He gas was passed in a process called cold-gas exchange. Prior to cooling the system was purged with the gas and then during operation a bleed valve (with a measurable pressure increase on the pressure gauge) indicated the levels flowing and which could be expected in the chamber. It was observed that the cold gas was effective in thermally shorting the connection from the isolated sample to both the stages. The platform in the absence of prolonged heat loading was typically well below the target temperature of the sample, and so this short between the two was always

favourable. However, the radiation shield typically reached 50 K and so if the sample was below this it would instead be drastically heated up. The cold gas exchange was therefore useful in expediting the initial cooldown of the sample towards 50 K. After this point, the radiative cooling effects for this degree of thermal isolation were shown to dominate.

Previous studies at the University of Glasgow by a colleague Peter Murray showed that, in order for cool silicon samples down towards 10 K, a shroud thermally anchored to the platform was required. This reduced the minimum temperature reached and therefore the susceptibility of the sample to ambient heat loading from both the Montana cryostat's own radiation shield and the ambient environment outside the cryostat. As a result, copper shielding was placed around the QM sample figure 7.4.

The first cryogenic measurement run proceeded with the QM sample in place and with only one DT-670 temperature sensor attached (middle of the sample). The sample cooled from room temperature to 28 K in 17 hrs. Once minimum temperature was reached, the effects of heating with the red calibration laser (632.8 nm) and of (separately) heating with the measurement laser (1550 nm) were measured, by turning the relevant laser on for a period of time and monitoring the temperature of the sample. Prior to the measurement, the power of each beam was measured and entered into a real-time record captured with a graphical user interface (GUI) software written by the author in LABVIEW [5] [330]. After this, provided that the background gradient had been relatively stabilised, each laser was turned on by manually revealing it from behind a blocker. Within human reaction time, a timestamp was instantaneously started in the GUI.

The sample was cooled to a minimum of 27.7 K. The first calibration heating steps are shown on figure 7.6 (A). Over the temperature trace for the sensor (red line) the fitted gradient over the duration of the heating window is shown (cyan line). Then for each gradient, an offset is subtracted to account for background drifts in the system prior to the heating window (light blue) and the recovered heating gradient after subtracting the offset is plotted (pink). For a small amount of heat applied using the red laser (20 μW), the recovered fraction (R_{633}) (first defined in equation 7.5) ranged from 0.65-0.73 (see figure 7.7) compared to the expected value of 1 for the ideal isolation. When the power was increased to 80 μW this increased to 0.87. Shortly after this, the sample was decreasing at a steady state of gradual cooling from 28.7 K and so measurement proceeded at the wavelength of interest (1550 nm) shown in figure 7.6 (B). For this wavelength, the fitted gradient over the duration of the heating window is shown (dark blue). Then for each

5. The LABVIEW program simultaneously interacted with the Lake Shore model 336 temperature controller and the Montana s100 cryostat.

gradient, an offset is subtracted to account for background drifts in the system prior to the heating window (indigo) and the recovered heating gradient after subtracting the offset is plotted (violet). Two measurements were made at 1550 nm with a heating power of 200 μW and the recovered fraction R_{1550} was 0.4 and 0.41. As the recovered power ($0.4 \times 200\,\mu W = 80\,\mu W$) was approximately matched (80 μW) between both, it was the fairest point of comparison. The absorption evaluated through equations (7.6-7.7) and in account of the samples length (4 cm) was 11.4 % cm^{-1} (shown on figure 7.8). The 1550 nm heating power was reduced to ($40 - 80\,\mu$W range) in order to check the linearity of R_{1550} three further heating steps (shown in 7.6 (B)) were made. Similar to the low power R_{633}, the R_{1550} was slightly reduced at low powers. No linearity of R with power for either beam measuring at ≈ 28 K was established, given the finite sampling and the small induced temperature gradients, relative to the background gradient.

At 30 K, a small temperature step (≈ 2 K), another absorption measurement was made. The calibration also showed a significant reduction in the recovered fraction ($R_{633} \approx 0.6$) for small input powers, but similar levels to the 27.7 K step ($R_{633} \approx 0.84$) for a heating power of 80 μW. For measurements with the 1550 nm beam, the recovered power showed a remarkable linearity ($R_{1550} \approx 0.42 \pm 0.01$) over one order of magnitude of heating power $200 - 2000\,\mu$W. The absorption was evaluated to be higher at 12.8 % cm^{-1}. Increasing the temperature further to 40 K and the background oscillation (due to the cryostats cooling control) increased to 6 mK peak-trough and over similar timescale to the target measurement [6]. The evaluated absorption here high powers was 12.6 % cm^{-1}. However, there were significant variations with power due to the poor fitting and evaluation of R_{1550} at low heating powers. Increasing the base temperature to 58 K and the temperature oscillations (see figure 7.6 (C)) were even more pronounced (±10 mK) and the specific heat capacity was significantly higher. Instead of assessing the linearity of the response with power, a high power was simply input to maximise the signal. The recovered fractions were $R_{633} \approx 0.82$ and $R_{1550} \approx 0.37$. These evaluated to an absorption, in proximity to the other values, of 11.8 % cm^{-1}.

Beyond this temperature and up to 115 K (in close proximity to Voyager's proposed 123 K target operation temperature) and for the highest heating powers $R_{632} \approx 0.9$ ($20\,\mu W$) and $R_{1550} \approx 0.34$ (3 mW). This evaluated to a reduced absorption of 9.5 % cm^{-1}. The cryostat was then returned to room temperature (RT), the vacuum environment was held, and further measurements were made. Unfortunately, the laser power of the 632.8 nm HeNe source was too low at 3 mW to give a distinct temperature increase. In order to evaluate an absorption, the recovered fraction was assumed here to be the average of the other

6. This was expected to be coupling from the Cryostats cooling control. The frequency of this was 20 ms, independent of temperature.

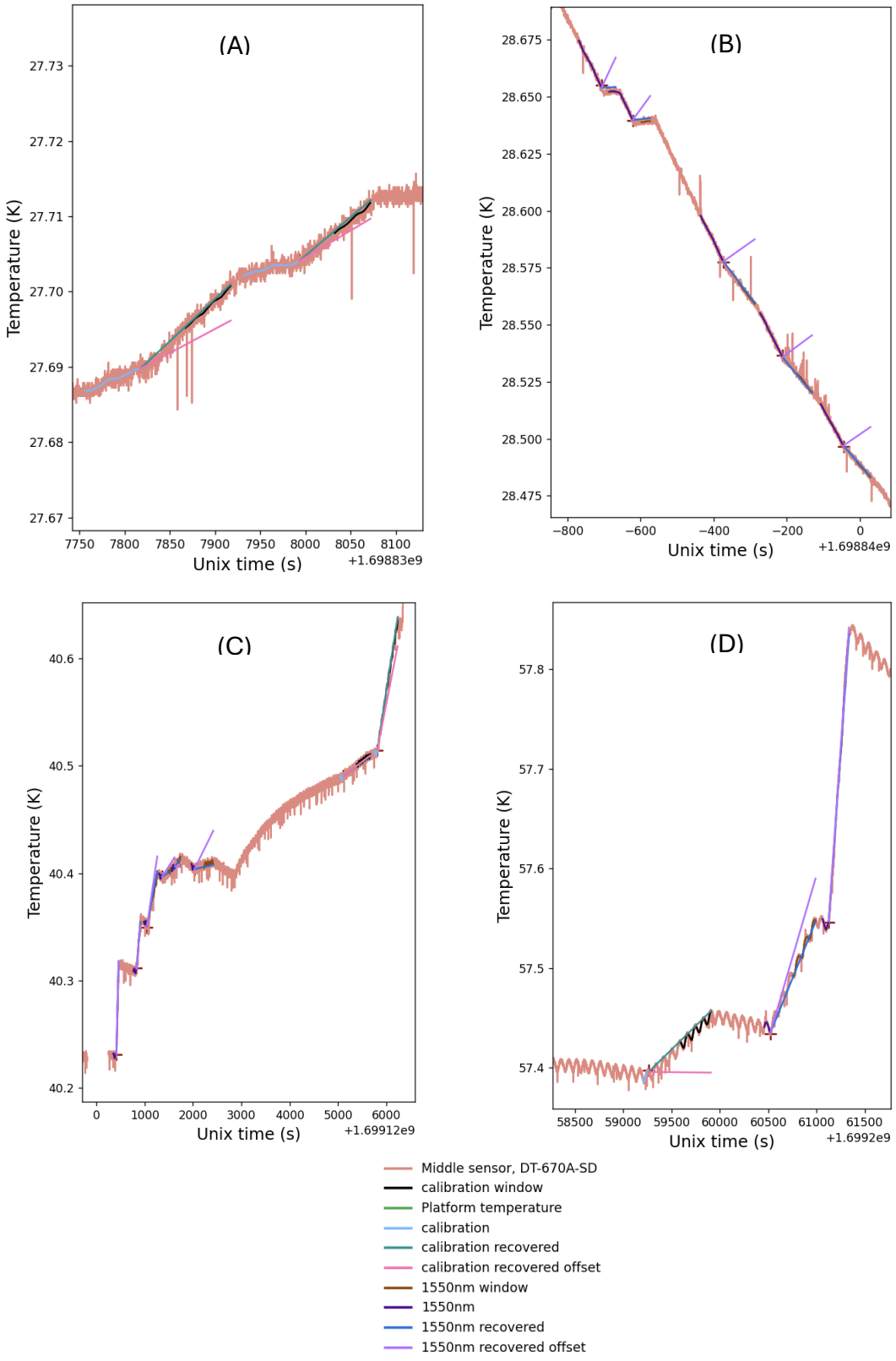

Figure 7.6: Measured temperature-time series for the QM sample during both calibration and measurement windows. (A-B) show the temperature step $\approx 28\,\mathrm{K}$, (C) $\approx 40\,\mathrm{K}$ and (D) $\approx 58\,\mathrm{K}$.

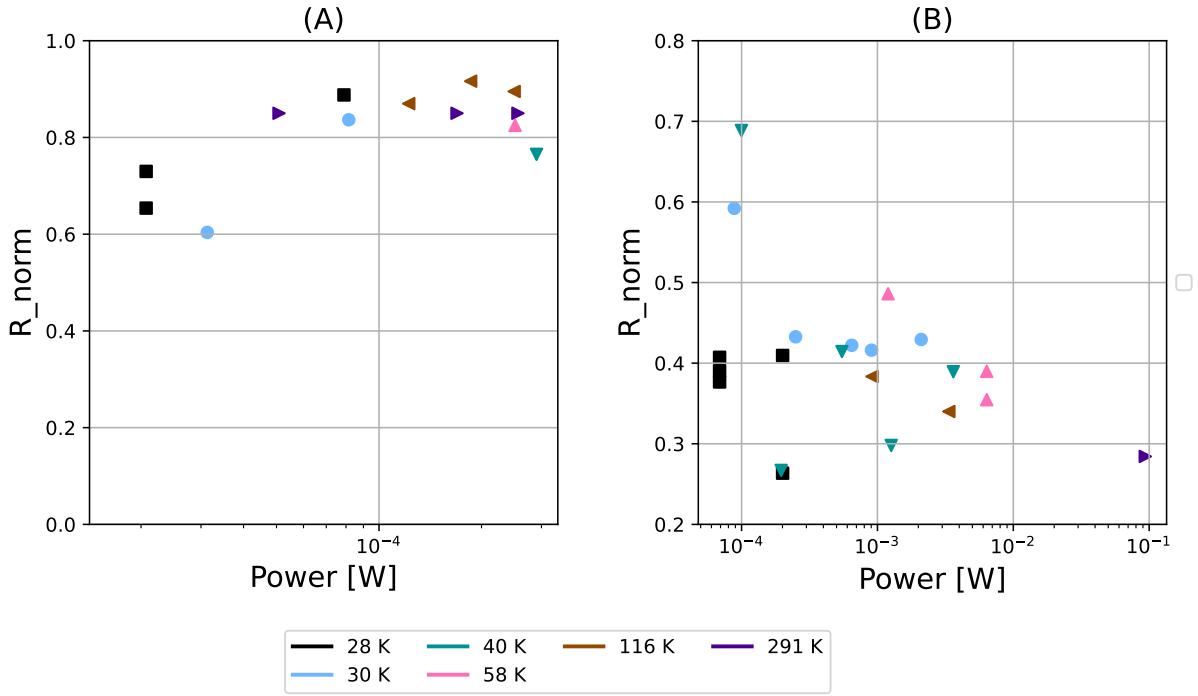

Figure 7.7: Recovered heat fractions for measurements of the QM sample that include the background temperature gradient offsets discussed in the main text.

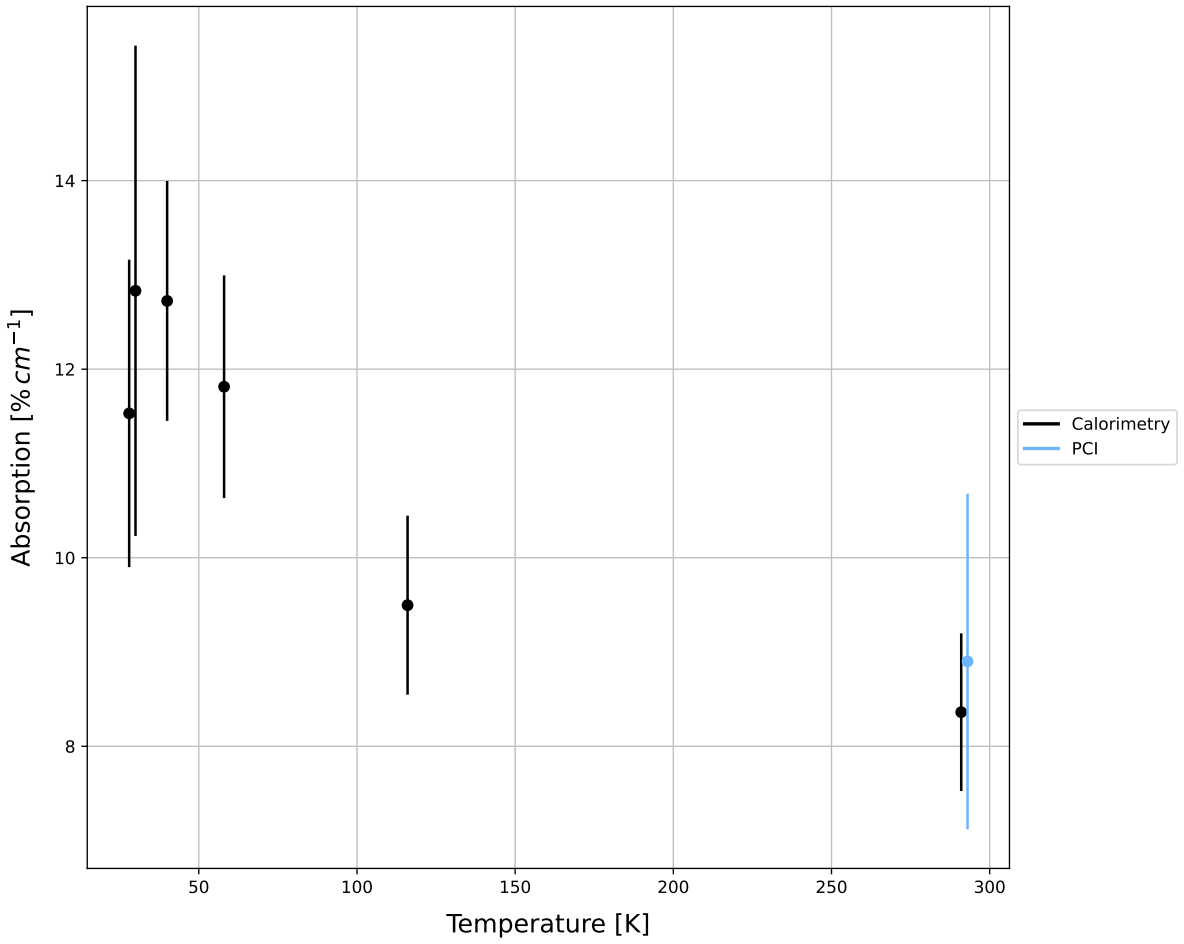

Figure 7.8: Temperature dependent absorption data for the QM sample.

measured values (at different temperatures) $R_{633} \approx 0.84$. As the previously measured R_{633} had no clear temperature dependence, the underlying thermal isolation of the sample was expected to carry from 27 K to RT. Given the distinctly higher power available with the 1550 nm beam, a measurement of its $R_{1550} \approx 0.28$ was made. This conditional absorption value was evaluated to be $8.4\,\%\,\mathrm{cm}^{-1}$ which was 50 % lower (due to the lower R_{1550}) than the peak of $12.8\,\%\,\mathrm{cm}^{-1}$ identified at 30 K. This value is also in close agreement with the 8.9 % measured in the PCI setup (see chapter 5). Although further measurements were not made, errors evaluated for the clearest heating gradients (typically at the highest powers) showed that error on this was comparably small and that the absorption increase was most likely genuine.

These are the first cryogenic absorption measurements that have been performed on directionally solidified (termed here as quasi-monolithic) silicon. Following the extensive research in chapter 5 this 50 % absorption increase upon cooling to $\approx$ 30 K should be measured again for boules grown at a higher purity to evaluate if measures taken to reduce the absorption of QM silicon also reduce this temperature dependence. Otherwise, it could significantly increase the heating of a test-mass if QM silicon was operated as at ET-LF test mass material at 20 K.

7.7 Cryogenic measurements of mid-resistivity CZ

This section will consider the setup and measure of a CZ silicon sample. This sample was 3.6 cm long and 2.5 cm in diameter. Although the resistivity was not known, the bulk absorption was previously measured to be $5000\,\mathrm{ppm\,cm}^{-1}$ at 1550 nm [255]. This would equate through a rearrangement of equation 4.4 to a resistivity of $\approx 20\Omega$·cm. Not only was this absorption considerably less (by a factor of $\times 20$) than measured for the QM sample, but it was expected to be closer to the ET-LF ITM design target of $20\,\mathrm{ppm\,cm}^{-1}$ (shown in table 1.1) and closer still to the higher $1000\,\mathrm{ppm\,cm}^{-1}$ target for the ETM (justified in chapter 5). Although, there is limited absorption data of CZ silicon in this range it was expected that cryogenic measurements would be applicable to other types. This sample was also of interest as its absorption was expected to be dominated by thermal donors (TDs) as opposed to the intrinsic doping. This followed after a $800°C$ heat treatment (having increased in absorption from $\approx 1000\mathrm{s\,ppm\,cm}^{-1}$ [255]) and discussion of TDs in 5.3. It is not clear if and how TDs contribute to the free carrier concentration (through their ionisation) down at cryogenic temperatures, compared to foreign doping atoms and

up at room temperature. At room temperature, they have been shown to dominate the absorption for silicon samples [284] such as the one here. As it is not currently clear if they can be fully mitigated with annealing procedures, it is important to understand their absorption contributions, down to the temperatures of ET-LF ($10 - 20\,\mathrm{K}$).

First, the adjustments made to the setup will be considered. To accommodate for the cylindrical profile, the PTFE stool was swapped for a PTFE v-block. This was held together itself with a horizontally threaded screw and secured into the breadboard on the cryostat base-plate (platform) with a vertical screw (see figure 7.11). To further secure the sample, the mounting structure and reduce through-coupled vibrations, thin layers of cryogenic varnish were placed at the interfaces from stool-platform and sample-stool. Prior to measuring this sample, checks with a lower absorption MCZ sample indicated that it was absorbing considerably (by two orders of magnitude) above the expected level of 10s ppm cm^{-1} and so the shielding was modified to focus on blocking stray light (close to the optical axis) reaching the temperature sensors. The previous copper shielding (see figure 7.4) was updated such that there were only two shields (front and back) of the sample. These shields (shown for the front shield only in figure 7.11) had a narrow aperture (1 cm) cut to be centred with the setups other apertures, optics and the incident beams. External to the cryostat, there were also two well-defined iris apertures to enable the input beams of 1550 nm and 980 nm (that had a significantly improved transmission by a factor of $\times 3.5$ 7.5) to reliably be realigned along a common optical path and incident on the centre of the sample's surface. Due to the short-term availability of a 2000 nm laser source, it was brought into a common path with the other beams and measurements alongside 1550 nm were carried out for nearly all the temperatures studied.

To further reduce the light lost to reflection and scatter inside the system, two additional improvements were made in this design. A well-defined beam block was placed to fully dump the power of the transmitted 1550 nm beam. The sample was also rotated such that the first reflection ($\approx 30\,\%$) of the light could be steered back out the cryostat with an angular offset in the range of $1 - 5\,^\circ$ and dumped with a beam block instead of against the iris aperture itself. Because of the extra isolation, due to reduced sample to stage contact area, it now took 27 hours for the sample to cool down to the baseline temperature of 30 K. In order to improve the accuracy and understand if the recovered fraction was dependent on the sensor's attached point on the sample (relative to the heating source) two sensors were attached to the sample. As shown on figure 7.11, for the CZ measurements the DT-670-A sensor was located at the middle of the sample's length and the CX-1070 towards the front and closer to the source of the surface heating (from the 980 nm beam).

The full range of the recovered fraction data is shown in figure 7.9. Each plot is distinguished for each sensor (column) and wavelength (row). At $27\,K$, the fractional power recovered from the 980 nm (surface calibration beam) R_{980} on the middle DT-670-A sensor (see figure 7.11 (A)) had a response of 0.35 ± 0.03, whereas the front CX-1070 sensor was 1 ± 0.05 for a power of $120\,\mu W$ (figure 7.11 (B)). On the other hand, the 1550 nm bulk absorbing beam had a fractional response R_{1550} of 0.026 on the middle sensor (figure 7.11 (C)) and 0.04 on the front 7.11 (D). The evaluated absorption was $2\,\%\,cm^{-1}$ for the middle sensor and distinctly lower as $1.1\,\%\,cm^{-1}$ for the front. Compared to the previously measured room temperature absorption for this sample $0.5\,\%\,cm^{-1}$, both of these values were considerably larger. The 2000 nm evaluates absorption values were at approximately the same levels of $1.9\,\%\,cm^{-1}$ for the middle and $1.2\,\%\,cm^{-1}$ for the front sensor. At $35\,K$, approximately the same recovered fraction levels were measured on both sensors for the 980 nm beam, but the 1550 nm was slightly higher. This equated to an expected 1550 nm absorption of $2.9\,\%\,cm^{-1}$ for the middle and $1.5\,\%\,cm^{-1}$ for the front sensor.

At higher temperatures of 112 K and 291 K there was an apparent non-uniform heating on the middle sensor, for both the 1550 nm and 2000 nm. This presented itself with a time constant (to reach steady gradient) of approximately 30 s. As the lasers were switched off, the gradient dropped towards the background level, with a steep slope and similar time-constant. This effect was not observed when heating with the 980 nm beam - possibly as the heating power was too low. As the effect was observed independently (for both 1550 nm and 2000 nm) of a specific laser source, it was believed to true to the sample physical 3D extent. At these higher temperatures, as discussed in section 7.3, the diffusion time constant over the same length is considerably larger. At 112 K, $R_{980} \approx 0.7$ for the middle and $R_{980} \approx 1$ for the front sensor and $R_{1550} \approx 0.076 - 0.078$ for both. This equated to an expected absorption of $4.1\,\%\,cm^{-1}$ for the middle and $2\,\%\,cm^{-1}$ for the front sensor. The 2000 nm beam was also used and gave $R_{2000} \approx 0.042$ for the middle and $R_{2000} \approx 0.058$ for the front sensor. This equated to an expected absorption of $2.4, \%\,cm^{-1}$ for the middle and $1.3\,\%\,cm^{-1}$ for the front sensor. Similar to the 27 K step, there were clearly increases in the estimated absorption from 2000 nm down to 1550 nm and from the front to the middle sensor.

At 291 K, for the 1550 nm $R_{1550} \approx 0.06$ on the middle sensor and $R_{1550} \approx 0.2$ for the front sensor. Only the middle sensor was capable of measuring the 2000 nm beam with $R_{2000} \approx 0.025$. However, the measured calibration was not clear enough due to background instability at the time. Therefore, a subsequent run was made 1-month later with the sample and sensors installed in the same configuration and more time given for the sample to stabilise at 292 K. The result of this was a responsivity that was measured as between $1 - 1.1$ for both sensors. Combining these together and the expected absorption for the

middle sensor was 1.6 % cm^{-1} at 1550 nm and 0.7 % cm^{-1} at 2000 nm. Compared to both the 27 K and 112 K temperature steps, the estimated absorption for the front sensor was at least a fact of three higher for both measured wavelengths. It is clear therefore that the absorption value appeared to correlate with accuracy of the sensors (shown in figure 7.5)) as the DT-670-A was only more accurate (out of these temperature steps) at 291 K. In particular, the trend of the electronic accuracy (as approximately the difference between total and calibration accuracies) which decreases with measurement temperature in contrast to the (CX-1070). In consideration of this, the best measurement of absorption at 112 K and below is given by sensor D (CX-1070) in figure 7.10. Aside from the low point measured at 27 K the data indicates that the absorption is slightly lower at cryogenic temperatures for this sample measured with a wavelength of 1550 nm by 30 % compared to the room temperature value measured by sensor C (DT-670).

The absorption value of this sample was previously measured at room temperature for 1550 nm was 0.5 % cm^{-1} [255]. As this value was a factor of three lower than the 1.6 % cm^{-1} measured here, there was expected to be significant optical scatter in the system that was recovered from the 1550 nm beam. Taking the difference and scaling by the length, the increase in recovered heating power was $\approx$ 3.6 % of the input beam's optical power. It is feasible therefore that internal reflections from the cryostat's windows or clipped from proximity to the apertures in the cryostat could contribute through to such an additional absorption level.

For every measurement, the absorption at a wavelength of 2000 nm was found to be distinctly lower than at 1550 nm. This is in contrast to expectations, as the absorption due to free carriers is expected to dominate the measured absorption. Since this increases proportionally to the wavelength squared (see equation 4.1), the 2000 nm value was expected to be 60 % higher than at 1550 nm at room temperature. Unfortunately, no further measurements were made at this wavelength due to faults that developed with the laser. Future studies should look to draw similar comparisons to better understand this reduced absorption at higher wavelengths.

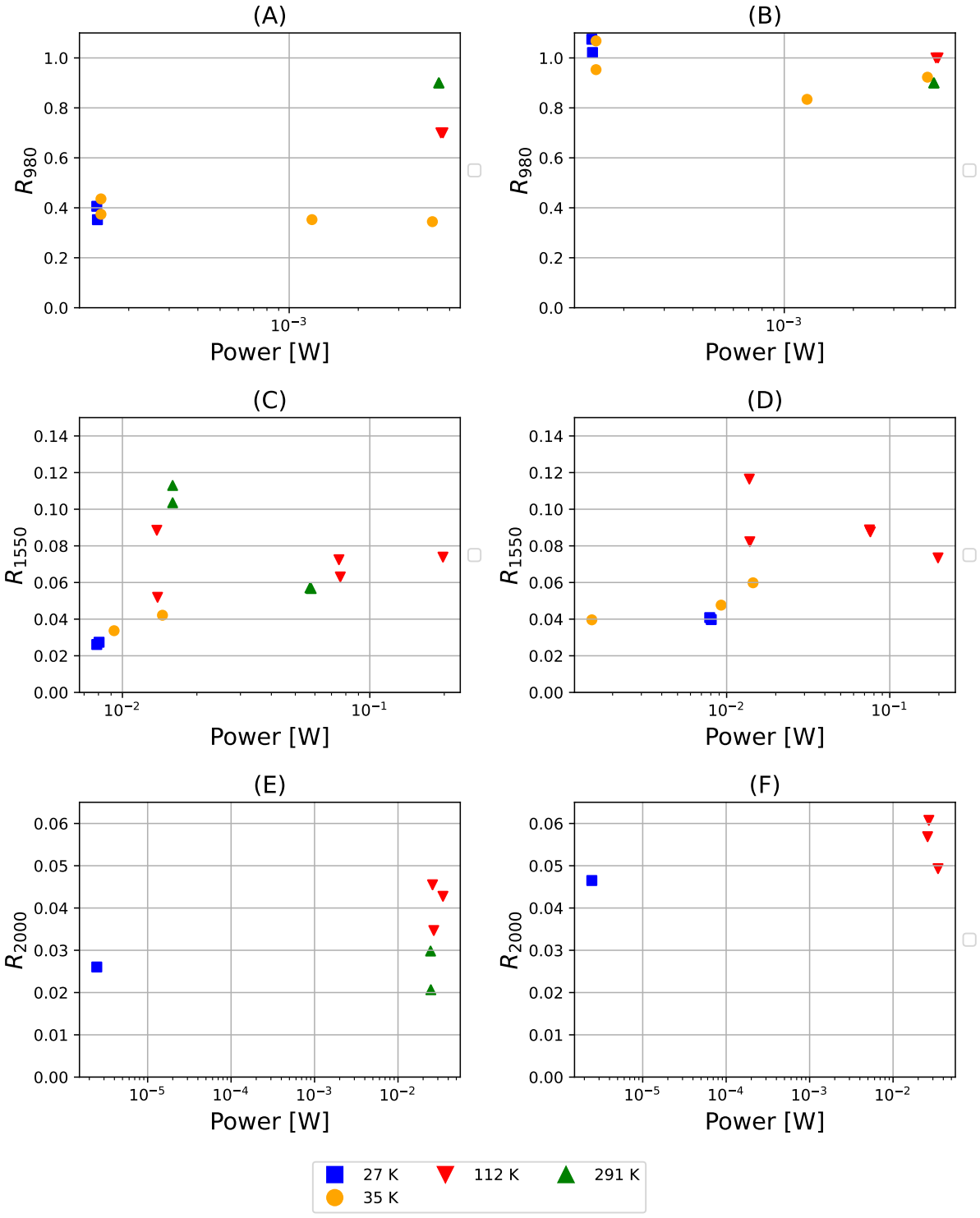

Figure 7.9: Measured heating power normalised to the applied power for the CZ silicon sample. (A,C,E) are plots of the recovered power fraction measured with the DT-670-A sensor placed in the middle of the sample's barrel for 980 nm, 1550 nm and 2000 nm respectively. Whereas (B,D,F) are for measurements with the CX-1070 sensor at the front of the barrel for the same wavelengths.

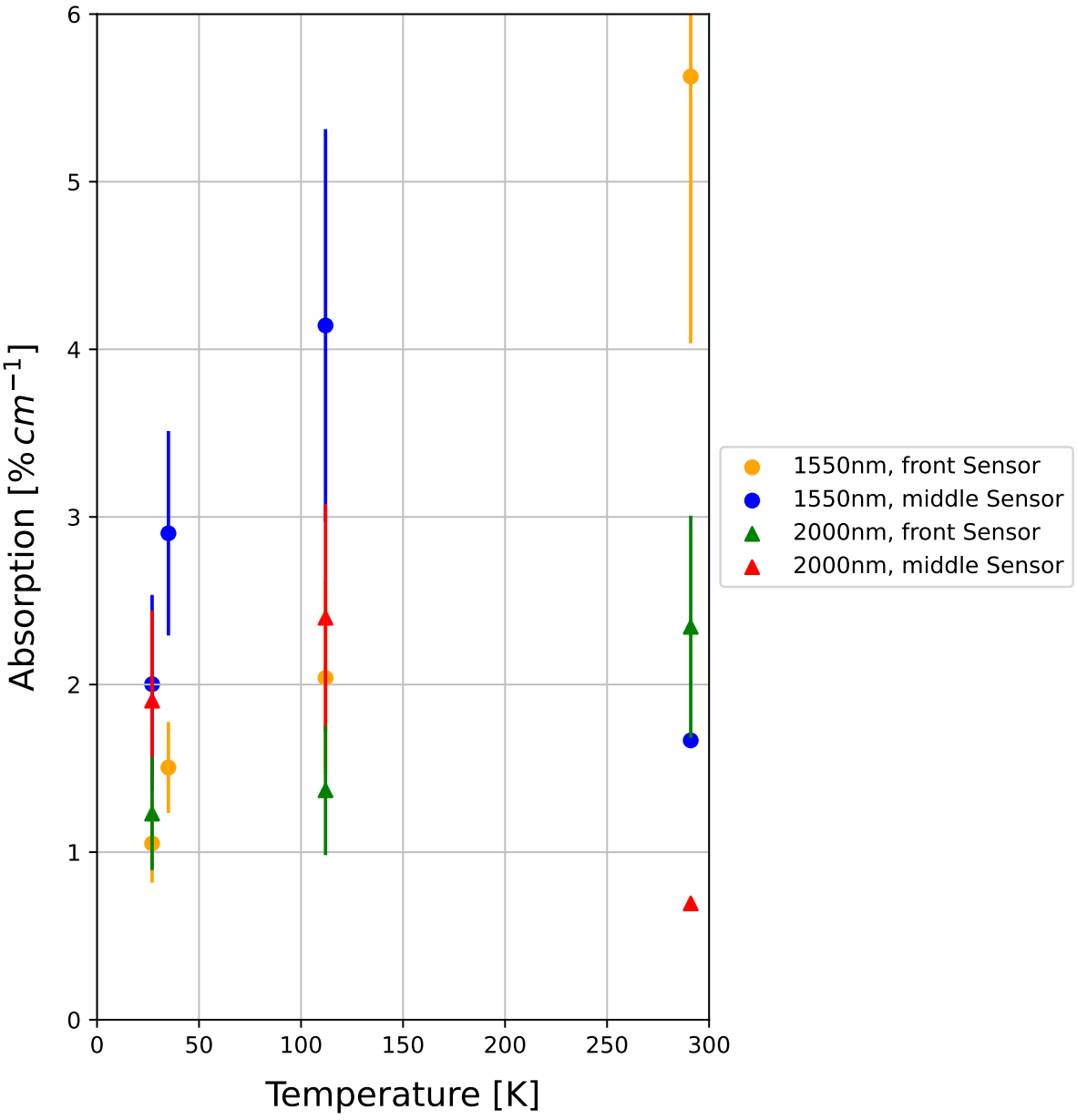

Figure 7.10: Temperature dependent absorption data for the CZ silicon sample.

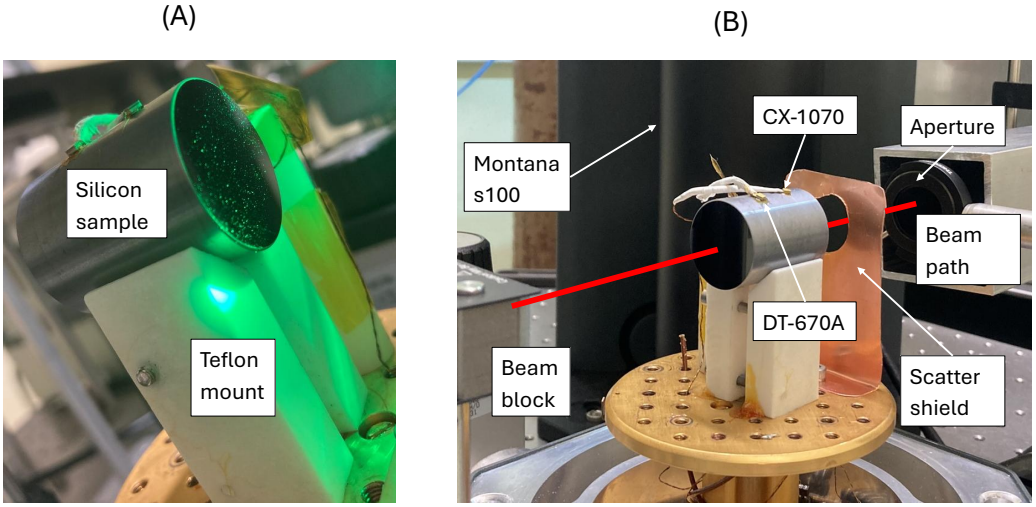

Figure 7.11: Calorimeter setup version 2 for measuring the mid-resistivity CZ and high-resistivity FZ silicon samples. (A) Close up of the silicon sample on the teflon mount. (B) optical calorimeter with the radiation and vacuum enclosures lifted away.

7.8 Characterisation of silicon for ET-pathfinder

ET-pathfinder is a prototype cryogenic GW detector [331, 332]. As it plans to do prolonged optical studies, in advance of ET-LF, with larger silicon samples, it is important to understand for its benefit the absorption down to cryogenic temperatures. The sample was float zone type and expected to have a high-resistivity between $2.5 - 10\,k\Omega$·cm which should at room temperature (through equation 4.4) should give an absorption value in the range of $6 - 25\,\mathrm{ppm\,cm^{-1}}$. The sample was cut to a size of 3 cm long by 2.54 cm diameter and polished using the same method as described in section 6.8.1. Checks at the University of Maastricht PCI system by Jessica Steinlechner on similar samples indicated no surface absorption beyond 100 ppm per surface. This would equate to an excess potential bulk absorption measured through the calorimeter of $63\,\mathrm{ppm\,cm^{-1}}$. Therefore, the maximum expected absorption was $90\,\mathrm{ppm\,cm^{-1}}$. To check this down to cryogenic temperatures, the same setup as described in the previous section and shown in figure 7.11 (B).

The sample was likewise cooled down from room temperature to 30 K in approximately 27 hours. Absorption values were then evaluated, as before, from the recovered power values measured for 980 nm and 1550 nm. The evaluated recovered power data is shown in figure 7.12. As observed for the CZ sample, the recovered power at low temperatures of 29 K and 36 K was within 5 % for both sensors and for repeated measurements. There was

also a significant increase in the recovered power measured on the middle sensor C (DT-670), as observed previously, compared to the front sensor (D) (CX-1070). This is again believed to be due to an excess electronic error that affected the fitting of the temperature gradient.

For the front sensor, the absorption evaluated at 29 K was 310 ppm cm^{-1}. This was then measured at 36 K and was a similar level at 260 ppm cm^{-1}. A significant drop was observed at 120 K by a factor of two as the absorption measured by the front sensor dropped to 90 ppm cm^{-1}. This drop was also observed with the middle sensor. The cryostat temperature was brought back to room temperature (291 K) and both sensors indicated an absorption level of 240 ppm cm^{-1}. For this measurement, the input power was distinctly higher and reached the maximum available for the laser. Therefore, the accuracy as shown for the these measurements was expected to be high. For most of the absorption measurements, the error shown was evaluated by combining the fitting errors of the heating and prior background gradients.

As was observed for the CZ sample, at every temperature as measured by middle sensor C (DT-670) and for a high heating power with the measurement wavelength there was a pronounced time-lag from the start of the heating window until the gradient reached a steady increase after approximately 30 s. For three distinct heating steps, figure 7.14 shows this effect (A) 30 K, (B) 120 K, and (C) 291 K. These plots were produced using an interactive GUI python notebook [303] and served as a clear visual guide for the analysis. Initially, the raw temperature data was plotted for each sensor (grey and red). On top of this, four lines were overlaid for each measurement to help visualise each stage of the responsivity analysis. For the measurement window (black and brown) this was shortened for the 1550 nm window in account of the shortened linear gradient range. Then this data was sampled and differentiated. The average of this was evaluated over the window. Likewise, such a fitting was performed on the background gradient prior to the heating window. Then both were combined before being normalised to give a responsivity that is normalised to the incident optical power.

Compared to the room temperature absorption estimated by a lower-bound's on the resistivity and upper bound on the surface absorption totalling 90 ppm cm^{-1}, the room temperature measurements here indicate an absorption level of 240 ppm cm^{-1}. Taking the residual and scaling it by the sample's length, an excess level of $\approx$ 450 ppm is expected to be scattered and absorbed. This equated, for example, for 2.5 W input power to $\approx$ 1 mW.

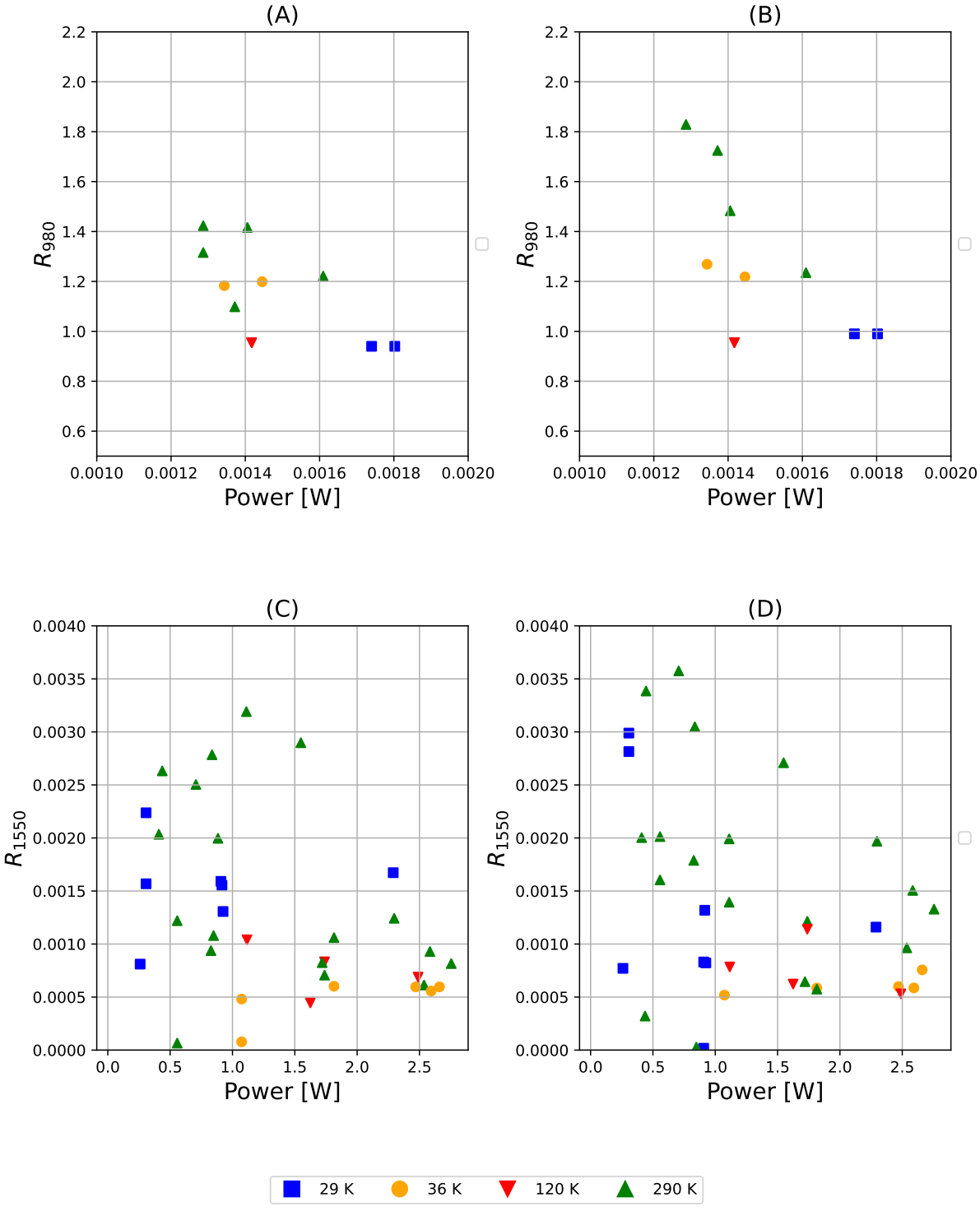

Figure 7.12: Measured heating power normalised to the applied power for the FZ silicon sample. (A,C) are plots of the recovered power fraction measured with the DT-670-A sensor placed in the middle of the sample's barrel for 980 nm and 1550 nm respectively. Whereas (B,D) are for measurements with the CX-1070 sensor at the front of the barrel for the same wavelengths.

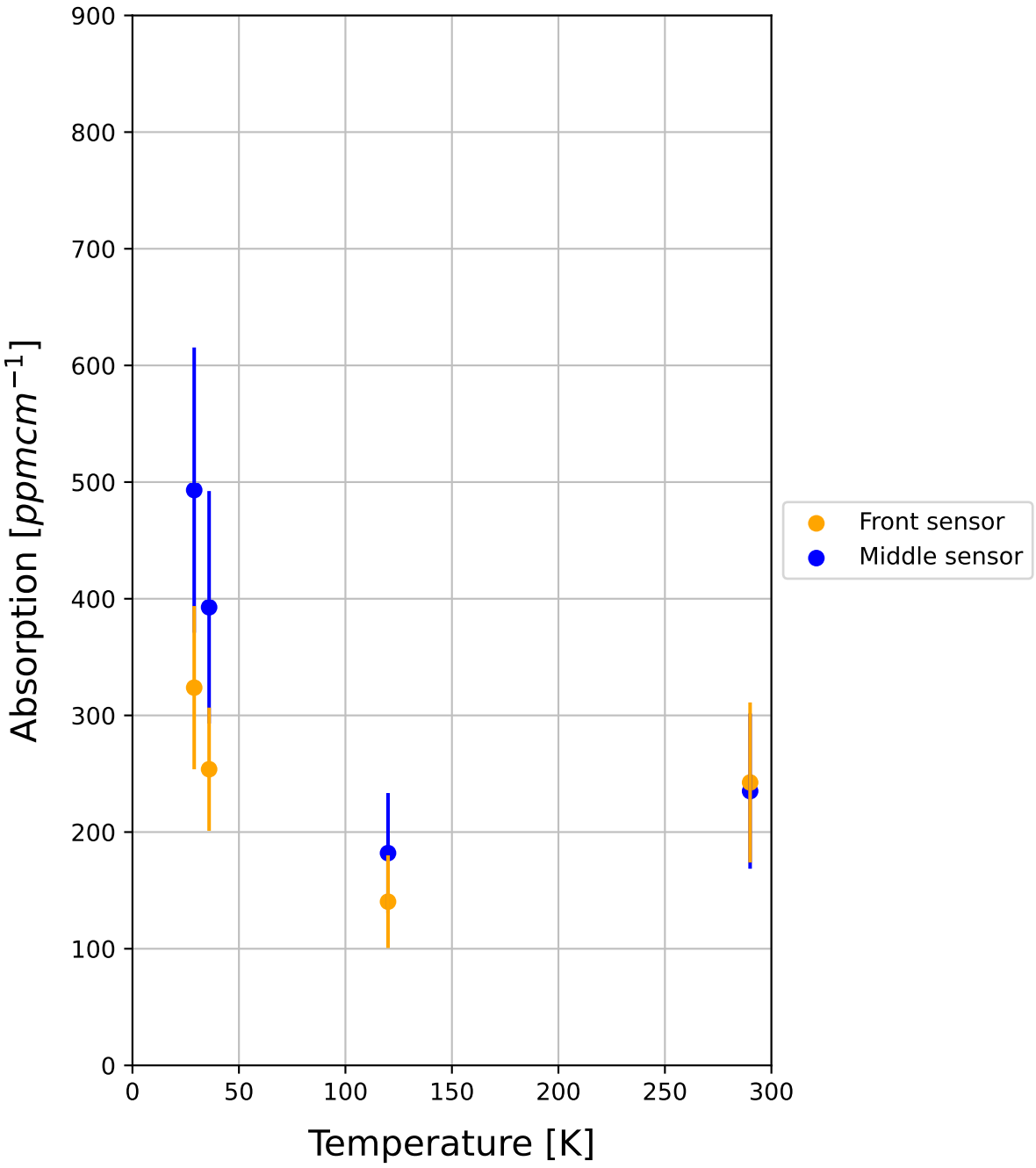

Figure 7.13: Temperature dependent absorption data for the ET-pathfinder sample.

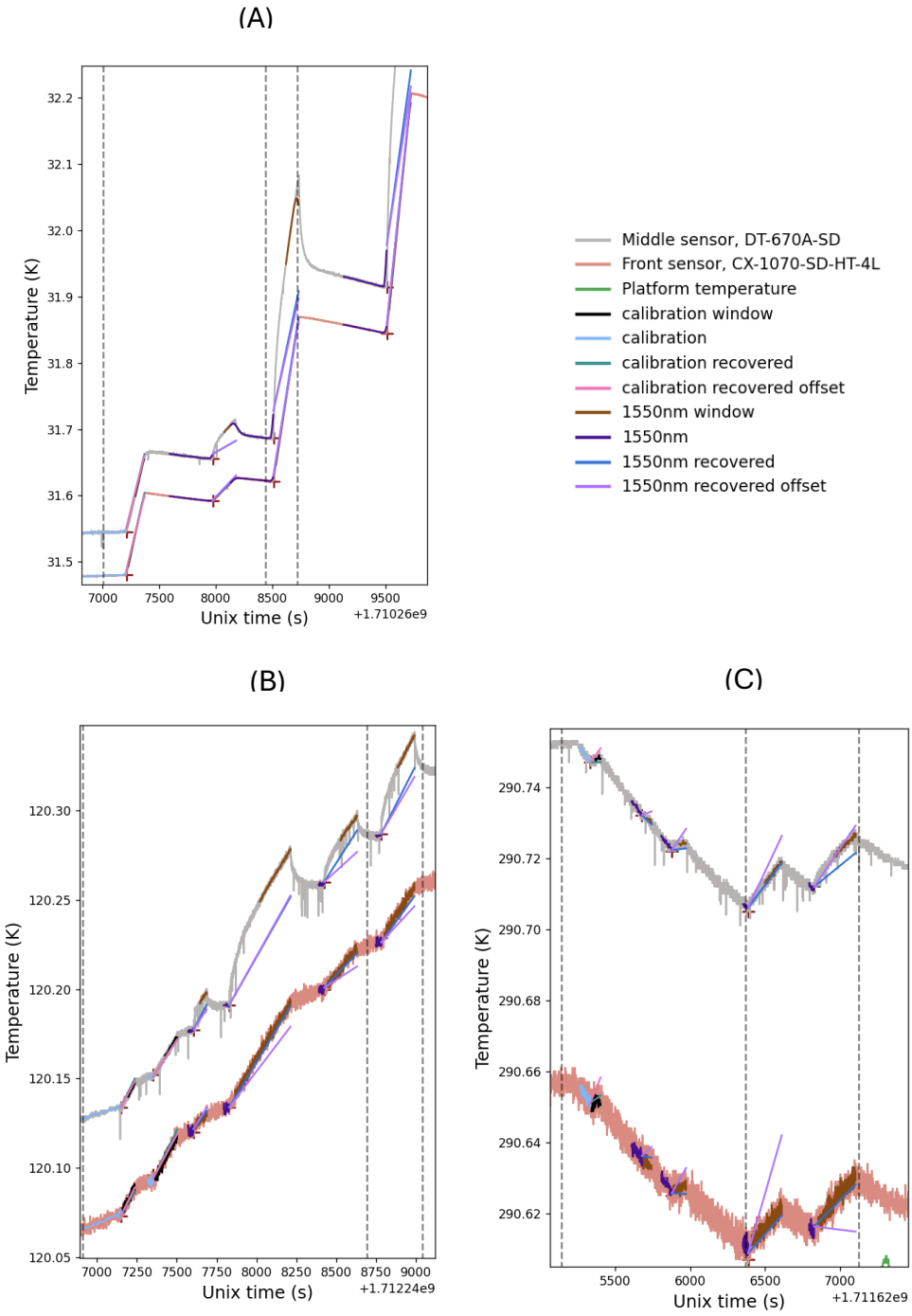

Figure 7.14: Samples of the measured heating response for the ET Pathfinder silicon sample during both calibration and measurement windows.

7.9 Comparison of absorption levels to other studies

The absorption values measured for three progressively higher purity (0.9 Ω·cm, ≈ 20 Ω·cm and > 2.5 kΩ·cm) and lower absorbing silicon samples showed up to a 50 % increase in 1550 nm absorption at ≈ 30 K compared to room temperature. It is believed, given the consistency with temperature and other studies which observed slight changes with temperature, that this shift could have been due to augmentations to the free carrier states (which dominate the absorption at room temperature). Previous studies have shown that the equivalent resistivity of CZ silicon increases drastically at low temperatures without being matched by an increase in absorption [262, 266]. However, a recent study has given evidence for a pronounced increase in the absorption of MCZ by a factor of up to four and 50 % for FZ [319] both down to 60 K. To further support the body of evidence that there is a differing temperature dependence which depends on the type of silicon, this research shows notably for QM a pronounced 43 % increase from 8.9 % cm^{-1} to 12.8 % cm^{-1} at 30 K. The absorption of this sample was p-type and confirmed to be dominated at room temperature with the absorption of its boron free carriers.

The ET-pathfinder FZ sample showed an absorption with a similar relative increase of 48 % from RT to 30 K. Measurements showed that there may be a temperature minimum with a minimum value observed at 120 K. The total absorption value of this sample at room temperature was at least factor of 2.6 higher than predicted in account of both the resistivity and any potential surface absorption effects. The discrepancy could be explained by excess scatter. For the ET-pathfinder and CZ studies, although care was taken to dump reflected beams and no significant power dependence was observed in the recovered power this was investigated further to rule it out.

Compared to the increases for the QM and FZ silicon, the CZ sample had a free carrier concentration and absorption that was known to be dominated at room temperature by thermal donors as opposed to the doping. The observed trend in absorption (with temperature) showed, instead of an increase, a reduction in absorption by 30 %. This would indicate that the thermal donors contribute less free carriers at this temperature. It was interesting, that without changing the optical setup from the mid-resistivity CZ to the FZ sample that the additional power that scattered from the 1550 nm beam reduced from 3.6 % to 0.045 % at room temperature, with similar levels expected down to the temperature of 27 K. As the FZ sample was known to be polished with a high level of precision this might indicate that the scatter for the CZ sample was due to scattering on the surfaces or inside the bulk of the sample.

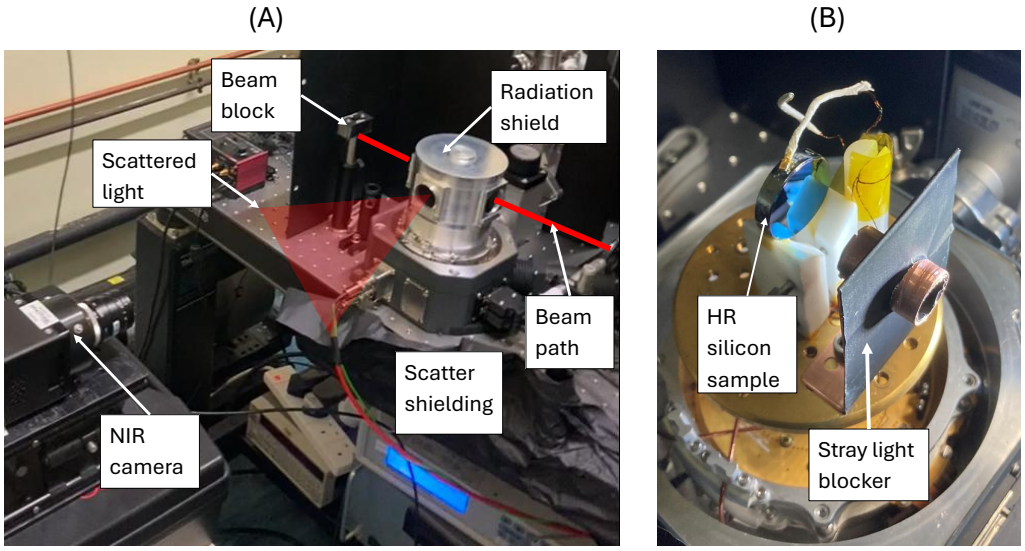

Figure 7.15: Position of a NIR camera for imaging the scattered light in the cryostat.

7.10 Investigation of scattering levels

The expected pathway for scatter to create an excess baseline absorption was expected to follow from light absorbing into the wires (in proximity) and along to the sensor directly. Given the use of copper apertures and the expectation of multiple high power beam reflections at the measurement wavelength, there were multiple interfaces at which light could scatter on towards this expected absorption site. As the inside of both the radiation shielding and chamber were metallic they were highly reflective at 1550 nm and so in account of multiple reflections a diffuse scatter field was expected to be found in the chamber.

To image the scattering level, a NIR sensitive camera was positioned in a plane close to perpendicular with the incident pump beam's optical-axis (see figure 7.15 (A)). This decreased the likelihood of light scattering directly from the main beam and on towards the camera sensor. The process for determining the fraction of light which scattered from a beam followed from the one defined by previously by both Garvin [333] and Tornasi [334] for measuring the scatter from the bulk of crystalline silicon.

The key steps of this process used to establish a relative metric for the optical scatter in the system will now be explained. The laser was set to a level of several μW's, then a strong neutral density filter was placed in front of the camera sensor. After this, a mirror was placed to establish a direct line of sight from the Gaussian beam to the camera sensor. The beam's power was measured separately and a short exposure image was captured. Now, with the scaling, the response of the camera could be determined for a defined exposure and gain. Preliminary test were carried out which showed that this response was independent of the gain and exposure time. After this, a scattering model had to be chosen for the scene under study. A Lambertian model was chosen as it was expected especially when imaging matt and diffuse materials that the light would be emanating isotropically from the cryostat.

Images were then captured of the calorimeter setup as it was used for both the CZ and ET-pathfinder measurements. To additionally stress test the scatter mitigation of reflected beams, a thin silicon sample that was HR and AR coated was positioned where the measurement sample was previously located. The AR side, was placed towards the front (right side of figure 7.15 (B)) and the HR at the back such that the beam would still scatter in the, albeit short length, of the bulk before returning out to be dumped. The initial scatter level is shown with an arbitrary photon count metric (normalised by the incoming power). For the system as shown in figure 7.15 (B) with the copper scatter shield, the intensity map of scattered light is shown in figure 7.16 (A). Although there is some slight specular reflection from the aperture, the Lambertian model is not accurately expected to capture this. Instead, the PTFE stool was expected to be a diffuse source of scatter from which the levels directed towards the sensor, inside the closed system, could be estimated. In figure 7.15 (A) the stool is shown (with a cyan hue) to have a scatter levels of 3×10^6. The inner radiation shielding (shown in figure 7.15 (A)) was then placed around this (figure 7.15 (B)) and it was clear that the scatter level drastically increased by a factor of twenty to a level of 8×10^7.

It was clear given the excess absorption measured for the CZ and FZ samples that there could have been an excess absorption due to optical scatter. As all the surfaces which surrounded the sample were highly-reflective metallic (with a third surface present when the outer chamber of the cryostat was installed) these were in part expected to contribute to setting the scattering limit for the optical system. To try to mitigate this, another set of scatter shield were prepared with a hole-punched to allow the beams to pass through. This set distinctly made use of black Acktar Velvet [335] which had a very low hemispherical (for any direction) reflectance in the NIR of 1 % compared to the ≈ 90 % level for copper. In addition to this, a baffle tube to be held in with mechanical tolerance alone was made

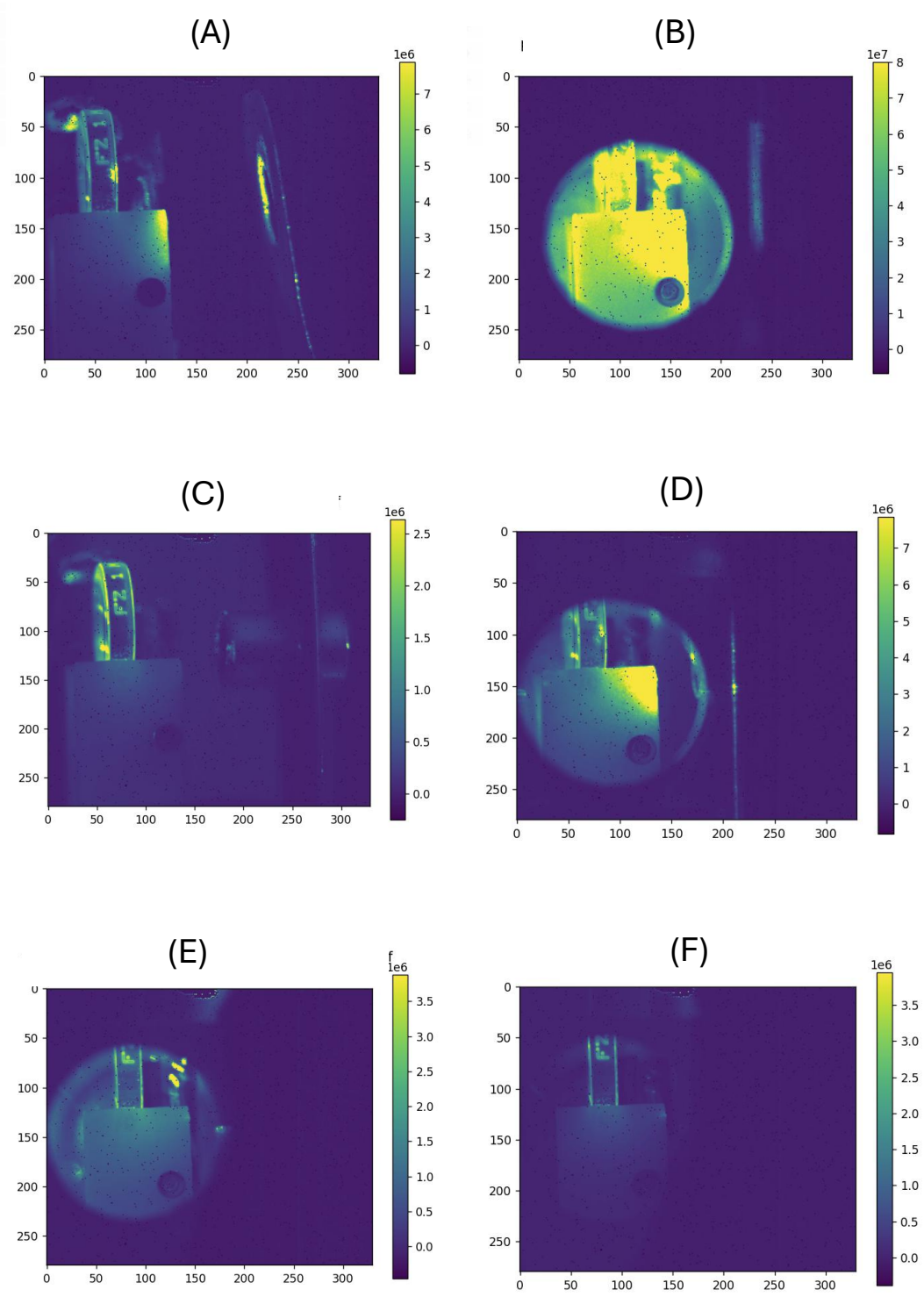

Figure 7.16: Figure showing the progressive improvements made to reduce scatter levels in the optical calorimeter.

[7]. This was also fitted internally with the Acktar coating by using a cylindrically extruded PTFE base as a post around which the metallic Acktar film could be held prior to sliding the baffle tube over. Another image was captured and a slight reduction was apparent in the scatter level coming from the PTFE stool of the open system (figure 7.15(C)). At this point the faint horizontal line representing the bulk scatter of the material was apparent and the scene looked to be illuminated by the scatter generated internally in the sample (compared to figure 7.15 (A)). The inner radiation shield was reinstated and the scatter levels from the PTFE stool dropped to a maximum level of 7×10^6. This was a factor of ten better than the copper shielding.

To further improve this, some small checks were made. The aperture effect of the iris prior to the cryostat (see figure 7.11 (B)) was checked, but had no effect. The sample was then rotated slightly in the mount and with live imaging of the scatter field, there appeared to be sample angles that were favourable to dark and therefore low scatter setup. Further investigation revealed that the optical window at the entrance to the inner shielding with a small 15° rotation was enough to drastically change the scatter levels. Closer inspection of the window under green illumination revealed small streaks and so it was swapped out for a replacement. The new window was rotated and likewise still showed some variance but allowed a lower minimum point on the PTFE stool of around 1×10^6 to be found (E). The scene also notably had fewer bright regions (high scatter) independent (expected through the normalisation) of power up to the maximum of 2.5 W available for the 1550 nm source. The cameras frame is also rotated round slightly so that the wiring components could also be imaged. There was a clear specular reflectance from the middle temperature sensor's wire in the background (shown in yellow). To show the significance of the improvement expected to be up to two orders of magnitude from scene (B) to (E) in figure 7.11 the last image shows the scene captured with the laser switched off. The residual difference in the light levels between the two is marginal.

Although there was no time to cross-check this improvement with another calorimetry run, it was believed that the measured two orders of magnitude reduction in the scatter imaged from the scene is likely to have reduced the measured absorption of the ET-pathfinder sample, which was believed to be significantly higher than the true absorption of this sample. With some further testing to validate the calorimeter's performance, it will be a useful tool for systematic studies of substrate materials for future cryogenic gravitational wave detectors.

---

7. This tube also made use of copper base material to maintain the high thermal conductivity (desired for cryogenic) shielding to prevent other stages of heat-loading.

7.11 Conclusions

The heat budget for the test-masses of future cryogenic gravitational wave detectors is expected to be of critical importance for determining if the detector can stably operate at the required temperature. In particular, ET-LF will operate in the temperature regime of $10 - 20\,\mathrm{K}$. Measurements made in this chapter go a long way in showing that obtaining a low-heat load is likely possible. The question of how much heat is too much heat has to be asked far enough in advance and such that suitably large safety margins can be placed on the acceptable levels. To this end, one such factor which has been seldom studied is the temperature dependence of the absorption of mono-crystalline silicon. Previous studies with photothermal based techniques have indicated a significant increase in absorption with temperature. Since these techniques were limited in their temperature range, the work of this chapter looked to devise a calorimetric setup that was favourable for operation at 10-20 K and enabled fast iterations and the testing of silicon of different geometries. The setup, improvements made and details of the analysis were all discussed in detail, and the capabilities of the technique were investigated through the measurement of three distinct types of silicon. For high absorbing silicon, the measured absorption level was accurate and verified at room temperature with comparison to PCI measurements of the QM sample. Down at cryogenic temperatures, the absorption level for the QM was shown to increase by 50 %. This is a significant factor which in the case of the QM must be further considered and factored into the previously considered improvements required for the material to be a strong candidate substrate for the ET-LF ETMs. A lower resistivity CZ silicon was also measured. This was distinct from the QM as it was known to have a room temperature free carrier absorption dominated by thermal donors. As the absorption decreased by 30 % it is believed that this is some of the first evidence which indicates a different temperature dependent absorption for silicon with different shallow donor profiles: that are not dominated at room temperature by the doping level.

The study continued onto set what is now believed to be an upper limit for the absorption of the ET-pathfinder FZ silicon. There appeared to again be a 30 % increase in the absorption from RT down to 30 K from $\approx 240\,\mathrm{ppm\,cm^{-1}} \approx 320\,\mathrm{ppm\,cm^{-1}}$. For this sample, the middle sensor indicated a higher absorption level. This also occurred in the CZ sample and correlated with the increased electronic noise of the sensor at this temperature. Also, at lower temperatures, the effect of scatter was expected to be more prominent if the light could couple directly to the sample and sensor through absorption in the wire then given its reduced thermal mass at low temperatures the same power could create a larger

offset. This was investigated with a relative measurement in a scattering setup. Strong evidence for significant scatter in the system was found through the implementation of high-absorbance radiation shielding, baffling and fine adjustment of the calorimeter's optics that the scatter could be reduced by up to two orders of magnitude.

For the benefit of future optical calorimeters, improvements will now be considered. To further mitigate scattered light and its potential coupling to the absorption, the appertures could be changed towards hourglass (conical) shapes and the surfaces could be ridged in order to mitigate scattered light propogating in either direction. The wires could also be routed through a hollowed tube without mechanically contacting them to further improve the optical isolation away from scattered light. In addition to this, future designs should quantify the scatter early early into the design phase and look to continue to measure with multiple NIR wavelengths input along a common path. This proved to be a useful tool for localising errors away, at least, from a specific laser source. Future work should also consider scanning through different regions of samples by finely adjusting the input angle whilst keeping it inside the tightly constrained cone of an optical baffle. For improved sensitivity, an optical chopper and lock-in detection scheme could be useful, as getting a high enough signal for samples with ppm-level absorption might be difficult. More accurate sensors such as paramagnetic temperature sensors should also be considered in order to detect shifts in temperature down to the nK level [321]. This would require further improvements to the isolation of the sample in this setup in order to not be limited by environmental noise and background temperature drifts. With further validation of this optical setup, it could be scaled up and utilised, provided the power was higher, to characterise large optics $\geq 10\,\mathrm{cm}$ optics. This work illuminates both the challenges and necessity of measuring silicon at cryogenic temperatures.

Chapter 8

Thesis conclusions

The first direct detection of gravitational waves was a landmark event that awakened a new sense by which humanity could better understand the Universe. To achieve this, myriad cornerstone technologies from the past century converged into the few kilometer-scale interferometric gravitational wave detectors we have today. As a result, they are sensitive enough to detect waves from astrophysical compact-binary coalescences and give valuable insights into the nature of each black hole and/or neutron star that are involved. Through persistent operation and upgrades, many detections have since followed, and some were even able to be studied electromagnetically, with near-simultaneous gamma ray burst observations and follow-up studies of the longer-lasting afterglow emission across the electromagnetic spectrum. These studies were made possible by having multiple gravitational wave detectors with enhanced strain sensitivity operating at once, in order to precisely localise signal origins, and they have heralded the new era of multi-messenger astronomy.

In current detectors, coating thermal noise is a limit to the sensitivity at the most sensitive frequencies. In order for new coatings to be suitable for use they need to have a lower thermal noise while also having low enough optical absorption. Pure germania coatings were studied, and showed to have a high absorption of $\approx 10\,\text{ppm}$ compared to the detector target of $< 1\,\text{ppm}$ and the level measured for other coatings. It is expected that deposition with an IBS instead of electron beam evaporation could reduce this absorption. Further parallel measurements of mechanical loss at cryogenic temperatures could prove the coating is good enough to use as a low-index material in detectors. The author received short-author recognition for his measurement of the absorption here.

Following on from the work on pure-germania films, the author was involved in a separate study investigating titania-doped germania single layers and HR stacks from two separate vendors, in two state-of-the-art laboratories. Titania-doped germania, initially the target for the previous coatings, was previously identified by the GW community as a coating of major interest for use in future room temperature detector upgrades scheduled late-2025. Two batches of the coating were produced through the IBS process and the effect of heat treatment on the optical absorption was studied. A batch produced by CEC was measured both by the author and a collaborator at Stanford University. Strong agreement was found between these measurements, and the best extinction value was a factor of forty less at 2.8×10^{-7} than what was achieved for the pure-germania with a different deposition process. The other batch by EPOC showed an excess absorption in the stack as deposited which indicated that the silica layers were perhaps more oxygen deficient, and hence contributing significantly to the as-deposited absorption. In fact, sub-stoichiometry was likely also prevalent across the titania-doped germania layers in the HR stack as heat treatments showed remarkable improvement to the absorption with the total absorption reducing from 12 ppm to 0.5 ppm after a 100 hr heat treatment at $600\,°C$. Although, this improvement was also found in the parallel CEC study, the EPOC coating did not crack or grow defects even after a heat treatment of 600° for 100 hours in contrast to the CEC which showed signs of blistering after, 300° with a dwell time of only 10 hours. This is a remarkable improvement. In light of the low-absorption and promising noise measurements, this coating was down selected for future upgrades for A+LIGO where it is hoped that through further refinement the risk of crystallisation and scatter in excess of the requirement could be mitigated.

Titania doped with silica was investigated as a possible coating for the A+ detectors and as a potential back-up to the currently selected but not-yet-fully-validated titania-doped germania coatings. Its potential was previously identified in a survey of candidate materials and with only a single subsequent coating batch produced by FiveNine had demonstrated very promising results. A detailed study of the absorption by the author and other researchers showed that the absorption of a full reflectivity coating design incorporating it could reach as low as 0.8 ppm. This coating also had better CTN than current detector mirrors, improved optical scatter, and was free from defects, making it a very promising material of interest. Most of the absorption improvement occurred after a heat treatment of 550 °C with a dwell time of ten hours. Beyond this temperature, the coating began to crystallise, but up to 850 °C heat treatment for a duration of one hundred hours, the absorption was found to be slightly improved. The scatter also stayed low, reaching 5 ppm at 850°C. When previously-amorphous materials transition into the crystalline phase the optical losses are typically expected to be significantly higher due to scattering. As both the absorption and scatter stayed low, this is contrary to a theory

for titania films which proposes, after higher heat treatments temperatures, that the scatter should significantly increase as the absorption drops. The author received short-author recognition in a Physics Review Letters publication for these absorption studies. Ultimately this work helped qualify the coating for future detector upgrades, as its thermal noise was shown to be 76 % of the aLIGO level.

Following this promising work, the current gravitational wave detector manufacturer, LMA, produced single layer and HR stacks incorporating titania-doped silica. This was in collaboration with the LIGO Scientific Collaboration after interest was re-ignited in the material following the aforementioned publication. LMA produced a stack meeting the full reflectivity requirement of advanced LIGO, and after a similar heat treatment temperature of 600 °C, the author showed that it reached a remarkably low absorption of 0.3 ppm. Single layers of the material also produced remarkably low extinction coefficients at this temperature of 2.3×10^{-7}. However, beyond this, with various different heat treatment procedures trialled by collaborators, these coatings all developed cracks at heat treatments beyond this temperature, though slight improvement to CTN above the FiveNine coatings have still been indicated. Although the cracking at higher heat treatment of the LMA coatings is not ideal, differences in the percentage of titania in the coatings and deposition recipes used between the vendors leaves plenty of opportunity for further improvement. Taken together, these two studies of defect-free, slightly high-absorption coatings and of low (within-target) absorption coatings that crack above 600,°C indicate the strong efficacy of titania-doped silica as a future coating material that, with further development, could meet all requirements of future detector upgrades. With further research investment, just as was done for titania-doped germania previously, the mechanisms for defect/cracking formation could be identified, and ideal new coatings meeting all detector requirements produced. As a result of all these studies to which the author contributed, the material is actively being researched for use in future upgrades to the LIGO and Virgo mirrors.

The extinction was evaluated, and it appeared that there was excess extinction (due to absorption) in the single layers that persisted even after heat treatment. If the coatings were, as expected, deposited under the same conditions then this might indicate a fundamental reduction in stoichiometry and perhaps for coatings deposited towards the top of the coated stack. To further understand this discrepancy and see if the coatings are truly some of the lowest total extinction below 10^{-7} level (in joint account of the low scatter) and suitable for other high finesse cavity experiments, other coatings should be prepared and heat treated as described here. Then in addition to absorption measurements elemental composition and bonding should be studied to see if stoichiometric effects are still the limiting factor. In the future, such studies should, hopefully, enable the extinction

of thin-films to improve towards the 10^{-10} level of bulk optical materials such as fused silica. To support these developments, research should also consider advances in tuneable high power lasers, as if integrated in a setup like the PCI they could provide spectral measurements and for correlation with other thin-film material properties such as the mechanical loss which are also critical to gravitational wave detectors. This would build upon recent studies which characterised the local atomic order of amorphous materials with absorption measurements up to 500 nm.

Looking ahead to the 2030s a new generation of detectors are expected to come online. Not only will these will push us closer to observing every CBC, but also allow us to detect additional astrophysical sources, such as continuous wave emission from (non-inspiralling) neutron stars and supernovae. One such detector, the Einstein Telescope, would look to reach ASD noise levels of the level of $\approx 10^{-24}\,\mathrm{Hz}^{\frac{1}{2}}$. The Einstein Telescope design includes a cryogenic interferometer designed to be sensitive at low frequencies around 10 Hz. Compared to current detectors, across almost an extra order of magnitude of frequency space ($1 - 10\,\mathrm{Hz}$) ET-LF will be at least three orders of magnitude more sensitive. As a result of this, massive and previously unseen CBCs will be detectable and signals coming from a distinct source of type 1A supernovae may be detectable. As these events can also have a detectable EM counterpart, they can provide lots of valuable astrophysical information, for example such as the abundance of heavy elements across the Universe.

To reach the required sensitivity limits, in part, these detectors will distinctly operate both their mirrors at temperature of $10 - 20\,\mathrm{K}$. The reduction in temperature necessitated a shift from the current materials. Silica, found in both the substrate and as the low-index coating layers, in the stacks of the mirrors in current detectors, would be undesirable due to its high and limiting contributions to the thermal noise. Inspired by improved mechanical-loss measurements of alumina coatings, the author investigated the same coatings. After a detailed heat treatment study an extremely low absorption of $\approx 1\,\mathrm{ppm}$ was found after a heat treatment of $850\,^{\circ}C$ for one hundred hours. It was expected that following this result, the coating could provide a promising low-index coating material for cryogenic detectors. Using a python code base developed by the author and verified against other equivalents, theoretical coatings were designed for the low-frequency Einstein Telescope detector at 20 K and operated at 1550 nm. Compared to the baseline design that includes silica-doped halfnia and other promising candidates such as silicon nitride, significant improvements are shown through the use of alumina materials. These models show that the coating designs developed have the potential to allow ET-LF to reach, or even slightly exceed, its design sensitivity.

As a result of the absorption measurements here, the heat load on the ITM is expected to be reduced through the use of asymmetric coating designs proposed here for the first time. Until optimally low absorbing and thermal noise coatings are produced, these designs give confidence that the detectors will be operational once the heat load is better constrained in account of the two other contributions, which currently carry a lot of uncertainty. These are heat loads from the ambient and substrate absorption.

In addition to new coatings, future cryogenic detectors will reach the required sensitivity by substituting their fused silica test mass substrates for either sapphire or monocrystalline silicon materials. Silicon is a candidate material because by comparison it has favourable thermal and mechanical properties at low temperatures. As such, silicon optics are considered as the baseline for the ET-LF detector. However, as they have not been demonstrated to have a low enough absorption at the growth scale required, it is imperative that they are actively researched. Motivated by this, two sample sets were sourced each from a novel silicon growth method. One type, grown through directional solidification was of interested due to it being the only method capable of meeting the required mirror size of ET-LF. The material had a low purity due to its originally intended use and so a high baseline absorption of at least $10{,}000\,\mathrm{ppm\,cm^{-1}}$ was found, as expected. The associated dopant profiles were expected to be uniform and so it was surprising to find a high variability in this absorption through the length of the 4 cm sample. Empirical modelling of the excess absorption due to known concentrations of additional impurities was investigated. However, these also did not explain the variability and so closer inspection of the sample found silicon carbide defects that spatially correlated with the excess absorption and therefore supported the notion that they were acting as formation sites for additional and absorbing donor states. Following the rigorous absorption characterisation, additional methods for improving it with future growth cycles were identified beyond the underlying purity of the feedstock. There is the possibility that the ETM due to the higher reflectivity of the coating can make use of higher absorbing silicon material up to $200-1000\,\mathrm{ppm\,cm^{-1}}$. This might be at odds with the asymmetric coating design proposed, but with some balance the same equivalent ITM heat load could be found. This substrate absorption level is two orders above the baseline level for the ITM and two orders below the level measured here for the QM silicon. Provided the absorption level was reduced, and multicrystalline boundaries were mitigated across the extent of the full silicon boule then the silicon could potentially have an asymmetric size between ITM and ETM. This new design possibility supported by this work would allow smaller and lower absorption FZ silicon, for example, to be implemented in the ITM to significantly reduce the heat load. As achieving this specific ITM heat load is a big challenge, further consideration of this design would ultimately increase the likelihood of achieving an operational ET-LF detector.

For the benefit of other cryogenic detectors such as Cosmic Explorer and Voyager, the limiting effect not just of a high absorption but for spatial variation as such for the first time. To mitigate this effect from limiting the operation of future detectors, it is important that the absorption profile of all bulk substrates is mapped prior to integration. Through the setup of a photothermal deflection technique at Glasgow, the potential for this technique was demonstrated. High absorbing samples were measured, but no variation was found. As the source of variation is expected to largely come from oxygen impurities, the second type of novel silicon called a-MCZ was sourced from Okmetic due to its distinctly low concentration. This is 4 ppma which is considerably lower than the 20 ppma expected for CZ silicon. The sample was processed and measurements made indicated an average absorption of ≈ 67 ppm from scans taken across a 20 diameter disk from the top of the boule. If this silicon production method could be further scaled, then these absorption measurements would support the use of this material in the ETM with adjusted requirements as described for the QM. Outwith this there was considerable variation $\pm 50\,\%$ to the highest and lowest average scans. This proportional range and the maximal drop of $70\,\%$ between ends of these large samples is less than previously observed for MCZ end pieces. Those by comparison have been shown to vary by a factor of 5 across the radius. The reduction in this variation, indicated that the heat load would not need to be further reduced to account for any cross-sectional heating profiles which had a significant spatial correlation with higher order HG beams that are orthogonal to the interferometer's main beam.

Although previous measurements of MCZ were shown to be as low as several -ppm the absorption of the a-MCZ only had on average an estimated 20 ppm of excess beyond the value estimated from resistivity measurements. Further studies with these samples should flash anneal and cool them to see if the excess is due to thermal oxygen donors and if they are annihilated as expected by this process. This reduction in oxygen levels and donors is critical to getting low-absorbing test-masses as the final heat treatment of any coated test mass will likely need to be, as supported by the detailed coating studies here, slow and prolonged. The need for high temperatures considerably above $450\,^{\circ}C$, as such, would support the use of the crystallisation (with expected low scatter) resistant materials of titania-doped silica and alumina as studied here.

Further studies should also consider measuring silicon samples taken from the centre of the boule where MCZ has shown considerably higher radial variation. The work here also through of a stepped absorption profile showed that the absorption of each a-MCZ extended into the surface beyond the longitudinal resolution ($200\,\mu$m) and therefore that

the surface polish procedure using col-k slurry was not limiting the absorption at the 30 ppm level and would be applicable for the preparation of these substrates for future gravitational wave detectors. However, should prominent Gaussian resolution peaks arise after annealing, then future studies should consider etching the surfaces to mitigate this.

The absorption levels of materials are typically considered to be independent of operational temperature. Recent free-carrier freeze out theories indicated that this would be significantly lower at cryogenic temperatures. However, measurements found for high absorbing CZ silicon of 800 ppm cm^{-1} dominated by the extrinsic doping level that there was no significant temperature dependence from room temperature 6 K. Further studies found that there was a significant increase by a factor of four for lower absorbing MCZ silicon down to 60 K. As ET-LF is looking to operate in the $10 - 20$ K range, all of these measurements are likely not directly applicable. If there is a physical and underlying temperature-dependent increase, beyond the theory, then the absorption target especially for the ITM of 20 ppm cm^{-1} might have to be considerably reduced.

To further clarify this, the author designed and set up an entirely optical based calorimetric technique. Initial measurements of QM silicon, previously considered, indicate the absorption of low-resistivity samples could increase by as much as 50 % down at 30 K. In contrast,further studies of CZ silicon that was higher-purity but dominated by absorption from thermal-donors showed an absorption that decreased by up to 30 %. Although the purities of samples were not at the level required for ET-LF they were in close agreement with recent studies stated above. After this, a high-resistivity sample was characterised for the benefit of ET-pathfinder. The work here set an upper bound on the for the absorption at 320 ppm cm^{-1} at 30 K. The sample, despite showing signs of excess absorption intrinsic to the setup, also showed clear signs of a 30 % higher absorption compared to RT where the value was 240 ppm cm^{-1}. To the benefit of continued studies for ET-pathfinder, on near term, this work will guide future absorption studies to help understand the physical origins of the excess absorption.

There is hope that these results and techniques developed and shown throughout this thesis for coatings and silicon materials can further be accelerated through upcoming industrial partnership. For coating materials, it was very promising that measured absorptions were not only consistent but showed consistent improvements between production vendors, measurements setups and heat treatment parameters. For the titania-doped germania produced from a new Scottish facility called EPOC, it was very promising to see a sub-ppm level that was comparable to the that from LMA who are the established vendor for the LIGO and VIRGO detectors. From the perspective of silicon, it is exciting

that the detailed absorption studies contained in this body of work has helped to double the number of viable growth techniques from only FZ and MCZ to a-MCZ and QM/DS. Looking ahead, it is promising to see that German research groups such as IKZ Berlin [336] and DZA [337] are pledging to bring production and measurement of silicon materials in house. This research adds yet another chapter to Glasgow Universities historical breadth in state-of-the-art materials but will also serve to benefit a vast range of optical metrology research where down to the sub parts-per-million absorption of small number of photons is of critical importance.

Appendices

A Fitting the material properties for silicon over the $10 - 300\,\mathbf{K}$ temperature range

To the best of the author's knowledge, there is no clear collection of silicon's thermo-optic properties, relevant for GW detectors, across the $10-300\,\mathrm{K}$ temperature range of interest. It is important to collect these together so that comparative levels of effects pertinent to future GW detectors such as thermo-optic distortions (figure 1.6) and tolerable heat loads (figure 1.8) can be established. The fitting made use of scipy's interp1d, UnivariateSpline fitting and numpy's polyfit.

B Absorption of perovskite coatings

To further explore potential high-index alternative layers and better understand the extinction of other coatings, some low-loss single layers of $LaTiO_3$ and $SrTiO_3$ were measured. These materials were prepared by collaborators in coating deposition at the University of Strathclyde.

These materials, classified as perovskites, are normally of particularly interest for optical coatings due to their high refractive index and high optical absorption [342]. To the best of the author's knowledge, this section shows for the first time shows distinctly low NIR absorption values.

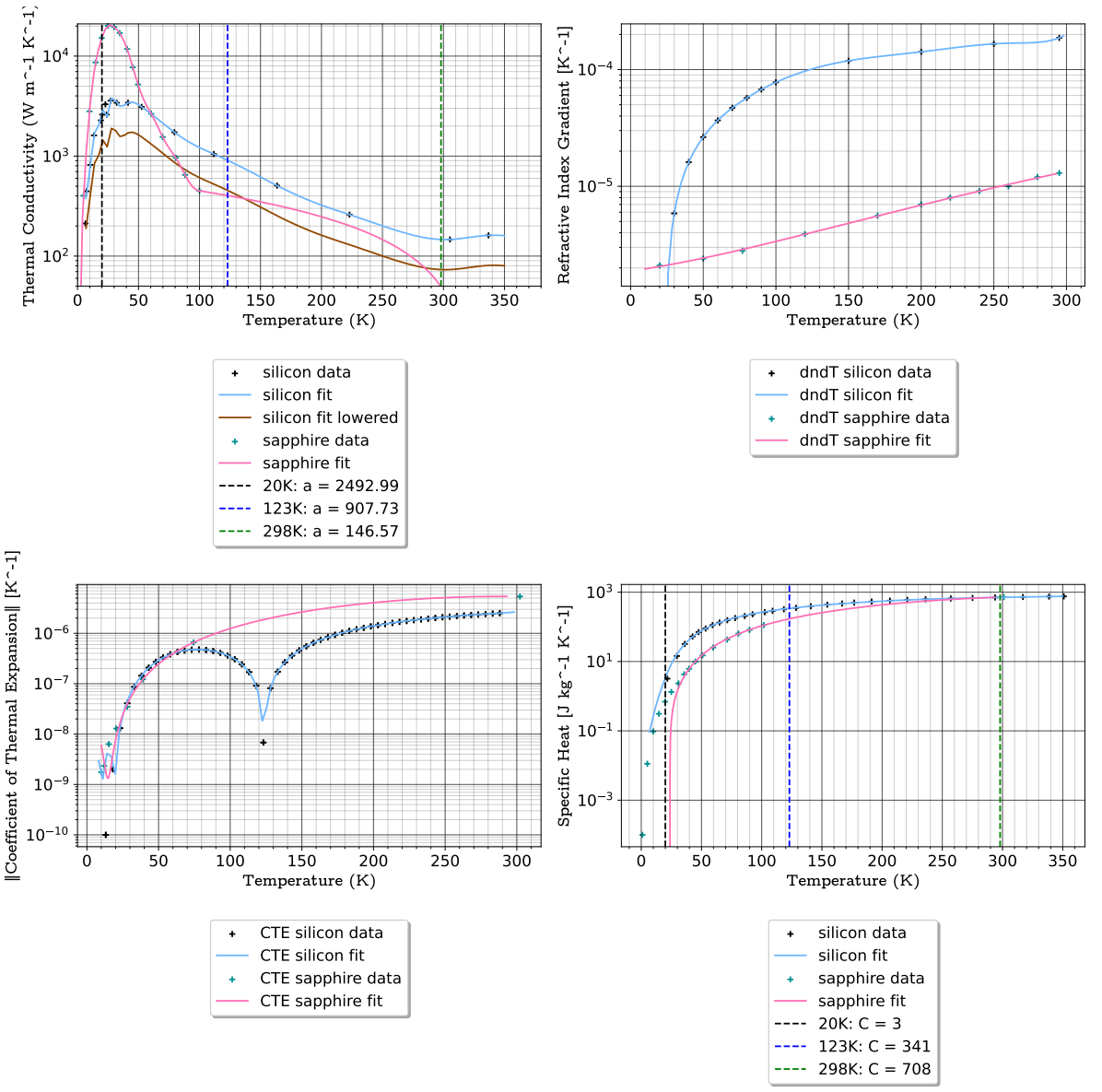

Figure 6: Properties for arbitrary crystalline silicon.
(Top left) thermal conductivity for silicon [338] and sapphire [135].
(Top right) refractive index gradient at a wavelength of 1550 nm for silicon and sapphire [339].
(Bottom left) magnitude of the coefficient of thermal expansion for silicon [133] and sapphire [340].
(Bottom right) specific heat capacity for silicon [341] and sapphire [135].

The coatings were initially a pilot study and so after measurement as deposited the entire coating was heat treated to 400 °C. The ramp up rate for these heat treatments was at 50 °C/hr, the hold time was 10 hr and the cooldown was targeted to be symmetric at 100 °C/hr. After the $SrTiO_3$ was heat treated, the coating layer appeared to be have had a milky haze. This might indicate that the coating was crystallised at after this heat treatment. The absorption measurements showed a considerable reduction at 1064 nm

from 38 ppm to 5.15 ppm or an extinction value of 4.3×10^{-6}. This significant reduction however was not found at 1550 nm. Due to time constraints, the full range of equivalent measurements was not made on the $LaTiO_3$ coatings. However, measurements as deposited showed that its extinction 7.4×10^{-6} was comparable to the heat treated $SrTiO_3$.

These absorption measurements from this pilot study suggest that perovskite materials and specifically those which contain a combination of alkaline earth metals, titanium and oxygen might be of interest for low-loss optical mirrors. Further measurements of a wide-range of thermo-mechanical properties could confirm if this interest extends to coatings of gravitational wave detector mirrors.

The samples studied here all had consistently low absorption at all measured points on each samples surface, and this trend was consistent across the two different wavelengths of measurement (1064 nm and 1550 nm).

Table 6: Measurements shared between the author and Graeme McGhee for two perovskite materials $SrTiO_3$ and $LaTiO_3$. The absorption improvement at 1064 nm and 1550 nm is shown, along with the reduction observed after heat treatments from as-deposited to 400 °C for the $SrTiO_3$ sample.

Coating	Wavelength [nm]	Thickness [nm]	n	α ADP [ppm]	α (400 °C) [ppm]	κ minimum $\times 10^{-6}$
$SrTiO_3$	1.064	8.35	2.1	38.4 ± 7.7	5.15 ± 0.3	4.3
$SrTiO_3$	1.550	8.35	2.1	21.2 ± 3.0	17.1 ± 3.0	22.9
$LaTiO_3$	1.064	1.236	1.99	6.9 ± 1.1	-	7.4
$LaTiO_3$	1.550	1.236	1.98	34.5 ± 1.5	-	46

C Overview of developed code

C.1 Thin film coating analysis using developed PyCoat code

This section will discuss the development of python package pyCoat.

To convert the absorption into an extinction value, for coatings, requires consideration of the reduced electric field intensity as the light propagates through the coating due to interference between layers: following from equation 2.10. The Theory for doing this was previously set out for single layers [343] and elsewhere for multilayer stacks [344]. This

theory was later developed into an accessible python module called TMM [343, 345]: short for the Transfer Matrix Method (TMM) that was used to encode the forward and back propagating light contributions from each boundary of the coating stack and substrate. When benchmarked against the industry standard TFCALC software [346], the evaluated absorption for single layers and stacks was found to agree within 1%. With confidence in the TMM module, the package further was integrated as a dependency the author's own pyCoat package.

The pyCoat package allowed the user to simply define complex dielectric coatings as class instances, which store dictionary objects of properties specific to both individual coating layers and materials. The coatings are initiated with a call to `Coating(property_light,material_substrate)` with the input of the incident light and substrate properties. Then the layers are added at specific indices using the function `Coating.add_layers(material_choice,indices_layer,k_force)`. The k_force input notably allows the extinction coefficient to be simply updated with a repeat call to the function.

In the case of a single layer coating, the extinction is fitted as shown in code listing 1. The extinction is first evenly sampled over a large logarithmic space and the theoretical absorption is evaluated at each point. A one to one mapping is then made between the two parameters by interpolating both ranges using the `scipy.interpolate.interp1d()` function. For single layer coatings with low extinction coefficients where the transmitted light is considerably greater than the absorption, this is sufficient. The absorption (`mu`) of the coating is then evaluated from the statistical average of the distribution of the measured data. The error in the fit is assumed to be dominated simply by the error in this distribution, and so the small errors in measured coating refractive index and thickness are not considered here.

```
1  # Import necessary libraries
2  import numpy as np
3  from scipy.interpolate import interp1d
4  from scipy.stats import norm
5  from pyCoat import Coating
6
7  # Evenly sample the extinction over a large logarithmic
       space
8  n_points = 20
9  k_range = np.logspace(-7,-4,n_points)
10 a_range = np.zeros_like(k_range)
```

```
11
12 # Evaluate absorption for each extinction value
13 for i,k in enumerate(k_range):
14     coating = Coating(wavelength=1550,material_sub='SiO2
          substrate',pol='p',angle=0)
15     coating.add_layers('SiO2_TiO2',indices_layer=[0],
          k_force=k,thickness_layer=274)
16     coating.update_tmm()
17     a_range[i] = coating.coating_TMM_dic['numbers']['A']*1
          e6
18
19 # Interpolate the absorption range with the extinction
     range
20 k_a_mapping = interp1d(a_range,k_range,kind='cubic')
21
22 # Fit the measured data with a gaussian distribution
23 mu, std = norm.fit(data_measured_absorption)
24
25 # Evaluate the extinction and its error from the absorption
     fit
26 k = k_a(mu)
27 k_error_range  = [k_a(mu-std),k_a(mu+std)]
```

Listing 1: High-Level Code Summary: Evaluation of single layer SiO_2:TiO_2 coating extinction coefficient. The light wavelength and layer thickness are both in nanometers

For fitting the extinction of a target materials layers in a HR stack coating, a similar analysis was performed: except that one of the bilayers such as the low-index silica had an extinction which was assumed to be fixed and considerably lower than that of the chosen high-index layer. The stacks, measured in chapter 2, were always HR at the measurement wavelength.

The theoretical Reflection and transmission from TMM were also benchmarked against PyGwinc [245] and found to be equivalent. However, there was a discrepancy in the absorption derived simply from the deficit of the 1-R-T for multilayer coatings. Instead, the absorption of a given multilayer medium was evaluated here with

$$a_{\mathrm{i}} = \alpha_{\mathrm{i}} \cdot d_{\mathrm{i}} \cdot P_{\mathrm{i}} \cdot \bar{E}_{\mathrm{i}} \tag{1}$$

where (α_{i}) is a rearrangement of the absorption term given in equation 2.2 but for an individual layer (i). This was then propagated to give an absorption in account of each material layers geometrical thickness (d_{i}). As the light power at the entry point to each layer is reduced in account of that which is reflected there has to be a power correction term (P_{i}).

$$P_{\mathrm{i}} = \prod \left| \frac{(1 - r_{\mathrm{i}}^2)}{(1 + r_i \cdot \bar{r_{\mathrm{i}}})^2} \right| \tag{2}$$

Also, due to the coherent nature of the light the electric field will vary across the thickness of the layer. In a Bragg reflector this evaluates to be sinusoid as a function of optical depth that regularly repeats over each bilayer. This effect can be seen on figure 3.10. Except the depth is shown here as a geometrical depth. The effect of this was that the average had to be taken and so the electric field was given by

$$\bar{E}_{\mathrm{i}} = \left(1 + |\bar{r_{\mathrm{i}}}|^2\right). \tag{3}$$

The total absorption is therefore given by evaluating equation 1 for each layer and simply adding each layers contribution together. In future work, this analysis could be further developed to accommodate for uncertainties in refractive index and thickness for different layers.

Bibliography

[1] LIGO Scientific Collaboration and Virgo Collaboration et al. 'Observation of Gravitational Waves from a Binary Black Hole Merger'. In: *Physical Review Letters* 116.6 (Feb. 2016), p. 061102. DOI: 10.1103/PhysRevLett.116.061102. (Visited on 28/04/2021) (cit. on pp. 1, 4, 6, 11).

[2] B. P. Abbott et al. 'GWTC-1: A Gravitational-Wave Transient Catalog of Compact Binary Mergers Observed by LIGO and Virgo during the First and Second Observing Runs'. In: *Physical Review X* 9.3 (Sept. 2019), p. 031040. ISSN: 2160-3308. DOI: 10.1103/PhysRevX.9.031040. (Visited on 28/04/2021) (cit. on pp. 1, 3, 11).

[3] R. Abbott et al. 'GWTC-2: Compact Binary Coalescences Observed by LIGO and Virgo During the First Half of the Third Observing Run'. In: *arXiv:2010.14527 [astro-ph, physics:gr-qc]* (Mar. 2021). arXiv: 2010.14527 [astro-ph, physics:gr-qc]. (Visited on 28/04/2021) (cit. on pp. 1, 3, 11).

[4] The LIGO Scientific Collaboration et al. 'GWTC-3: Compact Binary Coalescences Observed by LIGO and Virgo During the Second Part of the Third Observing Run'. In: *arXiv:2111.03606 [astro-ph, physics:gr-qc]* (Nov. 2021). arXiv: 2111.03606 [astro-ph, physics:gr-qc]. (Visited on 13/12/2021) (cit. on pp. 1, 3, 11, 17).

[5] Bernard F. Schutz. 'Networks of Gravitational Wave Detectors and Three Figures of Merit'. In: *Classical and Quantum Gravity* 28.12 (May 2011), p. 125023. ISSN: 0264-9381. DOI: 10.1088/0264-9381/28/12/125023. (Visited on 17/11/2023) (cit. on pp. 1, 11).

[6] The LIGO Scientific Collaboration et al. 'Prospects for Observing and Localizing Gravitational-Wave Transients with Advanced LIGO, Advanced Virgo and KAGRA'. In: *Living Reviews in Relativity* 23.1 (Dec. 2020), p. 3. ISSN: 2367-3613, 1433-8351. DOI: 10.1007/s41114-020-00026-9. arXiv: 1304.0670. (Visited on 02/05/2021) (cit. on p. 1).

[7] Einstein Telescope Science Team. *Einstein Telescope Design Report Update*. Tech. rep. Einstein Telescope, 2020 (cit. on pp. 1, 19, 26).

[8] Matthew Evans et al. *A Horizon Study for Cosmic Explorer: Science, Observatories, and Community*. Sept. 2021. DOI: 10.48550/arXiv.2109.09882. (Visited on 20/11/2023) (cit. on pp. 1, 18, 26).

[9] T. Uchiyama et al. 'Cryogenic Cooling of a Sapphire Mirror-Suspension for Interferometric Gravitational Wave Detectors'. In: *Physics Letters A* 242.4 (June 1998), pp. 211–214. ISSN: 0375-9601. DOI: 10.1016/S0375-9601(98)00205-9. (Visited on 25/01/2021) (cit. on p. 1).

[10] Angus S Bell et al. 'Anomalous Optical Surface Absorption in Nominally Pure Silicon Samples at 1550 Nm'. In: *Classical and Quantum Gravity* 34.20 (Oct. 2017), p. 205013. ISSN: 0264-9381, 1361-6382. DOI: 10.1088/1361-6382/aa8aac. (Visited on 21/10/2020) (cit. on pp. 1, 22, 105, 163).

[11] Albert Einstein. 'Näherungsweise Integration Der Feldgleichungen Der Gravitation'. In: *Sitzungsberichte der Königlich Preußischen Akademie der Wissenschaften (Berlin), Seite 688-696.* (1916). (Visited on 09/04/2021) (cit. on p. 2).

[12] A. Einstein. 'Die Grundlage der allgemeinen Relativitätstheorie'. In: *Annalen der Physik* 354.7 (1916), pp. 769–822. ISSN: 00033804, 15213889. DOI: 10.1002/andp.19163540702. (Visited on 11/10/2023) (cit. on p. 2).

[13] F. A. E. Pirani. 'Gravitational Waves in General Relativity. IV. The Gravitational Field of a Fast-Moving Particle'. In: *Proceedings of the Royal Society of London. Series A, Mathematical and Physical Sciences* 252.1268 (1959), pp. 96–101. ISSN: 0080-4630. JSTOR: 100716. (Visited on 06/01/2024) (cit. on p. 2).

[14] J. Weber. 'Detection and Generation of Gravitational Waves'. In: *Physical Review* 117.1 (Jan. 1960), pp. 306–313. ISSN: 0031-899X. DOI: 10.1103/PhysRev.117.306. (Visited on 23/05/2022) (cit. on p. 2).

[15] Ajit Kembhavi and Pushpa Khare. *Gravitational Waves: A New Window to the Universe*. Singapore: Springer Singapore, 2020. ISBN: 9789811557088 9789811557095. DOI: 10.1007/978-981-15-5709-5. (Visited on 09/05/2022) (cit. on pp. 2, 5, 7, 9).

[16] Thomas Callister et al. 'Polarization-Based Tests of Gravity with the Stochastic Gravitational-Wave Background'. In: *Physical Review X* 7.4 (Dec. 2017), p. 041058. DOI: 10.1103/PhysRevX.7.041058. (Visited on 06/01/2024) (cit. on p. 2).

[17] Gregory Harry, Timothy P. Bodiya and Riccardo DeSalvo, eds. *Optical Coatings and Thermal Noise in Precision Measurement*. Cambridge: Cambridge University Press, 2011. ISBN: 978-0-511-76231-4. DOI: 10.1017/CBO9780511762314. (Visited on 29/10/2020) (cit. on pp. 2, 15, 31, 44, 45).

[18] G. Cella and A. Giazotto. 'Invited Review Article: Interferometric Gravity Wave Detectors'. In: *Review of Scientific Instruments* 82.10 (Oct. 2011), p. 101101. ISSN: 0034-6748. DOI: 10.1063/1.3652857. (Visited on 18/11/2023) (cit. on pp. 2, 9).

[19] Mario Spera, Alessandro Alberto Trani and Mattia Mencagli. 'Compact Binary Coalescences: Astrophysical Processes and Lessons Learned'. In: *Galaxies* 10.4 (Aug. 2022), p. 76. ISSN: 2075-4434. DOI: 10.3390/galaxies10040076. (Visited on 13/06/2024) (cit. on p. 3).

[20] Miriam Cabero et al. 'Observational Tests of the Black Hole Area Increase Law'. In: *Physical Review D* 97.12 (June 2018), p. 124069. DOI: 10.1103/PhysRevD.97.124069. (Visited on 18/10/2023) (cit. on p. 4).

[21] K. Riles. 'Gravitational Waves: Sources, Detectors and Searches'. In: *Progress in Particle and Nuclear Physics* 68 (Jan. 2013), pp. 1–54. ISSN: 0146-6410. DOI: 10.1016/j.ppnp.2012.08.001. (Visited on 18/10/2023) (cit. on pp. 4, 6).

[22] B. S. Sathyaprakash and Bernard F. Schutz. 'Physics, Astrophysics and Cosmology with Gravitational Waves'. In: *Living Reviews in Relativity* 12.1 (Dec. 2009), p. 2. ISSN: 2367-3613, 1433-8351. DOI: 10.12942/lrr-2009-2. (Visited on 11/10/2023) (cit. on p. 4).

[23] Keith Riles. 'Recent Searches for Continuous Gravitational Waves'. In: *Modern Physics Letters A* 32.39 (Dec. 2017), p. 1730035. ISSN: 0217-7323. DOI: 10.1142/S021773231730035X. (Visited on 18/10/2023) (cit. on p. 5).

[24] The LIGO Scientific Collaboration et al. 'Upper Limits on Gravitational Wave Emission from 78 Radio Pulsars'. In: *Physical Review D* 76.4 (Aug. 2007), p. 042001. ISSN: 1550-7998, 1550-2368. DOI: 10.1103/PhysRevD.76.042001. arXiv: gr-qc/0702039. (Visited on 06/01/2024) (cit. on p. 5).

[25] Monica Colpi et al. *LISA Definition Study Report*. Feb. 2024. DOI: 10.48550/arXiv.2402.07571. arXiv: 2402.07571 [astro-ph, physics:gr-qc]. (Visited on 19/02/2024) (cit. on p. 5).

[26] Karan Jani, Deirdre Shoemaker and Curt Cutler. 'Detectability of Intermediate-Mass Black Holes in Multiband Gravitational Wave Astronomy'. In: *Nature Astronomy* 4.3 (Mar. 2020), pp. 260–265. ISSN: 2397-3366. DOI: 10.1038/s41550-019-0932-7. (Visited on 06/01/2024) (cit. on p. 5).

[27] Daniel Kasen et al. 'Origin of the Heavy Elements in Binary Neutron-Star Mergers from a Gravitational-Wave Event'. In: *Nature* 551.7678 (Nov. 2017), pp. 80–84. ISSN: 1476-4687. DOI: 10.1038/nature24453. (Visited on 09/01/2024) (cit. on p. 5).

[28] Jennifer A. Johnson, Brian D. Fields and Todd A. Thompson. 'The Origin of the Elements: A Century of Progress'. In: *Philosophical Transactions of the Royal Society A: Mathematical, Physical and Engineering Sciences* 378.2180 (Aug. 2020), p. 20190301. DOI: 10.1098/rsta.2019.0301. (Visited on 09/01/2024) (cit. on p. 5).

[29] M. Bailes et al. 'Gravitational-Wave Physics and Astronomy in the 2020s and 2030s'. In: *Nature Reviews Physics* 3.5 (May 2021), pp. 344–366. ISSN: 2522-5820. DOI: 10.1038/s42254-021-00303-8. (Visited on 06/08/2021) (cit. on p. 5).

[30] Scott E. Perkins, Nicolás Yunes and Emanuele Berti. 'Probing Fundamental Physics with Gravitational Waves: The next Generation'. In: *Physical Review D* 103.4 (Feb. 2021), p. 044024. DOI: 10.1103/PhysRevD.103.044024. (Visited on 09/01/2024) (cit. on p. 5).

[31] R. A. Hulse and J. H. Taylor. 'Discovery of a Pulsar in a Binary System.' In: *The Astrophysical Journal* 195 (Jan. 1975), pp. L51–L53. ISSN: 0004-637X. DOI: 10.1086/181708. (Visited on 14/11/2023) (cit. on p. 6).

[32] J. M. Weisberg and J. H. Taylor. 'The Relativistic Binary Pulsar B1913+16: Thirty Years of Observations and Analysis'. In: 328 (July 2005), p. 25. DOI: 10.48550/arXiv.astro-ph/0407149. (Visited on 24/10/2023) (cit. on p. 6).

[33] J. Weber. 'Observation of the Thermal Fluctuations of a Gravitational-Wave Detector'. In: *Physical Review Letters* 17.24 (Dec. 1966), pp. 1228–1230. DOI: 10.1103/PhysRevLett.17.1228. (Visited on 26/10/2023) (cit. on p. 6).

[34] Renata Sisto and Arturo Moleti. 'On the Sensitivity of Gravitational Wave Resonant Bar Detectors'. In: *International Journal of Modern Physics D* 13.04 (Apr. 2004), pp. 625–639. ISSN: 0218-2718. DOI: 10.1142/S021827180400475X. (Visited on 02/05/2021) (cit. on p. 6).

[35] Fulvio Ricci and Massimo Bassan. *Experimental Gravitation*. Vol. 998. Lecture Notes in Physics. Cham: Springer International Publishing, 2022. ISBN: 978-3-030-95595-3 978-3-030-95596-0. DOI: 10.1007/978-3-030-95596-0. (Visited on 06/11/2023) (cit. on p. 6).

[36] J. Weber. 'Gravitational-Wave-Detector Events'. In: *Physical Review Letters* 20.23 (June 1968), pp. 1307–1308. DOI: 10.1103/PhysRevLett.20.1307. (Visited on 14/11/2023) (cit. on p. 6).

[37] J. Weber. 'Evidence for Discovery of Gravitational Radiation'. In: *Physical Review Letters* 22.24 (June 1969), pp. 1320–1324. DOI: 10.1103/PhysRevLett.22.1320. (Visited on 14/11/2023) (cit. on p. 6).

[38] J. Weber. 'Anisotropy and Polarization in the Gravitational-Radiation Experiments'. In: *Physical Review Letters* 25.3 (July 1970), pp. 180–184. DOI: 10.1103/PhysRevLett.25.180. (Visited on 14/11/2023) (cit. on p. 6).

[39] Richard L. Garwin and James L. Levine. 'Single Gravity-Wave Detector Results Contrasted with Previous Coincidence Detections'. In: *Physical Review Letters* 31.3 (July 1973), pp. 176–180. DOI: 10.1103/PhysRevLett.31.176. (Visited on 14/11/2023) (cit. on p. 6).

[40] R. W. P. Drever et al. 'Search for Short Bursts of Gravitational Radiation'. In: *Nature* 246.5432 (Dec. 1973), pp. 340–344. ISSN: 1476-4687. DOI: 10.1038/246340a0. (Visited on 14/11/2023) (cit. on p. 6).

[41] Braginskii V.B. *An Upper Limit on the Density of Gravitational Radiation of Extraterrestrial Origin*. 1974 (cit. on p. 6).

[42] P. Astone et al. 'Long-Term Operation of the Rome "Explorer" Cryogenic Gravitational Wave Detector'. In: *Physical Review D* 47.2 (Jan. 1993), pp. 362–375. DOI: 10.1103/PhysRevD.47.362. (Visited on 14/11/2023) (cit. on p. 6).

[43] P. Astone et al. 'The next Science Run of the Gravitational Wave Detector NAUTILUS'. In: *Classical and Quantum Gravity* 19.7 (Mar. 2002), p. 1911. ISSN: 0264-9381. DOI: 10.1088/0264-9381/19/7/392. (Visited on 15/11/2023) (cit. on p. 6).

[44] A De Waard et al. 'MiniGRAIL, the First Spherical Detector'. In: *Classical and Quantum Gravity* 20.10 (May 2003), S143–S151. ISSN: 0264-9381, 1361-6382. DOI: 10.1088/0264-9381/20/10/317. (Visited on 15/11/2023) (cit. on p. 6).

[45] O. D. Aguiar et al. 'The Status of the Brazilian Spherical Detector'. In: *Classical and Quantum Gravity* 19.7 (Mar. 2002), p. 1949. ISSN: 0264-9381. DOI: 10.1088/0264-9381/19/7/397. (Visited on 15/11/2023) (cit. on p. 6).

[46] Francesco Ronga. 'Detection of Gravitational Waves with Resonant Antennas'. In: *Journal of Physics: Conference Series* 39 (May 2006), pp. 18–24. ISSN: 1742-6588, 1742-6596. DOI: 10.1088/1742-6596/39/1/005. (Visited on 26/10/2023) (cit. on p. 6).

[47] Jed Z. Buchwald, ed. *Einstein Was Right: The Science and History of Gravitational Waves*. Princeton University Press, 2020. ISBN: 978-0-691-19454-7. DOI: 10.2307/j.ctvz938v6. JSTOR: j.ctvz938v6. (Visited on 24/10/2023) (cit. on p. 6).

[48] Odylio Denys Aguiar. 'Past, Present and Future of the Resonant-Mass Gravitational Wave Detectors'. In: *Research in Astronomy and Astrophysics* 11.1 (Jan. 2011), p. 1. ISSN: 1674-4527. DOI: 10.1088/1674-4527/11/1/001. (Visited on 26/10/2023) (cit. on pp. 6, 9).

[49] V. Fafone. 'SFERA: The New Spherical Gravitational Wave Detector'. In: *Journal of Physics: Conference Series* 39.1 (May 2006), p. 42. ISSN: 1742-6596. DOI: 10.1088/1742-6596/39/1/010. (Visited on 15/11/2023) (cit. on p. 7).

[50] Rainer Weiss. 'Republication of: Electromagnetically Coupled Broadband Gravitational Antenna'. In: *Springer US* (Nov. 2022). (Visited on 13/06/2024) (cit. on p. 7).

[51] Rana X. Adhikari. 'Gravitational Radiation Detection with Laser Interferometry'. In: *Reviews of Modern Physics* 86.1 (Feb. 2014). ISSN: 0034-6861. DOI: 10.1103/RevModPhys.86.121 (cit. on p. 7).

[52] Jim Hough, Sheila Rowan and B S Sathyaprakash. 'The Search for Gravitational Waves'. In: *Journal of Physics B: Atomic, Molecular and Optical Physics* 38.9 (May 2005), S497–S519. ISSN: 0953-4075, 1361-6455. DOI: 10.1088/0953-4075/38/9/004. (Visited on 26/10/2023) (cit. on p. 7).

[53] Manuel Marchiò. 'Development of an Optical Absorption Measurement System to Characterize KAGRA Sapphire Mirrors and New High-Reflectivity Crystalline Coatings.' PhD thesis (cit. on pp. 8, 33–36).

[54] G. Vajente et al. 'Precision Interferometry for Gravitational Wave Detection: Current Status and Future Trends'. In: 68 (Jan. 2019), pp. 75–148. DOI: 10.1016/bs.aamop.2019.04.002 (cit. on pp. 8, 148).

[55] The LIGO Scientific Collaboration et al. 'Advanced LIGO'. In: *Classical and Quantum Gravity* 32.7 (Mar. 2015), p. 074001. ISSN: 0264-9381. DOI: 10.1088/0264-9381/32/7/074001. (Visited on 25/01/2024) (cit. on pp. 8–10).

[56] Ch Fabry and A. Perot. 'Théorie et Applications d'une Nouvelle Méthode de Spectroscopie Interférentielle'. In: *Annales de Chimie et de Physique, 7. Série* 16 (Jan. 1899) (cit. on p. 9).

[57] R. W. P. Drever et al. 'A Gravity Wave Detector Using Optical Cavity Sensing'. In: *9th International Conference on General Relativity and Gravitation*. 1980, pp. 265–267 (cit. on p. 9).

[58] Massimo Bassan, ed. *Advanced Interferometers and the Search for Gravitational Waves: Lectures from the First VESF School on Advanced Detectors for Gravitational Waves*. Vol. 404. Astrophysics and Space Science Library. Cham: Springer International Publishing, 2014. ISBN: 978-3-319-03791-2 978-3-319-03792-9. DOI: 10.1007/978-3-319-03792-9. (Visited on 15/02/2024) (cit. on pp. 9, 10).

[59] Brian J. Meers. 'Recycling in Laser-Interferometric Gravitational-Wave Detectors'. In: *Physical Review D* 38.8 (Oct. 1988), pp. 2317–2326. DOI: 10.1103/PhysRevD.38.2317. (Visited on 26/10/2023) (cit. on p. 10).

[60] K. A. Strain and B. J. Meers. 'Experimental Demonstration of Dual Recycling for Interferometric Gravitational-Wave Detectors'. In: *Physical Review Letters* 66.11 (Mar. 1991), pp. 1391–1394. DOI: 10.1103/PhysRevLett.66.1391. (Visited on 26/10/2023) (cit. on p. 10).

[61] *Ultra-High Vacuum*. https://www.ligo.caltech.edu/page/vacuum. (Visited on 13/06/2024) (cit. on p. 10).

[62] T. Accadia et al. 'Virgo: A Laser Interferometer to Detect Gravitational Waves'. In: *Journal of Instrumentation* 7.03 (Mar. 2012), P03012. ISSN: 1748-0221. DOI: 10.1088/1748-0221/7/03/P03012. (Visited on 13/06/2024) (cit. on pp. 10, 24).

[63] Fausto Acernese et al. 'Advanced Virgo: A Second-Generation Interferometric Gravitational Wave Detector'. In: *Classical and Quantum Gravity* 32.2 (Jan. 2015), p. 024001. DOI: 10.1088/0264-9381/32/2/024001 (cit. on p. 10).

[64] The KAGRA Collaboration et al. 'Interferometer Design of the KAGRA Gravitational Wave Detector'. In: *Physical Review D* 88.4 (Aug. 2013), p. 043007. DOI: 10.1103/PhysRevD.88.043007. (Visited on 17/05/2021) (cit. on p. 10).

[65] *About "aLIGO" by LIGO CALTECH*. https://www.ligo.caltech.edu/page/about-aligo. (Visited on 12/01/2024) (cit. on p. 10).

[66] *Gravitational waves: Virgo enters its scientific exploitation phase - CNRS - Archives of press releases*. https://archives.cnrs.fr/presse/article/1105. (Visited on 12/01/2024) (cit. on p. 10).

[67] B. Willke et al. 'The GEO 600 Gravitational Wave Detector'. In: *Classical and Quantum Gravity* 19.7 (Mar. 2002), p. 1377. ISSN: 0264-9381. DOI: 10.1088/0264-9381/19/7/321. (Visited on 17/11/2023) (cit. on p. 11).

[68] Masaki Ando and the TAMA Collaboration. 'Current Status of the TAMA300 Gravitational-Wave Detector'. In: *Classical and Quantum Gravity* 22.18 (Aug. 2005), S881. ISSN: 0264-9381. DOI: 10.1088/0264-9381/22/18/S02. (Visited on 17/11/2023) (cit. on p. 11).

[69] LIGO Scientific Collaboration et al. 'Search for Gravitational-Wave Bursts in the First Year of the Fifth LIGO Science Run'. In: *Physical Review D* 80.10 (Nov. 2009), p. 102001. DOI: 10.1103/PhysRevD.80.102001. (Visited on 17/11/2023) (cit. on p. 11).

[70] *2017 Nobel Prize in Physics*. http://www.aps.org/publications/apsnews/updates/nobel17.c (Visited on 17/11/2023) (cit. on p. 11).

[71] Stefano Valenti et al. 'The Discovery of the Electromagnetic Counterpart of GW170817: Kilonova AT 2017gfo/DLT17ck'. In: *The Astrophysical Journal* 848.2 (Oct. 2017), p. L24. ISSN: 2041-8205. DOI: 10.3847/2041-8213/aa8edf. (Visited on 02/05/2021) (cit. on p. 11).

[72] Evan D. Hall. 'Cosmic Explorer: A Next-Generation Ground-Based Gravitational-Wave Observatory'. In: *Galaxies* 10.4 (Aug. 2022), p. 90. ISSN: 2075-4434. DOI: 10.3390/galaxies10040090. (Visited on 05/10/2022) (cit. on pp. 11, 18).

[73] Ish Gupta et al. *Characterizing Gravitational Wave Detector Networks: From A$\^\sharp$ to Cosmic Explorer*. July 2023. DOI: 10.48550/arXiv.2307.10421. arXiv: 2307.10421 [astro-ph, physics:gr-qc]. (Visited on 12/01/2024) (cit. on p. 11).

[74] M. Saleem et al. 'The Science Case for LIGO-India'. In: *Classical and Quantum Gravity* 39.2 (Dec. 2021), p. 025004. ISSN: 0264-9381. DOI: 10.1088/1361-6382/ac3b99. (Visited on 17/11/2023) (cit. on p. 11).

[75] C. S. Unnikrishnan. 'IndIGO and LIGO-India: Scope and Plans for Gravitational Wave Research and Precision Metrology in India'. In: *International Journal of Modern Physics D* 22.1 (2013), p. 1341010. DOI: 10.1142/s0218271813410101 (cit. on p. 11).

[76] Alan Cumming. 'Aspects of Mirrors and Suspensions for Advanced Gravitational Wave Detectors'. PhD thesis (cit. on pp. 13, 15).

[77] Rana X. Adhikari et al. 'A Cryogenic Silicon Interferometer for Gravitational-wave Detection'. In: *arXiv: Instrumentation and Methods for Astrophysics* (Jan. 2020). DOI: 10.1088/1361-6382/ab9143. arXiv: 2001.11173 (cit. on pp. 13, 17, 18, 22, 23, 26, 105).

[78] F. Matichard et al. 'Seismic Isolation of Advanced LIGO: Review of Strategy, Instrumentation and Performance'. In: *Classical and Quantum Gravity* 32.18 (Aug. 2015), p. 185003. ISSN: 0264-9381. DOI: 10.1088/0264-9381/32/18/185003. (Visited on 19/11/2023) (cit. on p. 13).

[79] M. G. Beker et al. 'Seismic Attenuation Technology for the Advanced Virgo Gravitational Wave Detector'. In: *Physics Procedia*. Proceedings of the 2nd International Conference on Technology and Instrumentation in Particle Physics (TIPP 2011) 37 (Jan. 2012), pp. 1389–1397. ISSN: 1875-3892. DOI: 10.1016/j.phpro.2012.03.741. (Visited on 19/11/2023) (cit. on p. 13).

[80] Robert Brown F. R. S. Hon M. R. S. E. & R. I. Acad V.P.L.S. 'XXVII. A Brief Account of Microscopical Observations Made in the Months of June, July and August 1827, on the Particles Contained in the Pollen of Plants; and on the General Existence of Active Molecules in Organic and Inorganic Bodies'. In: *The Philosophical Magazine* 4.21 (Sept. 1828), pp. 161–173. ISSN: 1941-5850. DOI: 10.1080/14786442808674769. (Visited on 24/04/2021) (cit. on p. 13).

[81] Herbert B. Callen and Theodore A. Welton. 'Irreversibility and Generalized Noise'. In: *Physical Review* 83.1 (July 1951), pp. 34–40. DOI: 10.1103/PhysRev.83.34. (Visited on 19/11/2024) (cit. on p. 13).

[82] Richard F. Greene and Herbert B. Callen. 'On the Formalism of Thermodynamic Fluctuation Theory'. In: *Physical Review* 83.6 (Sept. 1951), pp. 1231–1235. DOI: 10.1103/PhysRev.83.1231. (Visited on 19/11/2024) (cit. on p. 13).

[83] Herbert B. Callen and Richard F. Greene. 'On a Theorem of Irreversible Thermodynamics'. In: *Physical Review* 86.5 (June 1952), pp. 702–710. DOI: 10.1103/PhysRev.86.702. (Visited on 19/11/2024) (cit. on p. 13).

[84] Iain William Martin. 'Studies of Materials for Use in Future Interferometric Gravitational Wave Detectors'. PhD thesis (cit. on p. 14).

[85] Peter R. Saulson. 'Thermal Noise in Mechanical Experiments'. In: *Physical Review D* 42.8 (Oct. 1990), pp. 2437–2445. DOI: 10.1103/PhysRevD.42.2437. (Visited on 08/02/2021) (cit. on p. 14).

[86] A. Gillespie and F. Raab. 'Thermally Excited Vibrations of the Mirrors of Laser Interferometer Gravitational-Wave Detectors'. In: *Physical Review D* 52.2 (July 1995), pp. 577–585. DOI: 10.1103/PhysRevD.52.577. (Visited on 15/01/2024) (cit. on p. 14).

[87] D. R. M. Crooks et al. 'Excess Mechanical Loss Associated with Dielectric Mirror Coatings on Test Masses in Interferometric Gravitational Wave Detectors'. In: *Classical and Quantum Gravity* 19.5 (Feb. 2002), p. 883. ISSN: 0264-9381. DOI: 10.1088/0264-9381/19/5/304. (Visited on 18/04/2024) (cit. on p. 14).

[88] Steven D. Penn et al. 'Mechanical Loss in Tantala/Silica Dielectric Mirror Coatings'. In: *Classical and Quantum Gravity* 20.13 (June 2003), p. 2917. ISSN: 0264-9381. DOI: 10.1088/0264-9381/20/13/334. (Visited on 15/01/2024) (cit. on pp. 14, 44).

[89] Yu. Levin. 'Internal Thermal Noise in the LIGO Test Masses: A Direct Approach'. In: *Physical Review D* 57.2 (Jan. 1998), pp. 659–663. ISSN: 0556-2821, 1089-4918. DOI: 10.1103/PhysRevD.57.659. (Visited on 15/10/2020) (cit. on pp. 14, 41).

[90] William Yam, Slawek Gras and Matthew Evans. 'Multi-Material Coatings with Reduced Thermal Noise'. In: *Physical Review D* 91.4 (Feb. 2015), p. 042002. ISSN: 1550-7998, 1550-2368. DOI: 10.1103/PhysRevD.91.042002. arXiv: 1411.3234. (Visited on 08/10/2020) (cit. on pp. 14, 88).

[91] Simon C. Tait et al. 'Demonstration of the Multimaterial Coating Concept to Reduce Thermal Noise in Gravitational-Wave Detectors'. In: *Physical Review Letters* 125.1 (July 2020), p. 011102. ISSN: 0031-9007, 1079-7114. DOI: 10.1103/PhysRevLett.125.011102. (Visited on 01/12/2020) (cit. on pp. 14, 42).

[92] Kieran Craig et al. 'Mirror Coating Solution for the Cryogenic Einstein Telescope'. In: *Physical Review Letters* 122.23 (June 2019), p. 231102. DOI: 10.1103/PhysRevLett.122.231102. (Visited on 21/04/2021) (cit. on pp. 15, 75, 84, 87, 93, 98, 99).

[93] I W Martin et al. 'Effect of Heat Treatment on Mechanical Dissipation in Ta $_2$ O $_5$ Coatings'. In: *Classical and Quantum Gravity* 27.22 (Nov. 2010), p. 225020. ISSN: 0264-9381, 1361-6382. DOI: 10.1088/0264-9381/27/22/225020. (Visited on 18/04/2024) (cit. on pp. 15, 75).

[94] Massimo Granata et al. 'Cryogenic Measurements of Mechanical Loss of High-Reflectivity Coating and Estimation of Thermal Noise'. In: *Optics Letters* 38.24 (Dec. 2013), pp. 5268–5271. ISSN: 1539-4794. DOI: 10.1364/OL.38.005268. (Visited on 03/05/2021) (cit. on pp. 15, 75).

[95] I W Martin et al. 'Low Temperature Mechanical Dissipation of an Ion-Beam Sputtered Silica Film'. In: *Classical and Quantum Gravity* 31.3 (Feb. 2014), p. 035019. ISSN: 0264-9381, 1361-6382. DOI: 10.1088/0264-9381/31/3/035019. (Visited on 05/10/2020) (cit. on p. 15).

[96] Peter G. Murray et al. 'Ion-Beam Sputtered Amorphous Silicon Films for Cryogenic Precision Measurement Systems'. In: *Physical Review D* 92.6 (Sept. 2015), p. 062001. ISSN: 1550-7998. DOI: 10.1103/PhysRevD.92.062001 (cit. on pp. 15, 84).

[97] Massimo Granata et al. 'Amorphous Optical Coatings of Present Gravitational-Wave Interferometers'. In: *Classical and Quantum Gravity* 37.9 (May 2020), p. 095004. ISSN: 0264-9381, 1361-6382. DOI: 10.1088/1361-6382/ab77e9. arXiv: 1909.03737. (Visited on 04/05/2021) (cit. on pp. 15, 46, 67, 70).

[98] A. Amato et al. 'Optical and Mechanical Properties of Ion-Beam-Sputtered ${\mathrm{Nb} and ${\mathrm{TiO}}_{2}\text{\ensuremath{-}}{\mathrm{Nb}}_{2}{\mathrm{O}}_ Thin Films for Gravitational-Wave Interferometers and an Improved Measurement of Coating Thermal Noise in Advanced LIGO'. In: *Physical Review D* 103.7 (Apr. 2021), p. 072001. DOI: 10.1103/PhysRevD.103.072001. (Visited on 26/04/2021) (cit. on p. 15).

[99] . *LIGO Instrument Science White Paper 2021*. 2021 (cit. on p. 15).

[100] S Gras and M Evans. 'Direct Measurement of Coating Thermal Noise in Optical Resonators'. In: *PHYS. REV. D* (2018), p. 7. DOI: 10.1103/PhysRevD.98.122001 (cit. on pp. 15, 51).

[101] Gabriele Vajente et al. 'Low Mechanical Loss ${\mathrm{TiO}}_{2}:{\mathrm{GeO}}_ Coatings for Reduced Thermal Noise in Gravitational Wave Interferometers'. In: *Physical Review Letters* 127.7 (Aug. 2021), p. 071101. DOI: 10.1103/PhysRevLett.127.071101. (Visited on 15/01/2024) (cit. on pp. 15, 43, 45, 60, 61, 63, 64, 70, 72).

[102] Graeme I. McGhee et al. 'Titania Mixed with Silica: A Low Thermal-Noise Coating Material for Gravitational-Wave Detectors'. In: *Physical Review Letters* 131.17 (Oct. 2023), p. 171401. DOI: 10.1103/PhysRevLett.131.171401. (Visited on 17/11/2023) (cit. on pp. 15, 30, 43, 45–48, 50, 55, 72).

[103] M. M. Fejer et al. 'Thermoelastic Dissipation in Inhomogeneous Media: Loss Measurements and Displacement Noise in Coated Test Masses for Interferometric Gravitational Wave Detectors'. In: *Physical Review D* 70.8 (Oct. 2004), p. 082003. DOI: 10.1103/PhysRevD.70.082003. (Visited on 19/11/2023) (cit. on p. 15).

[104] V. B. Braginsky, M. L. Gorodetsky and S. P. Vyatchanin. 'Thermo-Refractive Noise in Gravitational Wave Antennae'. In: *Physics Letters A* 271.5 (July 2000), pp. 303–307. ISSN: 0375-9601. DOI: 10.1016/S0375-9601(00)00389-3. (Visited on 19/11/2023) (cit. on p. 15).

[105] M. Evans et al. 'Thermo-Optic Noise in Coated Mirrors for High-Precision Optical Measurements'. In: *Physical Review D* 78.10 (Nov. 2008), p. 102003. DOI: 10.1103/PhysRevD.78.102003. (Visited on 19/11/2023) (cit. on p. 15).

[106] Raymond Robie. 'Characterisation of the Mechanical Properties of Thin-Film Mirror Coating Materials for Use in Future Interferometric Gravitational Wave Detectors'. PhD thesis (cit. on pp. 15, 46, 75–78, 84, 97).

[107] Carlton M. Caves. 'Quantum-Mechanical Radiation-Pressure Fluctuations in an Interferometer'. In: *Physical Review Letters* 45.2 (July 1980), pp. 75–79. ISSN: 0031-9007. DOI: 10.1103/PhysRevLett.45.75. (Visited on 06/05/2022) (cit. on p. 16).

[108] W A Edelstein et al. 'Limits to the Measurement of Displacement in an Interferometric Gravitational Radiation Detector'. In: *Journal of Physics E: Scientific Instruments* 11.7 (July 1978), pp. 710–712. ISSN: 0022-3735. DOI: 10.1088/0022-3735/11/7/030. (Visited on 23/05/2022) (cit. on p. 16).

[109] Peter R Saulson. *Fundamentals of Interferometric Gravitational Wave Detectors*. WORLD SCIENTIFIC, June 2016. ISBN: 978-981-314-307-4. DOI: 10.1142/10116. (Visited on 18/10/2023) (cit. on p. 16).

[110] Peter R Saulson. *Fundamentals of Interferometric Gravitational Wave Detectors*. 2nd ed. WORLD SCIENTIFIC, Apr. 2017. ISBN: 978-981-314-307-4 978-981-314-619-8. DOI: 10.1142/10116. (Visited on 17/01/2024) (cit. on p. 16).

[111] William Zachary Korth. 'Mitigating Noise in Interferometric Gravitational Wave Detectors'. PhD thesis (cit. on p. 16).

[112] James Lough et al. 'First Demonstration of 6 dB Quantum Noise Reduction in a Kilometer Scale Gravitational Wave Observatory'. In: *Physical Review Letters* 126.4 (Jan. 2021), p. 041102. DOI: 10.1103/PhysRevLett.126.041102. (Visited on 29/03/2024) (cit. on p. 16).

[113] Sheila E. Dwyer, Georgia L. Mansell and Lee McCuller. 'Squeezing in Gravitational Wave Detectors'. In: *Galaxies* 10.2 (Mar. 2022), p. 46. ISSN: 2075-4434. DOI: 10.3390/galaxies10020046. (Visited on 25/05/2022) (cit. on p. 16).

[114] Carlton M. Caves. 'Quantum-Mechanical Noise in an Interferometer'. In: *Physical Review D* 23.8 (Apr. 1981), pp. 1693–1708. DOI: 10.1103/PhysRevD.23.1693. (Visited on 19/11/2023) (cit. on p. 16).

[115] Lisa Barsotti, Jan Harms and Roman Schnabel. 'Squeezed Vacuum States of Light for Gravitational Wave Detectors'. In: *Reports on Progress in Physics* 82.1 (Dec. 2018), p. 016905. ISSN: 0034-4885. DOI: 10.1088/1361-6633/aab906. (Visited on 19/11/2023) (cit. on p. 16).

[116] J. Aasi et al. 'Enhanced Sensitivity of the LIGO Gravitational Wave Detector by Using Squeezed States of Light'. In: *Nature Photonics* 7.8 (Aug. 2013), pp. 613–619. ISSN: 1749-4893. DOI: 10.1038/nphoton.2013.177. (Visited on 19/11/2023) (cit. on p. 16).

[117] Vishal Baibhav et al. 'Gravitational-Wave Detection Rates for Compact Binaries Formed in Isolation: LIGO/Virgo O3 and Beyond'. In: *Physical Review D* 100.6 (Sept. 2019), p. 064060. ISSN: 2470-0010, 2470-0029. DOI: 10.1103/PhysRevD.100.064060. arXiv: 1906.04197. (Visited on 02/05/2021) (cit. on p. 17).

[118] Michele Maggiore et al. 'Science Case for the Einstein Telescope'. In: *Journal of Cosmology and Astroparticle Physics* 2020.03 (Mar. 2020), p. 050. ISSN: 1475-7516. DOI: 10.1088/1475-7516/2020/03/050. (Visited on 10/01/2024) (cit. on p. 17).

[119] M. E. Fine, H. Van Duyne and Nancy T. Kenney. 'Low-Temperature Internal Friction and Elasticity Effects in Vitreous Silica'. In: *Journal of Applied Physics* 25.3 (May 2004), pp. 402–405. ISSN: 0021-8979. DOI: 10.1063/1.1721649. (Visited on 17/01/2024) (cit. on p. 17).

[120] J. W. Marx and J. M. Sivertsen. 'Temperature Dependence of the Elastic Moduli and Internal Friction of Silica and Glass'. In: *Journal of Applied Physics* 24 (Jan. 1953), pp. 81–87. ISSN: 0021-8979. DOI: 10.1063/1.1721138. (Visited on 17/01/2024) (cit. on pp. 17, 76).

[121] Matteo Leonardi. *Sapphire Biref and Abs Comparisson*. LVK 2023 Conference in Toyama, Japan, 2023 (cit. on pp. 17, 23).

[122] R Nawrodt et al. 'High Mechanical Q-factor Measurements on Silicon Bulk Samples'. In: *Journal of Physics: Conference Series* 122 (July 2008), p. 012008. ISSN: 1742-6596. DOI: 10.1088/1742-6596/122/1/012008. (Visited on 15/11/2021) (cit. on p. 17).

[123] K. Ackley et al. 'Neutron Star Extreme Matter Observatory: A Kilohertz-Band Gravitational-Wave Detector in the Global Network'. In: *Publications of the Astronomical Society of Australia* 37 (2020). ISSN: 1323-3580, 1448-6083. DOI: 10.1017/pasa.2020.39. (Visited on 17/05/2021) (cit. on p. 18).

[124] Evan D. Hall et al. 'Gravitational-Wave Physics with Cosmic Explorer: Limits to Low-Frequency Sensitivity'. In: *Physical Review D* 103.12 (June 2021), p. 122004. DOI: 10.1103/PhysRevD.103.122004. (Visited on 20/11/2023) (cit. on pp. 18, 26).

[125] Einstein Telescope Science Team. *Einstein Gravitational Wave Telescope Conceptual Design Study*. 2011 (cit. on pp. 19, 26, 84, 88, 94, 128).

[126] Ryan Lawrence. 'Active Wavefront Correction'. PhD thesis (cit. on p. 20).

[127] Aidan F. Brooks et al. 'Overview of Advanced LIGO Adaptive Optics'. In: *Applied Optics* 55.29 (Oct. 2016), p. 8256. ISSN: 0003-6935, 1539-4522. DOI: 10.1364/AO.55.008256. arXiv: 1608.02934 [astro-ph, physics:physics]. (Visited on 11/08/2022) (cit. on pp. 20, 148, 149).

[128] Aidan F. Brooks et al. 'Point Absorbers in Advanced LIGO'. In: *Applied Optics* 60.13 (May 2021), pp. 4047–4063. ISSN: 2155-3165. DOI: 10.1364/AO.419689. (Visited on 20/11/2023) (cit. on p. 20).

[129] Wenxuan Jia et al. 'Point Absorber Limits to Future Gravitational-Wave Detectors'. In: *Physical Review Letters* 127.24 (Dec. 2021), p. 241102. DOI: 10.1103/PhysRevLett.127.241102. (Visited on 17/12/2021) (cit. on p. 20).

[130] David K. Biegelsen. 'Photoelastic Tensor of Silicon and the Volume Dependence of the Average Gap'. In: *Physical Review Letters* 32.21 (May 1974), pp. 1196–1199. ISSN: 0031-9007. DOI: 10.1103/PhysRevLett.32.1196. (Visited on 24/05/2024) (cit. on p. 20).

[131] Johannes Dickmann et al. 'Temperature-Dependent Photo-Elastic Coefficient of Silicon at 1550 Nm'. In: *Scientific Reports* 13.1 (Nov. 2023), p. 19455. ISSN: 2045-2322. DOI: 10.1038/s41598-023-46819-0. (Visited on 24/05/2024) (cit. on p. 20).

[132] J. Eichholz et al. 'Practical Test Mass and Suspension Configuration for a Cryogenic Kilohertz Gravitational Wave Detector'. In: *Physical Review D* 102.12 (2020), p. 122003. DOI: 10.1103/physrevd.102.122003 (cit. on pp. 21, 23, 26).

[133] Thomas Middelmann et al. 'Thermal Expansion Coefficient of Single Crystal Silicon from 7 K to 293 K'. In: *Physical Review B* 92.17 (Nov. 2015), p. 174113. ISSN: 1098-0121, 1550-235X. DOI: 10.1103/PhysRevB.92.174113. arXiv: 1507.06822. (Visited on 29/06/2021) (cit. on pp. 21, 210).

[134] G. Eddolls. 'Crystalline Silicon Suspensions'. PhD thesis (cit. on pp. 22, 26).

[135] T Akutsu et al. 'Overview of KAGRA: Detector Design and Construction History'. In: *Progress of Theoretical and Experimental Physics* 2021.5 (May 2021), 05A101. ISSN: 2050-3911. DOI: 10.1093/ptep/ptaa125. (Visited on 20/02/2024) (cit. on pp. 23, 24, 210).

[136] Eiichi Hirose et al. 'Characterization of Core Optics in Gravitational-Wave Detectors: Case Study of KAGRA Sapphire Mirrors'. In: *Physical Review Applied* 14.1 (July 2020), p. 014021. ISSN: 2331-7019. DOI: 10.1103/PhysRevApplied.14.014021. (Visited on 26/04/2022) (cit. on p. 23).

[137] A V Cumming et al. 'Silicon Mirror Suspensions for Gravitational Wave Detectors'. In: *Classical and Quantum Gravity* 31.2 (Jan. 2014), p. 025017. ISSN: 0264-9381, 1361-6382. DOI: 10.1088/0264-9381/31/2/025017. (Visited on 03/05/2021) (cit. on p. 23).

[138] A Khalaidovski et al. 'Evaluation of Heat Extraction through Sapphire Fibers for the GW Observatory KAGRA'. In: *Classical and Quantum Gravity* 31.10 (May 2014), p. 105004. ISSN: 0264-9381, 1361-6382. DOI: 10.1088/0264-9381/31/10/105004. (Visited on 13/01/2023) (cit. on p. 23).

[139] L. Busch and S. Grohmann. 'Conceptual Layout of a Helium Cooling System for the Einstein Telescope'. In: *IOP Conference Series: Materials Science and Engineering* 1240.1 (May 2022), p. 012095. ISSN: 1757-899X. DOI: 10.1088/1757-899X/1240/1/012095. (Visited on 22/02/2024) (cit. on p. 23).

[140] Xhesika Koroveshi et al. 'Cryogenic Payloads for the Einstein Telescope: Baseline Design with Heat Extraction, Suspension Thermal Noise Modeling, and Sensitivity Analyses'. In: *Physical Review D* 108.12 (Dec. 2023), p. 123009. DOI: 10.1103/PhysRevD.108.123009. (Visited on 20/02/2024) (cit. on p. 23).

[141] S. M. Aston et al. 'Update on Quadruple Suspension Design for Advanced LIGO'. In: *Classical and Quantum Gravity* 29.23 (Oct. 2012), p. 235004. ISSN: 0264-9381. DOI: 10.1088/0264-9381/29/23/235004. (Visited on 26/06/2024) (cit. on p. 24).

[142] Yusuke Sakakibara et al. 'Performance Test of Pipe-Shaped Radiation Shields for Cryogenic Interferometric Gravitational Wave Detectors'. In: *Classical and Quantum Gravity* 32.15 (July 2015), p. 155011. ISSN: 0264-9381. DOI: 10.1088/0264-9381/32/15/155011. (Visited on 22/02/2024) (cit. on p. 25).

[143] G. Eddolls. *Silicon Suspensions*. L'Aquila, Oct. 2022 (cit. on p. 27).

[144] L. Pinard et al. 'Mirrors Used in the LIGO Interferometers for First Detection of Gravitational Waves'. In: *Applied Optics* 56.4 (Feb. 2017), p. C11. ISSN: 0003-6935, 1539-4522. DOI: 10.1364/AO.56.000C11. (Visited on 12/10/2020) (cit. on pp. 29, 47, 57, 64, 71, 72, 83, 96).

[145] Gregory M Harry and the LIGO Scientific Collaboration. 'Advanced LIGO: The next Generation of Gravitational Wave Detectors'. In: *Classical and Quantum Gravity* 27.8 (Apr. 2010), p. 084006. ISSN: 0264-9381, 1361-6382. DOI: 10.1088/0264-9381/27/8/084006. (Visited on 17/12/2024) (cit. on p. 29).

[146] Anthony E. Siegman. *Lasers*. Mill Valley, California: University Science Books, 1986. ISBN: 978-0-935702-11-8 978-0-19-855713-5 (cit. on p. 29).

[147] D Diksha et al. 'Optical Properties of Germania and Titania at 1064 Nm and at 1550 Nm'. In: *Classical and Quantum Gravity* (2024). ISSN: 0264-9381. DOI: 10.1088/1361-6382/ad3c8c. (Visited on 13/05/2024) (cit. on pp. 30, 67, 68, 70).

[148] Richard J D Tilley. *Understanding Solids*. ISBN: 978-0-470-02084-5 (cit. on p. 30).

[149] Alex Amato. 'Low Thermal Noise Coating for New Generation Gravitational-Wave Detectors'. PhD thesis (cit. on p. 31).

[150] *A.Alexandrovski. Private Communication. 2024* (cit. on p. 31).

[151] *Edmund Optics: Metallic Mirror Coatings*. https://www.edmundoptics.co.uk/knowledge-center/application-notes/optics/metallic-mirror-coatings/. (Visited on 28/11/2024) (cit. on p. 31).

[152] C. M. Humphries and H. Seddon. 'Metallic Film Thickness Requirements for Mirrors in the Infrared'. In: *NASA STI/Recon Technical Report N* 82 (Feb. 1980), p. 13026. (Visited on 30/11/2024) (cit. on p. 31).

[153] Jai Singh, ed. *Optical Properties of Condensed Matter and Applications: Singh/-Optical Properties of Condensed Matter and Applications*. Chichester, UK: John Wiley & Sons, Ltd, Aug. 2006. ISBN: 978-0-470-02194-1 978-0-470-02192-7 978-0-470-02193-4. DOI: 10.1002/0470021942. (Visited on 24/01/2022) (cit. on p. 31).

[154] Olaf Stenzel and Miloslav Ohlídal, eds. *Optical Characterization of Thin Solid Films*. Vol. 64. Springer Series in Surface Sciences. Cham: Springer International Publishing, 2018. ISBN: 978-3-319-75324-9 978-3-319-75325-6. DOI: 10.1007/978-3-319-75325-6. (Visited on 05/05/2021) (cit. on pp. 31, 32).

[155] Max Born, Emil Wolf and A. B. Bhatia. *Principles of Optics: Electromagnetic Theory of Propagation, Interference, and Diffraction of Light*. Seventh (expanded) anniversary edition, 60th anniversary edition. Cambridge: Cambridge University Press, 2019. ISBN: 978-1-108-76991-4 (cit. on p. 31).

[156] G. I. McGhee. 'Studies of New Materials with Low Mechanical and Optical Losses for the Coatings of Future Gravitational Wave Detectors'. PhD thesis. 2024 (cit. on pp. 31, 51, 64, 72).

[157] O. Kienzle, J. Staub and T. Tschudi. 'Description of an Integrated Scatter Instrument for Measuring Scatter Losses of 'superpolished' Optical Surfaces'. In: *Measurement Science and Technology* 5.6 (June 1994), p. 747. ISSN: 0957-0233. DOI: 10.1088/0957-0233/5/6/017. (Visited on 09/02/2025) (cit. on p. 32).

[158] GariLynn Billingsley, Hiroaki Yamamoto and Liyuan Zhang. *CHARACTERIZATION OF ADVANCED LIGO CORE OPTICS* (cit. on pp. 32, 45, 55, 65).

[159] *Challenges of Specifying LIDT for CW Lasers*. https://www.edmundoptics.co.uk/knowledge-center/application-notes/lasers/challenges-of-specifying-lidt-for-cw-lasers/. (Visited on 17/12/2024) (cit. on p. 32).

[160] Caspar Clark et al. 'Comparison of Single-Layer and Double-Layer Anti-Reflection Coatings Using Laser-Induced Damage Threshold and Photothermal Common-Path Interferometry'. In: *Coatings* 6.2 (June 2016), p. 20. DOI: 10.3390/coatings6020020. (Visited on 27/09/2021) (cit. on p. 32).

[161] *The Impact of Surface Particulates and Laser-Accelerated Particles on Continuous-Wave Laser Damage*. 2021. (Visited on 17/12/2024) (cit. on p. 32).

[162] Detlev Ristau. *Laser-Induced Damage in Optical Materials*. CRC Press, Nov. 2014. ISBN: 978-0-429-19371-2 (cit. on p. 32).

[163] A. Alexandrovski et al. 'Photothermal Common-Path Interferometry (PCI): New Developments'. In: *SPIE LASE: Lasers and Applications in Science and Engineering*. Ed. by W. Andrew Clarkson, Norman Hodgson and Ramesh K. Shori. San Jose, CA, Feb. 2009, p. 71930D. DOI: 10.1117/12.814813. (Visited on 12/01/2021) (cit. on pp. 33, 37, 120, 146).

[164] K. V. Vlasova et al. 'High-Sensitive Absorption Measurement in Transparent Isotropic Dielectrics with Time-Resolved Photothermal Common-Path Interferometry'. In: *Applied Optics* 57.22 (Aug. 2018), p. 6318. ISSN: 1559-128X, 2155-3165. DOI: 10.1364/AO.57.006318. (Visited on 15/07/2021) (cit. on p. 33).

[165] Richard D. Snook and Roger D. Lowe. 'Thermal Lens Spectrometry. A Review'. In: *Analyst* 120.8 (Jan. 1995), pp. 2051–2068. ISSN: 1364-5528. DOI: 10.1039/AN9952002051. (Visited on 23/07/2021) (cit. on p. 33).

[166] Simon Bublitz and Christian Mühlig. 'Absolute Absorption Measurements in Optical Coatings by Laser Induced Deflection'. In: *Coatings* 9.8 (July 2019), p. 473. ISSN: 2079-6412. DOI: 10.3390/coatings9080473. (Visited on 20/05/2021) (cit. on p. 33).

[167] Lukas Terkowski. 'Silicon Based Mirror Coatings For Gravitational Wave Detectors'. PhD thesis (cit. on pp. 34, 36).

[168] A Alexandrovski. *PCI Manual 2021*. Tech. rep. STANFORD PHOTO-THERMAL SOLUTIONS (cit. on pp. 35, 39).

[169] *SciPy Documentation — SciPy v1.14.1 Manual*. (Visited on 27/11/2024) (cit. on pp. 37, 114, 125, 158, 163).

[170] Shojiro Nemoto. 'Waist Shift of a Gaussian Beam by a Dielectric Plate'. In: *Applied Optics* 28.9 (May 1989), pp. 1643–1647. ISSN: 2155-3165. DOI: 10.1364/AO.28.001643. (Visited on 22/06/2021) (cit. on p. 38).

[171] Alexei Alexandrovski. *PCI Software Guide*. 2021 (cit. on p. 40).

[172] Gregory M. Harry et al. 'Thermal Noise in Interferometric Gravitational Wave Detectors Due to Dielectric Optical Coatings'. In: *Classical and Quantum Gravity* 19.5 (Feb. 2002), pp. 897–917. ISSN: 0264-9381. DOI: 10.1088/0264-9381/19/5/305. (Visited on 12/10/2020) (cit. on p. 41).

[173] Martin J. Hart et al. 'Medium Range Structural Order in Amorphous Tantala Spatially Resolved with Changes to Atomic Structure by Thermal Annealing'. In: *Journal of Non-Crystalline Solids* 438 (Apr. 2016), pp. 10–17. ISSN: 0022-3093. DOI: 10.1016/j.jnoncrysol.2016.02.005. (Visited on 30/08/2021) (cit. on p. 41).

[174] K. Prasai et al. 'High Precision Detection of Change in Intermediate Range Order of Amorphous Zirconia-Doped Tantala Thin Films Due to Annealing'. In: *Physical Review Letters* 123.4 (July 2019), p. 045501. DOI: 10.1103/PhysRevLett.123.045501. (Visited on 05/05/2021) (cit. on p. 41).

[175] Alex Amato et al. 'Observation of a Correlation Between Internal Friction and Urbach Energy in Amorphous Oxides Thin Films'. In: *Scientific Reports* 10.1 (Feb. 2020), p. 1670. ISSN: 2045-2322. DOI: 10.1038/s41598-020-58380-1. (Visited on 24/07/2024) (cit. on pp. 41, 43).

[176] R. Bassiri et al. 'Correlations between the Mechanical Loss and Atomic Structure of Amorphous TiO2-doped Ta2O5 Coatings'. In: *Acta Materialia* 61.4 (Feb. 2013), pp. 1070–1077. ISSN: 1359-6454. DOI: 10.1016/j.actamat.2012.10.009. (Visited on 10/01/2025) (cit. on p. 41).

[177] O S Heavens. 'Optical Properties of Thin Films'. In: *Reports on Progress in Physics* 23.1 (Jan. 1960), pp. 1–65. ISSN: 00344885. DOI: 10.1088/0034-4885/23/1/301. (Visited on 27/05/2024) (cit. on p. 41).

[178] Jessica Steinlechner et al. 'Coatings for Gravitational Wave Detectors'. In: *Optical Interference Coatings Conference (OIC) 2022*. Vancouver, British Columbia: Optica Publishing Group, 2022, WA.4. ISBN: 978-1-957171-04-3. DOI: 10.1364/OIC.2022.WA.4. (Visited on 10/01/2025) (cit. on p. 42).

[179] Matt Evans et al. *Advanced LIGO Arm Length Stabilisation System Design* (cit. on p. 42).

[180] P Fritschel and D Coyne. *Advanced LIGO Systems Design* (cit. on p. 42).

[181] Jessica Steinlechner et al. 'Optical Absorption of Silicon Nitride Membranes at 1064 Nm and at 1550 Nm'. In: *Physical Review D* 96.2 (July 2017), p. 022007. DOI: 10.1103/PhysRevD.96.022007. (Visited on 16/07/2021) (cit. on p. 43).

[182] Rebecca B. Cummings et al. 'Argon Bubble Formation in Tantalum Oxide-Based Films for Gravitational Wave Interferometer Mirrors'. In: *Optical Materials Express* 11.3 (Mar. 2021), p. 707. ISSN: 2159-3930. DOI: 10.1364/OME.416038. (Visited on 08/09/2022) (cit. on p. 43).

[183] Mariana A. Fazio et al. 'Comprehensive Study of Amorphous Metal Oxide and ${\mathrm{Ta}}_{2}{\mathrm{O}}_{5}$-Based Mixed Oxide Coatings for Gravitationa Wave Detectors'. In: *Physical Review D* 105.10 (May 2022), p. 102008. DOI: 10.1103/PhysRevD.105.102008. (Visited on 26/06/2024) (cit. on pp. 43, 76).

[184] J. López - Medina et al. 'HfO2:Y2O3 Ultrathin Nanolaminate Structures Grown by ALD: Bilayer Thickness and Annealing Temperature Effects on Optical Properties'. In: *Ceramics International* 48.12 (June 2022), pp. 17564–17575. ISSN: 02728842. DOI: 10.1016/j.ceramint.2022.03.025. (Visited on 24/07/2024) (cit. on p. 43).

[185] Brecken Larsen et al. 'Crystallization in Zirconia Film Nano-Layered with Silica'. In: *Nanomaterials* 11.12 (Dec. 2021), p. 3444. ISSN: 2079-4991. DOI: 10.3390/nano11123444. (Visited on 24/07/2024) (cit. on p. 43).

[186] Jessica Steinlechner et al. 'Optical Absorption of Ion-Beam Sputtered Amorphous Silicon Coatings'. In: *Physical Review D* 93.6 (Mar. 2016), p. 062005. ISSN: 2470-0010, 2470-0029. DOI: 10.1103/PhysRevD.93.062005. (Visited on 24/04/2021) (cit. on pp. 44, 86).

[187] R. Birney et al. 'Amorphous Silicon with Extremely Low Absorption: Beating Thermal Noise in Gravitational Astronomy'. In: *Physical Review Letters* 121.19 (Nov. 2018), p. 191101. ISSN: 0031-9007, 1079-7114. DOI: 10.1103/PhysRevLett.121.191101. (Visited on 06/09/2021) (cit. on pp. 44, 45, 84, 87).

[188] M. Molina-Ruiz et al. 'Hydrogen-Induced Ultralow Optical Absorption and Mechanical Loss in Amorphous Silicon for Gravitational-Wave Detectors'. In: *Physical Review Letters* 131.25 (Dec. 2023), p. 256902. DOI: 10.1103/PhysRevLett.131.256902. (Visited on 10/01/2025) (cit. on p. 44).

[189] Ling-Chi Kuo et al. 'Low Cryogenic Mechanical Loss Composite Silica Thin Film for Low Thermal Noise Dielectric Mirror Coatings'. In: *Optics Letters* 44.2 (Jan. 2019), p. 247. ISSN: 0146-9592, 1539-4794. DOI: 10.1364/OL.44.000247. (Visited on 18/12/2020) (cit. on p. 44).

[190] J. Steinlechner et al. 'Silicon-Based Optical Mirror Coatings for Ultrahigh Precision Metrology and Sensing'. In: *Physical Review Letters* 120.26 (June 2018), p. 263602. ISSN: 0031-9007, 1079-7114. DOI: 10.1103/PhysRevLett.120.263602. (Visited on 05/10/2020) (cit. on pp. 44, 86).

[191] Kunihiko Hasegawa et al. 'Molecular Adsorbed Layer Formation on Cooled Mirrors and Its Impacts on Cryogenic Gravitational Wave Telescopes'. In: *Physical Review D* 99.2 (Jan. 2019), p. 022003. DOI: 10.1103/PhysRevD.99.022003. (Visited on 21/01/2021) (cit. on p. 44).

[192] Satoshi Tanioka et al. 'Optical Loss Study of the Cryogenic Molecular Layer Using a Folded Cavity for Future Gravitational-Wave Detectors'. In: *Optics Express* 29.5 (Mar. 2021), pp. 6780–6793. ISSN: 1094-4087. DOI: 10.1364/OE.415921. (Visited on 05/03/2021) (cit. on p. 44).

[193] R. Dupuy et al. 'Electron-Stimulated Desorption from Molecular Ices in the 0.15–2 keV Regime'. In: *Journal of Applied Physics* 128.17 (Nov. 2020), p. 175304. ISSN: 0021-8979, 1089-7550. DOI: 10.1063/5.0021832. (Visited on 03/12/2020) (cit. on p. 44).

[194] Jessica Steinlechner and Iain W. Martin. 'Thermal Noise from Icy Mirrors in Gravitational Wave Detectors'. In: *Physical Review Research* 1.1 (Aug. 2019), p. 013008. ISSN: 2643-1564. DOI: 10.1103/PhysRevResearch.1.013008. (Visited on 08/10/2020) (cit. on p. 44).

[195] Garrett D. Cole et al. 'Tenfold Reduction of Brownian Noise in High-Reflectivity Optical Coatings'. In: *Nature Photonics* 7.8 (Aug. 2013), pp. 644–650. ISSN: 1749-4893. DOI: 10.1038/nphoton.2013.174. (Visited on 17/12/2024) (cit. on p. 44).

[196] G. D. Cole et al. 'Substrate-Transferred GaAs/AlGaAs Crystalline Coatings for Gravitational-Wave Detectors'. In: *Applied Physics Letters* 122.11 (Mar. 2023), p. 110502. ISSN: 0003-6951. DOI: 10.1063/5.0140663. (Visited on 30/01/2024) (cit. on p. 44).

[197] Angie C. Lin et al. 'Epitaxial Growth of GaP/AlGaP Mirrors on Si for Low Thermal Noise Optical Coatings'. In: *Optical Materials Express* 5.8 (Aug. 2015), pp. 1890–1897. ISSN: 2159-3930. DOI: 10.1364/OME.5.001890. (Visited on 30/01/2024) (cit. on p. 44).

[198] J. Steinlechner. 'Development of Mirror Coatings for Gravitational-Wave Detectors'. In: *Philosophical Transactions of the Royal Society A: Mathematical, Physical and Engineering Sciences* 376.2120 (May 2018), p. 20170282. DOI: 10.1098/rsta.2017.0282. (Visited on 09/01/2021) (cit. on pp. 44, 88).

[199] Donald M. Mattox. *Handbook of Physical Vapor Deposition (PVD) Processing*. 2. ed. Amsterdam: Elsevier, 2010. ISBN: 978-0-8155-2037-5 (cit. on pp. 45, 67).

[200] G. Vajente et al. 'Effect of Elevated Substrate Temperature Deposition on the Mechanical Losses in Tantala Thin Film Coatings'. In: *Classical and Quantum Gravity* 35.7 (Feb. 2018), p. 075001. ISSN: 0264-9381. DOI: 10.1088/1361-6382/aaad7c. (Visited on 25/07/2024) (cit. on p. 46).

[201] Xiao Liu et al. 'Hydrogen-Free Amorphous Silicon with No Tunneling States'. In: *Physical Review Letters* 113.2 (July 2014), p. 025503. ISSN: 0031-9007, 1079-7114. DOI: 10.1103/PhysRevLett.113.025503. (Visited on 05/10/2020) (cit. on p. 46).

[202] Wen-Hsiang Wang and Shiuh Chao. 'Annealing Effect on Ion-Beam-Sputtered Titanium Dioxide Film'. In: *Optics Letters* 23.18 (Sept. 1998), p. 1417. ISSN: 0146-9592, 1539-4794. DOI: 10.1364/OL.23.001417. (Visited on 03/05/2021) (cit. on pp. 46, 55, 66, 72).

[203] *Ion Beam Deposited Coatings* (cit. on p. 46).

[204] Mariana Fazio et al. 'Growth and Characterization of Sc_2O_3 Doped Ta_2O_5 Thin Films'. In: *Applied Optics* 59.5 (Feb. 2020), A106–A111. ISSN: 2155-3165. DOI: 10.1364/AO.59.00A106. (Visited on 12/01/2025) (cit. on p. 46).

[205] Zoltán Balogh-Michels et al. 'Crystallization Behavior of Ion Beam Sputtered HfO2 Thin Films and Its Effect on the Laser-Induced Damage Threshold'. In: *Journal of the European Optical Society-Rapid Publications* 17.1 (Mar. 2021), p. 3. ISSN: 1990-2573. DOI: 10.1186/s41476-021-00147-w. (Visited on 11/01/2025) (cit. on pp. 46, 55).

[206] Giulio Favaro et al. 'Reduction of Mechanical Losses in Ion-Beam Sputtered Tantalum Oxide Thin Films via Partial Crystallization'. In: *Classical and Quantum Gravity* 41.10 (Apr. 2024), p. 105009. ISSN: 0264-9381. DOI: 10.1088/1361-6382/ad3c8a. (Visited on 11/01/2025) (cit. on pp. 46, 55).

[207] Carmen S. Menoni et al. 'Survey of Metal Oxides for Coatings of Ultra-Stable Optical Cavities'. In: *Conference on Lasers and Electro-Optics (2021), Paper STu1C.7*. Optica Publishing Group, May 2021, STu1C.7. DOI: 10.1364/CLEO_SI.2021.STu1C.7. (Visited on 09/02/2025) (cit. on p. 47).

[208] *FiveNine Optics*. https://www.fivenineoptics.com/. (Visited on 27/02/2024) (cit. on p. 49).

[209] Wei-Kan Chu, James W. Mayer and Marc-A. Nicolet. 'Chapter 3 - Concepts of Backscattering Spectrometry'. In: *Backscattering Spectrometry*. Ed. by Wei-Kan Chu, James W. Mayer and Marc-A. Nicolet. Academic Press, Jan. 1978, pp. 54–88. ISBN: 978-0-12-173850-1. DOI: 10.1016/B978-0-12-173850-1.50008-9. (Visited on 30/11/2024) (cit. on p. 49).

[210] *Carbolite Gero: Laboratory & Industrial Furnace Manufacturer*. https://www.carbolite-gero.com/. (Visited on 04/11/2024) (cit. on p. 49).

[211] *Laboratoire Des Matériaux Avancés*. http://lma.in2p3.fr/Lmagb.htm. (Visited on 27/05/2024) (cit. on p. 56).

[212] *Cutting Edge Coatings GmbH, Hollerithallee 18, 30419 Han378 Nover, Germany*. https://cutting-edge-coatings.com/en/home-eng/. (Visited on 25/07/2024) (cit. on p. 60).

[213] *Extreme Performance in Optical Coatings*. https://epoc.scot/ (cit. on p. 60).

[214] Mariana Fazio. *Update on TiO2:GeO2 Coatings Developed at EPOC*. Sept. 2024 (cit. on pp. 60, 65).

[215] markborn119. *What Is JGS1, JGS2, JGS3 in Optical Quartz Glass In Singapore|*. July 2021. (Visited on 17/12/2024) (cit. on pp. 61, 62).

[216] *Corning Glass Materials*. https://www.corning.com/media/worldwide/csm/documents/HF (cit. on pp. 61, 62, 67).

[217] M Fazio et al. *Low Thermal Noise Mirror Coatings Utilising Titanium Dioxide and Germanium Dioxide Mixtures*. (Paper under Development) (cit. on pp. 62–65, 73).

[218] *A.Markosyan. Private Communication. 2024* (cit. on pp. 62, 65, 73, 83, 97).

[219] *Heraeus Suprasil 313 Datasheet*. https://sydor.com/wp-content/uploads/Heraeus-SUPRASIL-313-Fused-SIlica.pdf (cit. on p. 62).

[220] Émile Lalande et al. 'Ar Transport and Blister Growth Kinetics in Titania-Doped Germania-Based Optical Coatings'. In: *Classical and Quantum Gravity* 41.11 (May 2024), p. 115013. ISSN: 0264-9381. DOI: 10.1088/1361-6382/ad3ffb. (Visited on 25/07/2024) (cit. on p. 64).

[221] Mariana Fazio. *Updated Results from Ti-Germania Stacks*. July 2024. (Visited on 09/02/2025) (cit. on p. 64).

[222] *PANALYTICAL XRD*. https://www.malvernpanalytical.com/en. (Visited on 09/02/2025) (cit. on p. 65).

[223] *Helia Photonics Ltd – The Ultimate Innovators in Thin Film Optical Coatings*. (Visited on 27/05/2024) (cit. on p. 67).

[224] Le Yang et al. 'Enhanced Medium-Range Order in Vapor-Deposited Germania Glasses at Elevated Temperatures'. In: *Science Advances* 7.37 (Sept. 2021), eabh1117. DOI: 10.1126/sciadv.abh1117. (Visited on 27/01/2025) (cit. on p. 67).

[225] E. Talebian and M. Talebian. 'A General Review on the Derivation of Clausius–Mossotti Relation'. In: *Optik* 124.16 (Aug. 2013), pp. 2324–2326. ISSN: 0030-4026. DOI: 10.1016/j.ijleo.2012.06.090. (Visited on 27/01/2025) (cit. on p. 67).

[226] *High-Performance UV-Vis, Cary 5000 UV-Vis-NIR Spectrophotometer | Agilent*. https://www.agilent.com/en/product/molecular-spectroscopy/uv-vis-uv-vis-nir-spectrosco vis-uv-vis-nir-systems/cary-5000-uv-vis-nir. (Visited on 17/12/2024) (cit. on p. 69).

[227] M. R. Abernathy et al. 'Cryogenic Mechanical Loss Measurements of Heat-Treated Hafnium Dioxide'. In: *Classical and Quantum Gravity* 28.19 (Sept. 2011), p. 195017. ISSN: 0264-9381. DOI: 10.1088/0264-9381/28/19/195017. (Visited on 24/07/2024) (cit. on p. 70).

[228] *C-WAVE Series*. (Visited on 19/07/2024) (cit. on p. 73).

[229] *Materials Project*. https://next-gen.materialsproject.org/apps. (Visited on 10/11/2024) (cit. on p. 74).

[230] Re-Long Chiu and Peng-Heng Chang. 'Thickness Dependence of Refractive Index for Anodic Aluminium Oxide Films'. In: () (cit. on p. 76).

[231] Pradeep Kumar et al. 'Optical Properties of Al_2O_3 Thin Films Grown by Atomic Layer Deposition'. In: *Applied Optics* 48.28 (Oct. 2009), pp. 5407–5412. ISSN: 2155-3165. DOI: 10.1364/AO.48.005407. (Visited on 03/10/2024) (cit. on p. 76).

[232] D R M Crooks et al. 'Experimental Measurements of Mechanical Dissipation Associated with Dielectric Coatings Formed Using SiO $_2$, Ta $_2$ O $_5$ and Al $_2$ O $_3$'. In: *Classical and Quantum Gravity* 23.15 (Aug. 2006), pp. 4953–4965. ISSN: 0264-9381, 1361-6382. DOI: 10.1088/0264-9381/23/15/014. (Visited on 03/10/2024) (cit. on p. 76).

[233] M. E. Fine, H. Van Duyne and Nancy T. Kenney. 'Low-Temperature Internal Friction and Elasticity Effects in Vitreous Silica'. In: *Journal of Applied Physics* 25.3 (Mar. 1954), pp. 402–405. ISSN: 0021-8979. DOI: 10.1063/1.1721649. (Visited on 10/02/2025) (cit. on p. 76).

[234] O. L. Anderson and H. E. Bömmel. 'Ultrasonic Absorption in Fused Silica at Low Temperatures and High Frequencies'. In: *Journal of the American Ceramic Society* 38.4 (1955), pp. 125–131. ISSN: 1551-2916. DOI: 10.1111/j.1151-2916.1955.tb14914.x. (Visited on 10/02/2025) (cit. on p. 76).

[235] R. E. Strakna. 'Investigation of Low-Temperature Ultrasonic Absorption in Fast-Neutron Irradiated Si${\mathrm{O}}_{2}$ Glass'. In: *Physical Review* 123.6 (Sept. 1961), pp. 2020–2026. DOI: 10.1103/PhysRev.123.2020. (Visited on 10/02/2025) (cit. on p. 76).

[236] Anja Schroeter et al. *On the Mechanical Quality Factors of Cryogenic Test Masses from Fused Silica and Crystalline Quartz*. Sept. 2007. arXiv: 0709.4359 [gr-qc]. (Visited on 03/10/2024) (cit. on p. 76).

[237] *Advanced Thin Films*. https://www.idexot.com/about-us-advanced-thin-films. (Visited on 03/10/2024) (cit. on p. 77).

[238] *Model 15 Diamond Wire & Disc Saw* (cit. on p. 78).

[239] *PHOTON RT UV-VIS-MWIR Spectrophotometers for Coaters*. https://www.essentoptics.c (Visited on 03/10/2024) (cit. on p. 79).

[240] *OptiLayer GmbH – OptiLayer GmbH*. (Visited on 03/10/2024) (cit. on p. 79).

[241] Zhao et al. 'Different Techniques of Alumina Film Deposition'. In: *Chinese Optics Letters* 8 (Apr. 2010), pp. 83–86. DOI: 10.3788/COL201008S1.0083 (cit. on pp. 79, 83, 97).

[242] Mario Birkholz. *Thin Film Analysis by X-Ray Scattering*. John Wiley & Sons, Ltd, 2005. ISBN: 978-3-527-60759-4. DOI: 10.1002/3527607595.fmatter. (Visited on 13/02/2025) (cit. on p. 81).

[243] V. Edlmayr et al. 'Thermal Stability of Sputtered Al2O3 Coatings'. In: *Surface and Coatings Technology* 204.9 (Jan. 2010), pp. 1576–1581. ISSN: 0257-8972. DOI: 10.1016/j.surfcoat.2009.10.002. (Visited on 27/01/2025) (cit. on p. 81).

[244] Dung-Sheng Tsai et al. 'Amorphous Silicon Nitride Deposited by an NH3-free Plasma Enhanced Chemical Vapor Deposition Method for the Coatings of the next Generation Laser Interferometer Gravitational Waves Detector'. In: *Classical and Quantum Gravity* 39.15 (July 2022), 15LT01. ISSN: 0264-9381. DOI: 10.1088/1361-6382/ac79f6. (Visited on 27/01/2025) (cit. on pp. 84, 95).

[245] *Gwinc · GitLab*. https://git.ligo.org/gwinc. Aug. 2024. (Visited on 04/10/2024) (cit. on pp. 84, 94, 213).

[246] A. Amato et al. *Development of Ion-Beam Sputtered Silicon Nitride Thin Films for Low-Noise Mirror Coatings of Gravitational-Wave Detectors*. Sept. 2024. DOI: 10.48550/arXiv.2409.07147. arXiv: 2409.07147 [physics]. (Visited on 27/01/2025) (cit. on p. 85).

[247] Matthew Pitkin. 'Prospects of Observing Continuous Gravitational Waves from Known Pulsars'. In: *Monthly Notices of the Royal Astronomical Society* 415.2 (Aug. 2011), pp. 1849–1863. ISSN: 0035-8711. DOI: 10.1111/j.1365-2966.2011.18818.x. (Visited on 10/02/2025) (cit. on p. 99).

[248] David Falta, Robert Fisher and Gaurav Khanna. 'Gravitational Wave Emission from the Single-Degenerate Channel of Type Ia Supernovae'. In: *Physical Review Letters* 106.20 (May 2011), p. 201103. DOI: 10.1103/PhysRevLett.106.201103. (Visited on 10/02/2025) (cit. on p. 99).

[249] Hui Jing Lee et al. 'Absorption Coefficient of Bulk III-V Semiconductor Materials: A Review on Methods, Properties and Future Prospects'. In: *Journal of Electronic Materials* (2022). DOI: 10.1007/s11664-022-09846-7 (cit. on p. 101).

[250] Hieu T. Nguyen et al. 'Temperature Dependence of the Band-Band Absorption Coefficient in Crystalline Silicon from Photoluminescence'. In: *Journal of Applied Physics* 115.4 (Jan. 2014), p. 043710. ISSN: 0021-8979, 1089-7550. DOI: 10.1063/1.4862912. (Visited on 01/05/2021) (cit. on p. 101).

[251] T. Trupke et al. 'Temperature Dependence of the Radiative Recombination Coefficient of Intrinsic Crystalline Silicon'. In: *Journal of Applied Physics* 94.8 (Oct. 2003), pp. 4930–4937. ISSN: 0021-8979, 1089-7550. DOI: 10.1063/1.1610231. (Visited on 14/03/2024) (cit. on pp. 101, 104).

[252] G G Macfarlane et al. 'FINE STRUCTURE IN THE ABSORPTION-EDGE SPECTRUM OF SI'. In: *Physical Review* (1957). DOI: 10.1103/physrev.108.1377 (cit. on p. 101).

[253] T. G. Kim, Jeffrey M. Warrender and Michael J. Aziz. 'Strong Sub-Band-Gap Infrared Absorption in Silicon Supersaturated with Sulfur'. In: *Applied Physics Letters* 88.24 (June 2006), p. 241902. ISSN: 0003-6951. DOI: 10.1063/1.2212051. (Visited on 17/11/2024) (cit. on p. 101).

[254] Jerome Degallaix et al. 'Bulk Optical Absorption of High Resistivity Silicon at 1550 Nm'. In: *Optics Letters* 38.12 (June 2013), p. 2047. ISSN: 0146-9592, 1539-4794. DOI: 10.1364/OL.38.002047. (Visited on 01/03/2021) (cit. on pp. 102, 103).

[255] *A.Bell. Private Communication. 2023* (cit. on pp. 102–104, 183, 186).

[256] Jianming Dai et al. 'Terahertz Time-Domain Spectroscopy Characterization of the Far-Infrared Absorption and Index of Refraction of High-Resistivity, Float-Zone Silicon'. In: *JOSA B* 21.7 (July 2004), pp. 1379–1386. ISSN: 1520-8540. DOI: 10.1364/JOSAB.21.001379. (Visited on 15/04/2024) (cit. on p. 101).

[257] Safa Kasap and Peter Capper, eds. *Springer Handbook of Electronic and Photonic Materials*. Springer Handbooks. Cham: Springer International Publishing, 2017. ISBN: 978-3-319-48931-5 978-3-319-48933-9. DOI: 10.1007/978-3-319-48933-9. (Visited on 17/04/2022) (cit. on pp. 101, 109, 110).

[258] Richard A. Soref and Brian R. Bennett. 'Electrooptical Effects in Silicon'. In: *IEEE Journal of Quantum Electronics* (1987). DOI: 10.1109/jqe.1987.1073206 (cit. on p. 101).

[259] Chin-Yi Tsai and Chin-Yi Tsai. 'Interband and Intraband Absorption Coefficients of Silicon: Theoretical Frameworks and Formulations'. In: *IEEE Journal of Selected Topics in Quantum Electronics* (2020). DOI: 10.1109/jstqe.2019.2943389 (cit. on p. 102).

[260] Martin A. Green. *Silicon Solar Cells: Advanced Principles & Practice*. Sydney, Australia: Centre for Photovoltaic Devices and Systems, 1995. ISBN: 978-0-7334-0994-3 (cit. on p. 102).

[261] *ASTM F723-99: Standard Practice for Conversion Between Resistivity and Dopant Density for Boron-Doped, Phosphorus-Doped, and Arsenic-Doped Silicon* (cit. on p. 103).

[262] J. Degallaix et al. 'Measurement of the Optical Absorption of Bulk Silicon at Cryogenic Temperature and the Implication for the Einstein Telescope'. In: *Classical and Quantum Gravity* 31.18 (Sept. 2014), p. 185010. DOI: 10.1088/0264-9381/31/18/185010 (cit. on pp. 103, 104, 167, 171, 194).

[263] W. Spitzer and H. Y. Fan. 'Infrared Absorption in n-Type Silicon'. In: *Physical Review* 108.2 (Oct. 1957), pp. 268–271. DOI: 10.1103/PhysRev.108.268. (Visited on 08/02/2021) (cit. on pp. 103, 104).

[264] Koji Arai. *Free Carrier Absorption in Silicon*. 2015 (cit. on p. 104).

[265] Jessica Steinlechner et al. 'Optical Absorption Measurements on Crystalline Silicon at 1550nm'. In: *Classical and Quantum Gravity* 30.9 (May 2013), p. 095007. ISSN: 0264-9381, 1361-6382. DOI: 10.1088/0264-9381/30/9/095007. arXiv: 1210.7763. (Visited on 12/03/2021) (cit. on p. 104).

[266] D.K. Schroder, R.N. Thomas and J.C. Swartz. 'Free Carrier Absorption in Silicon'. In: *IEEE Journal of Solid-State Circuits* 13.1 (Feb. 1978), pp. 180–187. ISSN: 0018-9200. DOI: 10.1109/JSSC.1978.1051012. (Visited on 03/08/2022) (cit. on pp. 104, 194).

[267] Walter Dickmann et al. 'Intensity Dependent Deflection Spectroscopy for the Characterization of Absorption Mechanisms in Semiconductors'. In: *Journal of Applied Physics* 128.4 (July 2020), p. 045701. ISSN: 0021-8979. DOI: 10.1063/5.0012702. (Visited on 21/06/2021) (cit. on p. 105).

[268] Roel Baets. 'Nonlinear Absorption in Silicon at Mid-Infrared Wavelengths'. In: (). (Visited on 10/02/2021) (cit. on p. 105).

[269] W Zulehner. 'The Growth of Highly Pure Silicon Crystals'. In: *Metrologia* 31.3 (Jan. 1994), pp. 255–261. ISSN: 0026-1394, 1681-7575. DOI: 10.1088/0026-1394/31/3/012. (Visited on 15/11/2021) (cit. on p. 106).

[270] Flavio Francesco Villa. 'Silicon Properties and Crystal Growth'. In: *Silicon Sensors and Actuators: The Feynman Roadmap*. Ed. by Benedetto Vigna et al. Cham: Springer International Publishing, 2022, pp. 3–33. ISBN: 978-3-030-80135-9. DOI: 10.1007/978-3-030-80135-9_1. (Visited on 03/06/2024) (cit. on pp. 106, 157).

[271] Vemuri Prakash, Abhishek Agarwal and Eswara Krishna Mussada. 'Processing Methods of Silicon to Its Ingot: A Review'. In: *Silicon* 11.3 (June 2019), pp. 1617–1634. DOI: 10.1007/s12633-018-9983-0 (cit. on pp. 106, 107).

[272] Deren Yang, ed. *Handbook of Photovoltaic Silicon*. Springer Reference. Berlin [Heidelberg]: Springer, 2019. ISBN: 978-3-662-56472-1 978-3-662-56471-4 (cit. on pp. 106, 108–110).

[273] Francesca Ferrazza. 'Chapter IB-1 - Crystalline Silicon: Manufacture and Properties'. In: *Practical Handbook of Photovoltaics (Second Edition)*. Ed. by Augustin McEvoy, Tom Markvart and Luis Castañer. Boston: Academic Press, Jan. 2012, pp. 79–97. ISBN: 978-0-12-385934-1. DOI: 10.1016/B978-0-12-385934-1.00004-0. (Visited on 10/07/2024) (cit. on p. 107).

[274] Lihui Song and Xuegong Yu. 'Defect Engineering in Cast Mono-like Silicon: A Review'. In: *Progress in Photovoltaics: Research and Applications* 29.3 (2021), pp. 294–314. ISSN: 1099-159X. DOI: 10.1002/pip.3364. (Visited on 24/01/2022) (cit. on p. 107).

[275] Gabriel Cibira. 'Silicon Resistivity Behaviour'. In: *Advances in Electrical and Electronic Engineering* 19.2 (June 2021), pp. 179–185. DOI: 10.15598/aeee.v19i2.4140 (cit. on p. 108).

[276] Frank M. Kiessling et al. 'Quasi-Monocrystalline Silicon for Low-Noise End Mirrors in Cryogenic Gravitational-Wave Detectors'. In: *Physical Review Research* 4.4 (Oct. 2022), p. 043043. ISSN: 2643-1564. DOI: 10.1103/PhysRevResearch.4.043043. (Visited on 07/09/2023) (cit. on pp. 108, 110, 117, 119, 123, 124, 128, 129).

[277] Zheng Lu and Steven Kimbel. 'Growth of 450 Mm Diameter Semiconductor Grade Silicon Crystals'. In: *Journal of Crystal Growth*. The 16th International Conference on Crystal Growth (ICCG16)/The 14th International Conference on Vapor Growth and Epitaxy (ICVGE14) 318.1 (Mar. 2011), pp. 193–195. ISSN: 0022-0248. DOI: 10.1016/j.jcrysgro.2010.10.122. (Visited on 23/07/2024) (cit. on p. 110).

[278] Alexandra Junkes et al. 'Novel MCz-silicon Material and Application for the Radiation Detection Community'. In: (2017), p. 20 (cit. on p. 110).

[279] Wilfried von Ammon. 'FZ and CZ Crystal Growth: Cost Driving Factors and New Perspectives: FZ and CZ Crystal Growth'. In: *physica status solidi (a)* 211.11 (Nov. 2014), pp. 2461–2470. ISSN: 18626300. DOI: 10.1002/pssa.201400043. (Visited on 06/12/2021) (cit. on p. 110).

[280] Angus S Bell et al. '(Draft) Silicon Test-Masses for Future Gravitational-Wave Detectors: Spatial Characterization of the Optical Absorption at 1550 Nm'. In: (), p. 7 (cit. on pp. 110, 160).

[281] T Aventin et al. *Update on Sapphire Growth in Lyon* (cit. on p. 110).

[282] 'CONVERSION OF UNITS FOR IMPURITY CONCENTRATIONS IN SILICON'. In: (2011), p. 4 (cit. on p. 109).

[283] Yoshio Nishi and Robert Doering, eds. *Handbook of Semiconductor Manufacturing Technology*. 2nd ed. Boca Raton: CRC Press, Jan. 2017. ISBN: 978-1-315-21393-4. DOI: 10.1201/9781420017663 (cit. on pp. 109, 111).

[284] A Markosyan. *Annealing Effects on the Optical Absorption of Magnetic-Field Assisted Czochralski-Grown Crystalline Silicon (MCZ Si)* (cit. on pp. 109, 162, 164, 184).

[285] Iain Martin et al. 'Development of Silicon Mirrors and Coatings'. In: (2017), p. 29 (cit. on pp. 109, 110, 147, 161, 162, 167).

[286] G. Fisher, M. R. Seacrist and R. W. Standley. 'Silicon Crystal Growth and Wafer Technologies'. In: *Proceedings of the IEEE* 100.Special Centennial Issue (May 2012), pp. 1454–1474. ISSN: 0018-9219, 1558-2256. DOI: 10.1109/JPROC.2012.2189786. (Visited on 15/11/2021) (cit. on p. 111).

[287] Yutaka Yoshida and Guido Langouche, eds. *Defects and Impurities in Silicon Materials: An Introduction to Atomic-Level Silicon Engineering*. Vol. 916. Lecture Notes in Physics. Tokyo: Springer Japan, 2015. ISBN: 978-4-431-55799-9 978-4-431-55800-2. DOI: 10.1007/978-4-431-55800-2. (Visited on 01/03/2022) (cit. on p. 111).

[288] David B Tanner. *Optical Effects in Solids*. 2019. ISBN: 978-1-316-67277-8 (cit. on p. 112).

[289] Kazuhiko Ogusu, Keijiro Suzuki and Hajime Nishio. 'Simple and Accurate Measurement of the Absorption Coefficient of an Absorbing Plate by Use of the Brewster Angle'. In: *Optics Letters* 31.7 (Apr. 2006), p. 909. ISSN: 0146-9592, 1539-4794. DOI: 10.1364/OL.31.000909. (Visited on 09/05/2022) (cit. on pp. 113, 115).

[290] *Thorlabs - S425C Thermal Power Sensor Head, Surface Absorber, 0.19 - 20 Mm, 2 mW - 10 W, Ø25.4 Mm*. https://www.thorlabs.com. (Visited on 26/06/2024) (cit. on p. 113).

[291] *SCHOTT NG3, NG4, NG5, NG11, NG12 ND-filters Transmission*. https://www.pgo-online.com/intl/curves/optical_glassfilters/NG12-NG11-NG5-NG4-NG3-filters.html. (Visited on 28/06/2024) (cit. on p. 120).

[292] Jason M. Larkin and Alan J. H. McGaughey. 'Thermal Conductivity Accumulation in Amorphous Silica and Amorphous Silicon'. In: *Physical Review B* 89.14 (Apr. 2014), p. 144303. ISSN: 1098-0121, 1550-235X. DOI: 10.1103/PhysRevB.89.144303. (Visited on 19/12/2024) (cit. on p. 120).

[293] C. A. Londos et al. 'Effect of Oxygen Concentration on the Kinetics of Thermal Donor Formation in Silicon at Temperatures between 350 and 500 °C'. In: *Applied Physics Letters* 62.13 (Mar. 1993), pp. 1525–1526. ISSN: 0003-6951, 1077-3118. DOI: 10.1063/1.108628. (Visited on 26/04/2021) (cit. on pp. 124–126).

[294] U. Gösele and T. Y. Tan. 'Oxygen Diffusion and Thermal Donor Formation in Silicon'. In: *Applied Physics A* 28.2 (June 1982), pp. 79–92. ISSN: 1432-0630. DOI: 10.1007/BF00617135. (Visited on 19/12/2024) (cit. on p. 125).

[295] Endre Suli and David F Mayers. *An Introduction to Numerical Analysis*. 2003 (cit. on pp. 125, 161).

[296] Wenjia Su et al. 'Numerical Analysis and Optimization of Gas Flow and Impurity Control in Directional Solidification Multi-Crystalline Si'. In: *Journal of Crystal Growth* 527 (Dec. 2019), p. 125244. ISSN: 0022-0248. DOI: 10.1016/j.jcrysgro.2019.125244. (Visited on 23/07/2024) (cit. on p. 129).

[297] Iain William Martin and Jessia Steinlechner. *ET MAD Workshop: Silicon Mirrors – an Asymmetric Test Mass Configuration*. Nov. 2024 (cit. on p. 129).

[298] Walter Dickmann et al. 'Key Signal Contributions in Photothermal Deflection Spectroscopy'. In: *Journal of Applied Physics* 126.2 (July 2019), p. 025106. ISSN: 0021-8979. DOI: 10.1063/1.5098304`. (Visited on 24/12/2020) (cit. on pp. 133, 159).

[299] V. Loriette and D. Boccara. 'Absorption of Low-Loss Optical Materials Measured at 1064 Nm by a Position-Modulated Collinear Photothermal Detection Technique'. In: *Applied Optics* 42.4 (Feb. 2003), pp. 649–656. ISSN: 1559-128X. DOI: 10.1364/AO.42.000649 (cit. on p. 133).

[300] Michael Bukshtab. *Applied Photometry, Radiometry, and Measurements of Optical Losses*. Vol. 163. Springer Series in Optical Sciences. Dordrecht: Springer Netherlands, 2012. ISBN: 978-94-007-2164-7 978-94-007-2165-4. DOI: 10.1007/978-94-007-2165-4. (Visited on 29/10/2021) (cit. on pp. 133, 139, 140).

[301] W. B. Jackson et al. 'Photothermal Deflection Spectroscopy and Detection'. In: *Applied Optics* 20.8 (Apr. 1981), p. 1333. ISSN: 0003-6935, 1539-4522. DOI: 10.1364/AO.20.001333. (Visited on 01/12/2020) (cit. on p. 135).

[302] *Single Frequency Fiber Laser up to 15W : CEFL-KILO*. (Visited on 17/11/2024) (cit. on p. 137).

[303] *Jupyter-Widgets/Ipywidgets*. Jupyter Widgets. Nov. 2024. (Visited on 23/11/2024) (cit. on pp. 141, 190).

[304] *Thorlabs - SFL1620P 1620 Nm, 40 mW, Butterfly External Cavity Laser, PM Fiber, FC/APC*. https://www.thorlabs.com. (Visited on 07/01/2025) (cit. on p. 142).

[305] *Thorlabs - PDQ30C Quadrant Detector Sensor Head, 1000 to 1700 Nm*. https://www.thorla (Visited on 07/01/2025) (cit. on p. 142).

[306] *Manual Signal Analyzer Sr780* (cit. on p. 143).

[307] *SR830 Lock-in Amplifier Manual*. https://www.thinksrs.com/downloads/pdfs/manuals/SR (cit. on p. 143).

[308] *Moku:Lab - Liquid Instruments*. https://liquidinstruments.com/products/hardware-platforms/mokulab/. (Visited on 07/01/2025) (cit. on p. 144).

[309] Vladimir A Martinez. 'Far-Infrared Spectroscopy of Shallow Thermal Donors and Dilute Impurities in High-Purity Silicon'. In: (2021), p. 10 (cit. on pp. 147, 161).

[310] Jean-Yves Vinet. 'On Special Optical Modes and Thermal Issues in Advanced Gravitational Wave Interferometric Detectors'. In: *Living Reviews in Relativity* 12.1 (Dec. 2009), p. 5. ISSN: 1433-8351. DOI: 10.12942/lrr-2009-5. (Visited on 08/12/2024) (cit. on pp. 148, 149).

[311] *Finesse 3.0a29 : Simulation Tool for Modelling Laser Interferometers*. (Visited on 08/12/2024) (cit. on p. 148).

[312] *M. Soinenen. (Okmetic) Private Communication. 2024* (cit. on p. 153).

[313] *ASTM International - ASTM F121-83 - Test Method for Interstitial Atomic Oxygen Content of Silicon by Infrared Absorption | GlobalSpec*. https://standards.globalspec.com/st f121-83. (Visited on 10/12/2024) (cit. on p. 153).

[314] *Colloidal Silica Polishing Suspension (CMP Slurry) - Kemet*. https://www.kemet.co.uk/pro k-polishing-suspension. (Visited on 10/12/2024) (cit. on p. 154).

[315] Wolfgang Stumpf. *Investigation and Simulation of the Optical Properties of Doped Silicon*. 2001 (cit. on p. 155).

[316] Serdar Yilmaz. 'The Geometric Resistivity Correction Factor for Several Geometrical Samples'. In: *Journal of Semiconductors* 36.8 (Aug. 2015), p. 082001. ISSN: 1674-4926. DOI: 10.1088/1674-4926/36/8/082001. (Visited on 10/05/2023) (cit. on p. 156).

[317] Alan D. Bristow, Nir Rotenberg and Henry M. van Driel. 'Two-Photon Absorption and Kerr Coefficients of Silicon for 850–2200nm'. In: *Applied Physics Letters* 90.19 (May 2007), p. 191104. ISSN: 0003-6951. DOI: 10.1063/1.2737359. (Visited on 08/09/2021) (cit. on p. 159).

[318] A Markosyan. *Ashot Silicon Slides for FTIR Twin Study*. (Visited on 13/09/2021) (cit. on p. 162).

[319] Ashot Markosyan and Angus Bell. *Optical Properties of a Float-Zone Rectified and Czochralski Grown in a Steady Magnetic Field Crystalline Si* (cit. on pp. 167, 194).

[320] Takayuki Tomaru et al. 'Cryogenic Measurement of the Optical Absorption Coefficient in Sapphire Crystals at 1.064 Mm for the Large-Scale Cryogenic Gravitational Wave Telescope'. In: *Physics Letters A* 283.1-2 (May 2001), pp. 80–84. ISSN: 03759601. DOI: 10.1016/S0375-9601(01)00191-8. (Visited on 11/01/2021) (cit. on p. 167).

[321] Behshad Roshanzadeh. 'Development and Demonstration of a Pico-Watt Calorimeter for Optical Absorption Spectroscopy'. PhD thesis (cit. on pp. 168, 200).

[322] I.A. Bajenova et al. 'A New Thermodynamic Description of Pure Silicon from 0 K at 1 Bar'. In: *Calphad* 81 (June 2023), p. 102554. ISSN: 03645916. DOI: 10.1016/j.calphad.2023.102554. (Visited on 03/07/2023) (cit. on p. 169).

[323] Mikhail N. Polyanskiy. 'Refractiveindex.Info Database of Optical Constants'. In: *Scientific Data* 11.1 (Jan. 2024), p. 94. ISSN: 2052-4463. DOI: 10.1038/s41597-023-02898-2. (Visited on 09/02/2025) (cit. on p. 172).

[324] *Montana Instruments | Home*. https://www.montanainstruments.com/. (Visited on 09/01/2025) (cit. on pp. 171, 173).

[325] *GE Low Temperature Varnish (59-C5-101) - Adhesives*. https://estore.oxinst.com/uk/produ consumables/adhesives-&-tapes/adhesives/zidC5-101. (Visited on 13/02/2025) (cit. on p. 172).

[326] *Cernox® | Lake Shore Cryotronics*. https://www.lakeshore.com/products/categories/overvi products/cryogenic-temperature-sensors/cernox. (Visited on 30/01/2025) (cit. on pp. 175, 176).

[327] *Lake Shore - Temperature Measurement and Control Catalog* (cit. on pp. 175–177).

[328] *Lake Shore Selection Guide*. https://qd-uki.co.uk/wp-content/uploads/2023/01/Lake-Shore-Temperature-Sensors-Selection-Guide.pdf (cit. on p. 175).

[329] *Lake Shore Model 336 Temperature Controller* (cit. on pp. 176, 177).

[330] *National Instruments - LABVIEW*. https://www.ni.com/en.html (cit. on p. 179).

[331] *ETpathfinder-Design-Report* (cit. on p. 189).

[332] A Utina et al. 'ETpathfinder: A Cryogenic Testbed for Interferometric Gravitational-Wave Detectors'. In: *Classical and Quantum Gravity* 39.21 (Sept. 2022), p. 215008. ISSN: 0264-9381. DOI: 10.1088/1361-6382/ac8fdb. (Visited on 13/02/2025) (cit. on p. 189).

[333] Amani Garvin, Mentor Andrew Wade and Rana Adhikari. 'Characterizing Bulk Scatter in Crystalline Silicon'. In: (), p. 13. DOI: https://dcc.ligo.org/LIGO-T1700275-v1 (cit. on p. 195).

[334] Zeno Tornasi. *Optical Scattering at 1550 Nm from Bulk Magnetic Czochralski Silicon*. 2017. (Visited on 18/08/2021) (cit. on p. 195).

[335] *Acktar Black Coatings*. https://acktar.com/coating-type/metal-velvet/. (Visited on 23/02/2025) (cit. on p. 196).

[336] *IKZ has joined the international Einstein Telescope collaboration as a Research Unit (RU-Berlin)*. https://www.ikz-berlin.de/en/public-relations/news/article/ikz-has-joined-the-international-einstein-telescope-collaboration-as-a-research-unit-ru-berlin. (Visited on 10/02/2025) (cit. on p. 208).

[337] *Research | DZA | Deutsches Zentrum Für Astrophysik*. https://www.deutscheszentrumastro (Visited on 10/02/2025) (cit. on p. 208).

[338] C. J. Glassbrenner and Glen A. Slack. 'The Thermal Conductivity of Germanium and Silicon between 2 an d 300° K'. In: *Physical Review* 134.4A (May 1964), A1058–A1069. DOI: 10.1103/PhysRev.134.A1058. (Visited on 01/05/2021) (cit. on p. 210).

[339] A. C. DeFranzo and B. G. Pazol. 'Index of Refraction Measurement on Sapphire at Low Temperatures and Visible Wavelengths'. In: *Applied Optics* 32.13 (May 1993), pp. 2224–2234. ISSN: 2155-3165. DOI: 10.1364/AO.32.002224. (Visited on 29/04/2024) (cit. on p. 210).

[340] C.T. Taylor et al. 'Measurement of the Thermal Expansion Coefficient of a Cryogenic All-Sapphire Optical Cavity'. In: *Proceedings of 20th Biennial Conference on Precision Electromagnetic Measurements* (1996), pp. 134–135. DOI: 10.1109/CPEM.1996.546654. (Visited on 24/05/2024) (cit. on p. 210).

[341] Haruka Abe, Hideyuki Kato and Tetsuya Baba. 'Specific Heat Capacity Measurement of Single-Crystalline Silicon as New Reference Material'. In: *Japanese Journal of Applied Physics* 50.11 (Nov. 2011), 11RG01. ISSN: 0021-4922, 1347-4065. DOI: 10.1143/JJAP.50.11RG01. (Visited on 15/11/2021) (cit. on p. 210).

[342] Liyang Yue et al. 'Light Absorption in Perovskite Solar Cell: Fundamentals and Plasmonic Enhancement of Infrared Band Absorption'. In: *Solar Energy* 124 (Feb. 2016), pp. 143–152. ISSN: 0038-092X. DOI: 10.1016/j.solener.2015.11.028. (Visited on 19/10/2024) (cit. on p. 209).

[343] O. Arnon and P. Baumeister. 'Electric Field Distribution and the Reduction of Laser Damage in Multilayers'. In: *Applied Optics* 19.11 (June 1980), p. 1853. ISSN: 0003-6935, 1539-4522. DOI: 10.1364/AO.19.001853. (Visited on 12/04/2022) (cit. on pp. 211, 212).

[344] Gautam Venugopalan et al. *Global Optimization of Multilayer Dielectric Coatings for Precision Measurements*. Dec. 2023. DOI: 10.48550/arXiv.2110.13437. arXiv: 2110.13437 [astro-ph, physics:physics]. (Visited on 09/02/2024) (cit. on p. 211).

[345] Steven J. Byrnes. 'Multilayer Optical Calculations'. In: *arXiv:1603.02720 [physics]* (Dec. 2020). arXiv: 1603.02720 [physics]. (Visited on 20/09/2021) (cit. on p. 212).

[346] *TFCalc Demo and Manual*. http://www.sspectra.com/demo.html. (Visited on 15/07/2024) (cit. on p. 212).